Electronic Thesis and Dissertation Repository

1-10-2014 12:00 AM

Effects of Surface Topographies on Heat and Fluid Flows

Hadi Vafadar Moradi
The University of Western Ontario

Supervisor
Dr. Jerzy Maciej Floryan
The University of Western Ontario

Graduate Program in Mechanical and Materials Engineering
A thesis submitted in partial fulfillment of the requirements for the degree in Doctor of Philosophy
© Hadi Vafadar Moradi 2014

Follow this and additional works at: https://ir.lib.uwo.ca/etd

Recommended Citation

Effects of Surface Topographies on Heat and Fluid Flows

(Thesis format: Monograph)

by

Hadi Vafadar Moradi

Graduate Program in Engineering Science
Department of Mechanical and Materials Engineering

A thesis submitted in partial fulfillment
of the requirements for the degree of
Doctor of Philosophy

The School of Graduate and Postdoctoral Studies
The University of Western Ontario
London, Ontario, Canada

Abstract

Responses of annular and planar flows to the introduction of grooves on the bounding surfaces have been analyzed. The required spectral algorithms based on Fourier and Chebyshev expansions have been developed. The difficulties associated with the irregularities of the physical domain have been overcome using either the immersed boundary conditions (IBC) concept or the domain transformation method (DT).

Steady flows in annuli bounded by walls with longitudinal grooves have been studied. Analysis of pressure losses showed that the groove-induced changes can be represented as a superposition of a pressure drop due to a change in the average position of the bounding cylinders and a pressure drop due to the flow modulations induced by the shape of the grooves. The former effect can be evaluated analytically while the latter requires explicit computations. It has been shown that the reduced-order model is an effective tool for extraction of features of the groove geometry that lead to flow modulations relevant to drag generation. It has been shown that the presence of the longitudinal grooves may lead to a reduction of the pressure loss in spite of an increase of the wetted surface area. The form of the optimal grooves from the point of view of the maximization of the drag reduction has been determined.

When mixing augmentation is not available, heat can be transported across micro-channels by conduction only. A method to increase this heat flow has been proposed. The method relies on the use of grooves parallel to the flow direction. It has been shown that it is possible to find grooves that can increase the heat flow and, at the same time, can decrease the pressure losses. The optimal groove shape that maximizes the overall system performance has been determined. Since it has been assumed that the flow must be laminar, it is of interest to determine the maximum Reynolds number for which this assumption remains valid.

The stability characteristics of flow in a grooved channel have been studied. Only disturbances corresponding to the travelling waves in the limit of zero groove amplitude have been found. It has been shown that disturbances corresponding to two-dimensional waves in a smooth channel play the critical role in the grooved channel. The highly three-dimensional disturbance flow topology at the onset of the instability has been described. It has been demonstrated that the presence of the grooves leads to flow stabilization for groove wave

numbers $\beta < \beta_{tran} \approx 4.22$ and flow destabilization for larger β. The stabilizing/destabilizing effects increase with the groove amplitude. Variations of the critical Reynolds number over the whole range of groove wave numbers and groove amplitudes of interest have been determined. Special attention has been paid to the effects of long wavelength, drag reducing grooves. It has been shown that such grooves lead to a small increase of the critical Reynolds number compared with the smooth channel.

Keywords

Co-Authorship Statement

The following dissertation is presented in the monograph format. Chapters 2 through 5 are based on manuscripts that have been previously published, or submitted, or finalized for submission. I, Hadi Vafadar Moradi, am the first author of all these manuscripts with Prof. J. M. Floryan as the co-author.

To my wife and my parents

for their endless love, encouragement and support.

Acknowledgments

It is a pleasure to thank the many people who made this thesis possible. It is difficult to overstate my gratitude to my Ph.D. supervisor, Dr. Jerzy Maciej Floryan. I will remain indebted to Prof. Floryan for his precious time, patience, enthusiasm, inspiration, and his great efforts to explain things clearly and simply. The completion of this dissertation would not have been possible without his incomparable assistance and invaluable guidance.

I would like to extend my sincerest thanks to the member of my advisory committee, Dr. A. G. Straatman, for his valuable suggestions and encouragement.

I would also like to thank all of my colleagues (past and present), Dr. Syed Zahid Husain, Dr. Mohammad Zakir Hossain, Dr. Alireza Mohammadi, Mohammad Fazel Bakhsheshi, David César Del Rey Fernandez, Ali Asgarian for their friendship, cooperation and helping attitude. I am particularly grateful to Alireza not only for the insightful scientific discussions I had with him that have been tremendously helpful for me in achieving my research objectives but also because of friendship, courage, motivation, and support I have received from him.

Words are not enough to express my gratitude towards my wife, Shima Ahmadi. Without her unconditional love, encouragement, tremendous patience and understanding, I would not have been able to accomplish my goals.

Lastly, and most importantly, I wish to thank my parents, Ali Vafadar Moradi and Marziyeh Vafadar Moradi. Their love provided my inspiration and was my driving force. I owe them everything and wish I could show them just how much I love and appreciate them.

Table of Contents

List of Figures

List of Appendices

List of Abbreviations, Symbols, Nomenclature

Abbreviations

APF	Annular Poiseuille flow
DT	Domain transformation
FFT	Fast Fourier transform
HPF	Hagen-Poiseuille flow
HTE	Heat transfer enhancement
IB	Immersed boundary
IBC	Immersed boundary conditions
LES	Large eddy simulation
NSERC	Natural sciences and engineering research council
NURBS	Non-uniform rational B-spline
OS	Orr-Sommerfeld
PPF	Planar Poiseuille flow
TS	Tollmien-Schlichting

Nomenclature used in Chapter 1

k	Average height of roughness
Re_k	Roughness Reynolds number
U_k	Undisturbed velocity at height k
ν	Kinematic viscosity

Nomenclature shared in Chapters 2–5

D	Derivative with respect to the transverse direction
$H_{in}^{(n)}, H_{out}^{(n)}$	Fourier coefficients of the groove geometries at the inner and outer cylinders
$H_L^{(n)}, H_U^{(n)}$	Fourier coefficients of the groove geometries at the lower and upper walls
N_A	Number of Fourier modes used in description of geometry of the grooves

N_M	Number of Fourier modes used for discretization in the direction associated with periodicity of the grooves
N_T	Number of Chebyshev polynomials used for discretization of the modal functions in the transverse direction
Pr	Prandtl number
R_1	Average radius of the inner annulus
Re	Reynolds number
T_k	Chebyshev polynomials of the kth order
U_{max}	Maximum of the streamwise velocity component of the reference flow
c_p	Specific heat
i	Imaginary unit
k	Thermal conductivity
p	Pressure
ρ	Density
μ	Dynamic viscosity
ν	Kinematic viscosity
$\langle f, g \rangle$	Inner product of two functions
in, out	Inner and outer cylinders (as subscript)
U, L	Upper and lower walls (as subscript)
$*$	Complex conjugate (as superscript)

Nomenclature used in Chapter 2

A_{in}, A_{out}	Groove locations at the inner and outer cylinders in the transformed domain
C	Pressure normalization constant
E_i	Coefficients of the governing equation for the field equation
$F_{in}^{(n)}, F_{out}^{(n)}$	Coefficients of Fourier expansions representing velocity of the reference flow at the inner and outer cylinders
$G_k^{(n)}$	Coefficients of the Chebyshev expansions representing modal functions in the Fourier expansion of the stream function

$G_{rr,k}^{(n)}, G_{zr,k}^{(n)}, G_{zz,k}^{(n)}$	Coefficients of the Chebyshev expansions of the modal functions in the Fourier expansions representing velocity products
L	Average annulus opening
N_R	Number of Fourier modes used to represent the function r^{-1} evaluated at the inner and outer cylinders
N_S	Number of Fourier modes used to describe the Chebyshev polynomials and their derivatives evaluated at the inner and outer cylinders
$P^{(n)}$	Modal functions in the Fourier expansion of the pressure field
Q	Volume flow rate
$Q_{total}, Q_{ref}, Q_{mod}$	Volume flow rates of the total, reference, and modification flows
RF	Relaxation factor
R_{in}, R_{out}	Locations of the groove extremities at the inner and outer cylinders
S	Groove amplitude
$Z_{in}^{(n)}, Z_{out}^{(n)}$	Fourier coefficients of the Fourier expansion of the function r^{-1} evaluated at the inner and outer cylinders
c	Constant of transformation for the IBC method
$d_{in,k}^{(n)}, d_{out,k}^{(n)}$	Coefficients of the Fourier expansions of the first derivative of the Chebyshev polynomials evaluated at the inner and outer cylinders
r_{in}, r_{out}	Locations of the inner and outer cylinders
v_z, v_r	Axial and radial components of velocity vector
$\{v_z v_z\}, \{v_z v_r\}, \{v_r v_r\}$	Velocity products in physical space
$v_{rr}^{(n)}, v_{rz}^{(n)}, v_{zz}^{(n)}$	Modal functions in the Fourier expansions of the velocity products
$w_{in,k}^{(n)}, w_{out,k}^{(n)}$	Coefficients of the Fourier expansions representing the Chebyshev polynomials evaluated at the inner and outer cylinders
z, r, θ	Axial, radial, and circumferential directions
L, x, R	Coefficients matrix, vector of unknowns and the right-hand-side vector
$\mathbf{x_{comp}}$	Current solution
A, B, C, D	Different sections of the re-arranged coefficients matrix **L**
$\mathbf{x_1}$	Vector of unknowns containing $G_k^{(n)}$ for $n \in [-N_M, N_M]$ and $k \in [4, N_T]$

$\mathbf{x_2}$	Vector of unknowns containing $G_k^{(n)}$ for $n \in [-N_M, N_M]$ and $k \in [0,3]$
Γ	Factor in the coordinate transformation for the IBC method
α	Groove wave number in the axial direction
λ	Groove wavelength in the axial direction
ξ	Transformed radial coordinate
ξ_{in}, ξ_{out}	Geometries of the inner and outer cylinders expressed in the transformed radial coordinate
$\phi^{(n)}$	Modal function in the Fourier expansion representing the stream function
ψ	Stokes stream function
ω	Weight function
$\|V_{in}\|_\infty$	L_∞ norm of error in the velocity vector in the whole computational domain
$\|D\phi^{(n)}\|_\omega$	Chebyshev norm for $D\phi^{(n)}$
0, 1	Reference flow and flow modifications (as subscript)

Nomenclature used in Chapter 3

$A_{1,in}, \dots, A_{n,in}$	Fourier coefficients in the Fourier expansion representing the groove geometry at the inner cylinder expressed in terms of real variables
$A_{1,out}, \dots, A_{n,out}$	Fourier coefficients in the Fourier expansion representing the groove geometry at the outer cylinder expressed in terms of real variables
$A_{grooved}, A_{smooth}$	Cross-sectional area of the grooved and smooth annuli
A, B	Geometric functions
Er	Error in the evaluation of the pressure gradient
$F_{A,1}, F_{A,2}, F_{A,3}, F_{A,4}$	Geometric coefficients in boundary oriented coordinates system
$F_{total,z}$	Total axial component of the shear stress acting on the wall
$G_k^{(n)}$	Unknown coefficients of the Chebyshev expansion of the modal function of the axial velocity component
$G_{l,w1}^{(n)}, G_{l,w2}^{(n)}, G_{l,w3}^{(n)}$	Coefficients of the Chebyshev expansions representing the geometrical coefficients
L	Gap between the reference cylinders

M	Number of identical grooves along the circumference
Q	Flow rate
$R_{in,c}, R_{out,c}$	Correction in the location of the grooved inner and outer cylinders that must be applied in order to have the same cross-sectional area as the smooth cylinder
$S_{ave,in}, S_{ave,out}$	Shifts in the average locations of the grooves at the inner and outer cylinders
S_{in}	Groove amplitude at the inner cylinder
$S_{in,i}, S_{in,o}$	Maximum permissible depth and height of the grooves at the inner cylinder
S_{out}	Groove amplitude at the outer cylinder
$S_{out,i}, S_{out,o}$	Maximum permissible depth and height of the grooves at the outer cylinder
W_1, W_2, W_3, W_4	Geometrical coefficients in the polar coordinates system
$dF_{total,z}$	Axial component of the shear stress acting on the wall
f	Friction factor
n_r, n_θ	Normal unit vector pointing outward in the r and θ directions
$\hat{p}_0, \hat{p}_1, \hat{Q}_0, \hat{Q}_1, \hat{v}_0, \hat{v}_1$	Terms in the asymptotic expansions for the pressure field, the volume flow rate, and the axial velocity component
r_{in}, r_{out}	Locations of the inner and outer cylinders in radial direction
t	Distance measured along the inner cylinder
v	Axial velocity component
$w_1^{(n)}, w_2^{(n)}, w_3^{(n)}, w_4^{(n)}$	Coefficients of Fourier expansions expressing the geometrical coefficients
y	Distance measured outward from the inner cylinder
y_{in}, y_{out}	Locations of the inner and outer cylinders in boundary oriented coordinates
z, r, θ	Axial, radial, and circumferential directions
α	Groove wave number
η, ξ	Transverse and circumferential directions in the computational domain

$\varphi_{2,in}, \dots, \varphi_{n,in}$	Phase shifts between modes in the Fourier expansion describing geometry of the grooves at the inner cylinder expressed in terms of real variables
$\varphi_{1,out}, \dots, \varphi_{n,out}$	Phase shifts between modes in the Fourier expansion describing geometry of the grooves at the outer cylinder expressed in terms of real variables
$\phi^{(n)}$	Modal function in the Fourier expansions expressing the axial velocity
$\tau_{rz}, \tau_{\theta z}$	Component of the stress tensor
$0, 1$	Reference flow and flow modifications (as subscript)

Nomenclature used in Chapter 4

$A_{1,L}, \dots, A_{n,L}$	Coefficients of Fourier expansion describing groove geometry at the lower wall expressed in terms of real variables
$A_{1,U}, \dots, A_{n,U}$	Coefficients of Fourier expansion describing groove geometry at the upper wall expressed in terms of real variables
G_1, G_2, G_3, G_4	Geometric coefficients
M	Volume flow rate
Q	Heat transfer per unit length
S_L	Groove amplitude at the lower wall
$S_{L,min}, S_{L,max}$	Maximum permissible depth and height of the grooves at the lower wall
$S_{U,min}, S_{U,max}$	Maximum permissible depth and height of the grooves at the upper wall
T_C, T_H	Temperatures of the cold and hot plates
c	Pressure normalization constant
dF_z	Component of the shear stress acting on the wall in the z-direction
f	Friction factor
n_x, n_y	Normal unit vector pointing outward in the x- and y- directions
q	Local heat flux
y_L, y_U	Locations of the lower and upper walls
Ω	Thermal enhancement factor
α	Groove wave number in the x-direction

β	Weight factor
γ	Adjustment factor
θ	Dimensionless temperature
$\hat{\theta}_0, \hat{\theta}_1, \hat{\theta}_2, \hat{\theta}_3$	Terms in the asymptotic expansions for temperature
λ	Groove wavelength
η, ξ	Transverse and spanwise directions in the computational domain
$\eta_x, \eta_{xx}, \eta_y$	Geometric derivatives
τ_{xz}, τ_{yz}	Components of stress tensors
$\varphi_{2,L}, \dots, \varphi_{n,L}$	Phase shifts between modes in the Fourier expansion describing geometry of the grooves at the lower wall expressed in terms of real variables
$\varphi_{1,U}, \dots, \varphi_{n,U}$	Phase shifts between modes in the Fourier expansion describing geometry of the grooves at the lower wall expressed in terms of real variables
0	Reference smooth channel (as subscript)

Nomenclature used in Chapter 5

A_L, A_U	Groove locations at the lower and upper walls in the transformed y-direction
E	Eigenvector
$G_{k,v}^{(m)}, G_{k,\eta}^{(m)}$	Coefficients of the Chebyshev expansions of the vertical components of the disturbance velocity and vorticity
Q_0	Volume flow rate of the reference flow
P_0, P_1, P_2, P_3	Terms in the asymptotic expansions for the pressure
U_0, U_1, U_2, U_3	Terms in the asymptotic expansions for the streamwise velocity component
$d_{L,k}^{(n)}, d_{L,k}^{(n)}$	Coefficients of the Fourier expansions for the derivatives of the Chebyshev polynomials evaluated at the lower and upper walls
$g_u^{(m)}, g_v^{(m)}, g_w^{(m)}$	Modal functions in the Fourier expansions for the disturbance velocity components in x-, y-, and z-directions

$g_\xi^{(m)}, g_\eta^{(m)}, g_\varphi^{(m)}$	Modal functions in the Fourier expansions for the disturbance vorticity components in the x-, y-, and z-directions
u, v, w	Components of the velocity vector in the x-, y-, and z-directions
$u_1^{(n)}$	Modal function in the Fourier expansion for the flow modification
$w_{L,k}^{(n)}, w_{L,k}^{(n)}$	Coefficients of the Fourier expansions for the first derivative of the Chebyshev polynomials evaluated at the lower and upper walls
y_L, y_U	Locations of the lower and upper walls
y_t, y_b	Locations of the rib extremities at the upper and lower walls
$\hat{y}$	Transformed y-direction
Γ	Constant in the coordinate transformation for the IBC method
β	Groove wave number in the z-direction
δ	Disturbance wave number in the x-direction
μ	Disturbance wave number in the z-direction
σ	Eigenvalue
σ_i	Rate of growth of disturbances
σ_r	Frequency of disturbances
ψ_0	Stream function of the reference flow
ψ_1	Stream function of the modification flow
ζ, χ	Transverse and spanwise directions in the computational domain
$\zeta_x, \zeta_z, \zeta_{zz}$	Geometric derivatives
ξ, η, φ	Components of the vorticity vector in the x-, y-, and z-directions
ω	Vorticity vector
$\left\| \Phi^{(n)}(y) \right\|_\omega$	Chebyshev norm for $\Phi^{(n)}$
$0, 1$	Reference flow and flow modifications (as subscript)
B, D	Mean and disturbance quantities (as subscript)
T	Transpose (as superscript)
a, c	Analytical and computational solutions (as subscript)

Chapter 1

1 Introduction

1.1 Objective

The main objective of this dissertation is to study the effects of different forms of surface topographies on fluid flow and heat transfer in conduits. It includes analysis of the effects of axisymmetric and longitudinal grooves in annular Poiseuille flow (APF), and effects of longitudinal grooves in planar Poiseuille flow (PPF). The first reference flow, i.e. APF, is defined as the flow driven by a constant axial pressure gradient in an annulus formed by two co-axial circular cylinders. The second reference flow, i.e. PPF, is defined as the flow between two parallel plates driven by a constant streamwise pressure gradient. We are interested in the determination of the effects of the surface topography on the friction factor, the laminar-turbulent transition, and the heat transfer.

1.2 Motivations

Boundary irregularities are found in many biological systems and are encountered in many practical engineering problems. It is known that such irregularities affect the flow characteristics as well as the heat transfer. In particular, it is well known that grooved surfaces have effects on the skin friction drag (McLean 1983; Croce & D'Agaro 2005), heat transfer rate (Ligrani et al. 2003; Croce & D'Agaro 2005), the form of turbulence (Jimenez 2004), and the laminar-turbulent transition (Floryan 2003; Floryan 2007).

Different types of surface topographies have been widely used in many heat transfer augmentation techniques (Ligrani et al. 2003) and in the development of flow control strategies (Gad-el-Hak et al. 1997). Performance improvements can be achieved through the use of properly selected surface structures, assuming that one can attain a complete understanding of how these structures affect the flow.

Surface topographies may have an uncountable number of geometric forms with each of them leading to a potentially different response. The multitude of possible geometries prevents formulation of a general conclusion that would correlate geometric features of

the bounding surfaces with changes in the flow and heat transfer characteristics. Therefore, achieving the complete understanding of the possible system responses to the presence of grooves represents a significant challenge. This challenge forms the main motivation for the present work. The aim of this dissertation is to explore effects of surface topographies on APF, PPF and the heat transfer. Since proper selection of surface topography may lead to an overall improvement in the performance of the heat and flow systems, the optimal shapes of the grooved surfaces subject to suitable constraints are also sought.

1.3 Literature review

The existing literature on the effects of surface structures on the heat and fluid flows is very diverse. Thus, this review is limited a few examples of many possible application areas with focus on the effects of surface topography on the drag generation, the laminar-turbulent transition and the heat transfer.

1.3.1 Grooved surfaces

Variations in the structure of surface topography offers potential for improving the performance of flow systems, following examples found in biology (Jung & Bhushan 2010). The leaves of the lotus plant provide an example of a super-hydrophobic and low drag surface. The special properties of this surface are associated with wax tubules that create a certain surface topography. Shark skin represents another good example of a low drag surface. The skin is covered with very small tooth-like scales ribbed with longitudinal grooves which reduce the formation of vortices present on a smooth surface.

The relationship between the surface topography and the form of movement of the adjacent fluid has been studied primarily in the context of analysis of surface roughness effects. This is one of the classical but, nevertheless, still not well understood topics in fluid dynamics. A large variety of possible responses, which depend on the details of roughness shape as well as on the flow conditions, prevents the lack of closure. The direct response can be measured in terms of resistance experienced by a flow. It has been thought, since the original experiments of Hagen (1854) and Darcy (1857), that roughness always increases this resistance. Nikuradse (1933) and Moody (1944)

introduced the concept friction factor to quantify the drag and carried out extensive measurements. Their results demonstrate that roughness does not affect the laminar drag or, at least, the effect is too small to be measured using the techniques available at that time, and it always increases turbulent flow drag, with the increases being a function of the form of the roughness.

Surface roughness can affect fluid flow indirectly by changing the flow regime from laminar to turbulent. This subject was first studied experimentally with a focus on Hagen-Poiseuille flow (HPF), i.e., flow in a pipe with constant cross-sectional area driven by a constant streamwise pressure gradient, by Hagen, Poiseuille, and Reynolds (Eckhardt *et al.* 2007). Reynolds showed that for a range of flow velocities, pipe diameters, and viscosities, the transition from the laminar to the turbulent regime happened at almost the same value of the dimensionless parameter that today bears his name, Reynolds number. He mentioned that the critical value of the Reynolds number was not unique and strongly depends on the level of background disturbances (Jackson & Launder 2007). Theoretical work on the laminar-turbulent transition was started based on the linear hydrodynamic stability at the same time being pioneered by Rayleigh, Kelvin, and Helmholtz (Bayly *et al.* 1988). General linear stability theory for inviscid plane-parallel shear flows was developed by Lord Rayleigh (1880). His theory successfully described the instability associated with inflectional shear flow, but failed in the case of wall-bounded flows such as PPF.

Most of the recent work dealing with surface corrugations has been conducted in the context of PPF. Kleinstreuer & Koo (2004) determined pressure losses in laminar flow by modeling corrugations as layers of porous material. Kandlikar *et al.* (2005) introduced a set of roughness parameters. Wibel & Ehrhard (2006) measured pressure losses in grooved channels with grooves produced by a milling process. Wang (2003) analyzed flow over rectangular grooves while Thomas *et al.* (2001) worked with sinusoidal grooves. Wibel & Ehrhard (2007) studied the effects of grooves on the laminar-turbulent transition in rectangular micro-channels. Ligrani *et al.* (2003) reviewed flow characteristics and mechanisms that are responsible for the heat transfer enhancement and friction factor augmentations produced by different types of grooved surfaces.

Hydrophobic surfaces represent a fairly new area where surface grooves play an important role. Maynes *et al.* 2007 studied laminar flow with micro-ribs oriented in the flow direction. Cheng *et al.* 2009 carried out detailed studies of slip performance and correlated them with groove patterns. Davis & Lauga (2009) studied friction associated with mesh-like surfaces. Ng & Wang (2009) focused their attention on the Stokes flow over gratings.

The recent use of the reduced-order method (Floryan 1997) offers the potential for extraction of geometric features that are relevant for flow dynamics and elimination of the irrelevant details that clutter the analysis and mask the relevant mechanisms. Use of such techniques may lead to general conclusions regarding the effects of roughness shape. The global shape properties can be extracted using a projection of the surface geometry onto a convenient functional space, e.g. Fourier space, with the expectation that only a few leading Fourier modes matter. Such spectral models of surface geometry (Floryan 1997) have proved very successful as it has been demonstrated that, in many instances, it is sufficient to use only the leading Fourier mode to capture the main physical processes with accuracy sufficient for most applications (Floryan 2007).

1.3.2 Drag generation / reduction

The mechanisms of drag generation associated with surface corrugations have been clearly delineated only recently (Mohammadi & Floryan 2012). The shear drag is associated with surface-corrugation-induced changes in the wall shear, as well as an increase of the wetted area. The pressure form drag is associated with the mean pressure gradient driving the flow and the pressure interaction drag is generated by projection of the corrugation-modulated part of the pressure field on the surface geometry. The importance of pressure effects increases rapidly with the corrugation amplitude. Information about the types of drag and their dependence on the corrugation shape offers potential for identification of surface topographies that may result in a lower drag.

The reduction of pressure losses associated with the movement of fluids through conduits has been of continuous interest from the very beginning of modern fluid mechanics. It has attracted even more attention in recent times due to an increase in the cost of energy

and an interest in the reduction of environmental impact. Most of the fundamental work has been devoted to classical canonical flows, e.g. pressure driven flow either through a plane channel or through a circular pipe, kinematically driven flows (Couette flow) and various forms of boundary layers (the Blasius and the Falkner-Skan boundary layers).

One particular form of surface topography, i.e. longitudinal grooves, commonly referred to as riblets, have attracted attention due to their drag reducing capabilities in turbulent flow regimes (Walsh 1980, 1983; Seong-Ryong & Wallace, 1994). Such grooves have a wavelength of the order of the viscous scale and lead to reduced shear drag through an interference with the turbulence production (Tullis & Pollard, 1993). The viscous regime of vanishing riblet spacing is well understood (Bechert & Bartenwerfer 1989; Lucini *et al.* 1991) and detailed measurements of the drag reduction for various shapes have been carried out by Bechert *et al.* (1997) and Frohnapfel *et al.* (2007). For larger riblets, the minimum drag is related to the breakdown of the viscous regime and this process is less well understood (Garcia-Mayoral & Jimenez 2011).

Laminar riblets have attracted less attention. Mohammadi & Floryan (2013) considered pressure-driven laminar flows and demonstrated that the drag reducing abilities of long wavelength grooves was associated with a redistribution of the bulk flow. They showed that the presence of the grooves may lead to a reduction of pressure loss in spite of an increase of the wetted surface area. The drag-decreasing grooves are characterized by the groove wave number.

1.3.3 Laminar-turbulent transition

Surface roughness can affect the flow dynamics indirectly by promoting or delaying the laminar-turbulent transition. Reynolds (1883) demonstrated that the presence of roughness always promotes transition but recent evidence (Saric *et al.* 1998) demonstrates that roughness may play a stabilizing role. There is a large amount of relevant experimental data (Schlichting 1979) but a meaningful progress in the understanding of the mechanics of flow response has been achieved only recently (Floryan 2007). A frequently used criterion (Morkovin 1990) for determination of the critical roughness size is that the roughness Reynolds number $Re_k = U_k k/\nu < 25$, where

U_k is the undisturbed velocity at height k (the top of the roughness). This criterion does not account for the effect of roughness patterns when several roughness elements are present. A formal criterion for hydraulic smoothness in the case of distributed roughness states that such roughness is hydraulically active only when it is able to induce flow bifurcation (Floryan 2007); the relevant critical conditions can be identified using linear stability theory.

The two-dimensional distributed roughness destabilizes travelling wave disturbances (Floryan 2005; Asai & Floryan 2006) and the two-dimensional waves remain critical (Floryan 2007). The same roughness can amplify disturbances in the form of streamwise vortices (Floryan 2007). The first bifurcation can lead either to the onset of travelling waves or streamwise vortices, depending on the roughness amplitude and wave number and on the flow Reynolds number. Similar flow responses have been found in the Couette flow (Floryan 2002) and in the pressure driven flow in a converging-diverging channel (Floryan 2003; Floryan & Floryan 2009). Roughness has been found to increase transient growth, with the streamwise vortices playing the role of the optimal disturbances (Szumbarski & Floryan 2006). The effect of roughness patterns on the flow stability has been analyzed by Floryan & Asai (2011).

1.3.4 Heat transfer enhancement

With the increasing emphasis on energy savings, heat transfer enhancement (HTE) becomes crucial in many industrial applications. The available HTE techniques are primarily focused on the heat transfer between a solid body and a fluid with the fluid acting as the source/sink of energy. These methods may be classified as active, passive or compound, with the latter being a combination of the first two (Bergles 1998; Bergles 2001; Siddique *et al.* 2010). In active methods, the heat transport is increased by inputting additional energy to the system, e.g. surface vibration, suction or injection, mechanical mixing of the fluid, utilizing electrostatic fields, etc. (Marcello *et al.* 1992; Nesis *et al.* 1994; Allen & Karayiannis 1995). In passive methods, the improvement can be achieved without providing additional energy. Pin fins, dimples, eddy promoters, swirl chambers and rib turbulators are examples of such methods (Dewan *et al.* 2004). The

mechanisms responsible for various HTE techniques were reviewed by Jacobi *et al. (*1998); Ligrani *et al.* (2003); and Fiebig (1995).

There is a large volume of work focused on the understanding of flow mixing in systems with geometrical inhomogenities. Heat flow is increased by 100-200% in laminar flows (Bergles 2001) and by 250-450% (Chang *et al.* 2008) in turbulent flows through activation of different mechanisms, with all of them inevitably leading to an increase of the flow resistance (Xia *et al.* 2011). For example, the average Nusselt number is enhanced by as much as 200-400% depending on the pin-fin shapes but the friction factor is increased at the same time by 400%-7500% compared to the smooth-channel value (Ligrani *et al.* 2003). The mechanisms of the HTE and the pressure loss for a single protruding element with different shapes were studied by Chyu & Natarjan (1996). They showed that the upstream horseshoe vortex system, as well as the wake vortices downstream of the element, was responsible for the HTE and the pressure loss. In a channel with one smooth and one dimpled wall, the average Nusselt number can be elevated by as much as 160-350%, while the friction factor increases at the same time in the range of 120%-450% (Ligrani *et al.* 2003). The range of the HTE for turbulators in the form of ribs is about 1.7-5.9 times the reference smooth-channel value at the cost of a friction factor increase in the range of 2-70 times of the reference smooth-channel value (Ligrani *et al.* 2003). The mechanisms for the HTE and the pressure drop increase in such channels rely on the generation of recirculation zones followed by formation of secondary flow downstream of the ribs (Cho *et al.* 2000). The strength of the secondary flow can be intensified by using angled ribs and this leads to higher HTE but at the cost of a still higher pressure loss.

Heat transfer can also be intensified by reducing the size of the system. It is well known that in the laminar flow regime and for the constant heat transfer rate, the convective heat transfer coefficient is inversely proportional to the hydraulic diameter (Cheng *et al.* 2008). Hence, smaller channels are capable of providing higher heat removal rates. Because of that, micro-channels are widely used for thermal management in many industrial applications, e.g. consumer electronics, robotics and the process industry, to mention just a few. Analysis of their performance has attracted considerable attention

starting with the work of Tuckerman & Pease (1981). Some of the existing studies showed deviations in the heat transfer rates from those predicted by the classical correlations developed for macro-channels (Judy *et al.* 2002; Sobhan & Garimella 2001). More recent studies confirmed that there is no evidence that the continuum assumption is violated and, thus, conventional correlations apply to micro-channels, and the Navier-Stokes equations along with the energy equation are sufficient to predict the system behavior (Judy *et al.* 2002; Sobhan & Garimella 2001; Liu & Garimella 2004). Obviously, geometrical inhomogenities can be added to further increase the HTE. While smaller channels lead to higher heat transfer coefficients, the pressure loss greatly increases at the same time as the relevant Reynolds number becomes very small. The pressure drop depends strongly on the geometry of the micro-channels and, thus, is likely to be strongly affected by the presence of surface inhomogenities.

The design of the surface inhomogenities for HTE purposes should be based on detailed knowledge of the flow structures as additional flow resistance is the inevitable consequence. The best surface shape should be capable of maximizing the heat transfer and minimizing the flow resistance and, thus, the search for its form can be posed as a multi-objective optimization problem. There have been many studies using optimum design methodologies to determine the dimensions of the surface inhomogenities for optimal system performance. For example, Kim & Kim (2002) searched for the optimum shape of a single rib in a two-dimensional channel using gradient-based optimization techniques. They determined the width-to-height and pitch-to-height ratios which optimized the linear combination of the heat transfer and the friction drag coefficients. Fabri (1997; 1998a; 1998b; 1998c) studied the optimum shape of fins attached to planar surfaces using a genetic algorithm. He approximated the fin surface by a polynomial and concluded that the thermal effectiveness of the fin depended on the order of the polynomial. He further observed that fins with either undulated or rippled forms provided the best performance. Nobilo *et al.* (2006) studied the heat transfer in two-dimensional periodic wavy channels and performed an optimization using a multi-objective genetic algorithm. They approximated the shape of the channel, using either linear-piecewise profiles or non-uniform rational B-splines (NURBS), and concluded that the latter

provided better performance. They noted that the optimal shapes were not unique when NURBS were used and that different shapes may have the same thermal performance.

The mechanics of system response is somewhat different when one considers the heat flow between solid bodies kept at different temperatures and separated by a fluid. The fluid does not act as a source/sink of energy but as a transfer medium. Two horizontal plane walls separated by a fluid layer represent the simplest geometric configuration. The problem goes back to the work of Bénard (1900) who observed secondary flows in such systems. Rayleigh (1916) demonstrated that the heat is transported by conduction under subcritical conditions, and the transport is augmented by convection under the supercritical conditions. A recent review can be found in Bodenschatz *et al.* (2000). When the fluid is forced to move along the walls, its movement mitigates the heat transport by affecting the critical conditions. This problem was dealt for the first time by Gage & Reid (1968) and a recent bibliography can be found in Nicolas (2002).

One of the major goals of the present work is to seek improvements of the heat transport in the above system under the subcritical conditions without negatively affecting the fluid flow characteristics. We shall not attempt to create a secondary flow but, rather, we shall look for means that will lead to an increase of the effectiveness of conduction. Change of the mean distance between the walls is obviously not acceptable. It may, however, be possible to identify surface inhomogenities which modulate both the heat flow and the fluid flow in such a way that leads to an improvement of the overall system performance.

Since surface inhomogenities are likely to affect the drag experienced by the fluid, we shall focus our attention on a special class of grooves, i.e., riblets, which are known to able to reduce pressure losses. Walsh (1983) found that riblets were able to reduce the friction drag in turbulent flows despite the increase of the wetted surface area. This remarkable property makes riblet-covered walls a potential candidate for effective heat transfer applications. Riblets are formed by streamwise ridges of different cross-section. In the turbulent regime, riblets have a wavelength of the order of the viscous scale and lead to a reduced shear drag through an interference with the turbulence production. In heat transfer applications it is still unclear whether it is possible to identify surface

geometry that decreases the skin friction while, at the same time, increasing the heat transfer coefficient. Walsh & Weinstein (1980) found that the heat transfer coefficient in the turbulent regime was 10% larger than the smooth-wall value for a specific range of riblet widths. Lindemann (1985) found, experimentally, that triangular riblets were able to increase the heat transfer coefficient by as much as 36% of the smooth-wall value. Stalio & Nobile (2003) conducted direct numerical simulation of three dimensional, time dependent laminar and turbulent flows. Their results contradicted some of the experimental results and led to the conclusion that riblets were ineffective in reducing the skin friction and improving the heat transfer in the laminar regime (Choi & Orchard 1997). It has been recently shown that there exists a class of longitudinal grooves that leads to a reduction of the pressure losses for laminar flows in straight channels (Mohammadi & Floryan 2013). The use of such grooves provides the potential for improvement of the thermal performance of micro-channel.

1.3.5 Roughness modeling

There are an uncountable number of geometric roughness forms and, thus, their modeling represents a challenge. Most of the experimental investigations used artificially created roughness forms, e.g. sets of cones, spheres, prisms, parallelepipeds, etc., with different spatial distributions (Schlichting 1979). Sand paper with various grain sizes is an especially popular roughness representation due to the belief that it accounts for the "uncountability"/randomness of roughness forms. Roughness properties have been most commonly measured using the equivalent sand roughness (Moody 1944). A recent discussion of this and similar concepts is given in Herwig *et al*. (2008). The finite number of configurations that can be studied leads to an uncertainty regarding the generality of the conclusions.

Numerical simulations require the use of a well-defined geometry (Gamrat *et al.* 2008; Herwig *et al*. 2008). In most conventional numerical algorithms, discretization of the field equations on a number of finite points, volumes, or elements, results in a system of algebraic equations. Methods based on finite difference, finite volume, and finite element represent examples of discretization procedure. Typically these standard methods are based on a low-order discretization scheme which leads to a low spatial accuracy. Using

very fine grids can improve the absolute accuracy in the cost of unreasonable computational overhead while the use of higher-order schemes generally necessitates a substantial increase in effort associated with formulation, grid construction and programming implementations (Jiang & Floryan 2005). Additionally, the computational efficiency of all aforementioned methods drops significantly when a large array of boundary geometries is of concern, caused by the significant cost of generating the coefficient matrices associated with different boundary shapes.

The immersed boundary (IB) method proposed by Peskin (1982) presented a remedy for solving flow problems associated with irregular boundaries. The basic idea relies on the use of a computational rectangular box instead of an irregular physical domain. The physical domain is submerged into the computational rectangular box by extending the computational domain beyond the edges of the physical domain. In the IB method, the physical boundary conditions are imposed by using additional forcing. Different variants of IB method have been proposed by different researchers on the basis of the nature of the additional forcing required for enforcement of the boundary conditions (Mittal & Iaccarino 2005). The elimination of the cost of generating body conforming grids make the IB methods computationally very efficient as compared to methods that rely on constructing body conforming grids discussed above. However, most of the IB methods are based on the low-order finite-difference, finite-volume or finite-element techniques (Mittal & Iaccarino 2005) and as a result, suffer from a common issue of low spatial accuracy. Moreover, the physical concept of local forcing along the immersed boundaries used to enforce the no-slip and no-penetration conditions adds another level of uncertainty to these algorithms. The local flow physics around the boundaries can be affected by this local forcing along the boundaries which are submerged into the computational domain. This leads to contamination of local wall shear as well as other derivatives of the flow quantities. Furthermore, it results in an inaccurate prediction of the second derivative of the mean flow which can significantly affect the hydrodynamic stability analysis. This particular aspect of uncertainty associated with the IB methods has not been studied thoroughly and requires systematic investigation.

Spectral methods provide the lowest error for spatial discretization of the field equations but are generally limited to solution domains with regular geometries. The first spectrally accurate implementation of the immersed boundary concept was developed by Szumbarski & Floryan (1999) and is referred to as the Immersed Boundary Conditions (IBC) method. This method relies on a purely formal construction of boundary constraints in order to generate the required closing relations. The construction relies on the representation of the physical boundaries in the spectral space and nullifying the relevant Fourier modes. The IBC method does not depend on any fictitious forcing to impose the physical boundary conditions, rather transforms the original boundary value problem into an internal value problem. The discretized boundary conditions, therefore, enter the algorithm in the form of internal constraints. Such implementation is limited to geometries that can be represented by Fourier expansions but results in a gridless algorithm as all possible variations of boundary geometries are described in terms of the Fourier coefficients only. The programming effort associated with modeling the changes of geometry is minimal as the only information required for specification of geometry is limited to a set of Fourier coefficients. IBC method has been successfully extended to unsteady problems (Husain & Floryan 2007; Del Rey Fernandez *et al.* 2010), moving boundary problems involving Laplace, biharmonic and Navier-Stokes operators (Husain & Floryan, 2008a; Husain & Floryan 2008b; Husain & Floryan 2010), and also non-Newtonian fluid problems (Mohammadi *et al.* 2011; Fazel Bakhsheshi *et al.* 2011). This method has been successfully implemented to study hydrodynamic instabilities induced by corrugated surfaces (Floryan 2002; Floryan 2003; Szumbarski & Floryan 2006; Floryan 2007; Floryan & Floryan 2009) and determination of the effects of the grooves of an arbitrary shape in grooved channel (Mohammadi & Floryan 2013a).

IBC method is limited to the surface structures with moderate level of irregularities, i.e. grooves with small amplitudes and wave numbers. By increasing the level of complexity of the grooves, the inherent error associated with the enforcement of the boundary conditions unintentionally is increased which may defile the physical results (Szumbarski & Floryan 1999; Husain & Floryan 2007). Domain transformation (DT) method is an alternative to IBC method (Husain & Floryan 2010; Mohammadi & Floryan 2013a). This method relies on analytical mapping of the irregular physical domain onto a regular

computational domain allowing exact enforcement of flow boundary conditions. DT method coupled with spectral discretization of the transformed spatial coordinates is capable of delivering high spatial accuracy (Angelis *et al.* 1997; Husain & Floryan 2007). However, analytical mapping contributes to substantial complication in the transformed field equations resulting in a significant cost for generating the coefficient matrix. Therefore, spectral implementation of the DT method is recommendable for solving flow problems with high degree of irregularities only (Husain & Floryan 2007).

1.4 Overview of the present work

The present work is focused on the analysis of the effects of surface topography on the heat and fluid flows that are yet to be studied. In particular, we are interested in studying responses of APF and PPF to the introduction of grooves in different forms through evaluations of the friction factors as well as the critical conditions leading to the onset of instabilities. Additionally, we focus attention on the grooves that are able to reduce drag; we determine their optimal shapes and their effect on the heat transfer in micro-channels.

The main interest is in the grooves with small amplitudes including their effect on the flow stability. Accordingly, one must develop proper numerical techniques that are able to capture accurately effects of such grooves and can be efficiently applied to analysis of as wide class of geometries as possible. Spectral methods for analysis of steady flows in annuli bounded by walls with either axisymmetric or longitudinal ribs have been developed. The physical boundary conditions are enforced using the immersed boundary conditions (IBC) concept. The axisymmetric ribs are assumed to be periodic in the axial direction and this permits representation of the solution in terms of a Fourier expansion. The modal functions, which are functions of the radial coordinate, are represented using Chebyshev expansions. The problem formulations are closed using either a fixed volume flow rate constraint or a fixed pressure gradient constraint.

It has been shown that selection of the proper groove geometry may lead to drag reduction. Detailed analysis of pressure losses in flows through annuli fitted with longitudinal grooves has been carried out. It has been demonstrated that a reduced order model is an effective tool for extraction of features of geometry that lead to the flow

modulations relevant to the drag generation. It is shown that the presence of the grooves may lead to a reduction of pressure loss in spite of an increase of the wetted surface area. The drag decreasing grooves are characterized by the groove wave number M/R_1 being smaller than a certain critical value, where M denotes the number of grooves being used and R_1 stands for the radius of the annulus. The form of the optimal grooves from the point of view of the maximum drag reduction has been determined.

A method to increase the heat flow across a micro-channel has been proposed based on the use of longitudinal grooves. It has been shown that it is possible to find grooves that can increase the heat flow and, at the same, can decrease the flow pressure losses. The shape of the grooves that would produce the best improvement in the overall system performance has been determined. The system performance was measured using the thermal enhancement factor whose reduction measures the performance gains.

Stability analysis of the flow in a channel modified by longitudinal grooves has been carried out. It has been shown that disturbances corresponding to two-dimensional waves in the limit of zero groove amplitude play the critical role in the grooved channel. It has been demonstrated that presence of grooves leads to the flow stabilization for groove wave numbers $\beta < \beta_{tran} \approx 4.22$ and the flow destabilization for larger βs. It has been shown that presence of the drag reducing grooves leads to a small increase of the critical Reynolds number compared with the smooth channel.

1.5 Outline of the dissertation

This dissertation is organized into six chapters. The objectives and motivation as well as the review of the relevant literature are presented in Chapter 1. Development of the spectrally accurate IBC algorithms suitable for the determination of flows in annuli fitted with ribs is discussed in Chapter 2. Chapter 3 is devoted to the analysis of flows in an annulus fitted with longitudinal grooves. Detailed analysis of flow features as well as determination of the optimal grooves are discussed in this chapter. The heat transfer enhancement resulting from the use of longitudinal grooves is analyzed in Chapter 4, including determination of the best groove shape that simultaneously reduces the flow drag and increases the heat transfer. Chapter 5 is focused on the analysis of stability of

flow in a channel fitted with longitudinal grooves. Chapter 6 summarizes the main conclusions together with suggestions for the future work.

Chapter 2

2 Algorithm for Analysis of Flows in Ribbed Annuli[1]

2.1 Introduction

This chapter is focused on the development of a spectrally accurate IBC algorithm suitable for accurate and computationally efficient analysis of flows in geometries described in terms of the cylindrical coordinate system. The problem is posed as the problem of determination of flows in annuli fitted with either transverse or longitudinal ribs with arbitrary cross-sections. Section 2.2 discusses algorithm suitable for transverse ribs. In particular, Section 2.2.1 gives problem formulation, Section 2.2.2 discusses the reference flow, i.e., flow in an annulus without ribs, Section 2.2.3 provides description of the discretization of the field equations, the boundary conditions and the flow constraints, Section 2.2.4 is devoted to post-processing of the results, Section 2.2.5 discusses solution strategy used in the iterative solution of the non-linear algebraic system, Section 2.2.6 presents an efficient linear solver, and Section 2.2.7 discusses results of various tests carried out in order to validate the accuracy of the algorithm. Section 2.3 discusses algorithm suitable for analysis of flows in the presence of longitudinal ribs. In particular, Section 2.3.1 provides problem formulation, Section 2.3.2 discusses discretization procedures applied to the field equation, the boundary conditions and the flow constraints, and Section 2.3.3 describes results of various tests. Section 2.4 provides a short summary of the main conclusions.

---

[1] A version of this chapter has been published as –

Moradi, H. V. & Floryan, J. M. 2012 Algorithm for analysis of flows in ribbed annuli, *International Journal for Numerical Methods in Fluids*, **68**, 805-838.

2.2 Annulus with transverse grooves

2.2.1 Problem formulation

Consider steady flow of a viscous incompressible fluid in an annulus extending to $\pm\infty$ in the axial z-direction and fitted with transverse ribs. The flow is driven by an axial pressure gradient. The ribs are axisymmetric with geometry described by the following relations (see Figure **2-1**)

$$r_{in}(z) = R_1 + \sum_{n=-N_A}^{N_A} H_{in}^{(n)} e^{in\alpha z} \,, r_{out}(z) = 1 + R_1 + \sum_{n=-N_A}^{N_A} H_{out}^{(n)} e^{in\alpha z} \qquad (2.2.1a, b)$$

where $H_{in}^{(n)} = H_{in}^{(-n)*}$ and $H_{out}^{(n)} = H_{out}^{(-n)*}$ are the reality conditions, stars denote the complex conjugate, R_1 stands for the average radius of the inner annulus, subscripts "*out*" and "*in*" denote the outer and inner cylinders, respectively, and N_A is the number of Fourier modes required for description of the geometry. The ribs are periodic in the axial z-direction with the wavelength $\lambda = 2\pi/\alpha$, where α denotes the ribs' wave number.
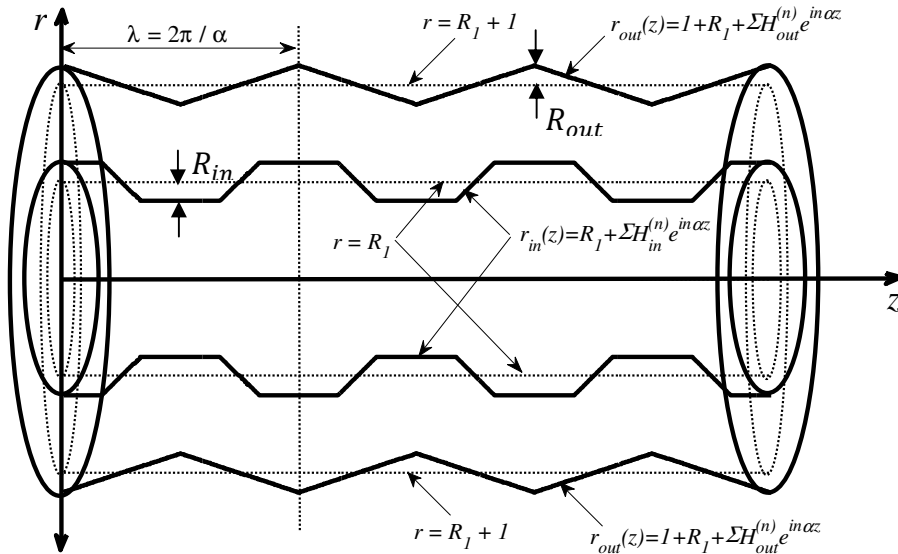
Figure 2-1: *Sketch of the flow geometry - axisymmetric annulus with transverse ribs of arbitrary cross-section.*

The velocity vector has $(v_z, v_r, 0)$ components in the z- (axial), r-(radial) and θ-(circumferential) directions, and thus the field equations can be reduced to the continuity, and axial and radial momentum equations in the form

$$\frac{1}{r}\frac{\partial(rv_r)}{\partial r} + \frac{\partial v_z}{\partial z} = 0, \qquad (2.2.2)$$

$$\frac{\partial\{v_z v_z\}}{\partial z} + \frac{\partial\{v_z v_r\}}{\partial r} + \frac{\{v_z v_r\}}{r} = -\frac{\partial p}{\partial z} + \frac{1}{Re}\left[\frac{1}{r}\frac{\partial v_z}{\partial r} + \frac{\partial^2 v_z}{\partial r^2} + \frac{\partial^2 v_z}{\partial z^2}\right], \qquad (2.2.3)$$

$$\frac{\partial\{v_r v_z\}}{\partial z} + \frac{\partial\{v_r v_r\}}{\partial r} + \frac{\{v_r v_r\}}{r} = -\frac{\partial p}{\partial r} + \frac{1}{Re}\left[\frac{1}{r}\frac{\partial v_r}{\partial r} + \frac{\partial^2 v_r}{\partial r^2} + \frac{\partial^2 v_r}{\partial z^2} - \frac{v_r}{r^2}\right], \qquad (2.2.4)$$

where $\{\ \}$ denotes velocity products and p denotes the pressure. These equations have been scaled using the average annulus opening L as the length scale, the maximum of the axial velocity component of the reference flow U_{max} as the velocity scale, and ρU_{max}^2 as the pressure scale, where ρ stands for the density. The Reynolds number is defined as $Re = U_{max}L/\nu$ where ν stands for the kinematic viscosity. The reader may note that $R_1 \to \infty$ corresponds to a plane channel flow (difference between cylinders` radii becomes small as compared to the average radius). There is a limit on the physically acceptable amplitude of the ribs at the inner cylinder when $R_1 \to 0$.

The no-slip and no-penetration conditions at the walls have the form

$$v_r[z, r_{in}(z)] = 0, v_z[z, r_{in}(z)] = 0, v_r[z, r_{out}(z)] = 0, v_z[z, r_{out}(z)] = 0. \qquad (2.2.5a\text{-}d)$$

The problem requires an additional closing condition. Typically one chooses this condition to be either in the form of the fixed flow rate constraint

$$Q = \int_{r=R_1}^{r=1+R_1} 2\pi v_z(r)dr = \text{Constant}, \qquad (2.2.6)$$

where Q denotes the known flow rate, or the fixed pressure gradient constraint

$$\frac{\partial p}{\partial z} = \text{Constant}. \qquad (2.2.7)$$

Introduction of the Stokes stream function, ψ, defined by

$$v_z = \frac{-1}{r}\frac{\partial\psi}{\partial r}, v_r = \frac{1}{r}\frac{\partial\psi}{\partial z} \qquad (2.2.8a, b)$$

permits elimination of pressure and transformation of the momentum equations into a single fourth-order partial differential equation in the form

$$\frac{E^4\psi}{r} = Re\left\{\frac{\partial}{\partial z}\left(\frac{\partial\{v_r v_r\}}{\partial r} + \frac{\partial\{v_r v_z\}}{\partial z}\right) - \frac{\partial}{\partial r}\left(\frac{\partial\{v_r v_z\}}{\partial r} + \frac{\partial\{v_z v_z\}}{\partial z}\right) + \frac{1}{r}\frac{\partial\{v_r v_r\}}{\partial z}\right.$$
$$\left. + \frac{\{v_r v_z\}}{r^2} - \frac{1}{r}\frac{\partial\{v_r v_z\}}{\partial z}\right\}, \qquad (2.2.9)$$

Where the E^2 operator is defined as

$$E^2 = \frac{\partial^2}{\partial r^2} + \frac{\partial^2}{\partial z^2} - \frac{1}{r}\frac{\partial}{\partial r}. \qquad (2.2.10)$$

The boundary conditions expressed in terms of the stream function take the form

$$\frac{-1}{r}\frac{\partial\psi}{\partial r} = 0, \qquad \frac{1}{r}\frac{\partial\psi}{\partial z} = 0 \quad \text{at } r = r_{in}(z) \text{ and } r = r_{out}(z). \qquad (2.2.11a\text{-}b)$$

Introduction of the stream function requires selection of an arbitrary normalization condition. This condition has been selected in the present study by assuming that the stream function takes zero value at the inner cylinder, i.e.,

$$\psi[z, r_{in}(z)] = 0. \qquad (2.2.12)$$

The fixed flow rate constraint can be expressed in terms of the stream function as

$$\psi[z, r_{out}(z)] = -Q/2\pi. \qquad (2.2.13)$$

The specification of the fixed pressure gradient constraint follows from (2.2.3), (2.2.7), and (2.2.8a, b).

2.2.2 Reference flow

Flow in a smooth annulus represents the reference flow. The flow is parallel to the z-axis with the axial velocity distribution in the form

$$v_z(r) = \frac{R_1^2}{k_1}\left[1 - \left(\frac{r}{R_1}\right)^2\right] + \frac{k_2}{k_1}ln\left(\frac{r}{R_1}\right), \tag{2.2.14}$$

where $k_1 = R_1^2 - k_2 lnR_1 + k_2/2\left[ln(k_2/2) - 1\right]$ and $k_2 = (1 + 2R_1)/ln[(1 + R_1)/R_1]$. Its maximum U_{max} used as the velocity scale occurs at $r = \sqrt{k_2/2}$. This flow is driven by the axial pressure gradient in the form

$$\frac{dp}{dz} = \frac{-4}{k_1 Re}, \tag{2.2.15}$$

leading to the flow rate

$$Q = \frac{2\pi}{k_1}\left[\frac{(1 + R_1)^2}{4}(R_1^2 - 2R_1 - 1 - k_2) + \frac{k_2(1 + R_1)^2}{2}ln\left(\frac{1 + R_1}{R_1}\right) + \frac{R_1^2}{4}(k_2 - 1)\right]. \tag{2.2.16}$$

2.2.3 Discretization

This section describes discretization of the field equation, the boundary conditions, the normalization condition and the most common flow constraint conditions. Our interest is in the use of spectral discretization based on the Fourier expansions in the axial direction and the Chebyshev expansions in the radial direction. Since the shape of the solution domain is irregular (see Figure **2-1**), we intend to utilize the immersed boundary conditions (IBC) method for the enforcement of the flow boundary conditions. In the IBC method the flow domain must be completely immersed inside a regular computational domain. Figure **2-1** shows that the flow domain is bounded in the radial direction by $-R_{in} + R_1$ from below and by $1 + R_1 + R_{out}$ from above, where R_{in} and R_{out} denote locations of the ribs' extremities. In order to use the standard definition of the Chebyshev polynomials, this domain has to be mapped into $[-1, 1]$. A convenient transformation used in this study has the form

$$\xi = \Gamma r + c, \Gamma = \frac{2}{1 + R_{in} + R_{out}}, c = \frac{R_{in} - R_{out} - 2R_1 - 1}{1 + R_{in} + R_{out}}. \tag{2.2.17}$$

The wall geometries can be expressed in terms of ξ variable as

$$\xi_{in}(z) = \sum_{n=-N_A}^{N_A} A_{in}^{(n)} e^{in\alpha z}, \xi_{out}(z) = \sum_{n=-N_A}^{N_A} A_{out}^{(n)} e^{in\alpha z}, \tag{2.2.18a, b}$$

where $A_{in}^{(n)} = c + \Gamma R_1 + \Gamma H_{in}^{(n)}$ for $n = 0$ and $A_{in}^{(n)} = \Gamma H_{in}^{(n)}$ for $|n| \geq 1$, $A_{out}^{(n)} = c + \Gamma(1 + R_1) + \Gamma H_{out}^{(n)}$ for $n = 0$ and $A_{out}^{(n)} = \Gamma H_{out}^{(n)}$ for $|n| \geq 1$. The field equation in the (z, ξ) coordinate system takes the form

$$
\begin{aligned}
Re^{-1} &\left[h^3 \left(\frac{\partial^4 \psi}{\partial z^4} + 2\Gamma^2 \frac{\partial^4 \psi}{\partial z^2 \partial \xi^2} + \Gamma^4 \frac{\partial^4 \psi}{\partial \xi^4} \right) - 2h^2 \frac{\Gamma}{R_1} \frac{\partial^3 \psi}{\partial z^2 \partial \xi} - 3 \frac{\Gamma}{R_1^3} \frac{\partial \psi}{\partial \xi} \right. \\
&\left. + 3h \frac{\Gamma^2}{R_1^2} \frac{\partial^2 \psi}{\partial \xi^2} - 2h^2 \frac{\Gamma^3}{R_1} \frac{\partial^3 \psi}{\partial \xi^3} \right] = h^3 \frac{\partial \{v_r v_r\}}{\partial z} + h^2 \frac{\{v_r v_z\}}{R_1} - h^3 \Gamma \frac{\partial \{v_r v_z\}}{\partial \xi} \\
&+ h^4 R_1 \left[\frac{\partial}{\partial z} \left(\Gamma \frac{\partial \{v_r v_r\}}{\partial \xi} + \frac{\partial \{v_r v_z\}}{\partial z} \right) - \Gamma \frac{\partial}{\partial \xi} \left(\Gamma \frac{\partial \{v_r v_z\}}{\partial \xi} + \frac{\partial \{v_z v_z\}}{\partial z} \right) \right],
\end{aligned} \tag{2.2.19}
$$

where $h = 1 + \xi(\Gamma R_1)^{-1} + (1 + R_{out} - R_{in})(2R_1)^{-1}$. Boundary conditions in the new coordinate systems can be written in the form

$$-\Gamma^2(\xi - c)^{-1} \frac{\partial \psi}{\partial \xi} = 0, \Gamma(\xi - c)^{-1} \frac{\partial \psi}{\partial z} = 0 \ at \ \xi = \xi_{in}(z) \ and \ \xi = \xi_{out}(z). \tag{2.2.20}$$

2.2.3.1 Discretization of field equation

The flow is periodic in the z-direction and thus all flow quantities can be expressed in terms of Fourier expansions in the form

$$\psi(z, \xi) \approx \sum_{n=-N_M}^{N_M} \phi^{(n)}(\xi) e^{in\alpha z}, \{v_r v_r\}(z, \xi) \approx \sum_{n=-N_M}^{N_M} v_{rr}^{(n)}(\xi) e^{in\alpha z}, \tag{2.2.21a-d}$$

$$\{v_z v_r\}(z,\xi) \approx \sum_{n=-N_M}^{N_M} v_{zr}^{(n)}(\xi)e^{in\alpha z},\{v_z v_z\}(z,\xi) \approx \sum_{n=-N_M}^{N_M} v_{zz}^{(n)}(\xi)e^{in\alpha z},$$

where $\phi^{(n)} = \phi^{(-n)*}$, $v_{rr}^{(n)} = v_{rr}^{(-n)*}$, $v_{zr}^{(n)} = v_{zr}^{(-n)*}$, $v_{zz}^{(n)} = v_{zz}^{(-n)*}$ and the series are truncated at $n = N_M$ ($N_M > N_A$). Substitution of the above expansions into the field equation and separation of Fourier modes lead to a system of $2N_M + 1$ fourth-order, ordinary differential equations for the modal functions $\phi^{(n)}$ in the form

$$
\begin{aligned}
&Re^{-1}[n^4(E_1\xi^3 + E_2\xi^2 + E_3\xi + E_4) + n^2(E_5\xi^2 + E_6\xi + 2E_7)D - 3E_8 D \\
&\quad -n^2(E_5\xi^3 + 6E_6\xi^2 + 6E_7\xi + E_9)D^2 + (3E_8\xi + E_{10})D^2 - 2(E_8\xi^2 \\
&\quad +2E_{10}\xi+2E_{11})D^3 + (E_8\xi^3 + 3E_{10}\xi^2 + E_{11}\xi + E_{12})D^4]\phi^{(n)}(\xi) \\
&= -n^2(E_{13}\xi^4 + 4E_{14}\xi^3)v_{zr}^{(n)}(\xi) + nE_{15}\xi^3 v_{rr}^{(n)}(\xi) + [(E_{18} - 6n^2 E_{16})v_{zr}^{(n)}(\xi) \\
&\quad +3nE_{17}v_{rr}^{(n)}(\xi)]\xi^2 + \left[2(E_{21} - 2n^2 E_{19})v_{zr}^{(n)}(\xi) + 3nE_{20}v_{rr}^{(n)}(\xi)\right]\xi \\
&\quad +\left[(E_{24} - n^2 E_{22})v_{zr}^{(n)}(\xi) + nE_{23}v_{rr}^{(n)}(\xi)\right] + E_{15}\xi^4\left[Dv_{rr}^{(n)}(\xi) - Dv_{zz}^{(n)}(\xi)\right] \\
&\quad +\left\{4E_{17}\left[Dv_{rr}^{(n)}(\xi) - Dv_{zz}^{(n)}(\xi)\right] - E_{18}Dv_{zr}^{(n)}(\xi)\right\}\xi^3 + \left\{6E_{20}\left[Dv_{rr}^{(n)}(\xi)\right.\right. \\
&\quad \left.\left.-Dv_{zz}^{(n)}(\xi)\right] - 3E_{21}Dv_{zr}^{(n)}(\xi)\right\}\xi^2 + \left\{4E_{23}\left[Dv_{rr}^{(n)}(\xi) - Dv_{zz}^{(n)}(\xi)\right]\right. \\
&\quad \left.-3E_{24}Dv_{zr}^{(n)}(\xi)\right\}\xi + \left\{E_{25}\left[Dv_{rr}^{(n)}(\xi) - Dv_{zz}^{(n)}(\xi)\right] - E_{26}Dv_{zr}^{(n)}(\xi)\right\} \\
&\quad -(E_{18}\xi^4 + 4E_{21}\xi^3 + 6E_{24}\xi^2 + 4E_{26}\xi + E_{27})D^2 v_{zr}^{(n)}(\xi),
\end{aligned}
$$

<div align="right">(2.2.22)</div>

where $E_1 = \alpha^4(\Gamma R_1)^{-3}$, $E_2 = 3\alpha^4 c_1(\Gamma R_1)^{-2}$, $E_3 = 3\alpha^4 c_1^2(\Gamma R_1)^{-2}$, $E_4 = \alpha^4 c_1^3$, $E_5 = 2\alpha^2\Gamma^{-1}R_1^{-3}$, $E_6 = \alpha^2 c_1 R_1^{-2}$, $E_7 = \Gamma(\alpha c_1)^2 R_1^{-1}$, $E_8 = \Gamma R_1^{-3}$, $E_9 = 2(\Gamma\alpha)^2 c_1^3$, $E_{10} = (\Gamma R_1^{-1})^2 c_1$, $E_{11} = \Gamma^3 c_1^2 R_1^{-1}$, $E_{12} = \Gamma^4 c_1^3$, $E_{13} = \alpha^2\Gamma^{-4}R_1^{-3}$, $E_{14} = \alpha^2 c_1\Gamma^{-3}R_1^{-2}$, $E_{15} = i\alpha(\Gamma R_1)^{-3}$, $E_{16} = (\alpha c_1\Gamma^{-1})^2 R_1^{-1}$, $E_{17} = i\alpha c_1(\Gamma R_1)^{-2}$, $E_{18} = \Gamma^{-2}R_1^{-3}$, $E_{19} = \alpha^2 c_1^3\Gamma^{-1}$, $E_{20} = i\alpha c_1^2(\Gamma R_1)^{-1}$, $E_{21} = c_1\Gamma^{-1}R_1^{-2}$, $E_{22} = \alpha^2 c_1^4 R_1$, $E_{23} = i\alpha c_1^3$, $E_{24} = c_1^2 R_1^{-1}$, $E_{25} = \Gamma i\alpha R_1 c_1^4$, $E_{26} = \Gamma c_1^3$, $E_{27} = \Gamma^2 R_1 c_1^4$, $D^4 = d^k/d\xi^k$, $k = 1, 2, 3, 4$, $n \in (-N_M, N_M)$, $c_1 = c(\Gamma R_1)^{-1}$ and the nonlinear coupling terms (velocity products), which will be treated as known quantities during iterative solution, have been placed on the right hand side of the above equations. The modal functions $\phi^{(n)}(\xi)$, $v_{rr}^{(n)}$, $v_{zr}^{(n)}$, $v_{zz}^{(n)}$ can be expressed in terms of Chebyshev expansions in the form

$$\phi^{(n)}(\xi) \approx \sum_{k=0}^{N_T} G_k^{(n)} T_k(\xi), \tag{2.2.23}$$

$$v_{rr}^{(n)}(\xi) \approx \sum_{k=0}^{N_T} G_{rr,k}^{(n)} T_k(\xi), v_{zr}^{(n)}(\xi) \approx \sum_{k=0}^{N_T} G_{zr,k}^{(n)} T_k(\xi), v_{zz}^{(n)}(\xi) \approx \sum_{k=0}^{N_T} G_{zz,k}^{(n)} T_k(\xi), \tag{2.2.24}$$

where T_k denotes Chebyshev polynomial of the kth order, $G_k^{(n)}$, $G_{rr,k}^{(n)}$, $G_{zr,k}^{(n)}$ and $G_{zz,k}^{(n)}$ stand for the unknown coefficients of the expansions which have been truncated at $N_T + 1$ terms. Substitution of the above relations into Eq. (2.2.22) and application of the Galerkin procedure lead to a set of algebraic equations for the unknown coefficients $G_k^{(n)}$ whose explicit form is given in Appendix A. The Galerkin procedure uses the inner product in the form $\langle f, g \rangle = \int_{-1}^{1} f(\xi) g(\xi) \omega(\xi) d\xi$ where $\omega(\xi) = (1 - \xi^2)^{-1/2}$ denotes the weight function; these products are evaluated using the orthogonality properties of Chebyshev polynomials. The Galerkin process leads to $N_T + 1$ algebraic equations for each Fourier modes without any coupling between these modes. Four equations corresponding to the highest Chebyshev polynomials are dropped for each Fourier mode to make space for the imposition of boundary conditions and constraints in the Tau-like manner.

2.2.3.2 Discretization of the boundary conditions

We shall limit the following discussion to description of numerical implementation of boundary conditions at the inner cylinder. Conditions (2.2.20) have to be enforced along the line $\xi_{in}(z)$ defined by Eq. (2.2.18a) and can be re-written as

$$\Gamma f_{in}(z) \frac{\partial \psi}{\partial z} = 0, -\Gamma^2 f_{in}(z) \frac{\partial \psi}{\partial \xi} = 0 \text{ at } \xi = \xi_{in}(z), \tag{2.2.25}$$

where $f_{in}(z) = [\xi_{in}(z) - c]^{-1}$. Method to be used for the enforcement of boundary conditions at the outer wall is identical to that used for the inner wall with the subscript "*in*" replaced by the subscript "*out*".

Expressing the stream function in (2.2.25) in terms of Fourier and Chebyshev expansions ((2.2.21a-d) , (2.2.23)) leads to

$$\Gamma f_{in}(z) \sum_{n=-N_M}^{N_M} \sum_{k=0}^{N_T} in\alpha G_k^{(n)} T_k(\xi) e^{in\alpha z} = 0,$$

$$-\Gamma^2 f_{in}(z) \sum_{n=-N_M}^{N_M} \sum_{k=0}^{N_T} G_k^{(n)} dT_k(\xi)/d\xi \, e^{in\alpha z} = 0. \tag{2.2.26}$$

The values of the Chebyshev polynomials T_k and their derivatives $dT_k/d\xi$ evaluated along the inner cylinder represent periodic functions and can be expressed in terms of Fourier series in the form

$$T_k(\xi) \approx \sum_{m=-N_S}^{N_S} w_{in,k}^{(m)} e^{im\alpha z} , dT_k(\xi)/d\xi \approx \sum_{m=-N_S}^{N_S} d_{in,k}^{(m)} e^{im\alpha z} \text{ at } \xi = \xi_{in}(z), \tag{2.2.27}$$

where $N_S = N_T \times N_A$. The method for evaluation of the coefficients $w_{in,k}^{(m)}$ and $d_{in,k}^{(m)}$ is presented in Appendix B. The function $f_{in}(z)$ in Eq. (2.2.25) is periodic in z and thus can be expressed in terms of a Fourier expansion in the form

$$f_{in}(z) \approx \sum_{p=-N_R}^{N_R} Z_{in}^{(p)} e^{ip\alpha z}. \tag{2.2.28}$$

Coefficients of this expansion are evaluated numerically using Fast Fourier transform. This expansion is truncated after N_R terms. The exact value of N_R depends on the geometry, however numerical experiments show that $N_R = N_M$ is most often sufficient. Substitution of (2.2.27) and (2.2.28) into (2.2.26) results in

$$\sum_{n=-N_M-N_S-N_R}^{N_M+N_S+N_R} \sum_{p=-N_M-N_S}^{N_M+N_S} \sum_{m=-N_M}^{N_M} \sum_{k=0}^{N_T} im\alpha G_k^{(n)} w_{in,k}^{(p-m)} Z_{in}^{(n-p)} e^{in\alpha z} = 0, \tag{2.2.29}$$

$$\sum_{n=-N_M-N_S-N_R}^{N_M+N_S+N_R} \sum_{p=-N_M-N_S}^{N_M+N_S} \sum_{m=-N_M}^{N_M} \sum_{k=0}^{N_T} G_k^{(n)} d_{in,k}^{(p-m)} Z_{in}^{(n-p)} e^{in\alpha z} = 0. \qquad (2.2.30)$$

Re-arrangement of the above relations leads to boundary relations (that need to be enforced of order to satisfy the flow boundary conditions) in the form

$$\sum_{m=-N_M}^{N_M} \sum_{k=0}^{N_T} im\alpha G_k^{(m)} \sum_{p=-N_M-N_S}^{N_M+N_S} Z_{in}^{(n-p)} w_{in,k}^{(p-m)} = 0, \qquad (2.2.31)$$

$$\sum_{m=-N_M}^{N_M} \sum_{k=0}^{N_T} G_k^{(m)} \sum_{p=-N_M-N_S}^{N_M+N_S} Z_{in}^{(n-p)} d_{in,k}^{(p-m)} = 0. \qquad (2.2.32)$$

In general the total number of the available boundary relations is $N_M + N_T N_A + N_R$. Since N_M Fourier modes are used in the solution, one can enforce only N_M of these conditions. The remaining conditions can be used *aposteriori* as a convenient test for consistency of the algorithm. Use of a larger number of such conditions leads to an over-determined formulation of the IBC method (Husain *et al.* 2009) which expands applicability of the method to more extreme geometries. The number of boundary relations used in this study was always equal to the number of Fourier modes used to represent the flow field resulting in a well posed algebraic problem.

2.2.3.3 Discretization of the normalization condition

The normalization condition (2.2.12) can be written using (2.2.21a-d) and (2.2.23) in the form

$$\psi[z, f_{in}(z)] \approx \sum_{n=-N_M}^{N_M} \sum_{k=0}^{N_T} G_k^{(n)} T_k[f_{in}(z)] e^{in\alpha z} = 0. \qquad (2.2.33)$$

Values of the Chebyshev polynomials evaluated along the periodic boundary represent periodic functions and can be expressed by Fourier expansions of type (2.2.27). Their substitution into (2.2.33) leads, after some re-arrangements and extraction of mode zero, to the following form of the normalization condition

$$\sum_{m=-N_M}^{N_M} \sum_{k=0}^{N_T} G_k^{(m)} w_{in,k}^{(-m)} = 0. \tag{2.2.34}$$

2.2.3.4 Discretization of the flow constraints

We shall begin discussion with the description of the discretization of the mass flow rate constraint. The total mass flow rate in the annulus can be expressed as a superposition of the volume flow rate of the reference flow Q_{ref} given by Eq. (2.2.16) and a change in the flow rate due to the presence of the ribs Q_{mod}, i.e.,

$$Q_{total} = Q_{ref} + Q_{mod}. \tag{2.2.35}$$

Substitution of the above relation into (2.2.13), where the value of the stream function at the outer cylinder is expressed in a manner analogous to that used in Section 2.2.3.3, lead to the following form of the flow constraint

$$\sum_{m=-N_M}^{N_M} \sum_{k=0}^{N_T} G_k^{(m)} w_{out,k}^{(-m)} = \frac{Q_{ref} + Q_{mod}}{2\pi}. \tag{2.2.36}$$

It had been assumed in all tests discussed in this study that addition of the ribs did not alter the mass flow through the annulus, i.e., $Q_{mod} = 0$.

Discretization of the fixed pressure gradient constraint begins with the z-momentum equation expressed in the (z, ξ) coordinate system, i.e.,

$$\frac{\partial \{v_z v_z\}}{\partial z} + \Gamma \frac{\partial \{v_z v_r\}}{\partial \xi} + \Gamma \frac{\{v_z v_r\}}{\xi - c} = -\frac{\partial p}{\partial z} +$$
$$+ \frac{1}{Re} \left[\frac{-\Gamma^4}{(\xi - c)^3} \frac{\partial \psi}{\partial \xi} + \frac{\Gamma^4}{(\xi - c)^2} \frac{\partial^2 \psi}{\partial \xi^2} - \frac{\Gamma^2}{\xi - c} \frac{\partial^3 \psi}{\partial \xi^3} - \frac{\Gamma^2}{\xi - c} \frac{\partial^3 \psi}{\partial z^2 \partial \xi} \right]. \tag{2.2.37}$$

Pressure can be expressed as Fourier expansion in the form

$$p(z, \xi) = Az + \sum_{n=-N_M}^{N_M} P^{(n)}(\xi)e^{in\alpha z}. \tag{2.2.38}$$

where the known constant A denotes the pressure gradient driving the flow. Substitution of (2.2.21a-d) and (2.2.38) into (2.2.37) and separation of Fourier modes lead to

$$in\alpha P^{(n)}(\xi) = -in\alpha v_{zz}^{(n)}(\xi) - \Gamma D v_{zr}^{(n)}(\xi) - \Gamma \frac{v_{zr}^{(n)}(\xi)}{\xi - c} + \frac{1}{Re}\left[-\Gamma^4 \frac{D\phi^{(n)}(\xi)}{(\xi - c)^3}\right.$$
$$+\Gamma^4 \frac{D^2\phi^{(n)}(\xi)}{(\xi - c)^2} - \Gamma^4 \frac{D^3\phi^{(n)}(\xi)}{\xi - c} + (\Gamma n\alpha)^2 \frac{D\phi^{(n)}(\xi)}{\xi - c}\right] \tag{2.2.39}$$

when $n \neq 0$ and

$$A + \Gamma D v_{zr}^{(0)}(\xi) + \Gamma \frac{v_{zr}^{(0)}(\xi)}{\xi - c} = \frac{-\Gamma^4}{Re}\left[\frac{D\phi^{(0)}(\xi)}{(\xi - c)^3} - \frac{D^2\phi^{(0)}(\xi)}{(\xi - c)^2} + \frac{D^3\phi^{(0)}(\xi)}{\xi - c}\right] \tag{2.2.40}$$

when $n = 0$. Substitution of the relevant Chebyshev expansions into Eq. (2.2.40) and enforcement of the resulting relation at any ξ-location provides form of the fixed pressure gradient constraint suitable for computations, e.g.,

$$\sum_{k=0}^{N_T}\left[\frac{DT_k(\xi)}{(\xi - c)^3} - \frac{D^2 T_k(\xi)}{(\xi - c)^2} + \frac{D^3 T_k(\xi)}{\xi - c}\right]G_k^{(0)}$$
$$= -Re\Gamma^{-4}\left[A + \Gamma D v_{zr}^{(0)}(\xi) + \frac{\Gamma v_{zr}^{(0)}(\xi)}{\xi - c}\right] \tag{2.2.41}$$

2.2.4 Post-processing of Results

Solution of the discretized system leads to determination of the flow field. We shall now discuss evaluation of the pressure field.

We begin with the z-momentum equation (2.2.37). Substitution of (2.2.21a-d) and (2.2.38) and separation of Fourier modes lead to Eq. (2.2.40) for evaluation of the constant A in the case of the fixed volume flow rate constraint. Equation (2.2.39) permits

evaluation of the remaining modal function $P^{(n)}$, $n \neq 0$. The r-momentum equation has to be used for evaluation of $P^{(0)}(\xi)$. This equation can be written in the form

$$\frac{\partial\{v_z v_r\}}{\partial z} + \Gamma \frac{\partial\{v_r v_r\}}{\partial \xi} + \Gamma \frac{\{v_r v_r\}}{\xi - c} = -\Gamma \frac{\partial p}{\partial \xi} +$$
$$+ \frac{1}{Re}\left[\frac{-\Gamma^3}{(\xi - c)^2}\frac{\partial^2 \psi}{\partial z \partial \xi} + \frac{\Gamma^3}{\xi - c}\frac{\partial^3 \psi}{\partial z \partial \xi^2} + \frac{\Gamma}{\xi - c}\frac{\partial^3 \psi}{\partial z^3}\right]. \tag{2.2.42}$$

Substitution of (2.2.21a-d), (2.2.38) and extraction of mode zero results in

$$DP^{(0)}(\xi) = -Dv_{rr}^{(0)}(\xi) - \frac{v_{rr}^{(0)}(\xi)}{\xi - c}. \tag{2.2.43}$$

Integration of the above relation gives an explicit formula for evaluation of $P^{(0)}(\xi)$, i.e.,

$$P^{(0)}(\xi) = -v_{rr}^{(0)}(\xi) - \int \frac{v_{rr}^{(0)}(\xi)}{\xi - c} d\xi + C. \tag{2.2.44}$$

where C can be integrated into the pressure normalization constant.

Evaluation of the mass flow rate in the case of flow subject to a fixed pressure gradient constraint follows from Eqs. (2.2.35) and (2.2.36).

2.2.5 Solution strategy

The problem to be solved consists of a system of nonlinear algebraic equations (field equations) shown in Appendix A, boundary relations of type (2.2.31)-(2.2.32), normalization condition (2.2.34) and either constraint (2.2.36) or (2.2.41). All equations and supplementary conditions can be expressed in matrix notation in the form

$$\boldsymbol{Lx} = \boldsymbol{R} \tag{2.2.45}$$

where $\boldsymbol{L}$ denotes the coefficient matrix of size $p \times p$ with $p = (2N_M + 1) \times (N_T + 1)$, $\boldsymbol{x}$ is a p-dimensional vector of the unknown Chebyshev coefficients $G_k^{(n)}$ and $\boldsymbol{R}$ stands for the p-dimensional right hand side vector which accounts for nonlinearities.

The solution process relies on iterations where the unknown x is corrected in a sequence of steps until a convergence criterion is satisfied. The iteration process begins with solution of (2.2.45) with nonlinear terms omitted from R to determine the first approximation of x denoted here as x_0. The first approximation of R denoted as R_0 is computed using x_0. This process is now repeated in the form

$$x_{j+1} = L^{-1}R_j, \tag{2.2.46}$$

where j denotes iteration number, until convergence criterion in the form

$$\left(|x_{j+1} - x_j|/|x_{j+1}|\right) < 10^{-14}. \tag{2.2.47}$$

has been satisfied. In the above, $|x_{j+1}|$ is the L^2-norm of the current vector of Chebyshev coefficients and $|x_{j+1} - x_j|$ is the L^2-norm of the difference between the coefficients' vectors computed at two consecutive iterations. The rate of convergence of the iterative process can be controlled using the under/over-relaxation. The relaxation process has been implemented using the following formula

$$x_{j+1} = x_j + RF|x_{comp} - x_j|, \tag{2.2.48}$$

where x_{comp} denotes the current solution, x_{j+1} stands for the accepted value of the next iterate and RF denotes the relaxation factor.

The nonlinear terms are updated based on the information available from the previous iteration. The velocity components v_r and v_z are computed by transferring data into the physical space using the known modal functions $\phi^{(n)}(\xi)$, i.e.,

$$
\begin{aligned}
v_z(z,\xi) &= -\Gamma^2(\xi - c)^{-1} \sum_{n=-N_M}^{N_M} D\phi^{(n)}(\xi)e^{in\alpha z}, \\
v_r(z,\xi) &= i\alpha\Gamma(\xi - c)^{-1} \sum_{n=-N_M}^{N_M} n\phi^{(n)}(\xi)e^{in\alpha z}.
\end{aligned}
\tag{2.2.49a, b}
$$

The multiplications are carried out in physical space and the Fourier expansions expressing velocity products are determined using FFT procedure. At each ξ-location, v_r and v_z are evaluated at equidistant points along the z-axis and the last point is discarded due to periodicity. $2M_M + 2$ locations (where $M_M = 3N_M/2$) are used, i.e., advantage is taken of the 3/2 rule to control the aliasing error. The velocity products $\{v_z v_z\}$, $\{v_r v_r\}$ and $\{v_z v_r\}$ are evaluated at this location and values of the modal functions of their Fourier expansions, i.e., $v_{zz}^{(n)}$, $v_{rr}^{(n)}$ and $v_{zr}^{(n)}$ are computed using FFT. Only modes from $-N_M$ to N_M are retained. The final step consists of determination of Chebyshev expansions of the modal functions, i.e., evaluation of coefficients $G_{zz,k}^{(n)}$, $G_{rr,k}^{(n)}$ and $G_{zr,k}^{(n)}$ in Eq. (2.2.24).

2.2.6 Efficient linear solver

Applicability of the algorithm depends on the computational efficiency and on the storage requirements. Computational cost depends on the efficiency of linear solver used to solve (2.2.45), on the efficiency of data storage strategy used to retain data required by (2.2.45) and on the efficiency of the FFT algorithm required to update the right side of (2.2.45). The latter one has been optimized while the efficiencies of the former ones strongly depend on the ability to take advantage of the special structure of matrix **L**. This structure is illustrated in Figure **2-2**A where the nonzero components have been marked in black and the unknowns have been organized according to the mode number $-N_M$, ..., 0, ..., N_M. The upper triangular blocks correspond to the modal equations, which are uncoupled, and black horizontal lines correspond to the boundary relations (four relations per block) which provide coupling between different modal equations. When a large number of Fourier modes needs to be used, the size of matrix **L** could be excessive resulting in the processing and storage requirements which might make the method impractical. We develop a special solution and storage strategy following concepts described in Husain & Floryan (2013).
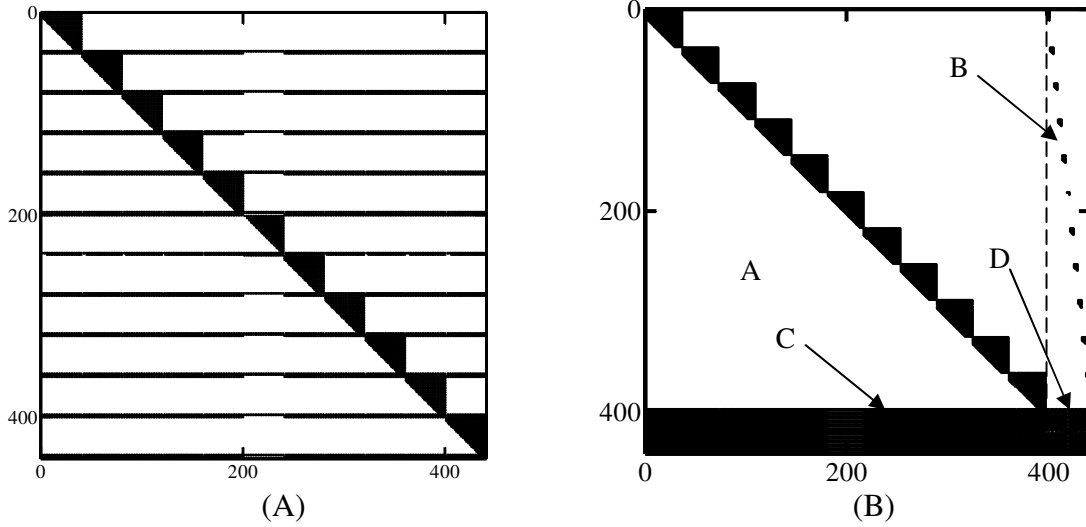
Figure 2-2: *Structure of the coefficient matrix for $N_M = 5$ and $N_T = 40$. The nonzero elements are marked in black. The total number of elements, the number of nonzero elements and the sparsity (ratio of the number of the zero elements to the total number of the elements) for this matrix are $(440)2 = 193600$, 27780 and 0.86, respectively. Figure 2-2A - the structure of the coefficient matrix before the re-arrangement, Figure 2-2B - the structure of the coefficient matrix after the re-arrangement (see Section 2.2.6 for a discussion).*

In the first step L is re-organized by moving entries corresponding to boundary relations to the bottom forming a block diagonal matrix L_1 of size $q \times p$, where $q = (2N_M + 1) \times (N_T - 3)$, and a full matrix L_2 (which contains all boundary relations) of size $r \times p$, where $r = 4 \times (2N_M + 1)$. The largest possible square matrix A (of size $q \times q$) is extracted from L_1 by moving the unknown Chebyshev coefficients corresponding to the four lowest polynomials to the end of the vector of unknowns resulting in the structure illustrated in Figure 2-2B. The resultant square matrix A of size $q \times q$ has a block diagonal structure with each block of size $(N_T - 3) \times (N_T - 3)$, the rectangular matrix B of size $q \times r$ also has a block diagonal form with blocks of size $(N_T - 3) \times 4$, the full rectangular matrix C has size $r \times q$ and the full square matrix D has size $r \times r$. Matrices B and D contain coefficients corresponding to $G_0^{(n)}$, $G_1^{(n)}$, $G_2^{(n)}$ and $G_3^{(n)}$, while information associated with the remaining coefficients is stored in matrices A and C (Figure 2-2B). Equation (2.2.45) takes the from

$$Ax_1 + Bx_2 = R_1, \quad Cx_1 + Dx_2 = R_2, \tag{2.2.50a, b}$$

where vector x_1 contains unknowns $G_k^{(n)}$ for $n \in \langle -N_M, N_M \rangle$, $k \in \langle 4, N_T \rangle$, and vector x_2 contains unknowns $G_k^{(n)}$ for $n \in \langle -N_M, N_M \rangle$, $k \in \langle 0,3 \rangle$. Solution of (2.2.50a, b) can be written as

$$x_2 = [D - CA^{-1}B]^{-1}(R_2 - CA^{-1}R_1), \quad x_1 = A^{-1}(R_1 - Bx_2). \tag{2.2.51}$$

The reader may note that the above procedure requires storage of the diagonal blocks of matrices A and B rather than complete matrices and thus leads to significant reduction of storage requirements. The processing efficiency is improved as one may construct A^{-1}, CA^{-1}, $CA^{-1}B$, $A^{-1}R_1$ and $A^{-1}B$ block by block rather than carrying operations on complete matrices. Additional savings result from the fact that only some of these matrices need to be re-computed at each iteration. Use of complex conjugate properties of the modal functions provides further efficiencies.

The effective acceleration of computations, when compared with standard solvers that do not take advantage of this specific matrix structure, is *O(100)* and the effective memory requirements reduction, when compared with full matrices, is at least *O(100).*

2.2.7 Testing of the algorithm

This section presents discussion of various tests carried out in order to demonstrate the spectral accuracy of the algorithm and to illustrate the effects of numerical and physical parameters on the accuracy of the solution. In order to focus discussion, most of the tests to be presented have been carried out for the model geometry consisting of a smooth outer cylinder and the inner cylinder fitted with ribs with a simple geometry described by one Fourier mode, i.e.,

$$r_{in}(z) = R_1 + S\cos(\alpha z), \quad r_{out}(z) = 1 + R_1, \tag{2.2.52}$$

where S denotes the amplitude and α stands for the wave number of the ribs.

Three aspects of the approximation should be considered. In the radial direction, the Chebyshev expansions (2.2.23) with coefficients calculated using Galerkin procedure (A-1) are guaranteed to be spectrally accurate with the increasing number of terms N_T (Manson 2003) and thus this aspect of accuracy does not need to be tested. The convergence is very rapid and in most cases 60-70 Chebyshev polynomials provide machine accuracy. The number of polynomials needs however to be increased when $\alpha \rightarrow \infty$ (corrugation with shorter wavelength), especially when higher Fourier modes begin to play a role. The need for more polynomials occurs because of the formation of boundary layers in the distributions of the modal functions $\phi^{(n)}(\xi)$ around the ribbed walls which need to be properly resolved. These layers become extremely thin for larger values of α and for higher Fourier modes (see Figure **2-3**).

(A)   (B)
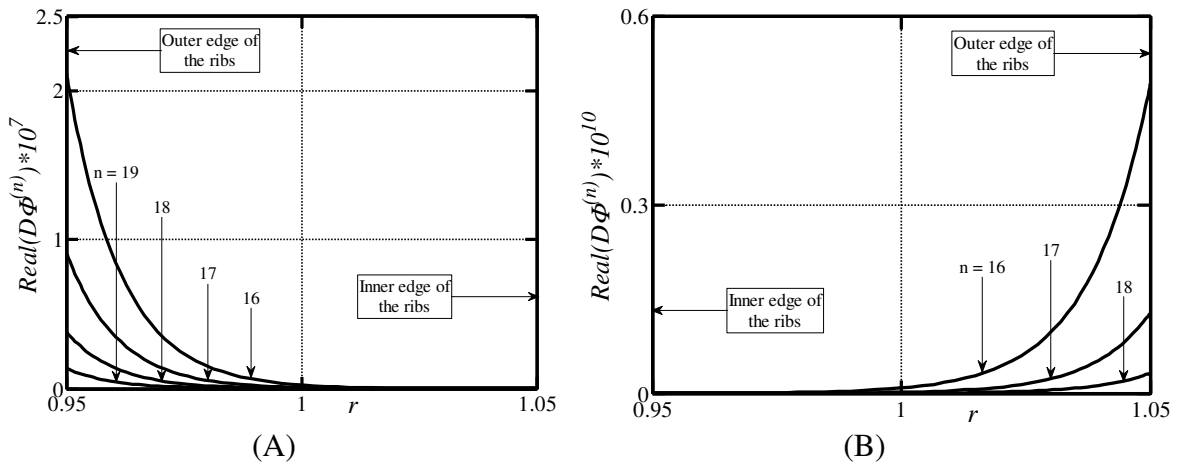
Figure 2-3: *Distribution of the real part of $D\phi^{(n)}$ as a function of r for higher Fourier modes $(n > 15)$ for ribs placed either at the inner cylinder (Figure **2-3**A) or at the outer cylinder (Figure **2-3**B). The geometry of the ribs' is given by Eq. (2.2.52) with the ribs' wave number $\alpha = 5$, the ribs' amplitude S = 0.05 and the average radius on the inner cylinder $R_1 = 1$. Computations have been carried out for the flow Reynolds number Re = 50 using $N_M = 20$ Fourier modes and $N_T = 70$ Chebyshev polynomials.*

Results displayed in Figure **2-3** demonstrate that placement of the same ribs either at the inner or at the outer cylinder results in more extreme boundary layers in the former case. Most of the tests to be reported have been therefore carried out with the ribs placed at the inner cylinder, as described by Eq. (2.2.52).

The second aspect of the spectral accuracy involves convergence of the truncated Fourier series (2.2.21a-d). In all tests dealing with this issue, the number of Chebyshev polynomials N_T was kept sufficiently large ($N_T = 70$) so that the associated error was reduced to machine accuracy. The "magnitude" of modal functions is measured using Chebyshev norm defined as

$$\left\|D\phi^{(n)}\right\|_\omega = \left[\int_{-1}^{1} D\phi^{(n)}(\xi)D\phi^{(n)*}(\xi)\omega(\xi)d\xi\right]^{1/2}, \tag{2.2.53}$$

where $\omega(\xi) = (1 - \xi^2)^{-1/2}$. Results displayed in Figure **2-4** demonstrate exponential decrease of $\left\|D\phi^{(n)}\right\|_\omega$ with the mode number n and thus confirm the spectral accuracy of the z-discretization.

(A)   (B)
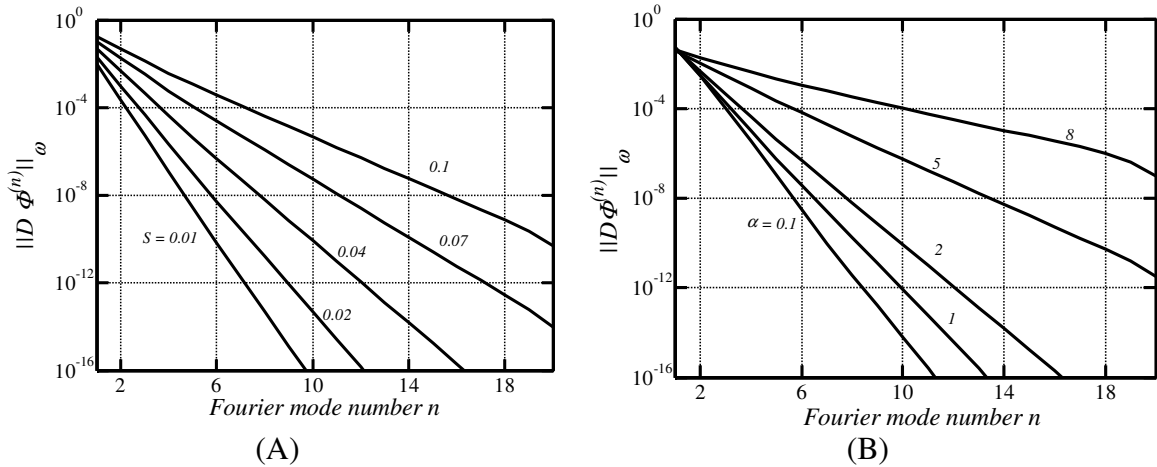
Figure 2-4: *Variations of the Chebyshev norm $\left\|D\phi^{(n)}\right\|_\omega$ defined by Eq. (2.2.53) as a function of the Fourier mode number n for the model geometry described by Eq. (2.2.52) with the ribs' wave number $\alpha = 2$ for selected values of the ribs' amplitude S (Figure **2-4**A) and with the ribs' amplitude S = 0.04 for selected values of the ribs' wave numbers α (Figure **2-4**B). Calculations have been carried out for the flow Reynolds number Re = 50 and the average radius of the inner cylinder $R_1 = 1.5$ using $N_M = 20$ Fourier modes and $N_T = 70$ Chebyshev polynomials.*

The rate of convergence is a function of the ribs' wave number α and the ribs' amplitude S, and increases with reduction of both of them. Results displayed in Figure **2-5**

demonstrate that the rate of convergence does not depend on the value of the Reynolds number *Re* as long as *Re* is not too large.
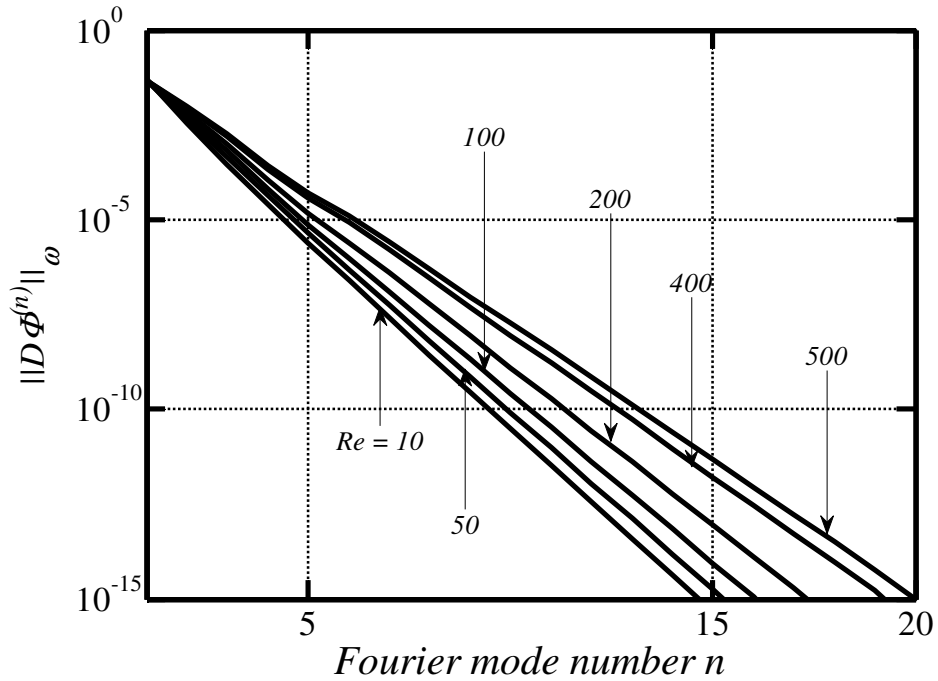
Figure 2-5: *Variations of the Chebyshev norm* $\left\|D\phi^{(n)}\right\|_\omega$ *defined by Eq. (2.2.53) as a function of the Fourier mode number n for the model geometry described by Eq. (2.2.52) with the ribs' amplitude S = 0.04, the ribs' wave number α = 2 and the average radius of the inner cylinder R_1 = 1.5 for selected values of the flow Reynolds number Re. Calculations have been carried out using N_M = 20 Fourier modes and N_T = 70 Chebyshev polynomials.*

The third aspect of accuracy involves enforcement of the flow boundary conditions using the IBC concept. For convenience, we introduce the L_∞ norm defined as

$$\|V_{in}\|_\infty = sup_{0 \leq z \leq 2\pi/\alpha} \left|\{v_z^2[z, r_{in}(z)] + v_r^2[z, r_{in}(z)]\}^{1/2}\right|, \qquad (2.2.54)$$

which provides a measure of error in the enforcement of boundary conditions at the inner cylinder. A similar norm can be defined for the outer cylinder. Results displayed in Figure **2-6** demonstrate exponential reduction of the error with an increase of the number of Fourier modes used in the discretization and thus confirm spectral accuracy of this part of discretization. The convergence rate increases with a decrease of both the amplitude

and the wave number of the ribs. The absolute accuracy may be improved by using the over-determined formulation of the IBC method (Husain *et al*. 2009).

(A)   (B)
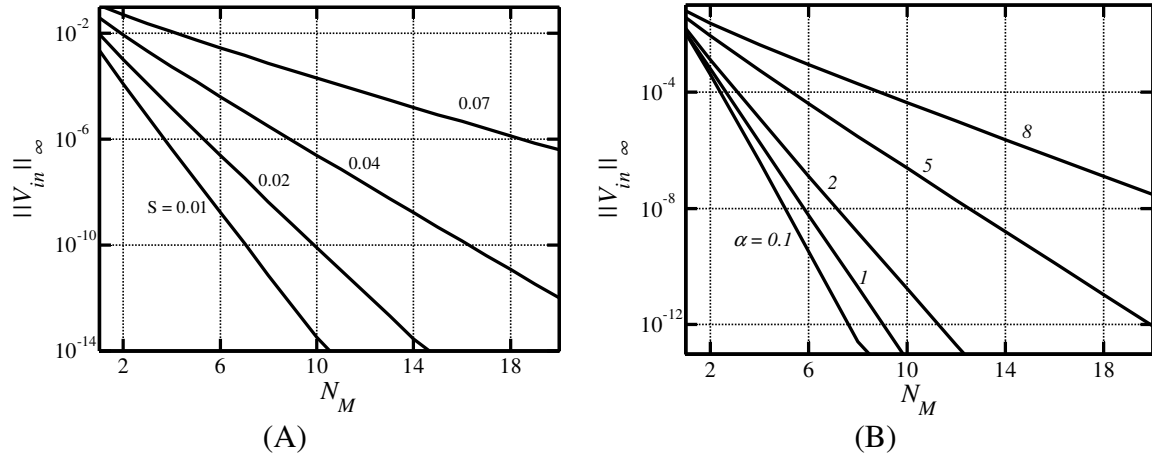
Figure 2-6: *Variations of the norm* $\|V_{in}\|_\infty$ *defined by Eq. (2.2.54) as a function of the number of Fourier modes* N_M *used in the computations for the model problem described by Eq. (2.2.52) with the ribs' wave number* $\alpha = 5$ *for selected values of the ribs' amplitude S (Figure* **2-6***A) and with the ribs' amplitude S = 0.04 for selected values of the ribs' wave number* α *(Figure* **2-6***B). Calculations have been carried out for the flow Reynolds number Re = 50 and the average radius of the inner cylinder* $R_1 = 1$ *using* $N_T = 70$ *Chebyshev polynomials.*

Variations of $v_z[z, r_{in}(z)]$ and $v_r[z, r_{in}(z)]$, which represent error of the IBC method, over a single period are displayed in Figure **2-7**. Both errors have spatially oscillatory character with the amplitudes' maxima occurring in the region corresponding to the widest opening of the annuli. The modal functions $\phi^{(n)}$ reach their maxima around the extremes of the solution domain (see Figure **2-3**) where omission of higher modes increases the absolute error and thus determines location of the error maxima.

Implementation of boundary conditions (2.2.31)-(2.2.32) using the IBC method guarantees that Fourier modes in the error spectrum of v_z and v_z at the flow domain boundaries do not contain harmonics of order lower than N_M. This property provides a test for accuracy and consistency of the method. Results shown in Figure **2-8**A demonstrate that the numerical solution does have this property.
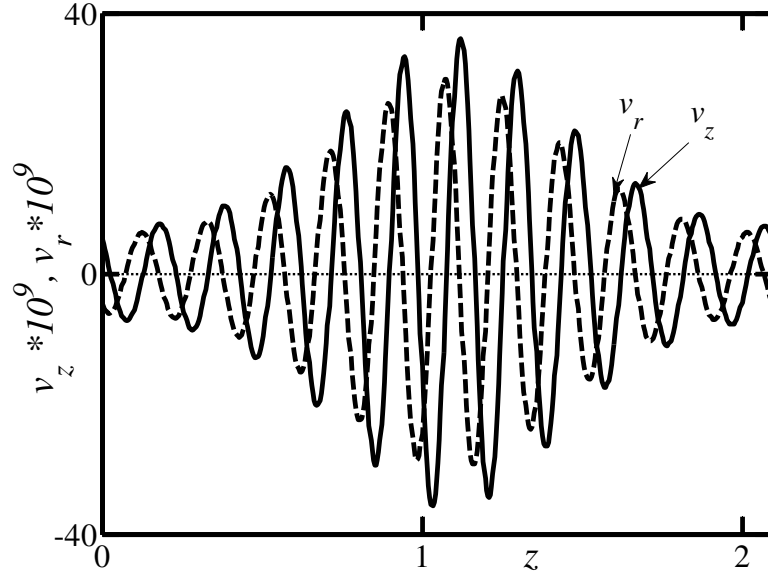
Figure 2-7: *Distributions of the velocity components v_z and v_r evaluated along the inner cylinder for the model geometry described by Eq. (2.2.52) with the ribs' wave number $\alpha = 3$, the ribs' amplitude S = 0.05 and the average radius of the inner cylinder $R_1 = 1$. Calculations have been carried out for the flow Reynolds number Re = 50 using $N_M = 10$ Fourier modes and $N_T = 40$ Chebyshev polynomials.*

The form of boundary conditions (2.2.25) suggests that the factor $[\xi_{in}(z) - c]^{-1}$ could be eliminated from the numerical implementation. The resulting boundary relations would be based on the elimination of the first N_M of the leading Fourier modes from $\partial\psi/\partial\xi$ and $\partial\psi/\partial z$. The eliminated factor represents a *z*-periodic function and its product with the derivatives of the stream function produces different periodic functions. Thus use of boundary relations based on the "primitive" form of boundary conditions represented by (2.2.25) results in slightly different boundary relations as compared with those based on the derivatives of the stream function. The full boundary conditions (2.2.25) have been implemented in the current work. Fourier spectra of the derivatives of the stream function computed at the ribbed wall on the basis of such boundary conditions are displayed in Figure **2-8**B. Presence of a small error in modes with $n < N_M$ can be observed, however its magnitude makes this error irrelevant for practical applications.
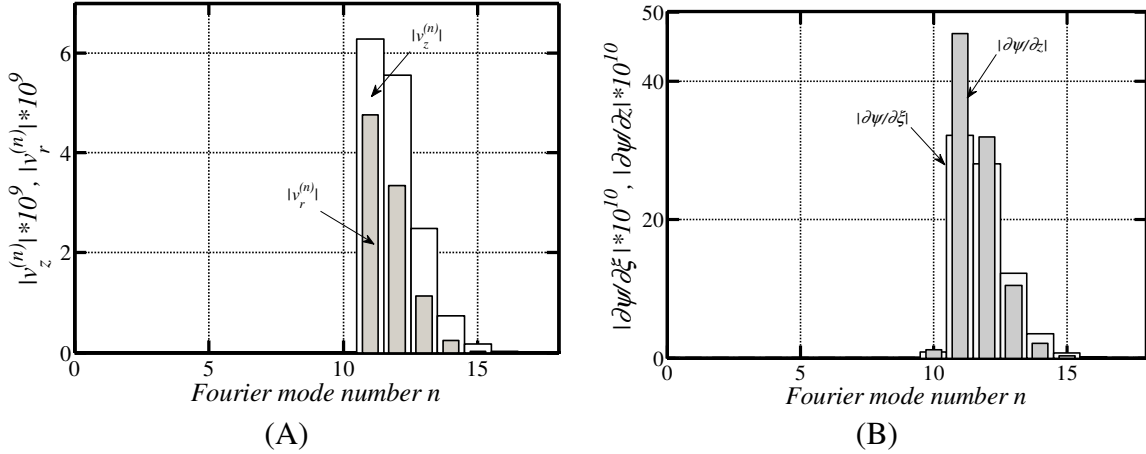
Figure 2-8: *Fourier spectra of the velocity components v_z and v_r (Figure **2-8**A) and of the stream function derivatives $\partial\psi/\partial\xi$ and $\partial\psi/\partial z$ (Figure **2-8**B) evaluated at the surface of the inner cylinder. Other conditions as in Figure **2-7**.*

Tests have been carried out in order to determine if the IBC method produces spurious spatial oscillations. Figure **2-9** illustrates results for the wall with the ribs' wave number $\alpha = 3$ and the ribs' amplitude $S = 0.05$. In case A, the shape of the ribs was assumed to be represented by the principal Fourier mode and the calculations were carried out with $N_M = 10$ Fourier modes. In case B, the same shape was assumed to be represented by the second Fourier mode (the principal mode had the wave number $\alpha = 1.5$), while in case C it was represented by the third Fourier mode (the principal mode had the wave number $\alpha = 1$). In order to have fully equivalent representations, the number of Fourier modes used in cases B and C was $N_M = 20$ and 30, respectively, and thus sub harmonics of the $1/2$ type in case B and the $1/3$ type in case C were admitted. The Fourier spectra of boundary error shown in Figure **2-10** demonstrate the equivalency of the results for all three cases. No subharmonics have been produced during the solution process and the modes expected to produce zero contributions in cases B and C behaved as expected.
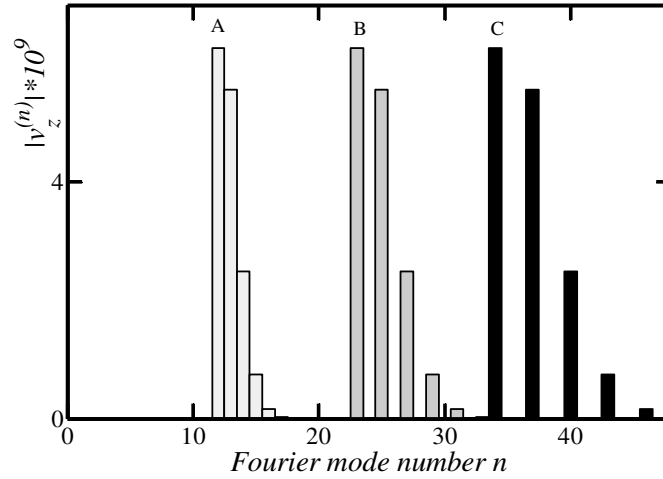
Figure 2-9: *Fourier spectra of the axial velocity component v_z evaluated at the surface of the inner cylinder for ribs with the wavelength $\lambda = 2\pi/3$. Other conditions as in Figure* **2-7***. Solution have been obtained with $\alpha = 3$ and $N_M = 10$ in case A, $\alpha = 1.5$ and $N_M = 20$ in case B, and $\alpha = 1$ and $N_M = 30$ in case C.*
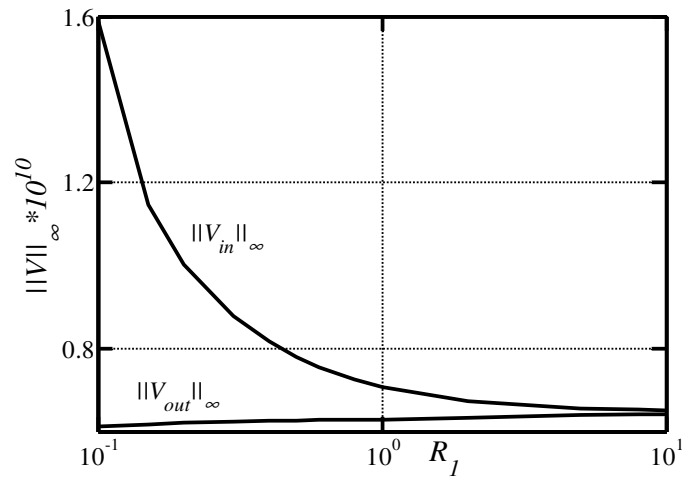
Figure 2-10: *Variations of the norms $\|V_{in}\|_\infty$ and $\|V_{out}\|_\infty$ defined by Eq. (2.2.54) as a function of the radius of the inner cylinder R_1. The former one corresponds to an annulus with geometry described by Eq. (2.2.52) with the ribs' wave number $\alpha = 4$ and the ribs' amplitude S = 0.06. The latter one corresponds to the same ribs but placed at the outer cylinder. Computations were carried out for the flow Reynolds number Re = 10 using $N_M = 20$ Fourier modes and $N_T = 70$ Chebyshev polynomials.*

Variations of the boundary error as a function of the average radius of the inner cylinder R_1 are illustrated in Figure **2-10**. It can be seen that the error is bigger if the ribs are placed at the inner cylinder as long as R_1 is sufficiently small. An increase of R_1 equilibrates errors associated with placements of the ribs at either cylinder and the magnitudes of these errors approach the error determined for a two-dimensional channel using algorithm described in Szumbarski & Floryan (1999). It can be seen that the curvature effects are important only for $R_1 < \sim2$.
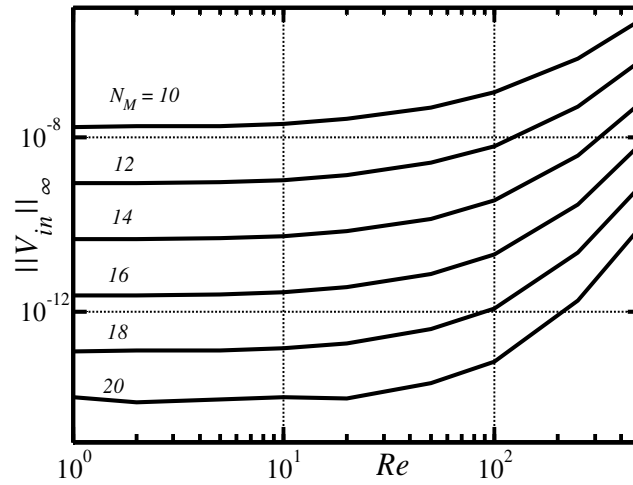
Figure 2-11: *Variation of the norm $\|V_{in}\|_\infty$ defined by Eq. (2.2.54) as a function of the flow Reynolds number Re for an annulus with geometry defined by Eq. (2.2.52) with the ribs' wave number $\alpha = 4$, the ribs' amplitude S = 0.04 and the average radius of the inner cylinder $R_1 = 1$ determined using different number of Fourier modes N_M and $N_T = 70$ Chebyshev polynomials.*

The absolute error of the method depends on the flow Reynolds number and on the geometry of the ribs. Variations of $\|V_{in}\|_\infty$ as a function of the flow Reynolds number are illustrated in Figure **2-11**. The error remains approximately constant as *Re* increases as long as *Re* remains smaller then *~50*. Further increase of *Re* results in an increase of the error as nonlinear terms begin to play a larger role. The error can be reduced by increasing the number of Fourier modes N_M used in the computations.

Variations of $\|V_{in}\|_\infty$ as a function of the ribs' geometry, i.e., their wave number α and amplitude *S*, are illustrated in Figure **2-12**. It can be seen that the error remains at machine level if *S* and α are sufficiently small. Increase of both *S* and α beyond certain

critical values causes the error to increase rapidly. The magnitude of this error can be reduced by increasing the number of Fourier modes used in the computations (see Figure **2-12**) and by using the over-determined formulation of the IBC method (Husain *et al.* 2009).
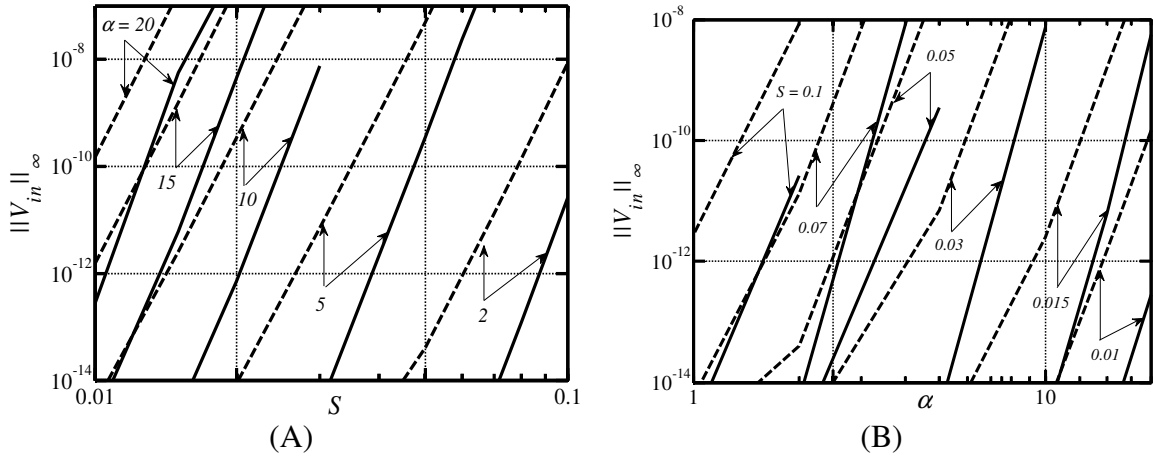
Figure 2-12: *Variations of the norm $\|V_{in}\|_\infty$ defined by Eq. (2.2.54) as a function of the ribs' amplitude S for selected values of the ribs' wave numbers α (Figure **2-12**A) and as a function of the ribs' wave number α for selected values of the ribs' amplitude S (Figure **2-12**B) for the model configuration described by Eq. (2.2.52). Calculations have been carried out for the flow Reynolds number Re = 50 and the average radius of the inner cylinder $R_1 = 1$ using $N_M = 20$ (solid lines) and $N_M = 15$ (dashed line) Fourier modes, and $N_T = 70$ Chebyshev polynomials.*

The proposed algorithm can be used for analysis of various effects associated with the presence of the ribs for various ribs' geometries. Figure **2-13** illustrates variations of the additional pressure loss induced by the ribs as a function of the amplitude *S* and the wave number α for the geometry described by Eq. (2.2.52). The required computation can be carried out very efficiently as modeling of changes of geometry is completely automatic and limited to specification of the range of variations of *S* and α. Figure **2-14** illustrates another possible study where one investigates variations of the additional pressure loss as a function of the flow Reynolds number *Re* and the average radius of the inner cylinder R_1.
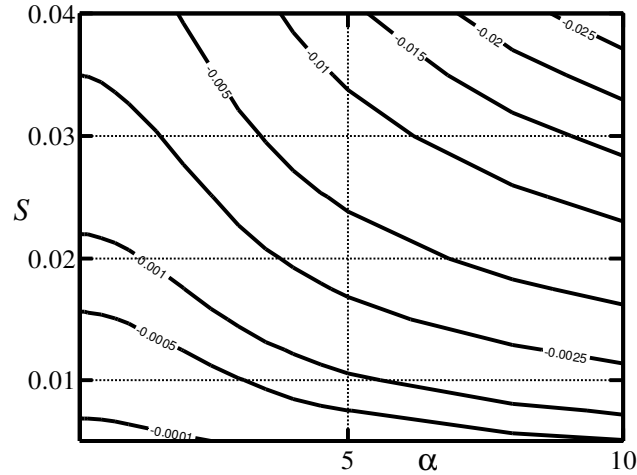
Figure 2-13: *Variations of the additional pressure loss generated by the ribs with geometry defined by Eq. (2.2.52) as a function of the rib's amplitude S and the ribs' wave number α for the flow Reynolds number Re = 10 and the average radius of the inner cylinder $R_1 = 1$.*
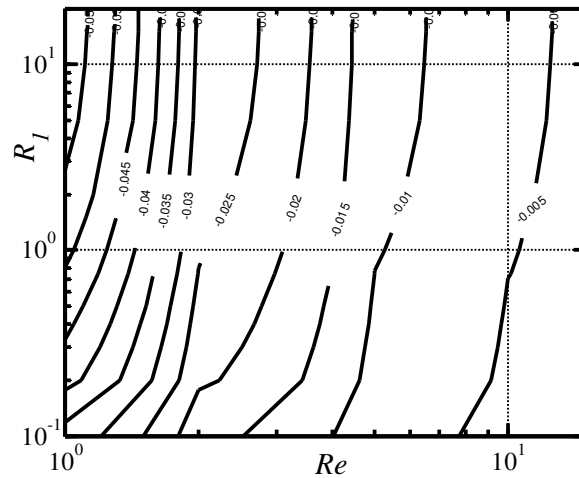
Figure 2-14: *Variations of the additional pressure loss generated by the ribs with geometry given by Eq. (2.2.52) as a function of the flow Reynolds number Re and the average radius of the inner cylinder R_1 for ribs with the wave number $\alpha = 2$ and the amplitude S = 0.04.*

Figure **2-15** illustrates flow pattern computed for a complex geometry where shape of the ribs at the inner cylinder is described by the following relation

$$r_{in}(z) = 1 + 0.03e^{iz} + 0.015ie^{3iz} + 0.01e^{4iz} + c.c., \quad r_{out}(z) = 1 + R_1, \qquad (2.2.55)$$

This figure illustrates flexibility of the algorithm for simulation of flows modified by ribs with complex geometries.
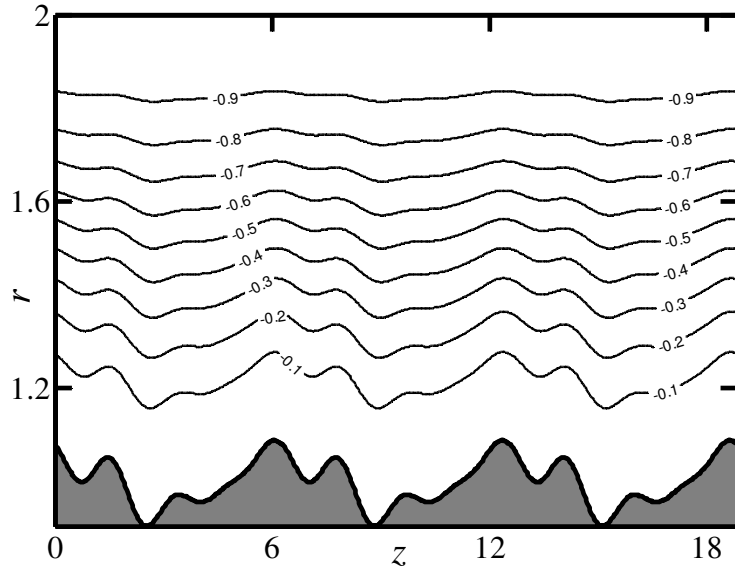
Figure 2-15: *Streamlines of a flow in an annulus with geometry defined by Eq. (2.2.55) for the flow Reynolds number Re = 10.*

2.3 Annulus with longitudinal grooves

2.3.1 Formulation of the problem

Consider the same annulus as in Section 2.2 but fitted with axial ribs, as illustrated in Figure **2-16**. The geometry of the inner and outer cylinders is described by the following relations

$$r_{in}(\theta) = R_1 + \sum_{n=-N_A}^{N_A} H_{in}^{(n)} e^{in\theta} \, , r_{out}(\theta) = 1 + R_1 + \sum_{n=-N_A}^{N_A} H_{out}^{(n)} e^{in\theta} \qquad \text{(2.3.1a, b)}$$

where $H_{in}^{(n)} = H_{in}^{(-n)*}$ and $H_{out}^{(n)} = H_{out}^{(-n)*}$ are the reality conditions, stars denote the complex conjugate, R_1 stands for the average radius of the inner annulus, subscripts "*out*" and "*in*" denote the outer and inner annuli, respectively, and N_A is the number of Fourier modes required for description of geometry. The wave number does not appear as a parameter as $\theta \in (0, 2\pi)$.
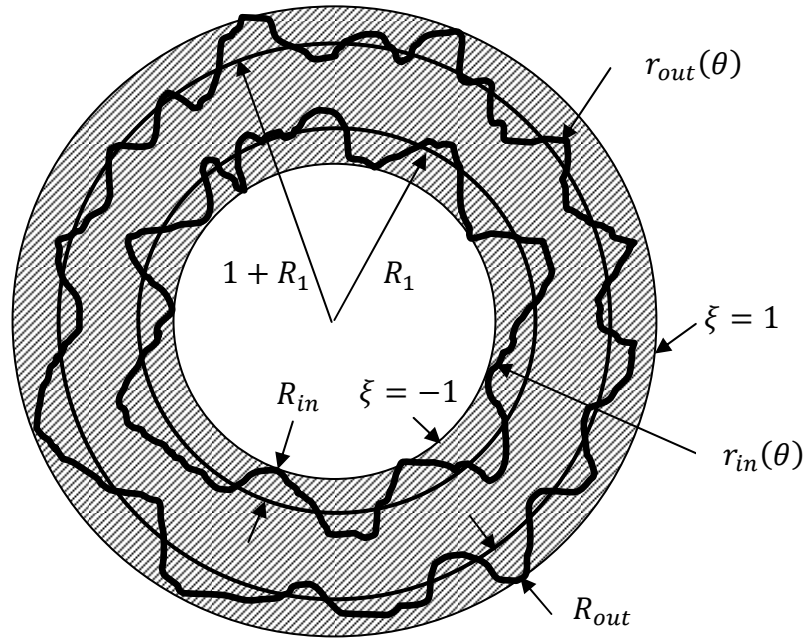
Figure 2-16: *Sketch of the flow geometry - annulus with axial ribs of arbitrary form. Shaded area represents computational domain.*

The velocity vector has components $(v_z, 0, 0)$ in the (z, r, θ) directions and thus the field equations reduce to the axial momentum equation in the form

$$\frac{\partial p}{\partial z} = \frac{1}{Re}\left(\frac{1}{r}\frac{\partial v_z}{\partial r} + \frac{\partial^2 v_z}{\partial r^2} + \frac{1}{r^2}\frac{\partial^2 v_z}{\partial \theta^2}\right) \tag{2.3.2}$$

The above equation has been scaled using the same scales as described in Section 2.2. Flow quantities can be split into a sum of the reference flow and flow modification due to the presence of the ribs, i.e.,

$$v_z(r, \theta) = v_{z_0}(r) + v_{z_1}(r, \theta), p(z) = p_0(z) + p_1(z) \tag{2.3.3a, b}$$

where subscripts 0 and 1 refer to the reference and the modification quantities, respectively. The reference flow has been discussed in Section 2.2.2. Equation governing flow modifications has the same form as (2.3.4), i.e.,

$$\frac{\partial p_1}{\partial z} = \frac{1}{Re}\left(\frac{1}{r}\frac{\partial v_{z_1}}{\partial r} + \frac{\partial^2 v_{z_1}}{\partial r^2} + \frac{1}{r^2}\frac{\partial^2 v_{z_1}}{\partial \theta^2}\right) \qquad (2.3.4)$$

and it is linear, as opposed to Eq. (2.2.9) considered in Section 2.2. Re does appear as a separate parameter as it can be incorporated into the pressure gradient. The no-slip conditions at the walls expressed in term of the flow modifications have the form

$$v_{z_1}(r,\theta) = -v_{z_0}(r,\theta), \text{at } r = r_{in}(\theta) \text{ and } r = r_{out}(\theta). \qquad (2.3.5a, b)$$

Pressure gradient modification $Re\, \partial p_1/\partial z$ is specified in the case of the fixed pressure gradient constraint. This pressure gradient is not known in the case of the fixed flow rate constraint, but can be determined by enforcing additional condition in the form

$$Q = Q_{ref} + Q_{mod} = \int_A v_z dA = \int_0^{2\pi}\int_{r_{in}(\theta)}^{r_{out}(\theta)} r\, v_z dr d\theta. \qquad (2.3.6)$$

where Q_{ref} and Q_{mod} denote the flow rate of the reference flow and the prescribed flow rate modification associated with the presence of the ribs. It has been assumed in all tests discussed in this study that the ribs did not alter the mass flow rate, i.e., $Q_{mod} = 0$.

2.3.2 Discretization

This section describes discretization of the above problem. Transformation (2.2.17) maps the computational domain from $r \in [-R_{in} + R_1, 1 + R_{out} + R_1]$ to $\xi \in [-1,1]$ in order to permit the use of the standard definition of Chebyshev polynomials. Shapes of the boundaries are given in terms of ξ as

$$\xi_{in}(\theta) = \sum_{n=-N_A}^{N_A} A_{in}^{(n)} e^{in\theta}, \xi_{out}(\theta) = \sum_{n=-N_A}^{N_A} A_{out}^{(n)} e^{in\theta}, \qquad (2.3.7a, b)$$

where $A_{in}^{(0)} = c + \Gamma R_1 + \Gamma H_{in}^{(0)}$, $A_{in}^{(n)} = \Gamma H_{in}^{(n)}$ for $n \neq 0$, $A_{out}^{(0)} = c + \Gamma(1 + R_1) + \Gamma H_{out}^{(0)}$ and $A_{out}^{(n)} = \Gamma H_{out}^{(n)}$ for $n \neq 0$. The field equation in the (ξ, θ) coordinate system takes the form

$$\frac{Re}{\Gamma^2}\frac{\partial p_1}{\partial z} = \left[\frac{1}{\xi - c}\frac{\partial v_{z_1}}{\partial \xi} + \frac{\partial^2 v_{z_1}}{\partial \xi^2} + \frac{1}{(\xi - c)^2}\frac{\partial^2 v_{z_1}}{\partial \theta^2}\right] \qquad (2.3.8)$$

and the boundary conditions can be expressed as

$$v_{z_1}(\xi, \theta) = -v_{z_0}(\xi, \theta), \text{ at } \xi = \xi_{in}(\theta) \text{ and } \xi = \xi_{out}(\theta). \qquad (2.3.9a, b)$$

2.3.2.1 Discretization of the field equation

The unknown v_{z_1} can be expressed in terms of Fourier series in the form

$$v_{z_1}(\xi, \theta) \approx \sum_{n=-N_M}^{N_M} \phi^{(n)}(\xi)e^{in\theta}. \qquad (2.3.10)$$

Substitution of (2.3.10) into (2.3.8) and separation of Fourier modes result in the following modal equations

$$\begin{cases} \dfrac{D\phi^{(n)}(\xi)}{\xi - c} + D^2\phi^{(n)}(\xi) - \dfrac{n^2\phi^{(n)}(\xi)}{(\xi - c)^2} = 0, n \neq 0 \\ \dfrac{D\phi^{(n)}(\xi)}{\xi - c} + D^2\phi^{(n)}(\xi) = \dfrac{Re}{\Gamma^2}\dfrac{\partial p_1}{\partial z}, n = 0 \end{cases} \qquad (2.3.11)$$

The above system is complete in the case of the fixed pressure gradient constraint, but must be supplemented by an additional condition when the pressure gradient correction is not known. The fixed flow rate constraint (2.3.6) represents such a supplementary condition and its discretization is described in Section 2.3.2.3.

Modal functions are discretized using Chebyshev expansions in the form

$$\phi^{(n)}(\xi) \approx \sum_{k=0}^{N_T} G_k^{(n)} T_k(\xi). \qquad (2.3.12)$$

Substitution of (2.3.12) into (2.3.11), multiplications by the largest power of ξ found in the denominators and application of the Galerkin procedure bring equations to the form

$$\sum_{k=0}^{N_T} \left[\langle T_j, \xi DT_k \rangle - c \langle T_j, DT_k \rangle + \langle T_j, \xi^2 D^2 T_k \rangle - 2c \langle T_j, \xi D^2 T_k \rangle + c^2 \langle T_j, D^2 T_k \rangle \right. \tag{2.3.13a}$$

$$\left. -n^2 \langle T_j, T_k \rangle \right] G_k^{(n)} = 0, n \neq 0$$

$$\sum_{k=0}^{N_T} \left[\langle T_j, DT_k \rangle + \langle T_j, \xi D^2 T_k \rangle - c \langle T_j, D^2 T_k \rangle \right] G_k^{(0)} = \frac{Re}{\Gamma^2} \frac{\partial p_1}{\partial z} \langle T_j, \xi \rangle \tag{2.3.10b}$$

$$- \frac{cRe}{\Gamma^2} \frac{\partial p_1}{\partial z} \langle T_j, 1 \rangle, n = 0$$

for $j \in [0, N_T - 2]$ leaving space for the imposition of two boundary conditions for each modal function in the Tau-like manner. Discretization of the flow rate constraint is discussed in Section 2.3.2.3.

2.3.2.2 Discretization of the boundary conditions

Boundary conditions (2.3.9a, b) have to be enforced along the lines $\xi_{in}(\theta)$ and $\xi_{out}(\theta)$ whose locations are given by Eqs (2.3.7a, b). While the numerical implementation of these conditions is similar to that described in Section 2.2.3.2, changes associated with the use of the flow modification as unknown warrant a separate explanation. We shall limit the following discussion to description of boundary condition at the inner cylinder while similar condition for the outer cylinder can be obtained by simple replacing subscript "*in*" with subscript "*out*".

Boundary condition at the inner cylinder has the form

$$v_{z_1}(\xi_{in}, \theta) = -v_{z_0}(\xi_{in}, \theta). \tag{2.3.14}$$

The reference flow evaluated at this wall represents a periodic function which can be expressed using Fourier series, i.e.,

$$v_{z_0}(\xi_{in}, \theta) = \frac{R_1^2}{k_1} \left[1 - \left(\frac{\xi_{in} - c}{\Gamma R_1} \right)^2 \right] + \frac{k_2}{k_1} ln \left(\frac{\xi_{in} - c}{\Gamma R_1} \right) = \sum_{n=-N_\theta}^{N_\theta} F^{(n)} e^{in\theta} \tag{2.3.15}$$

where the coefficients $F^{(n)}$ are known and can be explicitly evaluated using FFT algorithm. The discretized form of the velocity correction evaluated at the inner cylinder takes the form

$$v_{z_1}(\xi_{in}, \theta) = \sum_{n=-N_M}^{N_M} \sum_{k=0}^{N_T} G_k^{(n)} T_k(\xi_{in}) e^{in\theta} \tag{2.3.16}$$

where $T_k(\xi_{in})$ are periodic functions of θ and can be expressed in terms of Fourier series in the form

$$T_k(\xi_{in}) = \sum_{m=-N_S}^{N_S} w_{in,k}^{(m)} e^{im\theta}. \tag{2.3.17}$$

Algorithm for computing $w_{in,k}^{(m)}$ is presented in Appendix B. Substitution of (2.3.17) into (2.3.16) results in

$$v_{z_1}(\xi_{in}, \theta) = \sum_{m=-N_S}^{N_S} \sum_{n=-N_M}^{N_M} \sum_{k=0}^{N_T} G_k^{(n)} w_{in,k}^{(m)} e^{i(n+m)\theta}. \tag{2.3.18}$$

Re-arrangement of indices and comparison of (2.3.15) and (2.3.18) lead to boundary condition in the form

$$\sum_{n=-N_S-N_M}^{N_S+N_M} \sum_{m=-N_M}^{N_M} \sum_{k=0}^{N_T} G_k^{(m)} w_{in,k}^{(n-m)} e^{in\theta} = - \sum_{n=-N_\theta}^{N_\theta} F^{(n)} e^{in\theta}. \tag{2.3.19}$$

Separation of Fourier modes results in individual boundary relations in the form

$$\sum_{m=-N_M}^{N_M} \sum_{k=0}^{N_T} G_k^{(m)} w_{in,k}^{(n-m)} = -F^{(n)}. \tag{2.3.20}$$

that need to be enforced during the solution process.

In general the total number of the available boundary relations is $N_M + N_T N_A$. Since N_M Fourier modes are used in the solution, one can enforce only N_M of these conditions. The remaining conditions can be used *aposteriori* as a convenient test for consistency of the algorithm. Use of a larger number of such conditions leads to an over-determined formulation of the IBC method (Husain *et al.* 2009) which expands applicability of the method to more extreme geometries. As mentioned before, the number of boundary relations used in this study was always equal to the number of Fourier modes used to represent the flow field resulting in a well posed algebraic problem.

2.3.2.3 Discretization of the flow constraints

The fixed pressure gradient constraint enters the field equations directly and does need any special treatment. The fixed flow rate constraint represents an additional condition which needs to be discretized explicitly.

The fixed flow rate constraint (2.3.6) expressed in terms of the flow modification takes the form

$$Q_{ref} + Q_{mod} = \Gamma^{-2} \int_0^{2\pi} \int_{\xi_{in}(\theta)}^{\xi_{out}(\theta)} (\xi - c) \left[v_{z_0}(\xi) + v_{z_1}(\xi, \theta) \right] d\xi d\theta = I_0 + I_1. \quad (2.3.21)$$

where I_0 and I_1 specify contributions of the reference flow and flow modifications, respectively. I_0 can be written explicitly as

$$I_0 = \frac{1}{k_1 \Gamma^2} \int_0^{2\pi} \int_{\xi_{in}(\theta)}^{\xi_{out}(\theta)} \left[\left(\frac{c^3}{\Gamma^2} - cR_1^2 \right) + \left(R_1^2 - \frac{3c^2}{\Gamma^2} \right) \xi + \frac{3c}{\Gamma^2} \xi^2 - \frac{\xi^3}{\Gamma^2} \right. $$
$$\left. -k_2 c \ln \left(\frac{\xi - c}{\Gamma R_1} \right) + k_2 \ln \left(\frac{\xi - c}{\Gamma R_1} \right) \right] d\xi d\theta. \quad (2.3.22)$$

Analytical evaluation of the inner integral results in

$$I_0 = \frac{1}{k_1\Gamma^2}\int_0^{2\pi}\left[\left(\frac{c^3}{\Gamma^2} - cR_1^2 + \frac{k_2c}{2}\right)(\xi_{out} - \xi_{in}) + \left(\frac{R_1^2}{2} - \frac{3c^2}{2\Gamma^2} - \frac{k_2}{4}\right)\right.$$

$$(\xi_{out}^2 - \xi_{in}^2) + \frac{c}{\Gamma^2}(\xi_{out}^3 - \xi_{in}^3) + \frac{1}{4\Gamma^2}(\xi_{out}^4 - \xi_{in}^4) + \frac{k_2c^2}{2}ln(\xi_{out} - c)$$

$$-\frac{k_2c^2}{2}ln(\xi_{in} - c) - k_2c\xi_{out}ln\left(\frac{\xi_{out} - c}{\Gamma R_1}\right) + k_2c\xi_{in}ln\left(\frac{\xi_{in} - c}{\Gamma R_1}\right)$$

$$\left.+\frac{k_2\xi_{out}^2}{2}ln\left(\frac{\xi_{out} - c}{\Gamma R_1}\right) - \frac{k_2\xi_{in}^2}{2}ln\left(\frac{\xi_{in} - c}{\Gamma R_1}\right)\right]d\theta$$

(2.3.23)

Polynomials in ξ are expressed in terms of Chebyshev expansions (see Appendix A) resulting in

$$I_0 = \frac{1}{k_1\Gamma^2}\int_0^{2\pi}\left[\left(\frac{R_1^2}{4} - \frac{3c^2}{4\Gamma^2} - \frac{k_2}{8} - \frac{3}{32\Gamma^2}\right)[T_0(\xi_{out}) - T_0(\xi_{in})]\right.$$

$$+\left(\frac{c^3}{\Gamma^2} - cR_1^2 + \frac{k_2c}{2} + \frac{3c}{4\Gamma^2}\right)[T_1(\xi_{out}) - T_1(\xi_{in})] + \left(\frac{R_1^2}{4} - \frac{3c^2}{4\Gamma^2} - \frac{k_2}{8} - \frac{1}{8\Gamma^2}\right)$$

$$[T_2(\xi_{out}) - T_2(\xi_{in})] + \frac{c}{4\Gamma^2}[T_3(\xi_{out}) - T_3(\xi_{in})] - \frac{1}{32\Gamma^2}[T_4(\xi_{out}) - T_4(\xi_{in})] \quad (2.3.24)$$

$$+\frac{k_2c^2}{2}ln(\xi_{out} - c) - \frac{k_2c^2}{2}ln(\xi_{in} - c) - k_2c\xi_{out}ln\left(\frac{\xi_{out} - c}{\Gamma R_1}\right)$$

$$\left.+k_2c\xi_{in}ln\left(\frac{\xi_{in} - c}{\Gamma R_1}\right) + \frac{k_2\xi_{out}^2}{2}ln\left(\frac{\xi_{out} - c}{\Gamma R_1}\right) - \frac{k_2\xi_{in}^2}{2}ln\left(\frac{\xi_{in} - c}{\Gamma R_1}\right)\right]d\theta$$

The following functions of θ appearing in the above relation are expressed in terms of suitable Fourier series in the form

$$\frac{k_2c^2}{2}ln(\xi_{out} - c) = \sum_{n=-N_S}^{N_S} f_{1,out}^{(n)}e^{in\theta}, \frac{k_2c^2}{2}ln(\xi_{in} - c) = \sum_{n=-N_S}^{N_S} f_{1,in}^{(n)}e^{in\theta},$$

$$k_2c\xi_{out}ln\left(\frac{\xi_{out} - c}{\Gamma R_1}\right) = \sum_{n=-N_S}^{N_S} f_{2,out}^{(n)}e^{in\theta}, k_2c\xi_{in}ln\left(\frac{\xi_{in} - c}{\Gamma R_1}\right) = \sum_{n=-N_S}^{N_S} f_{2,in}^{(n)}e^{in\theta}$$

$$\frac{k_2\xi_{out}^2}{2}ln\left(\frac{\xi_{out} - c}{\Gamma R_1}\right) = \sum_{n=-N_S}^{N_S} f_{3,out}^{(n)}e^{in\theta}, \frac{k_2\xi_{in}^2}{2}ln\left(\frac{\xi_{in} - c}{\Gamma R_1}\right) = \sum_{n=-N_S}^{N_S} f_{3,in}^{(n)}e^{in\theta}$$

(2.3.25)

where coefficients $f_{1,out}^{(n)}$, $f_{1,in}^{(n)}$, $f_{2,out}^{(n)}$, $f_{2,in}^{(n)}$, $f_{3,out}^{(n)}$, and $f_{3,in}^{(n)}$ are evaluated numerically using FFT algorithm. Values of Chebyshev polynomials at the inner and outer cylinders

are expressed using Fourier expansions of type (2.3.17). Substitution of the resulting expressions as well as (2.3.25) into Eq. (2.3.24) result in

$$
\begin{aligned}
I_0 = \frac{1}{k_1\Gamma^2} \sum_{n=-N_S}^{N_S} &\left\{ \left(\frac{R_1^2}{4} - \frac{3c^2}{4\Gamma^2} - \frac{k_2}{8} - \frac{3}{32\Gamma^2} \right) \left[w_{out,0}^{(n)} - w_{in,0}^{(n)} \right] \right. \\
&+ \left(\frac{c^3}{\Gamma^2} - cR_1^2 + \frac{k_2 c}{2} + \frac{3c}{4\Gamma^2} \right) \left[w_{out,1}^{(n)} - w_{in,1}^{(n)} \right] + \left(\frac{R_1^2}{4} - \frac{3c^2}{4\Gamma^2} - \frac{k_2}{8} - \frac{1}{8\Gamma^2} \right) \\
&\left[w_{out,2}^{(n)} - w_{in,2}^{(n)} \right] + \frac{c}{4\Gamma^2} \left[w_{out,3}^{(n)} - w_{in,3}^{(n)} \right] - \frac{1}{32\Gamma^2} \left[w_{out,4}^{(n)} - w_{in,4}^{(n)} \right] \\
&\left. + f_{1,out}^{(n)} - f_{1,in}^{(n)} + f_{2,out}^{(n)} - f_{2,in}^{(n)} + f_{3,out}^{(n)} - f_{3,in}^{(n)} \right\} \int_0^{2\pi} e^{in\theta} d\theta.
\end{aligned}
\tag{2.3.26}
$$

Integrals in the above relation are nonzero only for $n = 0$ which reduces (2.3.26) to the final form used in the computations, i.e.,

$$
\begin{aligned}
I_0 = \frac{2\pi}{k_1\Gamma^2} \left[\left(\frac{R_1^2}{4} - \frac{3c^2}{4\Gamma^2} - \frac{k_2}{8} - \frac{3}{32\Gamma^2} \right) \left(w_{out,0}^{(0)} - w_{in,0}^{(0)} \right) + \right. \\
\left(\frac{c^3}{\Gamma^2} - cR_1^2 + \frac{k_2 c}{2} + \frac{3c}{4\Gamma^2} \right) \left(w_{out,1}^{(0)} - w_{in,1}^{(0)} \right) + \left(\frac{R_1^2}{4} - \frac{3c^2}{4\Gamma^2} - \frac{k_2}{8} - \frac{1}{8\Gamma^2} \right) \\
\left(w_{out,2}^{(0)} - w_{in,2}^{(0)} \right) + \frac{c}{4\Gamma^2} \left(w_{out,3}^{(0)} - w_{in,3}^{(0)} \right) - \frac{1}{32\Gamma^2} \left(w_{out,4}^{(0)} - w_{in,4}^{(0)} \right) \\
\left. + f_{1,out}^{(0)} - f_{1,in}^{(0)} + f_{2,out}^{(0)} - f_{2,in}^{(0)} + f_{3,out}^{(0)} - f_{3,in}^{(0)} \right].
\end{aligned}
\tag{2.3.27}
$$

Evaluation of the second integral in (2.3.21) begins with expressing axial velocity using discretized variables, i.e.,

$$
\begin{aligned}
I_1 &= \frac{1}{\Gamma^2} \int_0^{2\pi} \int_{\xi_{in}(\theta)}^{\xi_{out}(\theta)} (\xi - c) \sum_{n=-N_M}^{N_M} \sum_{k=0}^{N_T} G_k^{(n)} T_k(\xi) e^{in\theta} \, d\xi d\theta \\
&= \frac{1}{\Gamma^2} \int_0^{2\pi} \sum_{n=-N_M}^{N_M} \sum_{k=0}^{N_T} G_k^{(n)} \int_{\xi_{in}(\theta)}^{\xi_{out}(\theta)} \xi T_k(\xi) \, e^{in\theta} \, d\xi d\theta \\
&\quad + \frac{1}{\Gamma^2} \int_0^{2\pi} \sum_{n=-N_M}^{N_M} \sum_{k=0}^{N_T} G_k^{(n)} \int_{\xi_{in}(\theta)}^{\xi_{out}(\theta)} T_k(\xi) \, e^{in\theta} \, d\xi d\theta
\end{aligned}
\tag{2.3.28}
$$

All functions of ξ are expressed using Chebyshev expansions and the resulting products of Chebyshev polynomials are expressed using sums of such polynomials (see Appendix A). This process brings expression for I_1 to the form

$$I_1 = \frac{1}{2\Gamma^2} \sum_{n=-N_M}^{N_M} \sum_{k=0}^{N_T} G_k^{(n)} \left[I_{k+1}(\theta) + I_{|k-1|}(\theta) - 2cI_k(\theta) \right] e^{in\theta} \tag{2.3.29}$$

where

$$I_k(\theta) = \int_{\xi_{in}(\theta)}^{\xi_{out}(\theta)} T_k(\xi) d\xi = \frac{1}{2(k+1)} \left[T_{k+1}(\xi_{out}) - T_{k+1}(\xi_{out}) \right] \\ - \frac{(1-\delta_{1k})}{2(k-1)} \left[T_{k-1}(\xi_{out}) - T_{k-1}(\xi_{out}) \right]. \tag{2.3.30}$$

$I_k(\theta)$'s are known periodic functions of θ and can be expressed in terms of Fourier series in the form

$$I_k(\theta) = \sum_{m=-\infty}^{\infty} \hat{I}_k^{(m)} e^{im\theta}. \tag{2.3.31}$$

Evaluations of coefficients $\hat{I}_k^{(m)}$ of these expansions begins with substitution of Eq. (2.3.17) into (2.3.30), i.e.,

$$I_k(\theta) = \frac{1}{2(k+1)} \sum_{n=-N_S}^{N_S} \left(w_{out,k+1}^{(n)} - w_{in,k+1}^{(n)} \right) e^{in\theta} \\ - \frac{(1-\delta_{1k})}{2(k-1)} \sum_{n=-N_S}^{N_S} \left(w_{out,|k-1|}^{(n)} - w_{in,|k-1|}^{(n)} \right) e^{in\theta}. \tag{2.3.32}$$

It is simple to deduce that

$$\hat{I}_k^{(n)} = \frac{w_{out,k+1}^{(n)} - w_{in,k+1}^{(n)}}{2(k+1)} - \frac{(1-\delta_{1k})}{2(k-1)} \left(w_{out,|k-1|}^{(n)} - w_{in,|k-1|}^{(n)} \right). \tag{2.3.33}$$

Substitution of (2.3.33) into (2.3.30) leads to

$$I_1 = \frac{1}{2\Gamma^2} \sum_{n=-\infty}^{\infty} \sum_{m=-N_M}^{N_M} \sum_{k=0}^{N_T} G_k^{(m)} \left[\hat{I}_{k+1}^{(n-m)} + \hat{I}_{|k-1|}^{(n-m)} - 2c\hat{I}_k^{(n-m)} \right] \int_0^{2\pi} e^{in\theta} d\theta. \tag{2.3.34}$$

Integrals in the above relation are nonzero only for $n = 0$ which leads to

$$I_1 = \frac{\pi}{\Gamma^2} \sum_{m=-N_M}^{N_M} \sum_{k=0}^{N_T} G_k^{(m)} \left(\hat{I}_{k+1}^{(-m)} + \hat{I}_{|k-1|}^{(-m)} - 2c\hat{I}_k^{(-m)} \right). \tag{2.3.35}$$

Substitution of (2.3.27) and (2.3.35) into (2.3.21) provides the final form of the discretized fixed flow rate constraint

$$
\sum_{m=-N_M}^{N_M} \sum_{k=0}^{N_T} G_k^{(m)} \left(\hat{I}_{k+1}^{(-m)} + \hat{I}_{|k-1|}^{(-m)} - 2c\hat{I}_k^{(-m)} \right)
$$
$$
= \frac{-2}{k_1} \left[\left(\frac{R_1^2}{4} - \frac{3c^2}{4\Gamma^2} - \frac{k_2}{8} - \frac{3}{32\Gamma^2} \right) \left(w_{out,0}^{(0)} - w_{in,0}^{(0)} \right) + \right.
$$
$$
\left(\frac{c^3}{\Gamma^2} - cR_1^2 + \frac{k_2 c}{2} + \frac{3c}{4\Gamma^2} \right) \left(w_{out,1}^{(0)} - w_{in,1}^{(0)} \right) + \left(\frac{R_1^2}{4} - \frac{3c^2}{4\Gamma^2} - \frac{k_2}{8} - \frac{1}{8\Gamma^2} \right) \tag{2.3.36}
$$
$$
\left(w_{out,2}^{(0)} - w_{in,2}^{(0)} \right) + \frac{c}{4\Gamma^2} \left(w_{out,3}^{(0)} - w_{in,3}^{(0)} \right) - \frac{1}{32\Gamma^2} \left(w_{out,4}^{(0)} - w_{in,4}^{(0)} \right)
$$
$$
\left. + f_{1,out}^{(0)} - f_{1,in}^{(0)} + f_{2,out}^{(0)} - f_{2,in}^{(0)} + f_{3,out}^{(0)} - f_{3,in}^{(0)} \right] + \frac{\Gamma^2}{\pi} \left(Q_{ref} + Q_{mod} \right).
$$

which needs to be enforced numerically.

2.3.3 Testing of the algorithm

This section presents results of various tests carried out in order to demonstrate the spectral accuracy of the algorithm. Model geometry described by one Fourier mode, i.e.,

$$r_{in}(\theta) = R_1 + S_{in}cos\theta, r_{out}(\theta) = 1 + R_1 + S_{out}cos\theta, \tag{2.3.37}$$

has been used in most of the tests. The algorithm incorporates three elements of spectral discretization, i.e., discretizations in the r and θ directions and discretization of the boundary conditions. Since Galerkin procedure guarantees spectral convergence of the Chebyshev expansions (Manson 2003), it is sufficient to test only the absolute accuracy of this part of discretization. It had been found that convergence was very rapid in all cases considered and 60-70 polynomials would provide machines level accuracy. Formation of boundary layers in the distribution of modal functions has been observed when higher Fourier modes have to be included in the solution, similarly as in the case of the algorithm discussed in Section 2.2 (compare Figure **2-3** and Figure **2-17**). The reader

may note formation of more extreme boundary layers at the surface of the inner cylinder (Figure **2-17**A) as compared with the outer cylinder (Figure **2-17**B).
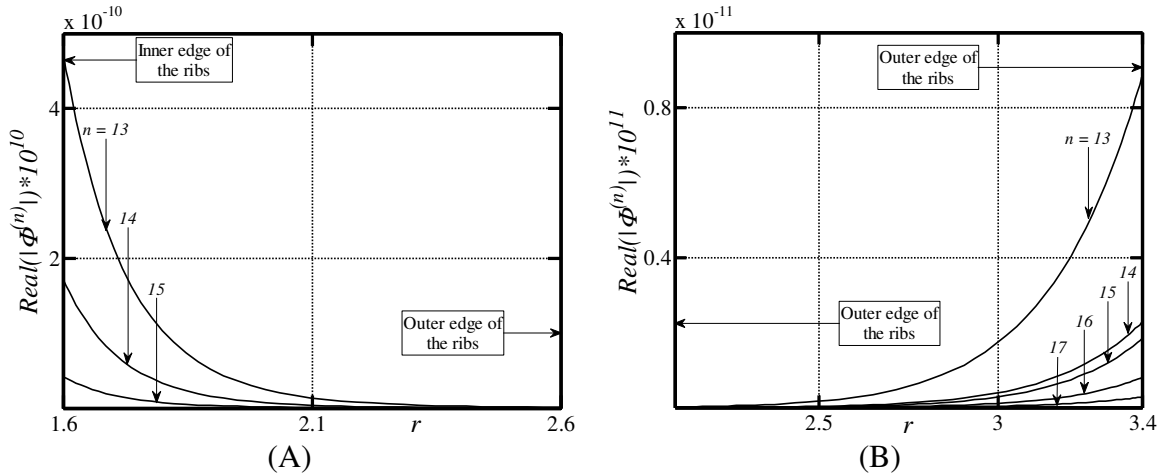
Figure 2-17: *Distribution of the real part of $\phi^{(n)}$ as a function of r for higher Fourier modes $(n > 13)$ in the region close to the surfaces of the inner (Figure **2-17**A) and outer (Figure **2-17**B) cylinders. The ribs' geometry is given by Eq. (2.3.37) with the inner and outer amplitudes $S_{in} = 0.4$ and $S_{out} = 0.4$, respectively, and the average radius on the inner cylinder $R_1 = 2$. Computations have been carried out using $N_M = 20$ Fourier modes and $N_T = 70$ Chebyshev polynomials.*

Figure **2-18** demonstrates spectral convergence of the discretization in the θ-direction. The rate of convergence depends weakly on the amplitude of the ribs; a very good convergence is observed even for ribs with the amplitude as high as $S_{in} = 0.2$.
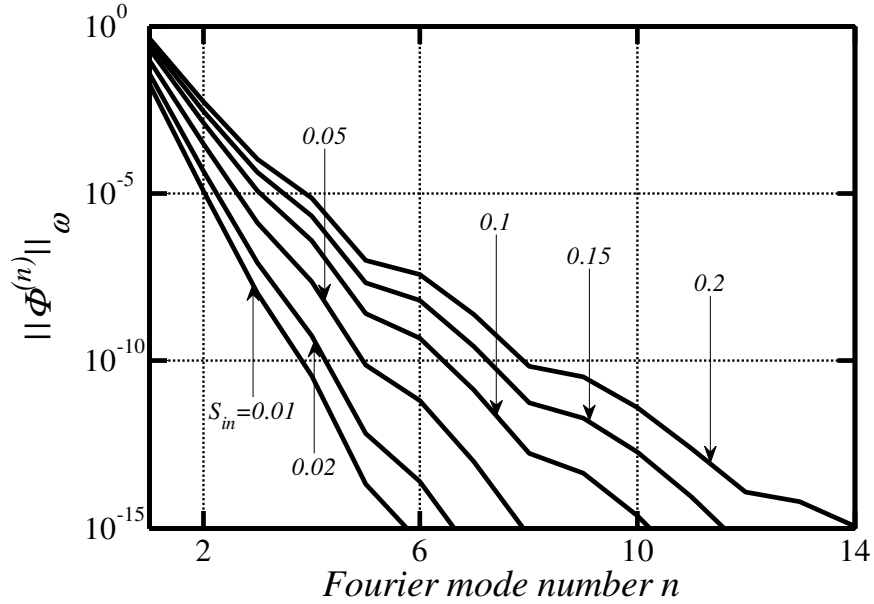
Figure 2-18: *Variations of the Chebyshev norm $\left\|\phi^{(n)}\right\|_\omega$ as a function of the Fourier mode number n for the model geometry described by Eq. (2.3.37) for selected values of the inner ribs' amplitude S_{in}. Calculations have been carried out for the smooth outer cylinder ($S_{out} = 0$) and the average radius of the inner cylinder $R_1 = 2$ using $N_M = 20$ Fourier modes and $N_T = 70$ Chebyshev polynomials.*

A suitable L_∞ norm that measures the accuracy in the enforcement of the flow boundary conditions is defined as

$$\|V_{in}\|_\infty = sup_{0 \le \theta \le 2\pi} |v_z[r_{in}(\theta)], \theta|, \tag{2.3.38}$$

and a similar norm can be defined for the outer cylinder. Figure **2-19** demonstrates spectral convergence of the error in the enforcement of the flow boundary conditions using the IBC method, even for ribs' amplitudes as high as $S_{in} = 0.2$. Results displayed in Figure **2-20** show that this accuracy could be significantly improved by increasing the number of Fourier modes N_M used in the computations.
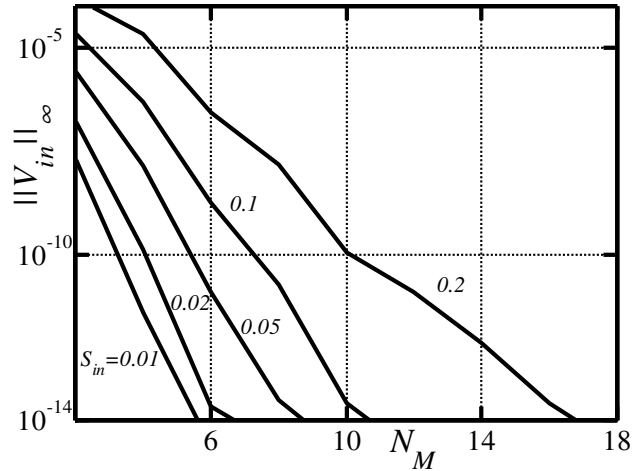
Figure 2-19: *Variations of the norm $\|V_{in}\|_\infty$ defined by Eq. (2.3.38) as a function of the number of Fourier modes N_M used in the computations for the model problem described by Eq. (2.3.37) for selected values of the inner ribs' amplitude S_{in}. Calculations have been carried out for the smooth outer cylinder ($S_{out} = 0$) and the average radius of the inner cylinder $R_1 = 1$ using $N_T = 70$ Chebyshev polynomials.*
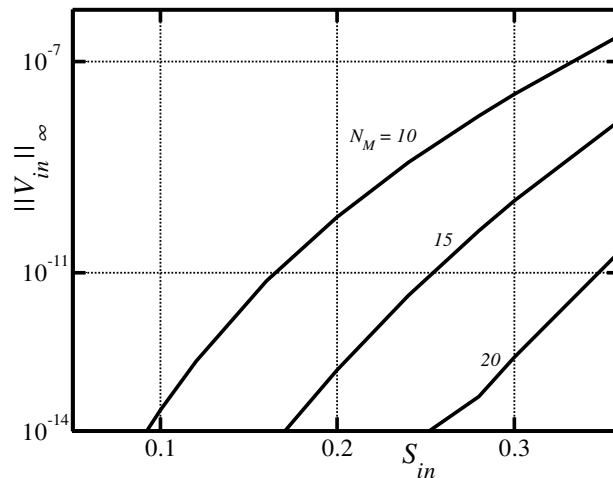
Figure 2-20: *Variations of the norm $\|V_{in}\|_\infty$ defined by Eq. (2.3.38) as a function of the ribs' inner amplitude S_{in} for the model configuration described by Eq. (2.3.37). Calculations have been carried out for the smooth outer cylinder ($S_{out} = 0$) and the average radius of the inner cylinder $R_1 = 1$ using $N_T = 70$ Chebyshev polynomials and selected number of the Fourier modes N_M.*

Figure **2-21** illustrates distribution of the axial velocity component v_z along the surfaces of both cylinders. This quantity represents an error in the enforcement of the flow boundary conditions. The error has an oscillatory distribution and locations of its minima/maxima at the inner cylinder correlate with the maximum/minimum of the diameter of the inner cylinder while an opposite correlation is observed at the outer cylinder.
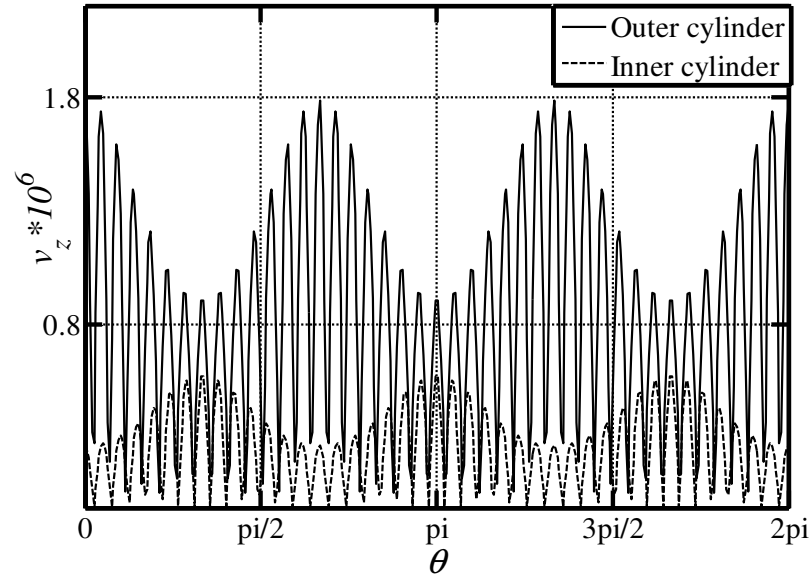
Figure 2-21: *Distributions of the axial velocity component v_z evaluated along the inner and outer cylinders for the model geometry described by Eq. (2.3.37) with the ribs' inner and outer amplitudes $S_{in} = 0.05$ and $S_{out} = 0.1$, respectively, and θ replaced by 3θ. Calculations have been carried out for the average radius of the inner cylinder $R_1 = 1$ using $N_M = 20$ Fourier modes and $N_T = 70$ Chebyshev polynomials.*

Figure **2-22** displays Fourier spectra of the error distribution displayed in Figure **2-21**. It can be seen that the first twenty modes are absent, in agreement with the construction of the boundary relations explained in Section 2.3.2.2.
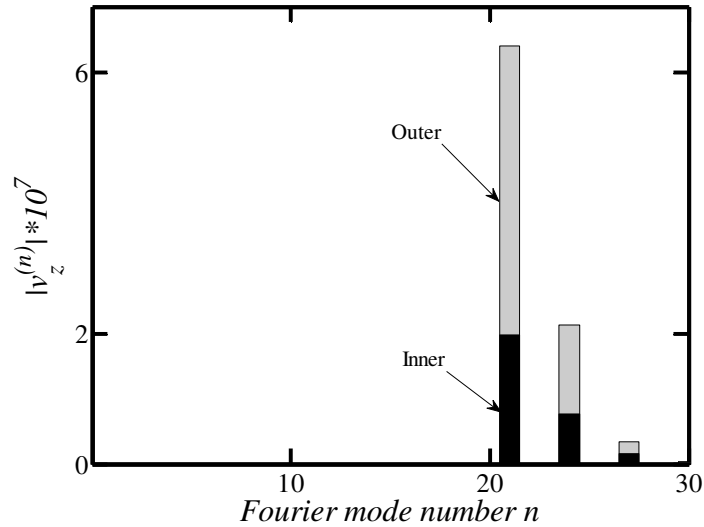
Figure 2-22: *Fourier spectra of the axial velocity component v_z evaluated along the inner and outer cylinders for the model geometry described by Eq. (2.3.37). Other conditions as in Figure* **2-21**.

Figure **2-23** illustrates variations of the boundary error as a function of the average radius of the inner cylinder R_1. It can be seen that the error is larger when the ribs are placed at the inner cylinder. An increase of R_1 causes the error on both cylinders to equilibrate and to approach the error found in the case of a two-dimensional channel.

Figure **2-24** shows variations of the additional pressure drop $Re\, \partial p_1/\partial z$ associated with the presence of the ribs as a function of the ribs' amplitude S_{in} and the average radius of the inner cylinder R_1, i.e., it illustrates potential use of the algorithm. This particular study requires analysis of many geometries but can be done very efficiently using the IBC method. Specification of geometry requires specification of coefficients of Fourier expansions only, the coefficient matrix is the same for each geometry and can be computed once and pre-inverted at the beginning of the analysis, and the boundary relations need to be adjusted for each geometry but the associated computational cost is minimal.
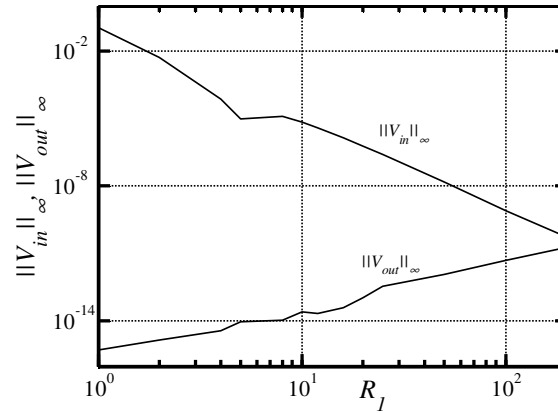
Figure 2-23: *Variations of the norms $\|V_{in}\|_\infty$ and $\|V_{out}\|_\infty$ defined by Eq. (2.3.38) as a function of the radius of the inner cylinder R_1. The former one corresponds to an annulus with geometry described by Eq. (2.3.37) with the inner ribs' amplitude $S_{in} = 0.15$ and smooth outer cylinder $(S_{out} = 0)$, and θ replaced by 5θ The latter one corresponds to the same annulus with the same ribs placed at the outer cylinder. Computations were carried out using $N_M = 20$ Fourier modes and $N_T = 70$ Chebyshev polynomials.*
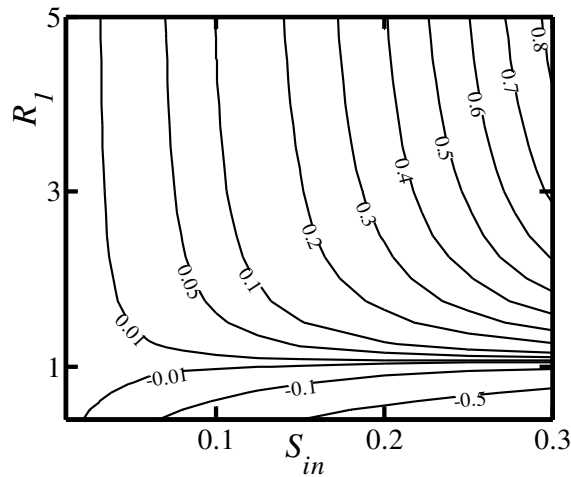
Figure 2-24: *Variations of the additional pressure loss $Re\ \partial p_1/\partial z$ associated with the presence of the ribs at the inner cylinder while the outer cylinder is kept smooth $(S_{out} = 0)$ as a function of the ribs' amplitude S_{in} and the average radius of the inner cylinder R_1. The ribs' geometry is defined by Eq. (2.3.37). Computations were carried out using $N_M = 20$ Fourier modes and $N_T = 70$ Chebyshev polynomials.*

Figure **2-25** illustrates flexibility of the algorithm in dealing with complex ribs' geometries. In this particular case the shape of the annulus is described by the following relations

$$r_{in}(\theta) = 1 + 0.05cos(3\theta), \qquad r_{out}(\theta) = 2 + 0.1cos(4\theta). \qquad (2.3.39)$$
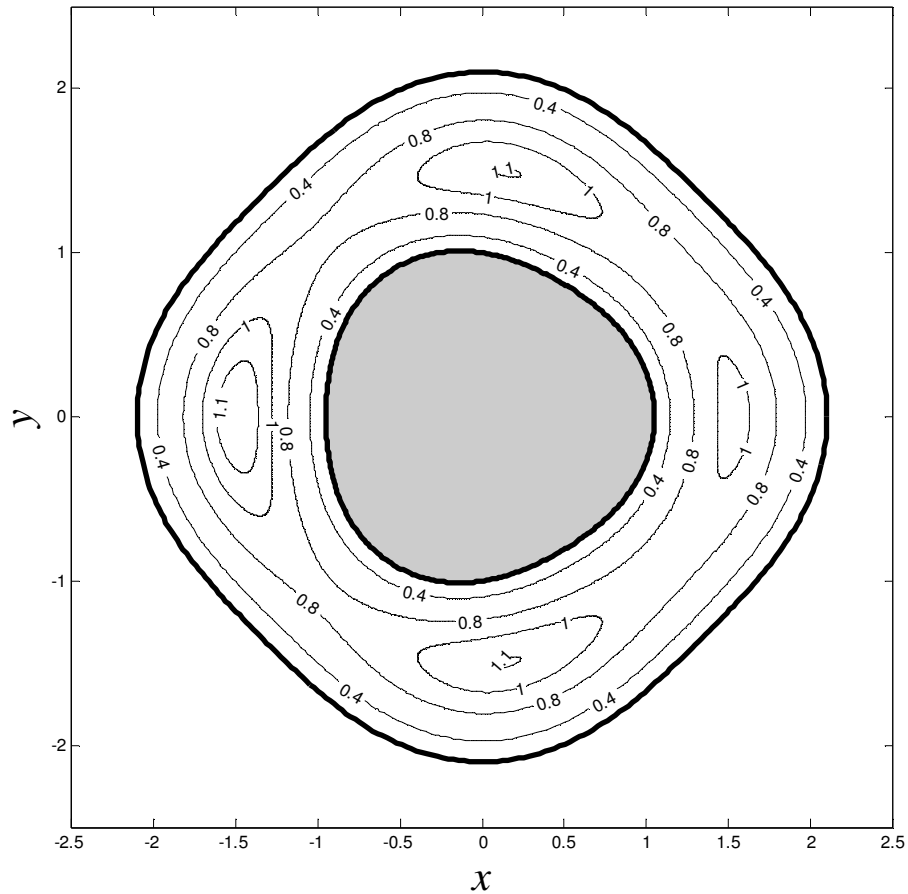
Figure 2-25: *Velocity contours for the model problem defined by Eq. (2.3.39).*

2.4 Summary

Spectral methods for analyses of steady flows in annuli bounded by walls with either axisymmetric or longitudinal ribs are developed. The physical boundary conditions are enforced using the immersed boundary conditions (IBC) concept. In the former case, the Stokes stream function is used to eliminate pressure and to reduce system of field equations to a single forth-order partial differential equation. The ribs are assumed to be

periodic in the axial direction and this permits representation of the solution in terms of Fourier expansion. In the latter case, the problem is reduced to the Laplace equations for the flow modifications which can be expressed in terms of Fourier expansions. The modal functions, which are functions of the radial coordinate, are discretized using Chebyshev polynomials. The problem formulations are closed using either the fixed volume flow rate constraint or the fixed pressure gradient constraint. Various tests have been carried out in order to demonstrate the spectral accuracy of the discretizations, as well as the spectral accuracy of the enforcement of the flow boundary conditions at the ribbed walls using the IBC concept. Special linear solver that takes advantage of the matrix structure has been implemented in order to reduce computational time and memory requirements. It is shown that the algorithm has superior performance when one is interested in the analysis of a large number of geometries, as the part of the coefficient matrix that corresponds to the field equation is always the same and one needs to change only the part of the matrix that corresponds to the boundary relations when changing geometry of the flow domain.

Chapter 3

3 Flows in Annuli with Longitudinal Grooves[1]

3.1 Introduction

It has been shown in Chapter 2 that introduction of surface topography in the form of longitudinal grooves may reduce flow resistance (Figure **2-24**). Thus this chapter is devoted to complete analysis of laminar, pressure driven flows in annuli fitted with longitudinal grooves of arbitrary shape and on the systematic search for the forms of such grooves that are able to reduce drag. The drag-reducing abilities are assessed by determining the additional pressure gradient required to maintain the same mass flow rate through the groove-fitted as well as through the smooth annuli. The problem formulation is given in Section 3.2. Curvature effects are discussed in Section 3.3, together with the form of the flow found in annuli with large radii. A spectrally accurate method of solution of the field equations for arbitrary geometric parameters is discussed in Section 3.4. The groove-induced flow modifications are described in Section 3.5. In particular, Section 3.5.1 discusses the effects of changing the mean position of the cylinders, Section 3.5.2 discusses the shape representation for arbitrary grooves and the reduced geometry models, Section 3.5.3 describes the effects of the dominant parameters and Section 3.5.4 discusses the mechanics of drag formation. Section 3.6 is focused on the identification of the optimal forms of the grooves which produce the maximum possible drag reduction. In particular, Section 3.6.1 discusses the shapes determined with the equal-depth constraint (equal-depth grooves) and Section 3.6.2 presents the shapes determined with the unequal-depth constraint (unequal-depth grooves). Section 3.7 provides a short summary of the main conclusions.

---

[1] A version of this chapter has been published as –

Moradi, H. V. & Floryan, J. M. 2013 Flows in Annuli with Longitudinal Grooves, *Journal of Fluid Mechanics*, **716**, 280-315.

3.2 Problem formulation

Consider steady axial flow in an annulus bounded by two co-axial cylinders fitted with longitudinal grooves (Figure **3-1**). There are *M* identical grooves of an arbitrary shape over the circumference and thus wall geometries can be expressed as

$$r_{in}(\theta) = R_1 + \sum_{n=-N_A}^{N_A} H_{in}^{(n)} e^{inM\theta} , r_{out}(\theta) = 1 + R_1 + \sum_{n=-N_A}^{N_A} H_{out}^{(n)} e^{inM\theta} \qquad (3.2.1a, b)$$

where R_1 and $1 + R_1$ are the radii of the smooth reference inner and outer cylinders, $H_{in}^{(n)} = H_{in}^{(-n)*}$, $H_{out}^{(n)} = H_{out}^{(-n)*}$ are the reality conditions, stars denote the complex conjugates, N_A is the number of Fourier modes required for description of the shape of the grooves, and all quantities have been scaled with the gap *L* between the reference cylinders as the length scale.
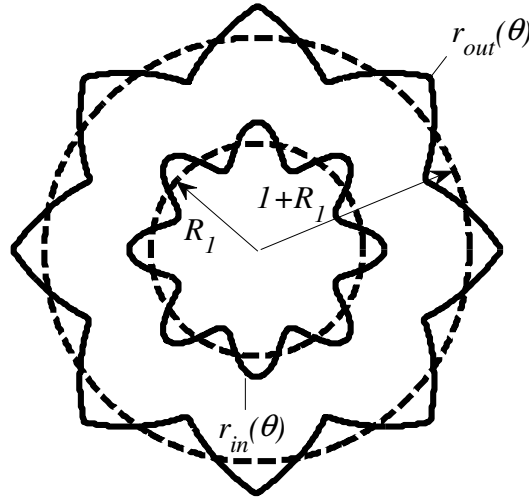
Figure 3-1: *Sketch of the flow geometry - annulus with longitudinal grooves with an arbitrary geometry.*

The flow is driven by a constant axial pressure gradient and this leads to a velocity field with the velocity vector having components $(v, 0, 0)$ in the (z, r, θ) directions. This field is completely described by the axial momentum equation in the form

$$\left(\frac{1}{r}\frac{\partial v}{\partial r} + \frac{\partial^2 v}{\partial r^2} + \frac{1}{r^2}\frac{\partial^2 v}{\partial \theta^2} \right) = Re\frac{\partial p}{\partial z} \qquad (3.2.2)$$

which has been scaled using the maximum of the axial velocity of the reference flow U_{max} as the velocity scale and ρU_{max}^2 as the pressure scale where ρ stands for the density. The Reynolds number is defined as $Re = U_{max}L/\nu$ where ν stands for the kinematic viscosity. The boundary conditions have the form

$$v(r,\theta) = 0 \text{ at } r = r_{in}(\theta) \text{ and } r = r_{out}(\theta). \tag{3.2.3a, b}$$

The problem of determination of the effects of the grooves is posed as the problem of determination of an additional pressure gradient required in order to maintain the same flow rate in the grooved annulus as in the reference smooth annulus. This necessitates introduction of the flow rate constraint in the form

$$Q = M \int_0^{2\pi/M} \int_{r_{in}(\theta)}^{r_{out}(\theta)} rv\,dr\,d\theta \tag{3.2.4}$$

where Q is the known flow rate; this flow rate is equal to the flow rate in the corresponding smooth annulus.

The reference flow, i.e. flow in a smooth annulus, has the velocity distribution, the pressure gradient and the flow rate expressed as (Tasos *et al.* 1999)

$$v_0(r) = R_1^2[1 - (r/R_1)^2]/k_1 + k_2 ln(r/R_1)/k_1, \tag{3.2.5}$$
$$dp_0/dz = -4/k_1 Re \tag{3.2.6}$$
$$Q_0 = 2\pi[(1 + R_1)^2(R_1^2 - 2R_1 - 1 - k_2)/4 +$$
$$k_2(1 + R_1)^2 ln((1 + R_1)/R_1)/2 + R_1^2(k_2 - 1)/4]/k_1 \tag{3.2.7}$$

where $k_1 = R_1^2 - k_2 lnR_1 + k_2/2\,[ln(k_2/2) - 1]$ and $k_2 = (1 + 2R_1)/ln[(1 + R_1)/R_1]$. The maximum of v_0 occurs at $r = \sqrt{k_2/2}$ and this defines the velocity scale U_{max}.

3.3 Curvature effects

The magnitude of the annulus curvature is expressed in terms of its radius R_1. It is more convenient to analyze the relative importance of curvature effects by expressing the

model equations using boundary oriented coordinate system (y, t), where y denotes the distance measured outward from the inner cylinder, i.e. $y = r - R_1$, and t stands for the arc length measured along the inner cylinder, i.e. $\theta = t/R_1$. Problem (3.2.2)-(3.2.4) takes the form

$$\left[\frac{R_1^{-1}}{1 + yR_1^{-1}}\frac{\partial v}{\partial y} + \frac{\partial^2 v}{\partial y^2} + \frac{1}{(1 + yR_1^{-1})^2}\frac{\partial^2 v}{\partial t^2}\right] = Re\frac{\partial p}{\partial z}, \tag{3.3.1}$$

$$v(y, t) = 0 \quad \text{at} \quad y = y_{in}(t) \quad \text{and} \quad y = y_{out}(t), \tag{3.3.2}$$

$$Q = \alpha R_1 \int_0^{2\pi/\alpha} \int_{y_{in}(t)}^{y_{out}(t)} (y/R_1 + 1)v\, dy\, dt, \tag{3.3.3}$$

where

$$y_{in}(t) = \sum_{n=-N_A}^{N_A} H_{in}^{(n)} e^{in\alpha t}, \quad y_{out}(t) = 1 + \sum_{n=-N_A}^{N_A} H_{out}^{(n)} e^{in\alpha t},$$

and $\alpha = M/R_1$ will be referred to as the groove wave number. The problems associated with the treatment of the boundary conditions on grooved surfaces are eliminated by introducing a transformation of the form

$$\xi = \alpha t, \quad \eta = 1 + 2[y - y_{out}(t)][y_{out}(t) - y_{in}(t)]^{-1} \tag{3.3.4}$$

which maps the solution domain into a strip $\eta \in [-1,1]$. The coordinate ξ is defined in such a way that it can play the role of a slow scale when $\alpha \to 0$. The problem expressed in the new coordinates takes the form

$$F_{A,1}\frac{\partial v}{\partial \eta} + F_{A,2}\frac{\partial^2 v}{\partial \eta^2} + F_{A,3}\frac{\partial^2 v}{\partial \eta \partial \xi} + F_{A,4}\frac{\partial^2 v}{\partial \xi^2} = Re\frac{\partial p}{\partial z},$$

$$v(\xi, \eta) = 0 \text{ at } \eta = \mp 1, \tag{3.3.5}$$

$$Q = 0.5R_1 \int_0^{2\pi} \int_{-1}^{1} [1 + R_1^{-1}F(\eta, \xi)]v(\eta, \xi)\, f(\xi)d\eta d\xi$$

where the coefficients are presented in Appendix C. It is convenient to carry out further discussion in the context of sinusoidal grooves placed at the inner cylinder, i.e.

$$y_{in}(t) = 0.5S_{in}cos(Mt/R_1), \quad y_{out}(t) = 1. \tag{3.3.6}$$

In the case of large R_1 it is possible to express the solution as asymptotic expansions of the form

$$v = \hat{v}_0 + R_1^{-1}\hat{v}_1 + O(R_1^{-2}), \qquad p = \hat{p}_0 + R_1^{-1}\hat{p}_1 + O(R_1^{-2}).$$

(3.3.7)

It is further assumed that the number of grooves increases with R_1 so that the wave number M/R_1 remains $O(1)$. This process is not continuous, as only integer numbers of grooves are permitted. However, it is still possible to consider the limit $R_1 \rightarrow \infty$. The flow rate can be expressed as

$$Q/2\pi R_1 = \hat{Q}_0 + R_1^{-1}\hat{Q}_1 + O(R_1^{-2}) = \frac{2}{3} + \frac{1}{3}R_1^{-1} + O(R_1^{-2}).$$

(3.3.8)

Expanding the coefficients, substituting Eq. (3.3.7) into Eq. (3.3.5) and retaining the terms of the two highest orders of magnitude results in the following problems:

$$O(1): \quad H_3(\eta,\xi)\frac{\partial \hat{v}_0}{\partial \eta} + [H_1^2(\eta,\xi) + H_2^2(\eta,\xi)]\frac{\partial^2 \hat{v}_0}{\partial \eta^2} + 2\alpha H_2(\eta,\xi)\frac{\partial^2 \hat{v}_0}{\partial \eta \partial \xi}$$
$$+ \alpha^2 \frac{\partial^2 \hat{v}_0}{\partial \xi^2} = Re\frac{\partial \hat{p}_0}{\partial z}.$$

$$\hat{Q}_0 = \frac{1}{4\pi}\int_0^{2\pi}\int_{-1}^{1}\hat{v}_0(\eta)f(\xi)d\eta d\xi,$$

(3.3.9)

$$\hat{v}_0(\eta) = 0 \text{ at } \eta = \pm 1,$$

$$O(R_1^{-1}): \quad [H_1(\eta,\xi) - 2H_3(\eta,\xi)F(\eta,\xi)]\frac{\partial \hat{v}_0}{\partial \eta} + H_3(\eta,\xi)\frac{\partial \hat{v}_1}{\partial \eta}$$
$$+ [H_1^2(\eta,\xi) + H_2^2(\eta,\xi)]\frac{\partial^2 \hat{v}_1}{\partial \eta^2} - 2H_2^2(\eta,\xi)F(\eta,\xi)\frac{\partial^2 \hat{v}_0}{\partial \eta^2}$$
$$+ 2\alpha H_2(\eta,\xi)\frac{\partial^2 \hat{v}_1}{\partial \eta \partial \xi} - 4\alpha H_2(\eta,\xi)F(\eta,\xi)\frac{\partial^2 \hat{v}_0}{\partial \eta \partial \xi} + \alpha^2 \frac{\partial^2 \hat{v}_1}{\partial \xi^2}$$
$$- 2\alpha^2 F(\eta,\xi)\frac{\partial^2 \hat{v}_0}{\partial \xi^2} = Re\frac{\partial \hat{p}_1}{\partial z}.$$

$$\hat{Q}_1 = \frac{1}{4\pi}\int_0^{2\pi}\int_{-1}^{1}[\hat{v}_0(\eta)F(\eta,\xi) + \hat{v}_1(\eta)]f(\xi)d\eta d\xi,$$

(3.3.10)

$$\hat{v}_1(\eta) = 0 \text{ at } = \pm 1.$$

Problem (3.3.9) describes the flow in a straight grooved channel studied by Mohammadi & Floryan (2013a). Curvature enters solution at $O(R_1^{-1})$. The effects of the grooves disappear in the limit $S_{in} \to 0$ and the above problems yield analytical solution of the form

$$\hat{v}_0(\eta) = 1 - \eta^2, \qquad \frac{\partial \hat{p}_0}{\partial z} = -\frac{8}{Re}, \tag{3.3.11}$$

$$\hat{v}_1(\eta) = -\eta(1 - \eta^2)/6, \qquad \frac{\partial \hat{p}_1}{\partial z} = 0 \tag{3.3.12}$$

where (3.3.11) and (3.3.12) are identical to the two-term expansion of the reference flow (3.2.5)-(3.2.7). Problem (3.3.10)-(3.3.11) can be further simplified by assuming that the number of grooves M remains the same while taking the limit $R_1 \to \infty$. This leads to $\alpha = M/R_1 \to 0$, ξ becomes a slow scale and additional simplifications lead to

$$O(1): \quad H_1^2(\eta, \xi)\frac{\partial^2 \hat{v}_0}{\partial \eta^2} = Re\frac{\partial \hat{p}_0}{\partial z}, \qquad \hat{Q}_0 = \frac{1}{4\pi}\int_0^{2\pi}\int_{-1}^1 \hat{v}_0(\eta)f(\xi)d\eta d\xi, \tag{3.3.13a-c}$$

$$\hat{v}_0(\eta) = 0 \text{ at } \eta = \pm 1$$

$$O(R_1^{-1}): \quad H_1^2(\eta, \xi)\frac{\partial^2 \hat{v}_1}{\partial \eta^2} = Re\frac{\partial \hat{p}_1}{\partial z} - H_1(\eta, \xi)\frac{\partial \hat{v}_0}{\partial \eta}, \hat{Q}_1$$

$$= \frac{1}{4\pi}\int_0^{2\pi}\int_{-1}^1 [\hat{v}_0(\eta)F(\eta, \xi) + \hat{v}_1(\eta)]f(\xi)d\eta d\xi \tag{3.3.14a-c}$$

$$\hat{v}_1(\eta) = 0 \text{ at } \eta = \pm 1$$

Problem $O(1)$ is identical to the small wave number approximation of the flow in a straight grooved channel (Mohammadi & Floryan, 2013a) and problem $O(R_1^{-1})$ combines contributions coming from the curvature (2nd term on the RHS of 3-14a) as well as from the small wave number approximation (LHS of 3-14a). Additional contributions from the curvature can be found in the flow rate constraint; $\hat{Q}_1 = 1/3$ in the case of an annulus but $\hat{Q}_1 = 0$ in the case of a straight channel. Equations (3.3.13a-c) and (3.3.14a-c) yield an analytical solution of the form

$$\hat{v}_0(\eta) = (1 + 3S_{in}^2/8)^{-1}f^2(\xi)(1 - \eta^2), \tag{3.3.15}$$

$$\frac{\partial \hat{p}_0}{\partial z} = -\frac{8}{Re}(1 + 3S_{in}^2/8)^{-1}, \tag{3.3.16}$$

$$\hat{v}_1(\eta) = f^2(\xi)(1 + 3S_{in}^2/8)^{-1}(1 - \eta^2)\, 3S_{in}^2(1 + 3S_{in}^2/8)^{-1}(1 + S_{in}^2/16)/16$$
$$- f^2(\xi)(1 + 3S_{in}^2/8)^{-1}(1 - \eta^2)\, \eta f(\xi)/6. \tag{3.3.17}$$

$$\frac{\partial \hat{p}_1}{\partial z} = \frac{-3S_{in}^2}{2Re}(1 + 3S_{in}^2/8)^{-2}(1 + S_{in}^2/16). \tag{3.3.18}$$

Solution for the same grooves but placed at the outer cylinder is given in Appendix D.

Figure **3-2** illustrates variations of the error *Er* in the evaluation of the pressure gradient using the above approximation. This error is defined as

$$Er = \left| \frac{\partial p}{\partial z} - \frac{\partial \hat{p}_0}{\partial z} - R_1^{-1}\frac{\partial \hat{p}_1}{\partial z} \right| \tag{3.3.19}$$

where the actual $\partial p/\partial z$ has been determined by solving the complete field equations using a spectrally accurate algorithm to be described in Section 3.4.
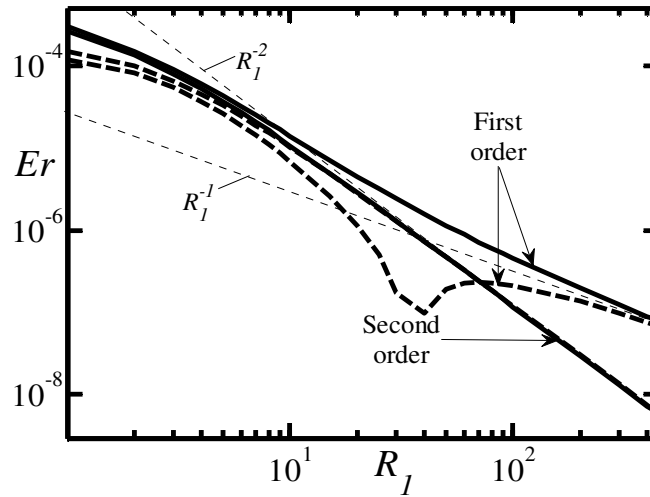
Figure 3-2: *Variations of the error of the asymptotic approximation for $R_1 \to \infty$. Solid lines correspond to grooves placed at the inner cylinder (Eq. 3-6) with M = 8 and $S_{in} = 0.15$ and dashed lines correspond to the same grooves placed at the outer cylinder (see Eq. B-1).*

It can be seen that the two-term approximation provides accuracy $O(10^{-7})$ at $R_1 = 10$. Since the first order approximation is identical to the flow in a straight grooved channel, the difference between this approximation and the full solution provides a means for quantifying the effects of curvature.

3.4 Numerical solution

This section describes a spectral algorithm used to solve the complete problem (3.2.2)-(3.2.4). The algorithm relies on a mapping that transforms the complex geometry into a straight strip suitable for implementation of spectral discretization. An alternative method, i.e. IBC method, proposed in Chapter 2, uses the physical domain and enforces boundary conditions on the corrugated boundaries using the concept of immersed boundary conditions. The former method provides better access to configurations with extreme geometries.

3.4.1 Discretization of the field equation

The corrugated annuli in the physical domain (r, θ) is mapped into a smooth annuli in the computational domain (η, ξ) using mapping of the form

$$\xi = \theta, \eta = 2[r - r_{out}(\theta)][r_{out}(\theta) - r_{in}(\theta)]^{-1} + 1. \tag{3.4.1}$$

The governing equation (3.2.2) is transformed into

$$W_1(\xi, \eta)\frac{\partial v}{\partial \eta} + W_2(\xi, \eta)\frac{\partial^2 v}{\partial \eta^2} + W_3(\xi, \eta)\frac{\partial^2 v}{\partial \eta \partial \xi} + \frac{\partial^2 v}{\partial \xi^2} = W_4(\xi, \eta)Re\frac{\partial p}{\partial z}, \tag{3.4.2}$$

where the coefficients

$$\begin{aligned} W_1(\xi, \eta) &= G_3(\eta, \xi) + [A(\xi) + B(\xi)\eta]/B(\xi), \\ W_2(\xi, \eta) &= G_2^2(\eta, \xi) + G_1^2(\eta, \xi)[A(\xi) + B(\xi)\eta]^2 \\ W_3(\xi, \eta) &= 2G_2(\eta, \xi), \\ W_4(\xi, \eta) &= [A^2(\xi) + 2A(\xi)B(\xi)\eta + B^2(\xi)\eta^2] \end{aligned} \tag{3.4.3}$$

contain information about the groove geometry. In the above

$$A(\xi) = 0.5[r_{out}(\xi) + r_{in}(\xi)], \qquad B(\xi) = 0.5[r_{out}(\xi) - r_{in}(\xi)], \tag{3.4.4}$$

$$G_1(\eta, \xi) = B^{-1}(\xi), \ G_2(\eta, \xi) = -[A_\xi(\xi) + \eta B_\xi(\xi)]B^{-1}(\xi),$$

$$G_3(\eta, \xi) = -[A_{\xi\xi}(\xi) + \eta B_{\xi\xi}(\xi) + 2G_2(\eta, \xi)B_\xi(\xi)]B^{-1}(\xi) \tag{3.4.5}$$

and r_{in} and r_{out} are given by Eq. (3.2.1a, b). The boundary conditions take the form

$$v(\xi, 1) = 0, \qquad v(\xi, -1) = 0 \tag{3.4.6}$$

and the flow constraint will be discussed in Section 3.4.2. Solution of (3.4.2) is periodic in the ξ-direction and thus can be represented in terms of Fourier expansions as

$$v(\xi, \eta) = \sum_{n=-\infty}^{+\infty} \Phi^{(n)}(\eta) e^{inM\xi} \approx \sum_{n=-N_M}^{N_M} \Phi^{(n)}(\eta) e^{inM\xi} \tag{3.4.7}$$

where $\Phi^{(n)} = \Phi^{(-n)*}$. All the known coefficients need to be represented using Fourier expansions, i.e.

$$W_1(\xi, \eta) = \sum_{n=-2N_M}^{2N_M} w_1^{(n)}(\eta) e^{inM\xi}, W_2(\xi, \eta) = \sum_{n=-2N_M}^{2N_M} w_2^{(n)}(\eta) e^{inM\xi},$$

$$W_3(\xi, \eta) = \sum_{n=-2N_M}^{2N_M} w_3^{(n)}(\eta) e^{inM\xi}, \tag{3.4.8}$$

$$W_4(\xi, \eta) = \sum_{n=-2N_M}^{2N_M} \left(A_1^{(n)} + 2\eta A_2^{(n)} + \eta^2 A_3^{(n)} \right) e^{inM\xi},$$

where $A_1^{(n)}$, $A_2^{(n)}$, and $A_3^{(n)}$ have the form

$$A_1^{(n)} = \sum_{m=-N_A}^{N_A} A_+^{(m)} A_+^{(n-m)}, A_+^{(n)} = \begin{cases} \left(1 + 2R_1 + H_{in}^{(0)} + H_{out}^{(0)} \right)/2, n = 0 \\ \left(H_{in}^{(n)} + H_{out}^{(n)} \right)/2, & n \neq 0 \end{cases}$$

$$A_2^{(n)} = \sum_{m=-N_A}^{N_A} A_+^{(m)} A_-^{(n-m)}, A_-^{(n)} = \begin{cases} \left(1 + H_{out}^{(0)} - H_{in}^{(0)} \right)/2, & n = 0 \\ \left(H_{out}^{(n)} - H_{in}^{(n)} \right)/2, & n \neq 0 \end{cases} \tag{3.4.9}$$

$$A_3^{(n)} = \sum_{m=-N_A}^{N_A} A_-^{(m)} A_-^{(n-m)}.$$

Substitution of Eqs. (3.4.7)-(3.4.9) into (3.4.2) and separation of the Fourier modes leads to

$$-(nM)^2\Phi^{(n)}(\eta) + \sum_{m=-N_M}^{N_M} \left\{ \left[w_1^{(n-m)}(\eta) + imM w_3^{(n-m)}(\eta) \right] D\Phi^{(m)}(\eta) \right.$$

$$\left. + w_2^{(n-m)}(\eta) D^2\Phi^{(m)}(\eta) \right\} - \left(A_1^{(n)} + 2\eta A_2^{(n)} + \eta^2 A_3^{(n)} \right) Re\, \partial p/\partial z = 0. \tag{3.4.10}$$

where $D = d/d\eta$, $-N_M < n < N_M$. The ordinary differential equations (3.4.10) form a system coupled through the variable coefficients.

The boundary conditions for the modal functions can be written in the form

$$\Phi^{(n)}(1) = 0, \qquad \Phi^{(n)}(-1) = 0. \tag{3.4.11}$$

Equations (3.4.10) are discretized using Chebyshev expansions. The unknown $\Phi^{(n)}(\eta)$ and known $w_1^{(n)}(\eta)$, $w_2^{(n)}(\eta)$, $w_3^{(n)}(\eta)$ and $w_4^{(n)}(\eta)$ functions are expressed using Chebyshev expansions of the form

$$\Phi^{(n)}(\eta) = \sum_{k=0}^{N_T} G_k^{(n)} T_k(\eta), w_1^{(n)}(\eta) = \sum_{l=0}^{N_T} G_{l,w1}^{(n)} T_l(\eta), w_2^{(n)}(\eta) = \sum_{l=0}^{N_T} G_{l,w2}^{(n)} T_l(\eta)$$

$$w_3^{(n)}(\eta) = \sum_{l=0}^{N_T} G_{l,w3}^{(n)} T_l(\eta), \tag{3.4.12}$$

$$w_4^{(n)}(\eta) = \left(A_1^{(n)} + A_3^{(n)}/2 \right) T_0(\eta) + 2 A_2^{(n)} T_1(\eta) + A_3^{(n)} T_2(\eta)/2$$

Substituting Eq. (3.4.12) into Eq. (3.4.10) leads to

$$\sum_{k=0}^{N_T} \left\{ -(nM)^2 G_k^{(n)} T_k(\eta) + \sum_{m=-N_M}^{N_M} \sum_{l=0}^{N_T} \left[\left(G_{l,w1}^{(n-m)} + imM G_{l.w3}^{(n-m)} \right) T_l(\eta) DT_k(\eta) \right. \right.$$

$$\left. + G_{l,w2}^{(n-m)} T_l(\eta) D^2 T_k(\eta) \right] G_k^{(m)} \right\}$$

$$- Re\, \partial p/\partial z \left[\left(A_1^{(n)} + A_3^{(n)}/2 \right) T_0(\eta) + 2 A_2^{(n)} T_1(\eta) + A_3^{(n)} T_2(\eta)/2 \right] = 0 \tag{3.4.13}$$

Application of the Galerkin procedure to (3.4.13) leads to $N_T - 1$ algebraic equations for the unknown coefficients $G_k^{(n)}$ for each Fourier mode of the form

$$\sum_{k=0}^{N_T} \left\{ -(nM)^2 \langle T_j, T_k \rangle G_k^{(n)} + \sum_{m=-N_M}^{N_M} \sum_{l=0}^{N_T} \left[\left(G_{l,w1}^{(n-m)} + imM G_{l,w3}^{(n-m)} \right) \langle T_j, T_l DT_k \rangle \right. \right.$$
$$\left. \left. + G_{l,w2}^{(n-m)} \langle T_j, T_l D^2 T_k \rangle \right] G_k^{(m)} \right\}$$
$$- Re\, \partial p / \partial z \left[\left(A_1^{(n)} + A_3^{(n)}/2 \right) \langle T_j, T_0 \rangle + 2A_2^{(n)} \langle T_j, T_1 \rangle + A_3^{(n)} \langle T_j, T_2 \rangle / 2 \right] = 0$$

(3.4.14)

Substitution of (3.4.12) into (3.4.11) leads to boundary conditions expressed in terms of coefficients of Chebyshev expansions of the form

$$\sum_{k=0}^{N_T} G_k^{(n)} = 0, \qquad \sum_{k=0}^{N_T} (-1)^k G_k^{(n)} = 0.$$

(3.4.15)

These conditions are enforced by replacing equations of type (3.4.14) for the two largest coefficients of Chebyshev expansions with (3.4.15), i.e. the tau method.

3.4.2 Flow constraint

The pressure gradient $\partial p / \partial z$ needs to be determined as a part of the solution process and the fixed flow rate constraint provides the required closing condition. Evaluation of the fixed flow rate constraint begins with expressing the axial velocity in terms of the discretized variables, i.e.

$$\frac{Q_{ref}}{M} = \int_0^{2\pi/M} \int_{\eta=-1}^{\eta=1} \left\{ [A(\xi)B(\xi) + B^2(\xi)\eta] \sum_{n=-N_M}^{N_M} \sum_{k=0}^{N_T} G_k^{(n)} T_k(\eta) e^{inM\xi} \right\} d\eta d\xi. \quad (3.4.16)$$

Substituting (3.4.9) into (3.4.16), expressing η in terms of Chebyshev expansion and evaluating the inner integral leads to

$$\frac{Q_{ref}}{M} = 0.5 \sum_{n=-2N_M}^{2N_M} \sum_{m=-N_M}^{N_M} \sum_{k=0}^{N_T} G_k^{(m)} \left[2\hat{I}_k A_2^{(n-m)} + \left(\hat{I}_{k+1} + \hat{I}_{|k-1|} \right) A_3^{(n-m)} \right] \times$$
$$\int_0^{2\pi/M} e^{inM\xi} d\xi.$$

(3.4.17)

where

$$\hat{I}_0 = 2, \hat{I}_1 = 0, \hat{I}_k = \int_{\eta=-1}^{\eta=1} T_k(\eta) d\eta = \frac{1}{2}\left[\frac{1-(-1)^{k+1}}{k+1} - \frac{1-(-1)^{k-1}}{k-1}\right], k \geq 2, \quad (3.4.18)$$

The integrals in Eq. (3.4.17) have the property

$$\int_0^{2\pi/M} e^{inM\xi} d\xi = \begin{cases} 2\pi/M, & n = 0 \\ 0, & n \neq 0 \end{cases}. \quad (3.4.19)$$

which leads to the form of the constant volume flow rate constraint suitable for computations, i.e.

$$\sum_{m=-N_M}^{N_M} \sum_{k=0}^{N_T} G_k^{(m)} \left[2\hat{I}_k A_2^{(-m)} + \left(\hat{I}_{k+1} + \hat{I}_{|k-1|}\right)A_3^{(-m)}\right] = Q_{ref}/\pi. \quad (3.4.20)$$

3.4.3 Evaluation of surface stress

This section describes the procedure used for the evaluation of the shear stresses acting on the inner cylinder. A similar procedure can be easily developed for the outer cylinder. The nonzero elements of the stress tensor are

$$\tau_{rz} = \frac{-1}{Re}\frac{\partial v}{\partial r}, \quad \tau_{\theta z} = \frac{-1}{rRe}\frac{\partial v}{\partial \theta}. \quad (3.4.21)$$

The component of the shear stress acting on the wall in the z-direction has the form

$$dF_{total,z} = n_\theta \tau_{\theta z} + n_r \tau_{rz} \quad (3.4.22)$$

where $\mathbf{n} = (n_\theta, n_r, n_z)$ is the normal unit vector pointing outward, $n_r = -N^{-1}$, $n_\theta = (r_{in}N)^{-1} dr_{in}/d\theta$, $n_z = 0$, $N = [1 + r_{in}^{-2}(dr_{in}/d\theta)^2]^{1/2}$. The total force acting on the wall can be computed as

$$F_{total,z} = \int_{S_{in}} dF_{total,z} dS_{in} \quad (3.4.23)$$

where $dS_{in} = r_{in}Nd\theta$. The components of the stress tensor expressed in terms of the discretized variables are given in Appendix E.

3.5 Groove-induced flow modifications

A constant pressure gradient needs to be applied along the annulus in order to produce a desired flow rate. We shall refer to this pressure gradient as a pressure loss. The introduction of grooves may increase/decrease this pressure loss depending on the groove geometry and the flow conditions. The main objective of this analysis is the determination of the role played by all these factors in the creation of the pressure loss and identification of the forms of the grooves that may reduce drag. The additional pressure gradient required to maintain the same flow rate in the grooved annulus as in the smooth reference (i.e. with the same flow cross-sectional area) annulus is adopted as the principal measure of the groove effects.

The pressure gradient is expressed, for convenience, in terms of a friction factor

$$f = -2\frac{\partial p}{\partial z} = -2\frac{\partial p_0}{\partial z} - 2\frac{\partial p_1}{\partial z} = f_0 + f_1 \tag{3.5.1}$$

where f denotes the total friction factor, $f_0 = 8/(k_1 Re)$ denotes the friction factor for the smooth annulus (we shall refer to it as the reference friction factor), f_1 stands for the modification friction factor associated with the presence of the grooves and f_1/f_0 will be referred to as the normalized modification friction factor.

There is an uncountable number of possible groove shapes and positions. In order to provide a systematic presentation, this discussion begins with the demonstration that the complete effect can be decomposed into (i) the effect due to a change in the average position of each cylinder (i.e. change of the flow cross-sectional area) and (ii) the effect due to spatial flow modulations created by the grooves.

3.5.1 Effect of the average position of the bounding cylinders

Changing the cross-sectional flow area has a very strong effect on the pressure losses and is unrelated to any flow modulations created by the grooves. This change can be

introduced intentionally through the direct specification of the coefficients of the 0th modes in Eq. (3.2.1a, b), i.e. $H_{in}^{(0)}$ and $H_{out}^{(0)}$. Specification of the remaining coefficients in Eq. (3.2.1a, b) produces inadvertent change in the cross-sectional area due to the radial effects. In order to provide a correct physical interpretation of the results, this change needs to be properly compensated for so that one can separate the pressure losses associated with the flow modulations from those associated with the change in the flow cross-sectional area. Evaluation of the required correction factor $R_{in,c}$ for the inner cylinder is explained below.

The cross-sectional area of the reference (smooth) cylinder is $A_{smooth} = \pi R_1^2$. The cross-sectional area of the grooved cylinder is expressed as

$$A_{grooved} = \pi\left(R_1 + R_{in,c}\right)^2 + 2\pi\left(R_1 + R_{in,c}\right)H_{in}^{(0)} + \pi\sum_{m=0}^{N_A}\left|H_{in}^{(m)}\right|^2$$

where $R_{in,c}$ denotes the correction that must be applied in order to have the same cross-sectional areas for the smooth and the grooved cylinders. Since $A_{smooth} = A_{grooved}$, the correction factor becomes

$$R_{in,c} = \sqrt{(R_1 + H_{in}^{(0)})^2 - \left(2R_1 H_{in}^{(0)} + \sum_{m=1}^{N_A}\left|H_{in}^{(m)}\right|^2\right)} - (R_1 + H_{in}^{(0)}). \qquad (3.5.2)$$

A similar procedure can be used to evaluate the correction factor $R_{out,c}$ for the outer cylinder. Variations of $R_{in,c}$ and $R_{out,c}$ as functions of R_1 are illustrated in Figure **3-3** for the groove geometry specified as

$$\begin{aligned} r_{in}(\theta) &= R_1 + S_{ave,in} + 0.5 S_{in}\cos(M\theta), \\ r_{out}(\theta) &= 1 + R_1 + S_{ave,out} + 0.5 S_{out}\cos\left[M(\theta + \varphi)\right] \end{aligned} \qquad (3.5.3)$$

with $S_{ave,in} = S_{ave,out} = \varphi = 0$. It can be observed that both $R_{in,c}$ and $R_{out,c}$ become negligible when $R_1 > 10$. The same grooves produce a larger correction when placed on the inner rather than on the outer cylinder.
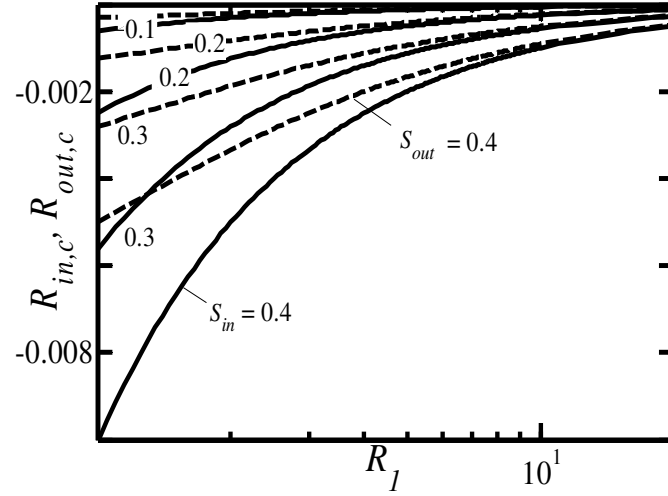
Figure 3-3: *Variations of the geometric correction factors $R_{in,c}$ and $R_{out,c}$ as functions of R_1 for the groove geometry described by Eq. (3.5.3) with $S_{ave,in} = S_{ave,out} = \varphi = 0$ with the same grooves placed either at the inner cylinder (solid lines, $S_{in} = 0.1$, $S_{out} = 0$) or at the outer cylinder (dashed lines, $S_{in} = 0$, $S_{out} = 0.1$).*

Flow modulation effects can be separated from the effects associated with the change of the average position of the wall by writing (3.2.1a, b) as

$$r_{in}(\theta) = \left\{ R_1 + R_{in,c} + \sum_{n=-N_A, n\neq 0}^{N_A} H_{in}^{(n)} e^{inM\theta} \right\} - R_{in,c} + H_{in}^{(0)},$$

$$r_{out}(\theta) = \left\{ R_1 + R_{out,c} + \sum_{n=-N_A, n\neq 0}^{N_A} H_{out}^{(n)} e^{inM\theta} \right\} - R_{out,c} + H_{out}^{(0)}$$

where the curly brackets capture the effects of spatial modulations and the remaining terms account for the change in the flow cross-sectional area.

In order to assess the effects of changes in the average position of the cylinders, consider an annulus with geometry given by Eq. (3.5.3) with $S_{in} = S_{out} = \varphi = 0$. To maintain the same flow rate as in the reference annulus, the following pressure gradient has to be imposed

$$\frac{dp}{dz} = -4(Rek_1)^{-1}\big[(R_1^2 - k_2/2)(1 + 2R_1) + k_2(1 + R_1)^2 ln\big((1 + R_1)R_1^{-1}\big)$$
$$- (1 + R_1)^4/2 + R_1^4/2\big]$$
$$\{-(e_1^4 - e_2^4)/2 + d_1 e_1^2 lne_1 - d_1 e_2^2 lne_2 + (d_2 - d_1/2)(e_1^2 - e_2^2)\}^{-1} \qquad (3.5.4)$$

where

$$d_1 = \frac{e_1^2 - e_2^2}{ln(e_1/e_2)} \qquad (3.5.5)$$

$$d_2 = \frac{e_2^2 lne_1 - e_1^2 lne_2}{ln(e_1/e_2)} \qquad (3.5.6)$$

and $e_1 = 1 + R_1 + S_{out,ave}$, $e_2 = R_1 + S_{in,ave}$. The change in the pressure gradient due the change in the average wall position can be easily determined by comparing (3.5.4) and (3.2.6).

Now consider the annulus sketched in Figure **3-4** with the geometry described by Eq. (3.5.3) with $S_{out} = 0$, $S_{ave,out} = 0$. Variations of the additional pressure loss as a function of the amplitude S_{in} are depicted in Figure **3-5** for three different average positions $S_{ave,in}$. Cases A, B, C correspond to $S_{ave,in} = 0.05$, 0, -0.05, respectively. Equation (3.5.4) gives the additional friction factors for the limit $S_{in} = 0$ (smooth annulus) as $f_1 Re = 2.3442, 0, -1.9355$ for cases A, B, and C, respectively.

Friction factors for the corrugated annuli have been determined numerically using the methodology described in Section 3.4. The results displayed in Figure **3-5** show that changes of the friction factor as a function of the grooves' amplitude are identical in all cases when the shift defined by Eq. (3.5.4) is accounted for. This demonstrates that the total modification friction factors can be represented as a superposition of the effects associated with the change in the mean position of the cylinders and the effects of the shape-induced spatial flow modulation. The former effects can be determined analytically, e.g., Eq. (3.5.4).
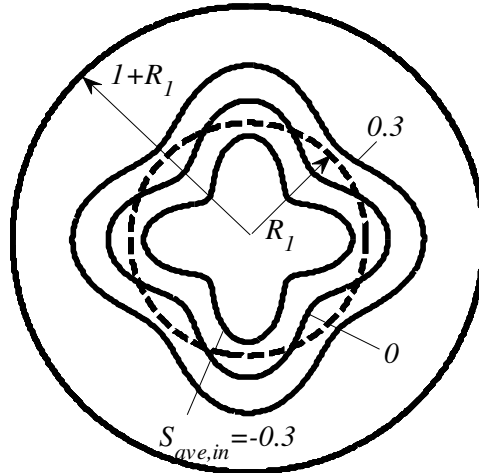
Figure 3-4: *Sketch of the test configuration used to demonstrate the effect of the average position $S_{ave,in}$ of the grooves. Four grooves (M = 4) with the shape defined by Eq. (3.5.3) with $S_{in} = 0.3, S_{out} = 0, S_{ave,out} = 0$ are placed at three different average locations: Case A – $S_{ave,in}$ = 0.3; Case B – $S_{ave,in}$ = 0; Case C – $S_{ave,in}$= −0.3. See text for details.*
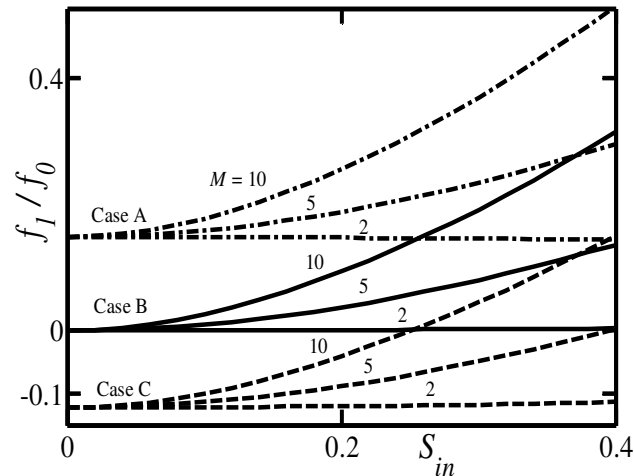
Figure 3-5: *Variations of the normalized modification friction factor f_1/f_0 as a function of the groove amplitude S_{in} for $R_1 = 1$. Four grooves (M = 4) are placed at the inner cylinder with their geometry described by Eq. (3.5.3) with $S_{ave,out} = S_{out} = 0$ and $S_{ave,in}$ = 0.05, 0, −0.05 in Cases A, B, C, respectively.*

3.5.2 Reduced order representation of groove shape

We shall now focus attention on the assessment of flow modulations created by the grooves. There is an uncountable number of possible shapes and general conclusions may not be possible as it is not possible to check all possible shapes. In order to overcome this difficulty, the "primitive" form of the specification of groove shape, e.g., the left side of Eqs (3.2.1a, b), is replaced with its projection onto a Fourier space, e.g., the right hand side of Eqs (3.2.1a, b), producing a reduced order geometry model. It has been shown by Floryan (2007) that use of the leading Fourier mode in the shape specification is sufficient for prediction of the critical stability conditions with an accuracy acceptable for most applications. The same conclusion has been reached by Mohammadi & Floryan (2013a) who studied pressure losses in grooved channels. We shall now determine if the same procedure provides acceptable accuracy for prediction of pressure losses in grooved annuli and determine the level of accuracy obtained by replacing the actual groove with the first term of its representation in the Fourier space.

Figure **3-6** depicts four shapes selected for this study, i.e. rectangular, trapezoidal, triangular and rectified. Tests have been carried out for cylinders with the same radius R_1 equipped with M identical grooves. The results displayed in Figure **3-7** demonstrate that the modification friction factor converges very rapidly to the actual value as the number of Fourier modes N_A used for representation of groove geometry increases (values computed with $N_A = 100$ were taken as representing the actual values). The use of just one Fourier mode for the geometry representation leads to an under prediction of losses by about 10%, which is most likely acceptable in the majority of applications. The convergence is noticeably slower in the case of the rectangular groove where the Gibb's phenomenon affects the convergence of the Fourier series for the shape representation. The reader should note that the one-Fourier-mode model is able to capture the properties of grooves that have the same maximum depth and height, but has to be supplemented by additional Fourier modes when depth and height are not the same. This issue will be discussed in Section 3.6.
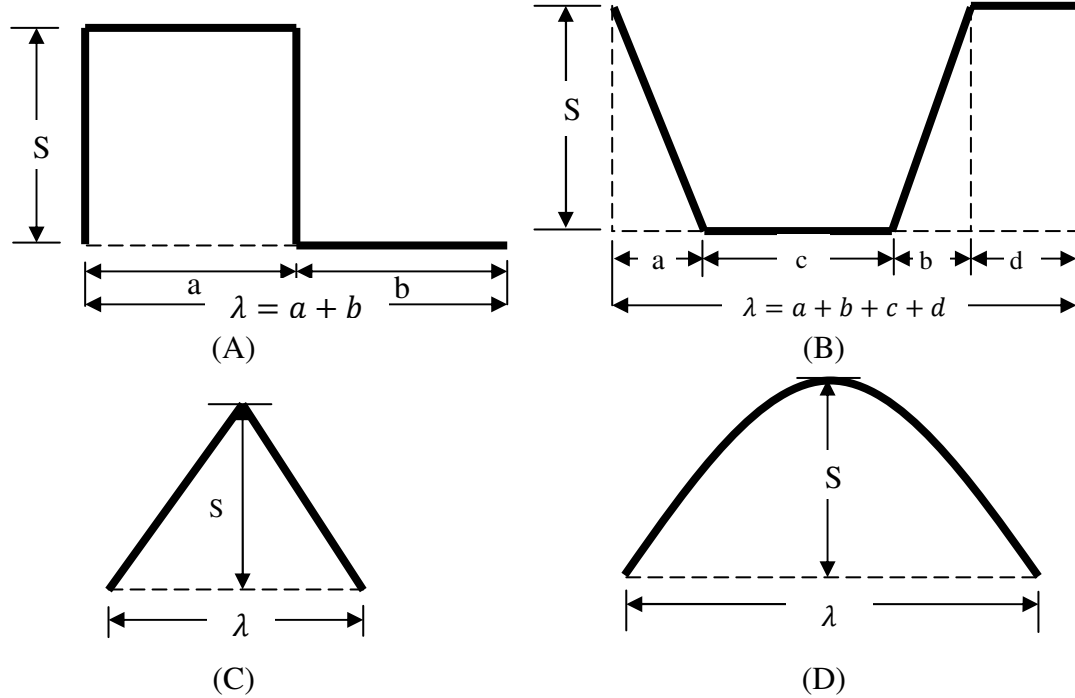
Figure 3-6: *Shapes of the grooves used in this study: A- rectangular groove, B- trapezoidal groove, C- triangular groove, D- rectified groove ($|sinM\theta|$). λ denotes the length of one groove segment.*

3.5.3 Effect of the dominant geometric parameters

The dominant effects created by flow modulations can be captured by replacing the actual groove geometry with the leading Fourier mode from its Fourier representation, as shown in Section 3.5.2. The reference geometry is therefore given by Eq. (3.5.3) with $S_{ave,in} = S_{ave,out} = 0$, with S_{in}, S_{out}, φ, M and R_1 being the main parameters. Evaluation of the friction factor for any geometry can be reduced to the determination of its leading Fourier mode and use of data to be presented later in this Section. More complete reference tables can be easily created. The accuracy of this procedure can be improved by taking advantage of the fact that the use of the leading Fourier mode always under predicts pressure losses (as discussed in Section 3.4.2). The reader should note that the number of Fourier modes required for an accurate description of the flow field is

larger than the number of Fourier modes required for description of the geometry; this number needs to be established through numerical experiments.
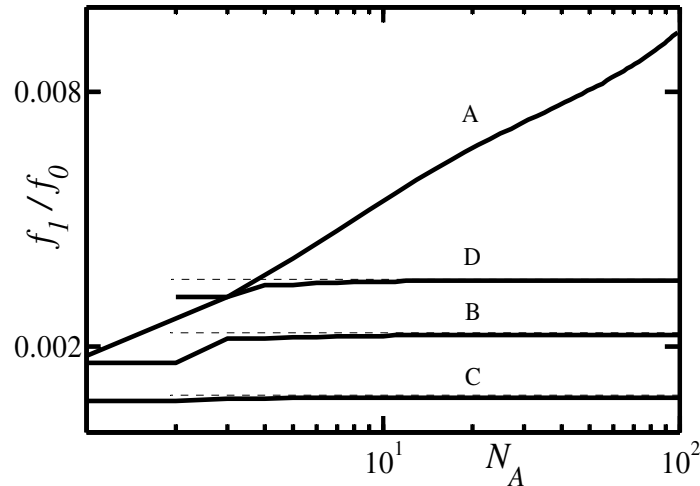
Figure 3-7: *Variations of the normalized modification friction factor f_1/f_0 as a function of the number of Fourier modes N_A used to describe the groove geometry. Four grooves (M = 4) with shapes described in Figure **3-6** and the same amplitude $S_{in} = 0.1$ are placed at the inner cylinder with the average radius $R_1 = 1$ in such a way that mode zero of their Fourier expansion is zero. For grooves A: $a = b = \pi/M$; for grooves B: $a = b = \pi/3M$, $c = 2\pi/3M$. Dotted lines show the normalized modification friction factor asymptote for $N_A = 100$.*

We shall begin discussion with an annulus fitted with grooves placed on only one of the cylinders. Figure **3-8** demonstrates that the most rapid changes of pressure gradient due to increase of R_1 occur for small values of R_1; the rate of change rapidly decreases and the pressure gradient approaches the asymptotic limit corresponding to a two-dimensional grooved channel. An increase in the number of grooves along the circumference increases losses. Grooves placed at the inner cylinder produce a greater change in the pressure gradient than the same grooves placed at the outer cylinder.
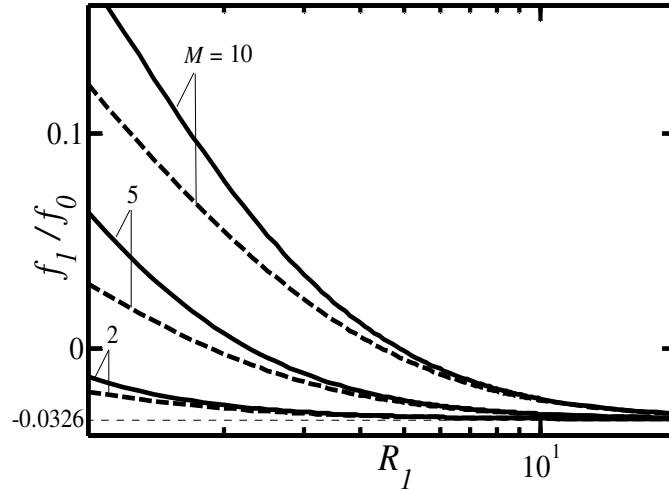
Figure 3-8: *Variation of the normalized modification friction factor f_1/f_0 as a function of R_1 for the geometry described by (3.5.3) with $S_{ave,out} = S_{out} = 0$ and $M = 2$, 5 and 10. Solid (dashed) lines correspond to the same grooves placed only on the inner (outer) cylinder with $S_{in} = 0.3$, $S_{out} = 0$ ($S_{out} = 0.3$, $S_{in} = 0$). Dotted line shows the normalized modification friction factor asymptote for $R_1 \rightarrow \infty$.*

It is remarkable that the presence of grooves leads to the reduction of the pressure loss (negative f_1) for large enough R_1. Since increase in the number of grooves (larger M) increases the pressure loss, larger R_1 is required to effect drag reduction under such conditions. Figure **3-9** illustrates variations of the modification friction factor as a function of the amplitudes S_{in}, S_{out} and the radius R_1 for annuli equipped with different numbers of grooves placed either at the inner or at the outer cylinder. Increase of both S_{in} and S_{out} increases losses for small R_1 but decreases losses for larger R_1; the border between the drag reduction and the drag increase marginally depends on the magnitudes of S_{in} and S_{out} and shifts towards larger values of R_1 when M increases. There is only drag reduction when the annulus is equipped with a small number of grooves, e.g., Figure **3-9**A for $M = 2$. An increase of M always increases drag. This can be counteracted by an increase of R_1 which eventually changes this trend and leads to drag reduction regardless of the value of M.

(A) (B) (C) (D)
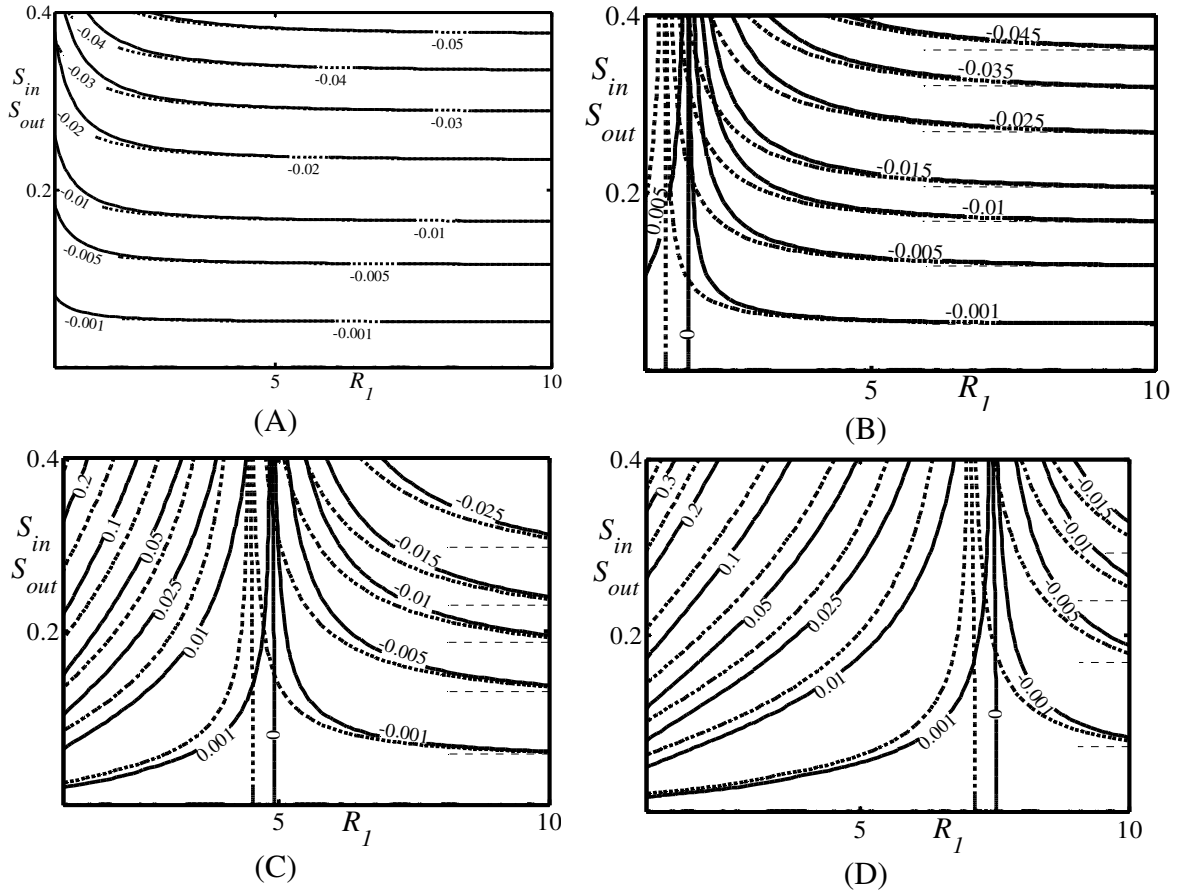
Figure 3-9: *Variations of the normalized modification friction factor f_1/f_0 as a function of the groove amplitudes S_{in} and S_{out} and the radius of the inner cylinder R_1 for the geometry described by Eq. (3.5.3) with $S_{ave,out} = S_{ave,in} = 0$. Results for M = 2, 4, 10, 15 grooves are displayed in Figure **3-9**A, B, C, D, respectively. Solid (dashed) lines correspond to grooves placed only at the inner (outer) cylinder. Dotted lines show the normalized modification friction factor asymptote for $R_1 \rightarrow \infty$.*

The results displayed in Figure **3-10** demonstrate that the conditions leading to the drag reduction correlate well with the groove wave number $\alpha = M/R_1$. Drag reduction is observed for M/R_1 smaller than the critical value α_c, where α_c does not depend on *Re* as change of *Re* cannot affect sign of the pressure loss (see Eq. (3.3.2)). The magnitude of the drag reduction increases proportionally to S^2 with S denoting the amplitude of the corrugation; $S = S_{in}$ when the corrugation is placed at the inner cylinder and $S = S_{out}$ when the roughness is placed at the outer cylinder.
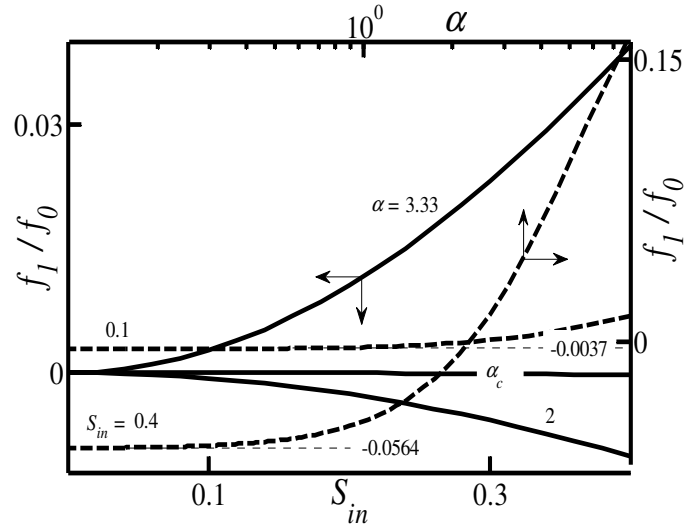
Figure 3-10: *Variations of the normalized modification friction factor f_1/f_0 induced by the grooves placed at the inner cylinder with the shape defined by Eq. (3.5.3) with $S_{ave,out} = S_{ave,in} = S_{out} = 0$ and M = 4, as a function of the amplitude S_{in} (solid lines) and as a function of the wave number $\alpha = M/R_1$ (dashed lines).*

The opposite occurs when M/R_1 is larger than α_c. The value of α_c depends on the number of grooves and approaches $\alpha_c \approx 1.92$ when M increases, as documented in Figure **3-11**. The friction factor does not depend on R_1 when the radius becomes large enough (see Figure **3-9**) as the effects of curvature become negligible and the flow behavior is very similar to flow in a two-dimensional grooved channel (see Section 3.3). The friction factor also loses its dependence on the groove wave number when M/R_1 becomes small enough (see Figure **3-10**) and rapidly approaches the limiting value given by the small wave number approximation of flow in a two-dimensional grooved channel (see Section 3.2).
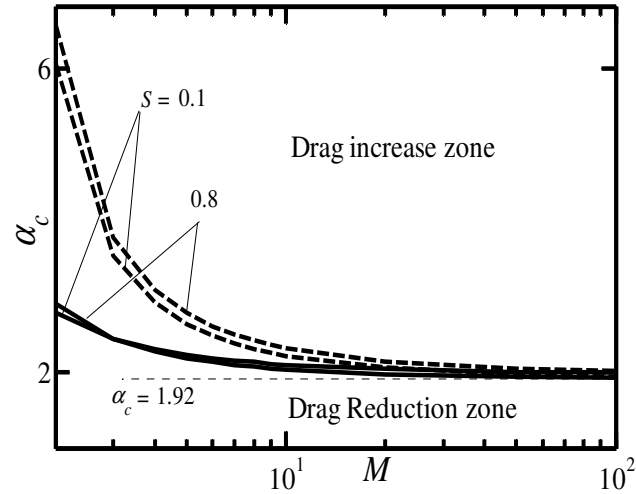
Figure 3-11: *Variations of the critical groove wave number α_c as a function of the number of grooves M for an annulus with geometry described by Eq. (3.5.3) with $S_{ave,out} = S_{ave,in} = 0$. Solid (dashed) line corresponds to the grooves placed only at the inner (outer) cylinder with $S_{in} = 0.1$ and 0.8, $S_{out} = 0$ ($S_{in} = 0, S_{out} = 0.1$ and 0.8).*
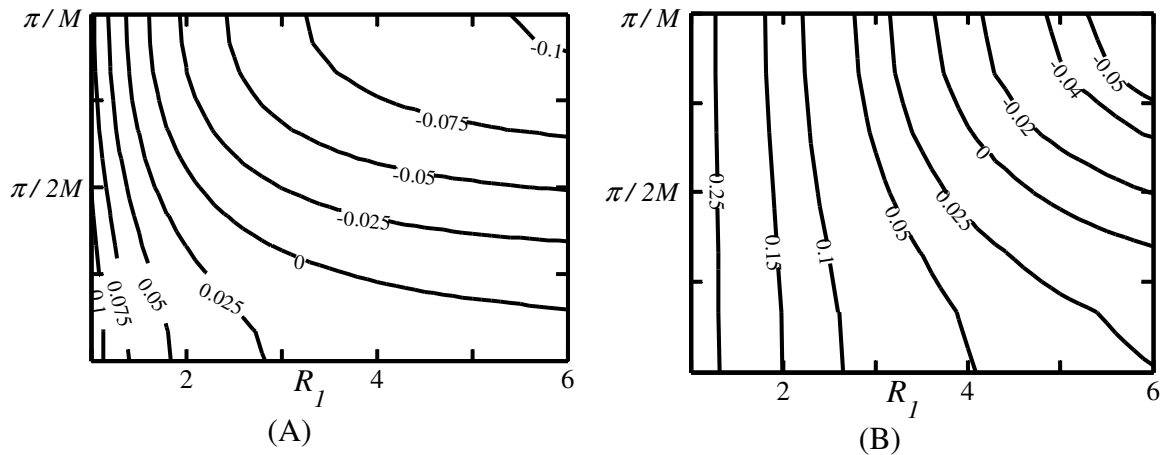
Figure 3-12: *Variations of the normalized modification friction factor f_1/f_0 as a function of the groove phase difference φ and the radius of the inner cylinder R_1 for the grooves described by Eq. (3.5.3) with $S_{in} = S_{out} = 0.3$ and $S_{ave,out} = S_{ave,in} = 0$. Results for M = 5, 10 grooves are displayed in Figure 3-12A and Figure 3-12B, respectively.*

Figure **3-12** displays variations of the modification friction factor as a function of the phase difference φ between the grooves on both cylinders and the cylinder radius R_1. It can be seen that the largest drag corresponds to $\varphi = 0$, i.e. grooves are in phase and the annular opening has a wavy pattern in the circumferential direction, and the smallest drag corresponds to grooves being out of phase ($\varphi = \pi/M$) and the converging-diverging pattern. Drag reduction can be induced for a sufficiently large R_1 for grooves with all possible phase differences, but this reduction is the largest and occurs for the smallest R_1 when grooves are out of phase.

3.5.4 Drag reduction mechanism

It is of interest to identify the processes that lead to the observed drag reduction. The distribution of the shear stress acting on the fluid displayed in Figure **3-13** shows a remarkable difference in the drag reducing and the drag increasing cases. In the former case the magnitude of the shear at the grooved cylinder (inner cylinder in the case shown in Figure **3-13**) reaches a minimum at locations corresponding to the minima of the annulus opening and reaches a maximum in locations corresponding to the maxima of the annulus opening. In the latter case, the distribution is reversed with the shear stress maxima occurring at locations corresponding to the minima of the annulus opening. The distribution of the shear stress at the outer (smooth) cylinder remains qualitatively the same under the drag reducing and the drag increasing conditions, with the maxima occurring at the locations corresponding to the minima of the annulus opening.

The difference between of the minimum and the maximum of the shear stress (amplitude of the shear stress variations) decreases as M increases in the drag reducing configuration. This amplitude passes through the value of smooth annulus for M corresponding to its critical value, and starts to increase again with further increase of M. The shear stress distribution has qualitatively different form in the drag increasing configuration as the stress maxima now correspond to the maxima of the annulus opening (see Figure **3-13**).
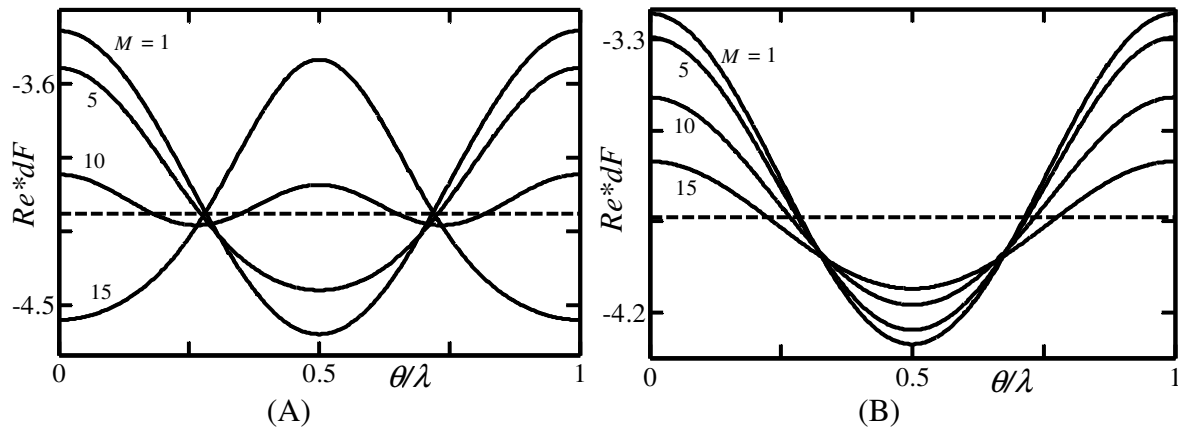
Figure 3-13: *Distribution of the axial component of shear stress acting on the fluid at the inner (Figure **3-13**A) and outer (Figure **3-13**B) cylinders for grooves with the geometry defined by Eq. (3.5.3) with $S_{in} = 0.3$, $S_{out} = 0$, $R_1 = 5$, and $S_{ave,out} = S_{ave,in} = 0$. Dashed lines provide reference values for the smooth cylinders.*
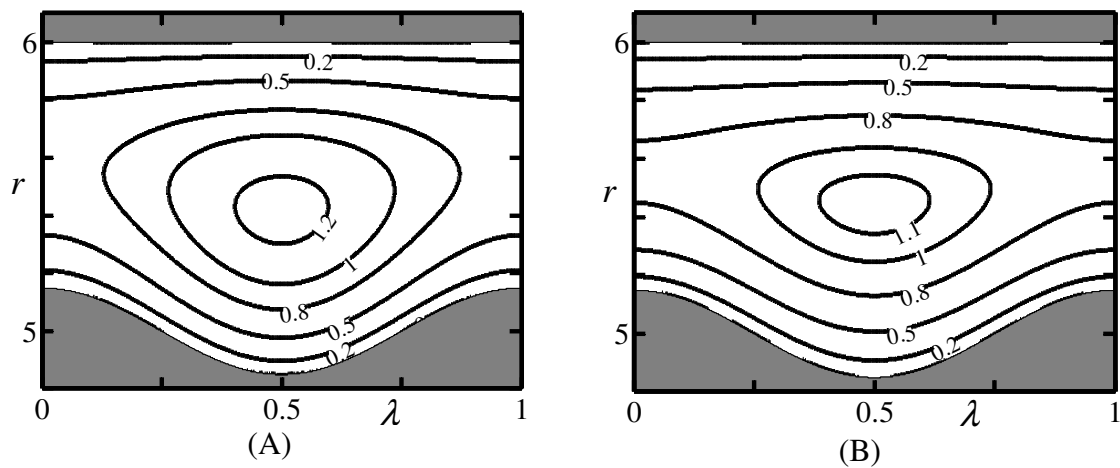
Figure 3-14: *Distribution of the axial velocity component in an annulus with the geometry defined by Eq. (3.5.3) with $S_{in} = 0.3$, $R_1 = 5$, $S_{ave,out} = S_{ave,in} = S_{out} = 0$ and $M = 5$ (Figure **3-14**A) and $M = 15$ (Figure **3-14**B).*
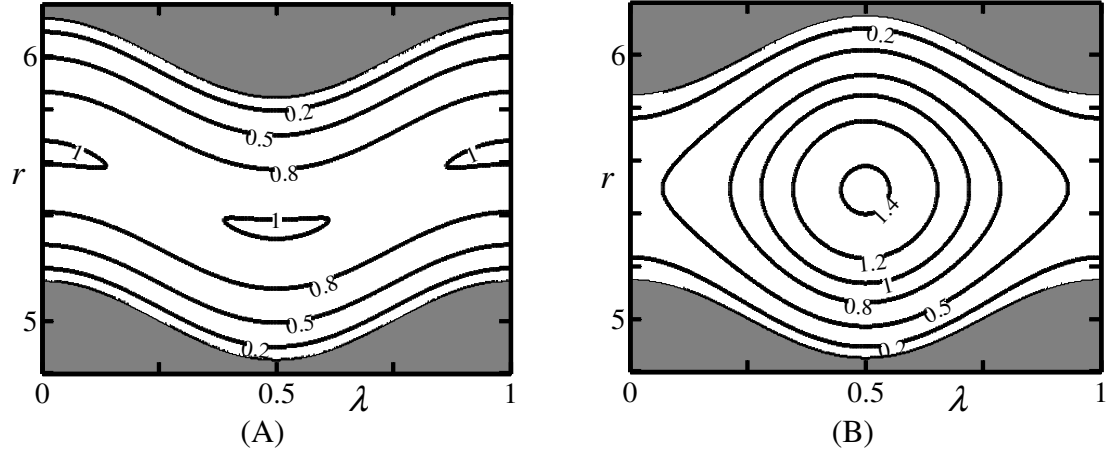
Figure 3-15: *Distribution of the axial velocity component in an annulus with the geometry defined by Eq. (3.5.3) with $S_{in} = S_{out} = 0.3$, $R_1 = 5$, $S_{ave,out} = S_{ave,in} = 0$, $M = 5$, and $\varphi = 0$ (Figure 3-15A) and $\varphi = \pi$ (Figure 3-15B).*

Figure **3-14** displays constant velocity lines. It can be seen that presence of grooves leads to a re-arrangement of the bulk flow, with stream tubes of high velocity fluid forming in the area of the largest annulus opening under drag reducing conditions (Figure **3-14**A). Changes in the groove geometry leading to a drag increase result in the reduction of the high-velocity stream tubes; this is demonstrated in Figure **3-14**B through the increase of M while keeping the remaining parameters the same. A similar reduction of these stream tubes can be observed when the phase difference between the grooves on both walls decreases to zero (see Figure **3-15**) which leads to a drag increase. It can be concluded that it is the re-arrangement of the bulk flow that is responsible for the drag reduction in spite of an increase of the wetted surface area.

3.6 Groove optimization for drag reduction

It has been shown is Sections 3.5.3 and 3.5.4 that presence of grooves may lead to a reduction of pressure losses. This section is focused on finding the groove shape that leads to the largest possible drag reduction in the case of an annulus with radius R_1 fitted with M grooves. It has been argued in Section 3.5.2 that a good approximation of the pressure loss can be found by replacing the actual grooves with the first mode of their Fourier representation (reduced order model). The optimization requires access to a wider

range of information about the geometry and thus one needs to include higher Fourier modes.

It is simpler to discuss the optimization by describing the groove geometry in terms of real variables, i.e.

$$
\begin{aligned}
r_{in}(\theta) &= R_1 + \\
A_{1,in}\cos(M\theta) + A_{2,in}\cos\left(2M\theta + \varphi_{2,in}\right) &+ \cdots + A_{n,in}\cos\left(nM\theta + \varphi_{n,in}\right), \\
r_{out}(\theta) &= 1 + R_1 + \\
A_{1,out}\cos\left(M\theta + \varphi_{1,out}\right) + A_{2,out}\cos\left(2M\theta + \varphi_{2,out}\right) &+ \cdots + \\
A_{m,out}\cos\left(mM\theta + \varphi_{m,out}\right).
\end{aligned}
\tag{3.6.1}
$$

The optimization problem involves finding the minimum of

$$
f_1 Re = F\left(A_{1,in}, \dots, A_{n,in}, \varphi_{2,in}, \dots, \varphi_{n,in}, A_{1,out}, \dots, A_{m,out}, \varphi_{1,out}, \dots, \varphi_{m,out}\right) \tag{3.6.2}
$$

subject to suitable constraints. It can be shown, on the basis of symmetry arguments as well as direct evaluations of pressure losses, e.g. Figure **3-12**, that the maximum drag reduction corresponds to either zero or π phase shift. Thus the optimization is reduced to finding the minimum of

$$
f_1 Re = F\left(A_{1,in}, \dots, A_{n,in}, A_{1,out}, \dots, A_{m,out}\right). \tag{3.6.3}
$$

The optimization is focused on the effects of flow modulations and thus the flow cross sectional area has to be kept constant during the search process. This leads to a nonlinear constrained optimization problem which is solved using the trust-region-reflective optimization algorithm (Coleman & Li, 1994,1996). Details related to the actual implementation of this algorithm are discussed in the next section.

The optimization requires specification of the range of acceptable geometries. In the present analysis, one needs to specify the constraints imposed on the maximum permissible depths and heights of the grooves measured from the reference cylinders. The depth and the height can be treated as unknowns to be determined by the optimization process. If this is the case and *M* is in the region of drag increase (see Figure **3-11**), the

optimization always results in the removal of the grooves. In the case of M corresponding to drag reduction, the results of the optimization depend on the type of the imposed constraint. The following discussion addresses this particular issue.

3.6.1 The equal-depth grooves

As the first case, consider grooves placed only at the inner cylinder. It is assumed that the maximum depth and the maximum height of these grooves are the same. We shall refer to such geometry as the equal-depth grooves. The relevant constraints can be expressed as

$$\max_\theta |r_{in}(\theta)| = R_1 + S_{in,o}, \quad \min_\theta |r_{in}(\theta)| = R_1 - S_{in,i}, \quad S_{in,i} = S_{in,o}, \qquad (3.6.4\text{a-c})$$
$$\max_\theta |r_{out}(\theta)| = \min_\theta |r_{out}(\theta)| = 1 + R_1 \qquad (3.6.4\text{d})$$

where $S_{in,i}$ and $S_{in,o}$ stand for the height and the depth of the groove, respectively. Constraints (3.6.4a-d) need to be supplemented by the constraint expressing conservation of the flow cross-sectional area. One may pose a constraint where the depth and the height of the groove cannot exceed certain threshold, i.e.

$$\max_\theta |r_{in}(\theta)| \le R_1 + S_{in,o}, \quad \min_\theta |r_{in}(\theta)| \le R_1 - S_{in,i}, \quad S_{in,i} = S_{in,o}, \qquad (3.6.5\text{a-c})$$
$$\max_\theta |r_{out}(\theta)| = \min_\theta |r_{out}(\theta)| = 1 + R_1. \qquad (3.6.5\text{d})$$

Such constraints need not be considered as the minimum drag always correspond to the maximum permitted height and depth.

The shapes of the optimal grooves are expressed by Fourier expansions with an unknown number of terms. The results displayed in Figure **3-16** for typical conditions of interest demonstrate that these expansions are fairly rapidly convergent. Use of just three Fourier modes allows approximation of the optimal shape with less than a 10% error for the pressure loss. The error can be reduced by using additional modes (see Figure **3-16**). These results, as well as those from many other similar tests (not reported), lead to a conclusion that the reduced order models based on 3-4 Fourier modes can capture the optimal shapes with an accuracy that is sufficient for most applications.
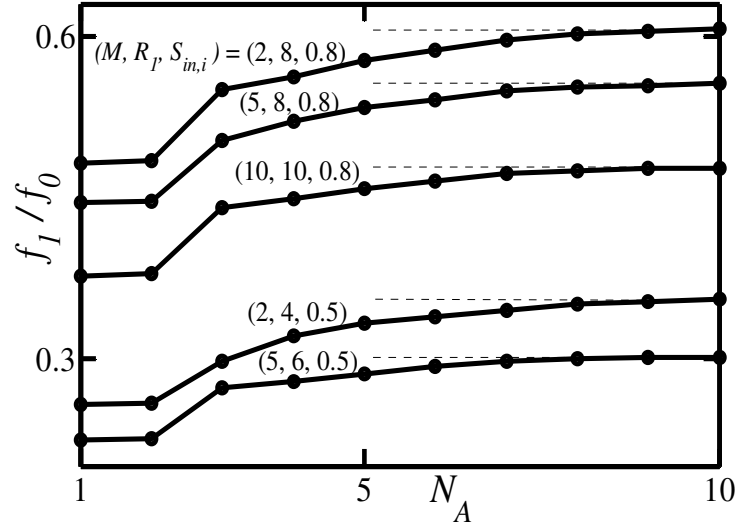
Figure 3-16: *Variations of the normalized modification friction factor f_1/f_0 as a function of the number of Fourier modes used for description of the optimal shape of the equal-depth grooves placed at the inner cylinder.*

The insensitivity of the pressure loss to details of the geometry expressed by higher Fourier modes should not be surprising as the action of viscosity is expected to smooth out such details. This, however, creates computational problems as gradients of the cost function with respect to higher Fourier modes that need to be computed by the optimizer become very small. These gradients are determined using low-order finite-difference quotients. Use of strict convergence criteria is able, however, to overcome these difficulties but at a considerable computational cost. Once the convergence of a Fourier series has been established, as illustrated in Figure **3-16**, the actual computations can be carried out using fewer Fourier modes and less strict convergence criteria. All of the results presented in this paper have been obtained with the convergence criteria set at 10^{-6} and the use of 10 Fourier modes depending of the form of the optimal grooves.

We shall now discuss the form of the optimal grooves. Evolution of the optimal shape when the inner cylinder is fitted with $M = 2$, 10 grooves with amplitudes $S_{in,i} = S_{in,o} = S = 0.2, 0.5, 0.8$, is illustrated in Figure **3-17**. Variations of the shape are fairly minor and, thus, it is possible to propose a universal shape that well approximates the optimal grooves over a wide range of parameters. This universal shape has the form of a trapezoid

characterized by $a = b = \lambda/6$ and $c = d = \lambda/3$ (see Figure **3-6** for definition of parameters). The deviations from the universal shape increase with an increase of the depth of the cut and reduction of R_1. The largest deviations correspond to the wave number $\alpha = M/R_1$ approaching its critical value (see Figure **3-11**) where the grooves begin to generate additional drag. Availability of the universal shape provides a general answer to the optimization problem which eliminates the need for detailed analysis if the associated error is viewed as acceptable.
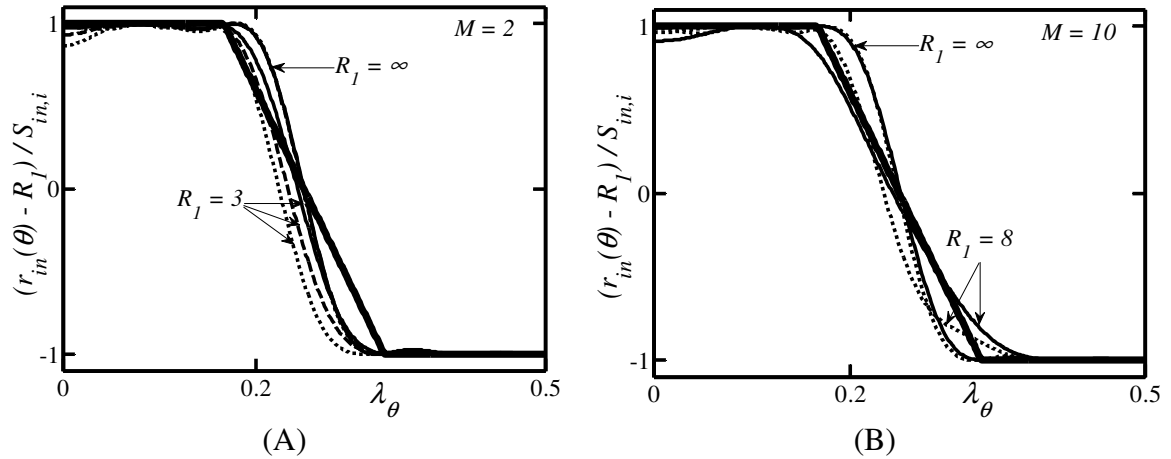
Figure 3-17: *Evolution of the optimal shape of M = 2, 10 equal-depth grooves placed at the inner cylinder as a function of the wall curvature R_1. Solid, dashed and dotted lines correspond to the depth of the grooves $S_{in,i} = S_{in,o} = S = 0.2, 0.5, 0.8$, respectively. All these lines overlap for $R_1 = \infty$. The other values of R_1 shown correspond to values close to those that cause a change from drag reduction to a drag increase (see Figure **3-11**). Thick lines describe the universal shape, i.e. trapezoid with $a = b = \lambda/6$ and $c = d = \lambda/3$ (see text for details).*

Replacement of the optimal shape by the universal trapezoid may lead to an error in the determination of the modification friction factor. Comparisons of the actual optimal modification friction factor and the modification friction factor for the universal trapezoid displayed in Figure **3-18** demonstrate that this error is negligible in most practical applications. This error may become excessive when R_1 becomes small as the difference between the actual optimal shape and the universal trapezoid becomes excessive (see Figure **3-16**). Such configurations are likely to be of marginal interest as they correspond

to the wave number $\alpha = M/R_1$ approaching its critical value and, thus, produce marginal reductions of pressure loss.
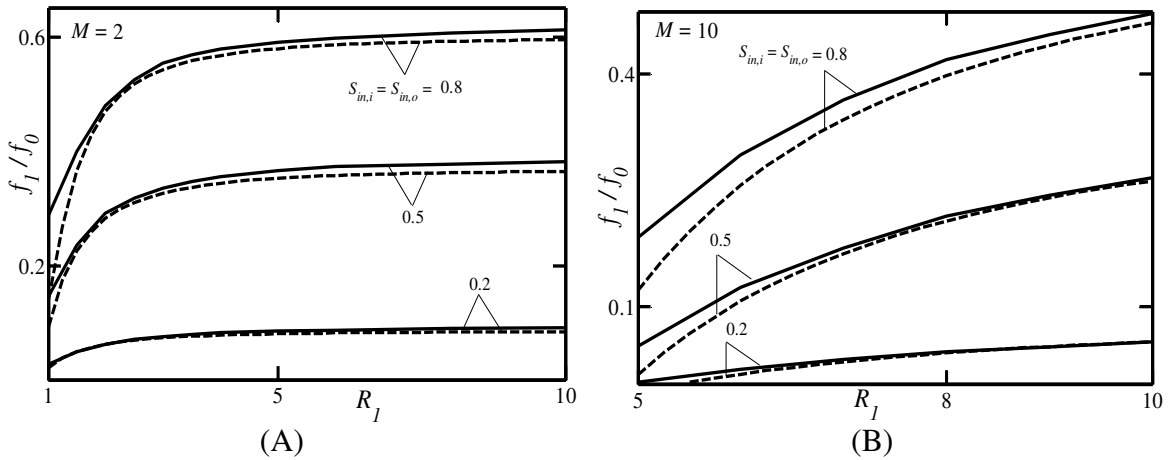
Figure 3-18: *Variations of the normalized modification friction factor f_1/f_0 for M = 2 equal-depth optimal grooves (Figure 3-18A) and M = 10 similar grooves (Figure 3-18B) placed at the inner cylinder (solid lines). Modification friction factors for the same grooves approximated using the universal trapezoid are marked using dashed lines. See text for details.*

Figure **3-19** illustrates variations of the modification friction factor for the optimal grooves approximated using the universal trapezoid over the whole range of groove amplitudes S and wall curvature R_1 of practical interest. These data provide information regarding the maximum potential drag reduction that can be produced by the grooves. The same figure also displays results for grooves described by one Fourier mode. The difference illustrates the potential gains due to the replacement of the simple sinusoidal grooves by the optimal grooves. It can be seen that this difference is generally smaller than 10% which supports the conclusions discussed in Section 3.5.2 and illustrates the power of the reduced order model.

Consider similar grooves added to the outer cylinder while the inner cylinder is kept smooth. Constraint (3.6.4a-d) is replaced by

$$\max_\theta |r_{in}(\theta)| = \min_\theta |r_{in}(\theta)| = R_1, \qquad\qquad (3.6.6a, b)$$
$$\max_\theta |r_{out}(\theta)| = 1 + R_1 + S_{out,o}, \quad \min_\theta |r_{out}(\theta)| = 1 + R_1 - S_{out,i}, \qquad (3.6.6c\text{-}e)$$
$$S_{out,i} = S_{out,o}$$

where $S_{out,i}$ and $S_{out,o}$ stand for the height and the depth of the groove, respectively. An analysis similar to that carried out in the case of grooves placed at the inner cylinder results in similar conclusions. Deviations from the universal shape (not shown) are, however, much smaller as the effective wave number $\alpha = M/(1 + R_1)$ is smaller.
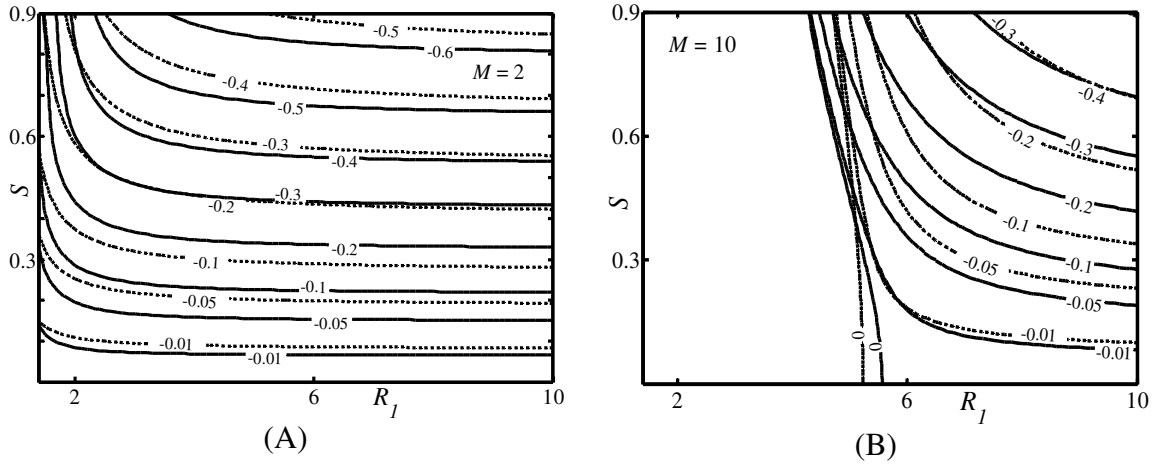
Figure 3-19: *Variations of the normalized modification friction factor f_1/f_0 as a function of the wall curvature R_1 and the groove amplitude $S_{in,i} = S_{in,o} = S$ for M = 2 universal equal-depth trapezoidal grooves (Figure **3-19**A) and M = 10 similar grooves (Figure **3-19**B) placed at the inner cylinder (see text for discussion). Dashed lines are for the sinusoidal grooves defined by Eq. (3.5.3) with $S_{ave,out} = S_{ave,in} = 0$.*

The general case corresponds to grooves placed on both cylinders, i.e. the constraints take the form

$$\max_\theta |r_{in}(\theta)| = R_1 + S_{in,o}, \ \min_\theta |r_{in}(\theta)| = R_1 - S_{in,i}, \ S_{in,i} = S_{in,o} , \qquad (3.6.7\text{a-c})$$
$$\max_\theta |r_{out}(\theta)| = 1 + R_1 + S_{out,o}, \ \min_\theta |r_{out}(\theta)| = 1 + R_1 - S_{out,i}, \qquad (3.6.7\text{d-e})$$
$$S_{out,i} = S_{out,o} \ .$$

The results displayed in Figure **3-20** demonstrate that the shapes of the optimal grooves are nearly the same as the shapes of the grooves determined for each cylinder separately, and the grooves on the outer cylinder are shifted with respect to those at the inner cylinder by a half wavelength in the circumferential direction.
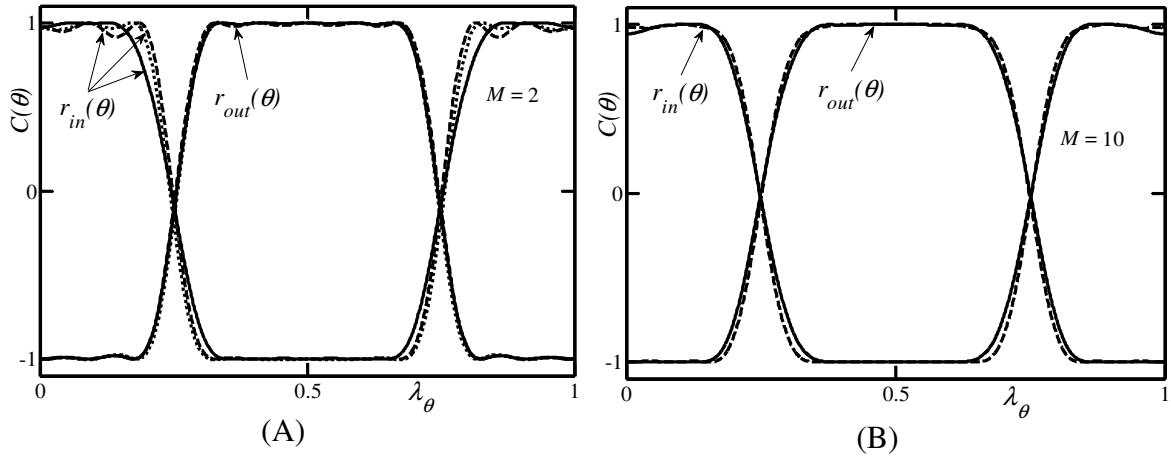
Figure 3-20: *Optimal shapes of the equal-depth grooves placed at both cylinders. $C(\theta)$ is defined as $[r_{out}(\theta) - 1 - R_1]/S_{out,i}$, $[r_{in}(\theta) - R_1]/S_{in,i}$. Figure **3-20**A displays results for M = 2 grooves; the solid lines are for $R_1 = 3$, $S_{in,o} = S_{in,i} = S_{out,o} = S_{out,o} = 0.2$, the dotted lines are for $R_1 = 5$, $S_{in,o} = S_{in,i} = S_{out,o} = S_{out,o} = 0.4$, and the dash lines are for $R_1 = 10$, $S_{in,o} = S_{in,i} = S_{out,o} = S_{out,o} = 0.4$. Figure **3-20**B displays results for M = 10 grooves; the solid lines are for $R_1 = 8$, $S_{in,o} = S_{in,i} = S_{out,o} = S_{out,o} = 0.2$, and the dashed lines are for $R_1 = 10$ and $S_{in,o} = S_{in,i} = S_{out,o} = S_{out,o} = 0.4$.*

The results displayed in Figure **3-21** show that the drag reduction produced by these grooves, with shapes approximated using the universal trapezoid, is approximately equal to the drag reduction produced by grooves placed only at one cylinder but with a double amplitude (compare Figure **3-19** and Figure **3-21**). Figure **3-21** also presents results for simple sinusoidal grooves placed at both cylinders. It can be seen that such grooves produce about 10% less drag reduction than the optimal grooves. The reader should recall, when reviewing these results, that predictions based on the universal trapezoid are not accurate when the groove wave number is close to its critical value.

3.6.2 The unequal-depth grooves

Consider grooves with unequal depth which are initially placed only at the outer cylinder. The maximum depth and the maximum height of the groove are not the same but, as before, they are specified by the user. Such grooves correspond to constraints in the form

$$\max_\theta |r_{out}(\theta)| = 1 + R_1 + S_{out,o}, \quad \min_\theta |r_{out}(\theta)| = 1 + R_1 - S_{out,i} \qquad (3.6.8a, b)$$

where the values of $S_{out,o}$ and $S_{out,i}$ are different and known. The constraints (3.6.8a, b) needs to be supplemented by the constraint expressing the need to maintain the constant flow cross-sectional area.
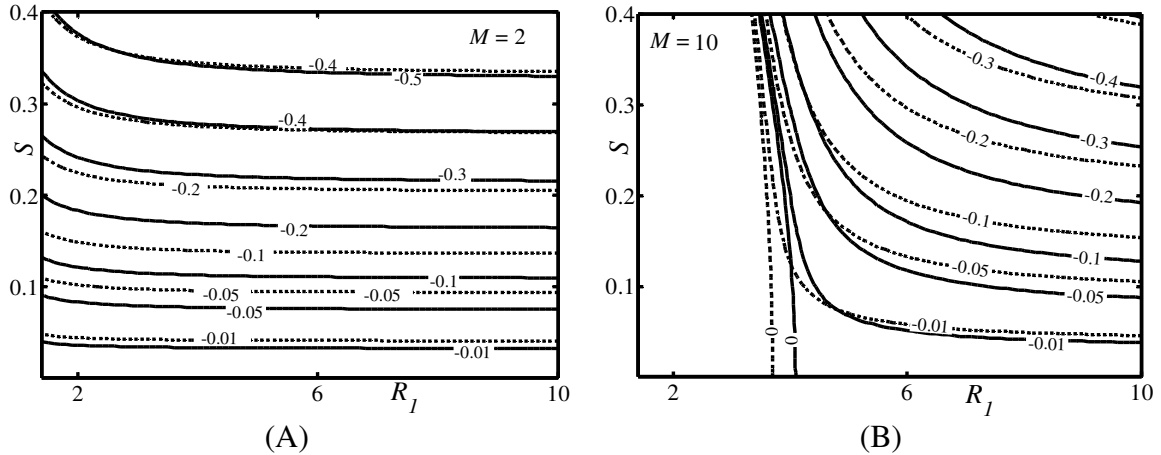
Figure 3-21: *Variations of the normalized modification friction factor f_1/f_0 as a function of the wall curvature R_1 and the groove amplitude $S_{in,i} = S_{in,o} = S_{out,i} = S_{out,o} = S$ for M = 2 universal equal-depth trapezoidal grooves (Figure **3-21**A) and M = 10 similar grooves (Figure **3-21**B) placed at both cylinders (see text for discussion). Dashed lines are for the sinusoidal grooves defined by Eq. (3.5.3) with $S_{ave,out} = S_{ave,in} = 0$. The reader should note that the universal trapezoid does not offer a good approximation for the optimal grooves under conditions close to transition between the drag increasing and the drag decreasing geometries.*

Variations of the modification friction factor, when the height of the groove is fixed at $S_{out,i} = 0.5$ while the depth $S_{out,o}$ is varied, are displayed in Figure **3-22**. It can be seen that there exists a depth that leads to the largest drag reduction. We shall refer to this depth as the optimal depth D_{opt} which, together with the corresponding shape, determines the optimal geometry.
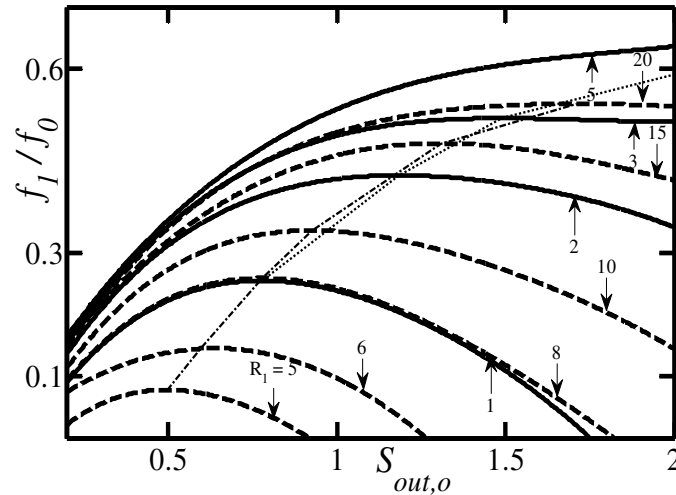
Figure 3-22: *Variations of the normalized modification friction factor f_1/f_0 as a function of the depth of the grooves, i.e. $S_{out,o}$, for the unequal-depth grooves. The grooves are placed at the outer cylinder and have the same maximum height set at $S_{out,i} = 0.5$. Solid and dashed lines correspond to the use of $M = 2$ and $M = 10$ grooves, respectively. The dotted ($M = 2$) and dashed-dotted ($M = 10$) lines identify the depth of the grooves that leads to the maximum drag reduction.*
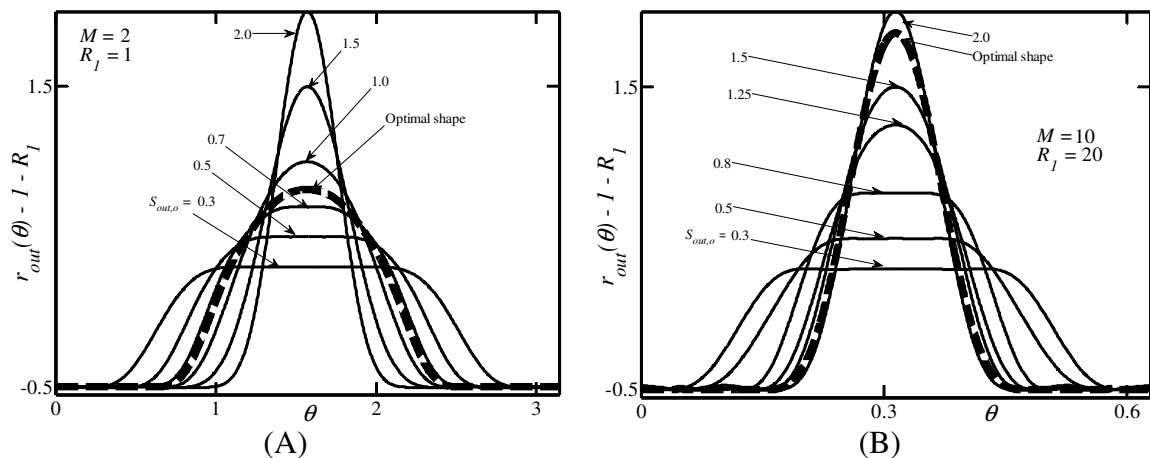
Figure 3-23: *Evolution of the optimal shape of the unequal-depth grooves placed at the outer cylinder as a function of the depth of the groove $S_{out,o}$. The height of the groove is set at $S_{out,i} = 0.5$. The results presented in Figure **3-23**A are for $M = 2$, $R_1 = 1$, and in Figure **3-23**B for $M = 10$, $R_1 = 20$. Dashed lines illustrate shapes corresponding to the optimal depth.*

Variations of the shape of the optimal grooves as a function of $S_{out,o}$ are illustrated in Figure **3-23**. For small enough $S_{out,o}$ this shape looks like the universal trapezoid discussed in the previous section.
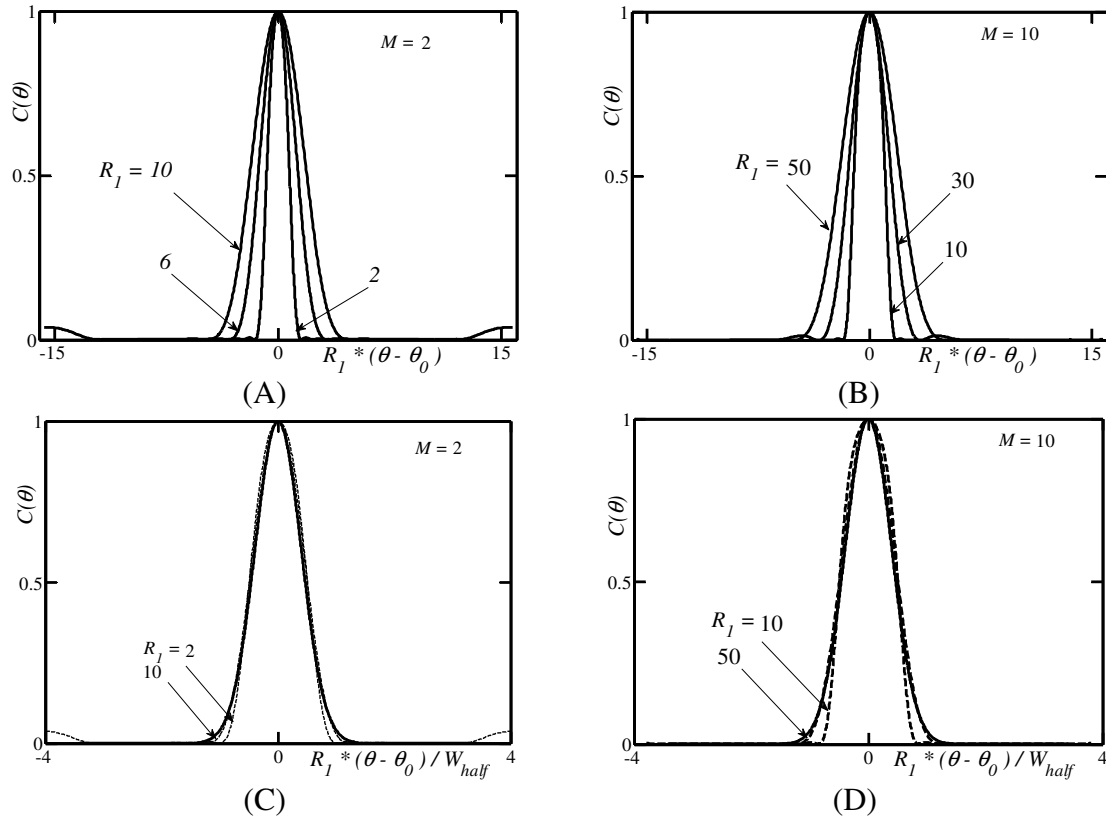
Figure 3-24: *Shapes of the unequal-depth optimal grooves corresponding to the optimal depth, i.e. the optimal geometry, for grooves placed at the outer cylinder for selected values of the wall curvature R_1. $C(\theta)$ is defined as $[r_{out}(\theta) - (r_{out})_{min}]/[(r_{out})_{max} - (r_{out})_{min}]$. The height of the groove is set at $S_{out,i} = 0.5$. Figure **3-24**A-B present results for M = 2 and M = 10, respectively. The same shapes, but normalized with the width at half height W_{half} are presented in Figure **3-24**C-D. The universal shape has the form of a Gaussian function defined by $y = e^{-3.2x^2}$ and is illustrated using solid lines.*

A sufficient increase of $S_{out,o}$ leads to a shape that resembles a Gaussian function. The shape that gives the largest drag reduction can be approximated by the Gaussian function which underlines the universality of the optimal geometry.

The optimal geometry can be determined directly by limiting the constraint to the following form

$$\min_\theta |r_{out}(\theta)| = 1 + R_1 - S_{out,i} \qquad (3.6.9)$$

and treating the depth of the groove $S_{out,o}$ as an unknown. Evolution of the optimal geometry is illustrated in Figure **3-24**A-B where the groove height has been scaled with its maximum. Rescaling of the width of the groove with its width at half height W_{half} leads to universal shapes displayed in Figure **3-24**C-D. These shapes are well approximated by the Gaussian function in the form $y = e^{-3.2x^2}$.   The complete information about the optimal geometry consists of the universal Gaussian function, and the values of W_{half} and D_{opt} displayed in Figure **3-25**. The same figure provides information about the drag reduction that can be produced by the optimal geometry. In general, an increase in the number of grooves M reduces the drag reduction as well as the optimal depth and the width of the grooves. While it is difficult to make direct comparisons between the optimal geometry and the simple sinusoidal grooves, the former generate a drag reduction that is up 50% higher than the latter.

Analysis of the same grooves placed at the inner cylinder leads to very similar conclusions regarding the optimal shape, the optimal depth and the optimal geometry. These results are, therefore, not presented. Figure **3-26** illustrates the properties of the optimal geometry made of grooves placed at both cylinders as well as the resulting drag reduction. Grooves at the outer cylinder are shifted by a half wavelength in the axial direction with respect to those at the inner cylinder. The grooves have shapes similar to those found in the case of only one grooved cylinder. The drag reduction is approximately twice the drag reduction obtained using grooves with the same height placed on only one cylinder.
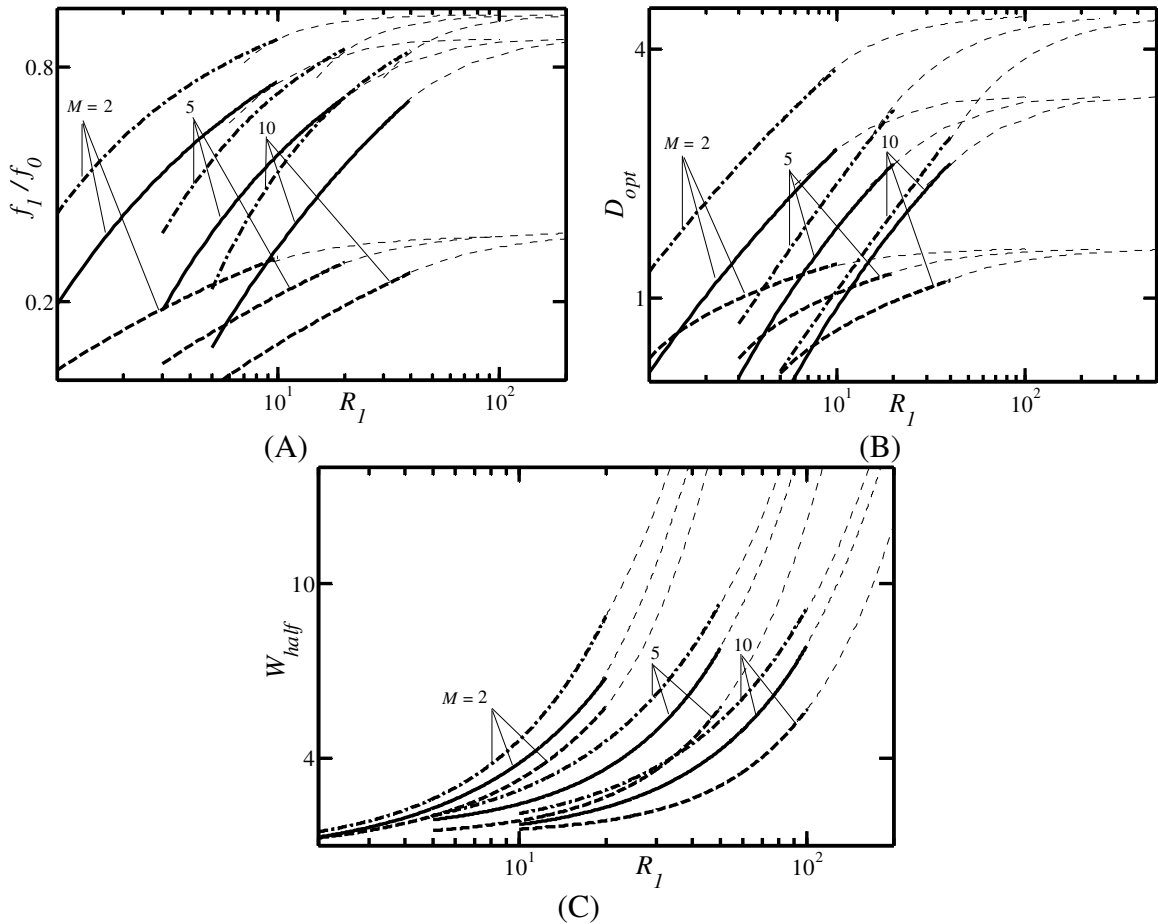
Figure 3-25: *Variations of the normalized modification friction factor (Figure **3-25***A), the optimal depth (Figure **3-25***B) and the half width of the optimal groove (Figure **3-25***C) as a function of the wall curvature R_1 for an annulus with the smooth inner cylinder and the optimal geometry of the outer cylinder. The maximum heights of the grooves are set as $S_{out,i} = 0.8$ (dashed-dotted lines), $S_{out,i} = 0.5$ (solid lines) and $S_{out,i} = 0.2$ (dashed lines). Dotted lines correspond to the asymptotic solution, i.e. $R_1 \to \infty$.*
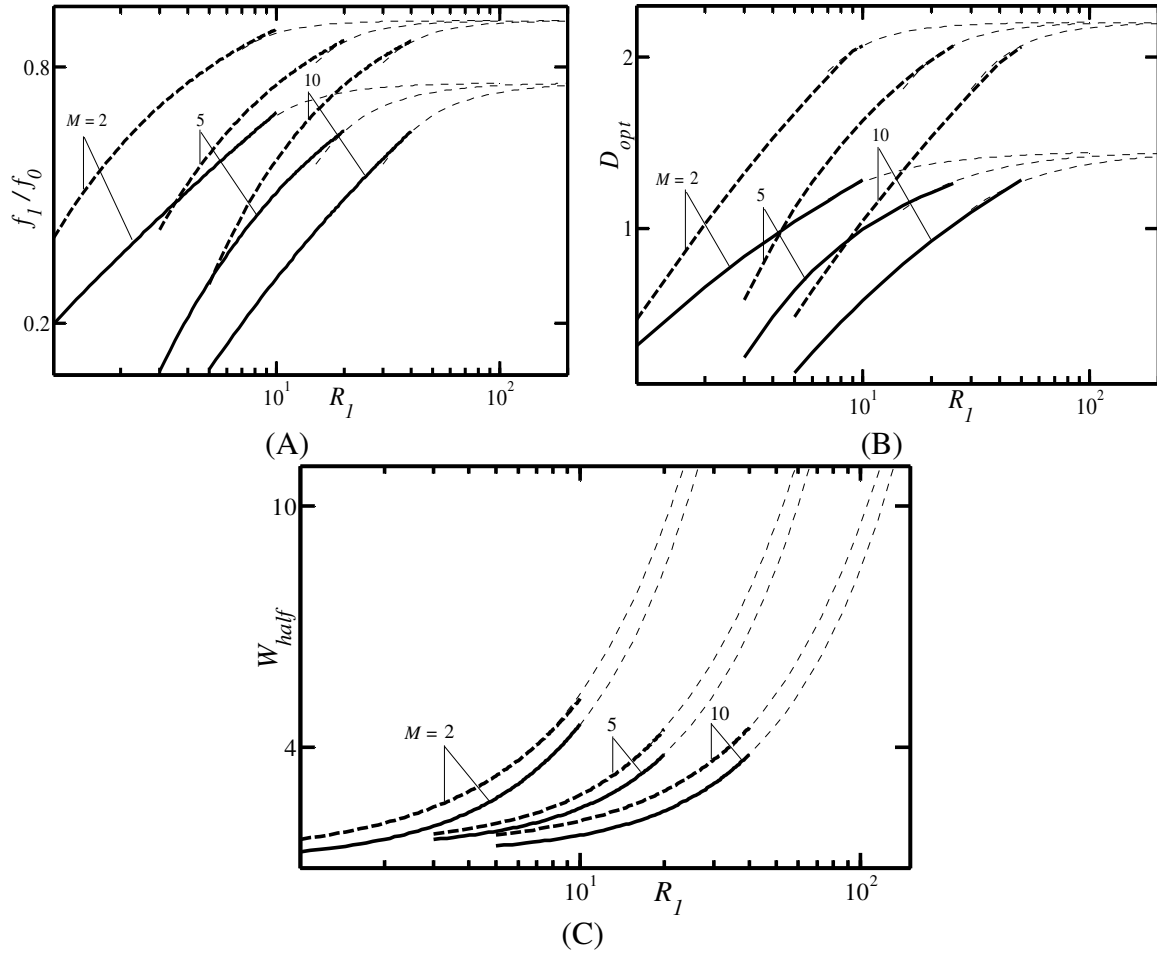
Figure 3-26: *Variations of the normalized modification friction factor (Figure* **3-26***A), the optimal depth (Figure* **3-26***B) and the half width of the optimal groove (Figure* **3-26***C) as a function of the wall curvature R_1 for an annulus with the optimal geometries of the inner and outer cylinders. The maximum heights of the grooves at the inner and outer cylinders are the same and set at the level of $S_{out,i} = 0.4$ (dashed lines) and $S_{out,i} = 0.2$ (solid lines). Dotted lines correspond to the asymptotic solution, i.e. $R_1 \to \infty$.*

3.7 Summary

Analysis of pressure losses in laminar flows through annuli fitted with longitudinal grooves has been carried out. An additional pressure gradient required in order to maintain the same flow rate in the grooved annuli, as well as in the reference smooth annuli, is used as a measure of the loss. The groove-induced changes can be represented as a superposition of a pressure drop due to a change in the average position of the

bounding cylinders and a pressure drop due to flow modulations induced by the shape of the grooves. The former effect can be evaluated analytically while the latter requires explicit computations. It has been demonstrated that a reduced order model is an effective tool for extraction of the features of groove geometry that lead to flow modulations relevant to drag generation. One Fourier mode from the Fourier expansion representing the annulus geometry is sufficient to predict pressure losses with an accuracy sufficient for most applications in the case of equal-depth grooves. It is shown that the presence of the grooves may lead to a reduction of pressure loss in spite of an increase of the surface wetted area. The drag decreasing grooves are characterized by the groove wave number M/R_1 being smaller than a certain critical value, where M denotes the number of grooves being used and R_1 stands for the radius of the annulus. This number marginally depends on the groove amplitude and does not depend on the flow Reynolds number. It is shown that the drag reduction mechanism relies on the re-arrangement of the bulk flow that leads to the largest mass flow taking place in the area of the largest annulus opening. The form of the optimal grooves from the point of view of the maximum drag reduction has been determined. This form depends on the type of constraints imposed. In general, the optimal shape can be described using the reduced order model involving only a few Fourier modes. It is shown that in the case of the equal-depth grooves, the optimal shape can be approximated using a special form of trapezoid. In the case of the unequal-depth grooves, where the groove depth needs to be determined as a part of the optimization procedure, the optimal geometry, consisting of the optimal depth and the corresponding optimal shape, can be approximated using a Gaussian function. The maximum possible drag reduction, corresponding to the optimal geometry, has been determined.

Chapter 4

4 Maximization of Heat Transfer Across Micro-Channels [1]

4.1 Introduction

In spite of the widespread use of micro-channels, there is a limited literature dealing with their optimization from the point of view of maximization of the heat transfer and minimizing pressure losses. It has been shown in Chapter 3 that there exists a class of longitudinal grooves that leads to a reduction of the pressure losses for laminar flows despite the increase of the wetted surface area. In this chapter, the heat transfer enhancement resulting from the introduction of longitudinal grooves (riblets) of arbitrary shape is analyzed, with the determination of the groove shape that simultaneously leads to the maximum drag reduction and the maximum heat transfer enhancement being the main objective. The problem formulation and definition of the thermal enhancement factor are given in Section 4.2. The methods used for evaluation of the thermal enhancement factor are described in Section 4.3, with Section 4.3.1 devoted to arbitrary grooves and Section 4.3.2 focused on the long wavelength grooves. Section 4.4 describes the heat transport and drag generation mechanisms active in the presence of the grooves. The best groove shape, the optimal shape, is determined through minimization of the thermal enhancement factor and the optimization process is discussed in Section 4.5. Section 4.6 describes the optimal shapes and discuses the performance of the optimal grooves determined with various additional constraints. In particular, Section 4.6.1 provides information about the performance of the equal depth grooves and Section 4.6.2 discusses the performance of the unequal-depth grooves. A short summary of the main conclusions is given in Section 4.7.

4.2 Problem formulation

Heat transfer across a channel fitted with longitudinal grooves (see Figure **4-1**) is considered. The walls are subject to a differential heating, resulting in a heat flow across the channel. The steady laminar flow is driven through the channel in the z-direction by a constant pressure gradient. We wish to determine the form of the grooves that maximizes the heat transfer and minimizes the flow losses. The study is carried out under the subcritical flow conditions, i.e., the flow remains laminar with no secondary structures after introduction of grooves. Such situation occurs in small Reynolds number flows and, as a result, the heat is carried across the channel by conduction only. While it is not known how the grooves affect conduction, it is known how they affect flow losses (see Chapter 3 for annular flow and Mohammadi & Floryan 2013a for planar flow). The optimum groove shape must result from a compromise between the groove-induced changes in the heat transport and the groove-induced flow losses.
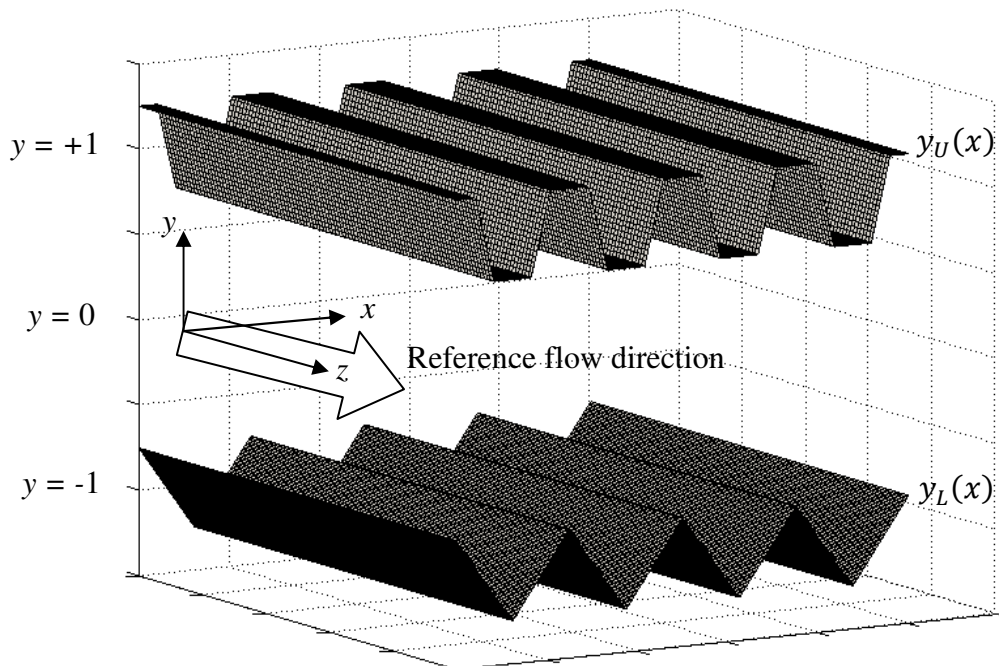
Figure 4-1: *Sketch of the heat transfer system.*

It is assumed that the grooves have an arbitrary but identical shape and extend to $\pm\infty$ in the x- and z-directions. The channel entry and exit effects as well as effects of the side

walls are neglected. The channel geometry can be described using Fourier expansions in the form

$$y_L(x) = -1 + \sum_{n=-N_A}^{N_A} H_L^{(n)} e^{in\alpha x}, \quad y_U(x) = 1 + \sum_{n=-N_A}^{N_A} H_U^{(n)} e^{in\alpha x} \qquad (4.2.1a, b)$$

where $\lambda = 2\pi/\alpha$ denotes the groove wavelength, α stands for the wave number, $y_L(x)$ and $y_U(x)$ describe locations of the lower and upper walls, respectively, N_A is the number of Fourier modes requires to describe the geometry, and $H_L^{(n)} = H_L^{*(-n)}$ and $H_U^{(n)} = H_U^{*(-n)}$ are the reality conditions where stars denote complex conjugates. All quantities have been scaled with the half channel height L as the length scale. The choice of $H_L^{(n)}$ and $H_U^{(n)}$ is restricted by the no-contact condition between the walls.

The system performance is a function of two independent transport mechanisms and this leads to a multi-objective optimization problem, which is replaced in this analysis by minimization of a single performance function, the thermal enhancement factor Ω (Gee & Webb 1980), defined as

$$\Omega = \frac{1}{Q/Q_0} + \beta (f/f_0)^{1/3} \qquad (4.2.2)$$

Here Q stands for the heat transfer per unit length, f is the friction factor, subscript 0 identifies the reference smooth-channel quantities and β is the weighting factor selected by the user. The smooth channel corresponds to $\Omega = 1 + \beta$. An increase of heat flow and a decrease of flow losses both result in the reduction of Ω. We define the optimum shape as the shape that minimizes Ω. The objective of the study can, therefore, be stated as finding the minimum of Ω over all possible $H_U^{(n)}$ and $H_L^{(n)}$ subject to suitable constraints, i.e., the minimum of

$$\Omega = \Omega \left(Re, Pr, H_L^{(0)}, H_L^{(1)}, \ldots, H_L^{(N_A)}, H_U^{(0)}, H_U^{(1)}, \ldots, H_U^{(N_A)}, \beta \right). \qquad (4.2.3)$$

The channel performance can be easily affected through a change of the average channel opening but this effect can be readily accounted for analytically (Mohammadi & Floryan 2013a) and is of no interest in this study. The focus of this study is, therefore, on the system performance enhancement associated with the flow and heat transfer modulations created by the grooves. Accordingly, the cross-sectional area of the channel is kept constant and equal to the flow cross-sectional area of the reference smooth channel, i.e. $H_U^{(0)} = H_L^{(0)} = 0$. Practical applications may impose constraints associated with the maximum permitted depth and height of the grooves. This issue will be discussed later in Section 4.5. The minimization of Ω represents a constrained nonlinear optimization problem. The interior-point algorithm (Coleman & Li 1994; 1996) is used for its solution. The derivatives of the cost function are determined using the central finite-difference quotients. The evaluation of the cost function, i.e. Ω, is discussed in the next section. The implementation of the optimization algorithm is discussed in the subsequent section.

4.3 Cost function evaluation

The cost function is evaluated through the solution of the field equations. The continuity, momentum, and energy equations have the form

$$\vec{\nabla}.\vec{V} = 0, \tag{4.3.1}$$
$$(\vec{V}.\vec{\nabla})\vec{V} = Re^{-1}\nabla^2\vec{V} - \vec{\nabla}p, \tag{4.3.2}$$
$$(\vec{V}.\vec{\nabla})\theta = (RePr)^{-1}\nabla^2\theta, \tag{4.3.3}$$

where $\vec{V}$ stands for the velocity vector with components (u, v, w) in the (x, y, z) directions, respectively, the maximum of the reference z-velocity w_{max} is used as the velocity scale and ρw_{max}^2 is used as the pressure scale where ρ is the density. The reference quantities are defined later in the text. The Reynolds number is defined as $Re = w_{max}L/\nu$ where ν stands for the kinematic viscosity, and the Prandtl number is defined as $Pr = c_p\mu/k$ where c_p is specific heat, μ stands for the dynamic viscosity and k denotes the thermal conductivity. The dimensionless temperature θ is defined as

$$\theta = \frac{T - T_C}{T_H - T_C} \tag{4.3.4}$$

where T_H and T_C are the temperatures of the hot and cold plates, respectively. Because of the special form of the grooves, the governing equations assume simpler forms

$$\nabla^2 w = Re^{-1} \, dp/dz, \qquad (4.3.5)$$
$$\nabla^2 \theta = 0. \qquad (4.3.6)$$

where (4.3.5) and (4.3.6) correspond to the z-momentum and energy equations, respectively, and are decoupled. The boundary conditions have the form

$$w = \theta = 0 \ \text{at} \ \ y = y_L(x), \qquad (4.3.7)$$
$$w = 0, \ \ \theta = 1 \ \ at \ \ y = y_U(x), \qquad (4.3.8)$$

with the shape of the grooves providing coupling between the heat and flow problems. In the case of the smooth (reference) channel, the solution has a simple form

$$\vec{V}_0 = (u_0, v_0, w_0) = (0, 0, 1 - y^2), p_0(z) = -2Re^{-1}z + c,$$
$$M = \lambda_x^{-1} \int_{x=0}^{x=\lambda_x} \int_{y=-1}^{y=1} w_0(y) dy dx = \frac{4}{3},$$
$$f_0 = -2\frac{dp_0}{dz} = 4Re^{-1} \qquad (4.3.9)$$

$$\theta_0(y) = 0.5(1 + y), \qquad Q_0 \lambda_x^{-1} = 0.5. \qquad (4.3.10)$$

where c denotes an arbitrary constant, M is the flow rate per unit width of the channel in the x-direction, and $Q_0\lambda_x^{-1}$ denotes the heat transfer per unit length.

In the case of the grooved channel, the solution of (4.3.6) and (4.3.8) determines the temperature θ and leads to the determination of the local heat flux entering the channel at the lower wall in the form

$$q[x, y_L(x)] = \frac{\partial \theta}{\partial x} n_x + \frac{\partial \theta}{\partial y} n_y \qquad (4.3.11)$$

where $\vec{n} = (n_x, n_y, 0)$ is the unit normal vector pointing outwards with components of the form

$$n_x = \frac{dy/dx}{\sqrt{1 + (dy/dx)^2}} \ , n_y = \frac{-1}{\sqrt{1 + (dy/dx)^2}} \ at \ y = y_L(x).$$

(4.3.12)

Similar expressions can be developed for the upper wall.

The change in the wetted surface area can be expressed as

$$\frac{A}{A_0} = \left\{ \frac{1}{\lambda} \int_{x=0}^{x=\lambda} \sqrt{1 + \left(\frac{dy}{dx}\right)^2} \ dx \right\}_{y=y_L(x)}.$$

(4.3.13)

where A and A_0 denote the total surface area of the grooved and smooth walls, respectively. The overall change in the heat flow across the channel per unit length, which is due to changes of the local heat flux and of the wetted area, can be expressed in terms of the ratio of the actual heat flow and the heat flow for the smooth channel Q/Q_0 can be evaluated by integrating the local heat flux and takes the form

$$\frac{Q}{Q_0} = \left\{ \frac{2}{\lambda_x} \int_{x=0}^{x=\lambda_x} q(x,y) \sqrt{1 + \left(\frac{dy}{dx}\right)^2} \ dx \right\}_{y=y_L(x)}.$$

(4.3.14)

The solution of the flow problem requires introduction of an additional closing condition as the pressure gradient dp/dz is not known. Since the addition of grooves changes the flow resistance, it is assumed in this analysis that the mass flow rate must remain the same in the smooth as well as in the grooved channel and this requires an appropriate adjustment of the pressure gradient. The preservation of the flow rate is expressed in terms of a constraint of the form

$$M = \lambda_x^{-1} \int_{x=0}^{x=\lambda_x} \int_{y=y_L(x)}^{y=y_U(x)} w(x,y) dx dy = \frac{4}{3}.$$

(4.3.15)

The solution of (4.3.5) with boundary conditions (4.3.7) and constraint (4.3.15) results in the determination of the velocity field and the pressure gradient. The component of the

shear stress acting on the wall in the *z*-direction, which is responsible for the drag generation, has the form

$$dF_z = \tau_{xz} n_x + \tau_{yz} n_y,$$

(4.3.16)

where the relevant components of the stress tensor have the form

$$\tau_{xz} = \frac{-1}{Re} \frac{\partial w}{\partial x}, \tau_{yz} = \frac{-1}{Re} \frac{\partial w}{\partial y}.$$

(4.3.17)

The integration of the shear stress over the wetted area gives the total drag. The same drag can be computed using the pressure gradient which is evaluated directly as a part of the solution process. Changes in the drag are expressed as the ratio of the friction factors in the grooved and reference smooth channels, i.e.

$$\frac{f}{f_0} = -0.5 Re \frac{dp}{dz}.$$

(4.3.18)

The reader may note that $f/f_0 < 1$ corresponds to a drag reduction.

4.3.1 Arbitrary grooves

The cost function evaluation requires determination of both the heat transfer per unit length and the friction factor. We wish to determine both quantities with spectral accuracy and, since the solution domain is irregular, we need to use either the immersed boundary condition method (IBC) (see Chapter 2) or the domain transformation method (DT) (Husain & Floryan 2007). The former method uses the physical domain and enforces the flow and temperature boundary conditions as internal constraints. The DT method relies on a transformation that maps the complex geometry onto a rectangular strip with the boundary conditions applied in a classical manner on the edges of this strip. The IBC method is computationally faster but the DT method permits analysis of limiting cases and, thus, is selected for use in the present study. The spatial discretization uses a Fourier expansion in the *x*-direction and Chebyshev expansions in the transverse direction.

The corrugated channel in the physical domain (x, y) is mapped into a smooth channel in the computational domain (η, ξ) using a mapping of the form

$$\xi = \gamma x, \eta = \frac{2[y - y_u(x)]}{y_u(x) - y_L(x)} + 1 \tag{4.3.19}$$

where γ is the adjustment factor. This factor is set to $\gamma = 1$ for the numerical solution but is set to $\gamma = \alpha$ for the analysis of the limit $\alpha \to 0$ where ξ plays the role of a slow scale. The governing equations in (η, ξ) coordinates have the form

$$G_1(\eta, \xi)\frac{\partial^2 \omega}{\partial \eta^2} + G_2(\eta, \xi)\frac{\partial^2 \omega}{\partial \eta \partial \xi} + G_3(\eta, \xi)\frac{\partial \omega}{\partial \eta} + G_4(\eta, \xi)\frac{\partial^2 \omega}{\partial \xi^2} - A = 0. \tag{4.3.20}$$

where ω could represent either the longitudinal velocity component w or the temperature θ. $A = Re^{-1} dp/dz$ in the former case and $A = 0$ in the latter case. The coefficients G_i contain information about the geometry of the grooves and have the form

$$G_1(\eta, \xi) = \eta_x^2 + \eta_y^2, G_2(\eta, \xi) = 2\gamma\eta_x, G_3(\eta, \xi) = \eta_{xx}, G_4(\eta, \xi) = \gamma^2 \tag{4.3.21a-c}$$

where

$$\eta_y = 2[y_u(\xi) - y_L(\xi)]^{-1}, \tag{4.3.22a}$$
$$\eta_x = -[y_u(\xi) - y_L(\xi)]^{-1}\{y_U'(\xi) + y_L'(\xi) + \eta[y_U'(\xi) - y_L'(\xi)]\}, \tag{4.3.22b}$$
$$\eta_{xx} = -[y_u(\xi) - y_L(\xi)]^{-1}\{y_U''(\xi) + y_L''(\xi) + \eta[y_U''(\xi) - y_L''(\xi)] + 2\eta_x[y_U'(\xi) - y_L'(\xi)]\}. \tag{4.3.22c}$$

In the above, the single and double superscripts denote the first and second derivatives with respect to ξ, respectively.

The boundary conditions and the volume flow rate constraint expressed in the (η, ξ) coordinate system assume the form

$$w(1, \xi) = w(-1, \xi) = 0, \tag{4.3.23a, b}$$
$$\theta(1, \xi) = 1, \quad \theta(-1, \xi) = 0, \tag{4.3.24a, b}$$
$$M = \frac{1}{2\lambda_x}\int_{\xi=0}^{\xi=\lambda_x}\int_{\eta=-1}^{\eta=1} w(\eta, \xi)[y_U(\xi) - y_L(\xi)]d\eta d\xi = \frac{4}{3}. \tag{4.3.25}$$

The solution of (4.3.20) is periodic in the ξ-direction and can be represented in terms of a Fourier expansion. The modal functions are discretized using Chebyshev expansions. A system of algebraic equations is developed using separation of modes and the Galerkin projection method. The equations for the two largest coefficients of the Chebyshev expansions for each modal function are replaced with the boundary conditions, i.e. the tau method. The resulting algebraic system is solved using standard solvers.

4.3.2 Long wavelength grooves

The temperature field and the friction factor can be evaluated analytically for the long wavelength grooves. Analytical expressions significantly reduce the cost of optimization and provide an accuracy test for the general solver.

Determination of the solution for the temperature field starts with a transformation in the form of Eq. (4.3.19) with $\gamma = \alpha$. Assume representation of the temperature in the form of an asymptotic expansion

$$\theta(\eta,\xi) = \widehat{\theta}_0(\eta,\xi) + \alpha\widehat{\theta}_1(\eta,\xi) + \alpha^2\widehat{\theta}_2(\eta,\xi) + \alpha^3\widehat{\theta}_3(\eta,\xi) + O(\alpha^4). \tag{4.3.26}$$

Substitution of (4.3.26) into (4.3.20) and (4.3.24a, b) and retention of the four leading-order terms results in the following systems:

$$O(1): \eta_y^2 \frac{\partial^2\widehat{\theta}_0}{\partial\eta^2} = 0, \widehat{\theta}_0(1) = 1, \widehat{\theta}_0(-1) = 0. \tag{4.3.27}$$

$$O(\alpha): \eta_y^2 \frac{\partial^2\widehat{\theta}_1}{\partial\eta^2} = 0, \widehat{\theta}_1(1) = \widehat{\theta}_1(-1) = 0. \tag{4.3.28}$$

$$O(\alpha^2): \eta_y^2 \frac{\partial^2\widehat{\theta}_2}{\partial\eta^2} = -\frac{\eta_x^2}{\alpha^2}\frac{\partial^2\widehat{\theta}_0}{\partial\eta^2} - \frac{\eta_{xx}}{\alpha^2}\frac{\partial\widehat{\theta}_0}{\partial\eta} - \frac{2\eta_x}{\alpha}\frac{\partial^2\widehat{\theta}_0}{\partial\eta\partial\xi} - \frac{\partial^2\widehat{\theta}_0}{\partial\xi^2}, \widehat{\theta}_2(1) = \widehat{\theta}_2(-1) = 0. \tag{4.3.29}$$

$$O(\alpha^3): \eta_y^2 \frac{\partial^2\widehat{\theta}_3}{\partial\eta^2} = -\frac{\eta_x^2}{\alpha^2}\frac{\partial^2\widehat{\theta}_1}{\partial\eta^2} - \frac{\eta_{xx}}{\alpha^2}\frac{\partial\widehat{\theta}_1}{\partial\eta} - \frac{2\eta_x}{\alpha}\frac{\partial^2\widehat{\theta}_1}{\partial\eta\partial\xi} - \frac{\partial^2\widehat{\theta}_1}{\partial\xi^2}, \widehat{\theta}_3(1) = \widehat{\theta}_3(-1) = 0. \tag{4.3.30}$$

The solutions of Eqs. (4.3.27)-(4.3.30) have the form

$$\widehat{\theta}_0(\eta) = \frac{1}{2}(\eta + 1). \tag{4.3.31}$$

$$\widehat{\theta}_1(\eta) = 0. \tag{4.3.32}$$

$$\hat{\theta}_2(\eta,\xi) = -\frac{(\eta^2-1)}{48} \sum_{n=-2N_A}^{2N_A} \sum_{m=-N_A}^{N_A} \left\{ m\left[\eta\left(H_U^{(m)} - H_L^{(m)}\right) + 3\left(H_U^{(m)} + H_L^{(m)}\right)\right] \right.$$
$$\left. \left[mH^{(n-m)} - 2(n-m)\left(H_U^{(n-m)} - H_L^{(n-m)}\right)\right] \right\} e^{in\xi} \tag{4.3.33}$$

$$\hat{\theta}_3(\eta,\zeta) = 0. \tag{4.3.34}$$

where

$$H^{(n)} = \begin{cases} H_U^{(n)} - H_L^{(n)} + 2, & n = 0 \\ H_U^{(n)} - H_L^{(n)}, & n \neq 0 \end{cases}. \tag{4.3.35}$$

A similar solution can be developed for the flow problem (4.3.5), (4.3.7) and (4.3.15) (Mohammadi & Floryan 2013b), resulting in

$$u_0(\eta) = I_1^{-1}\eta_y^{-2}(1-\eta^2), \qquad \frac{dp_0}{dx} = -2Re^{-1}I_1^{-1} \tag{4.3.36a, b}$$

$$u_1(\eta) = 0, \frac{dp_1}{dx} = 0 \tag{4.3.37a, b}$$

$$u_2(\eta) = -I_1^{-1}\eta_y^{-2}\acute{y}_U\acute{y}_L(1-\eta^2) - \frac{I_1^{-1}\eta_y^{-3}}{2}(\eta^2-1) \times$$
$$\left[y_U''\left(\frac{\eta}{3}+1\right) + y_L''\left(\frac{\eta}{3}-1\right)\right] - I_1^{-2}\eta_y^{-2}\left(-I_2 + \frac{I_3}{2} - \frac{I_4}{2}\right)(1-\eta^2), \tag{4.3.38a, b}$$
$$\frac{dp_2}{dx} = 2Re^{-1}I_1^{-2}\left(-I_2 + \frac{I_3}{2} - \frac{I_4}{2}\right)$$

$$u_3(\eta) = 0, \qquad \frac{dp_3}{dx} = 0 \tag{4.3.39a, b}$$

where

$$I_1 = \frac{1}{2\pi}\int_{\xi=0}^{\xi=2\pi} \eta_y^{-3}d\xi, I_2 = \frac{1}{2\pi}\int_{\xi=0}^{\xi=2\pi} \eta_y^{-3}y_U'y_L'd\xi,$$
$$I_3 = \frac{1}{2\pi}\int_{\xi=0}^{\xi=2\pi} \eta_y^{-4}y_U''d\xi, I_4 = \frac{1}{2\pi}\int_{\xi=0}^{\xi=2\pi} \eta_y^{-4}y_L''d\xi. \tag{4.3.40}$$

The friction factor can be evaluated as

$$\frac{f}{f_0} = I_1^{-1}[1 + 0.5\alpha^2 I_1^{-1}(2I_2 - I_3 + I_4)]. \tag{4.3.41}$$

The above solutions provide acceptable accuracy for $\alpha < 0.6$ as shown in Mohammadi & Floryan (2013b) and confirmed by comparisons with the numerical solutions determined using method described in Section 4.3.1 (Figure **4-2** and Figure **4-7**).
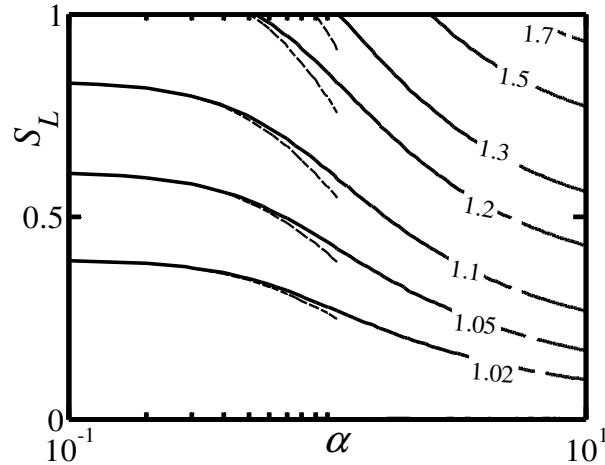
Figure 4-2: *Variation of Q/Q_0 as a function of the groove amplitude S_L and the wave number α for the geometry described by Eq. (4.4.1). Dashed lines identify asymptotic values for $\alpha \to 0$.*

4.4 Transport mechanisms

Conduction is the only transport mechanism available for energy transfer across the channel. As the first step, we shall assess how the presence of the grooves affects this process. Consider a channel with sinusoidal grooves at the lower wall and a smooth upper wall. The geometry is described as

$$y_L(x) = -1 + S_L \cos(\alpha x), \qquad y_U(x) = 1 \tag{4.4.1}$$

where S_L and α denote the groove amplitude and the wave number, respectively. Variations of Q/Q_0 as a function of S_L and α displayed in Figure **4-2** demonstrate that an increase of both S_L and α lead to the enhancements of the heat flow. For small α the heat flow can be approximated analytically as

$$\frac{Q}{Q_0} = \frac{6 + 2\alpha^2 S_L^2 - 8\alpha^2}{3\sqrt{(2 - S_L)(2 + S_L)}} + \frac{4\alpha^2}{3} \tag{4.4.2}$$

where the range of applicability of (4.4.2) can be judged from the data presented in Figure **4-2**.
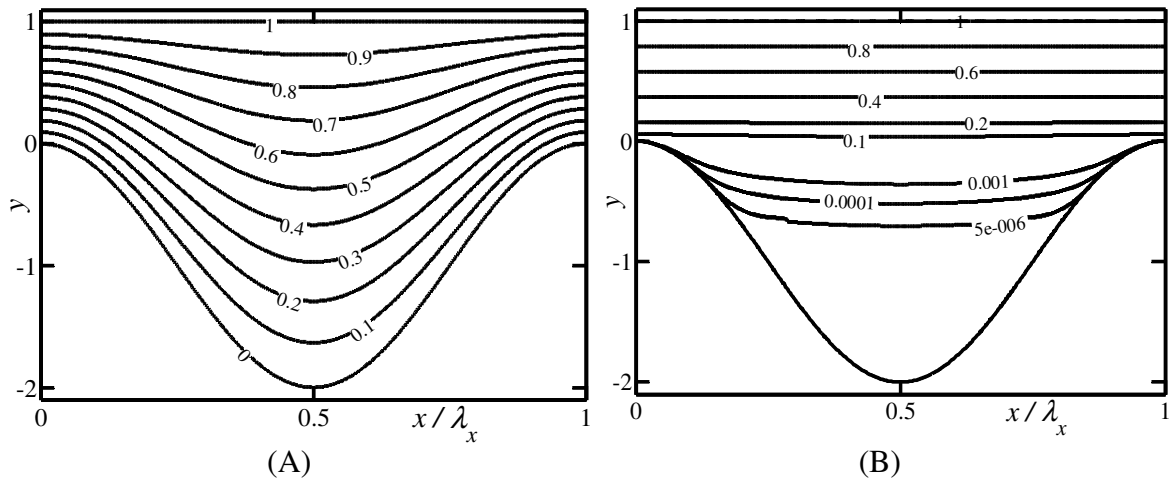
Figure 4-3: *Temperature distribution inside the channel for the grooves described by Eq. (4.4.1) with the amplitude $S_L = 1$ and the wave number $\alpha = 0.5$ (Figure **4-3**A) and $\alpha = 30$ (Figure **4-3**B).*

The form of the temperature field is illustrated in Figure **4-3** for two extreme values of the wave number, i.e. $\alpha = 0.5$ and $\alpha = 30$. The isotherms fill in the slot uniformly for small α (Figure **4-3**A) but the troughs become nearly isothermal for large α (Figure **4-3**B). This effect is well illustrated in Figure **4-4** which displays the temperature variations across the channel at its widest opening. The formation of an isothermal zone in the trough as α increases is clearly visible.

The heat flow pattern can be deduced from distributions of the local heat flux q along the walls displayed in Figure **4-5** as well as from changes of the wetted area displayed in Figure **4-6**. For small α the heat flux at the grooved wall increases above the smooth-wall value around the groove tips and decreases around the troughs; the increase is more pronounced than the decrease (see Figure **4-5**A) resulting in an overall increase of the heat flow. A similar process takes place at the upper wall (see Figure **4-5**B). An increase of α makes the differences between q at the groove tip and q at groove trough more pronounced at the grooved wall.
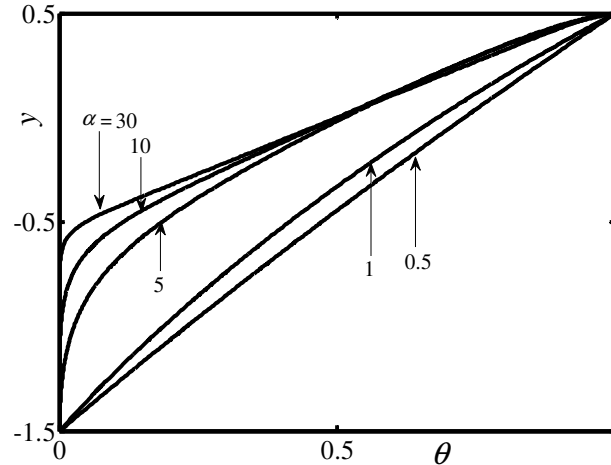
Figure 4-4: *Temperature profiles at $x = \lambda_x/2$ for the grooves described by Eq.* (4.4.1) *with the amplitude $S_L = 1$.*

For a large enough α the heat flux disappears altogether at the troughs, with the width of the thermally inactive zone (measured by % of the wavelength) increasing with α. Peaks of q form at the groove tips, with their magnitude rapidly increasing with α. The process of re-arrangement of q at the upper wall is qualitatively different, with q becoming nearly constant for a large enough α. The overall increase of the heat flow can be easily deduced from Figure **4-5**B, in agreement with the data presented in Figure **4-2**.

(A)

(B)
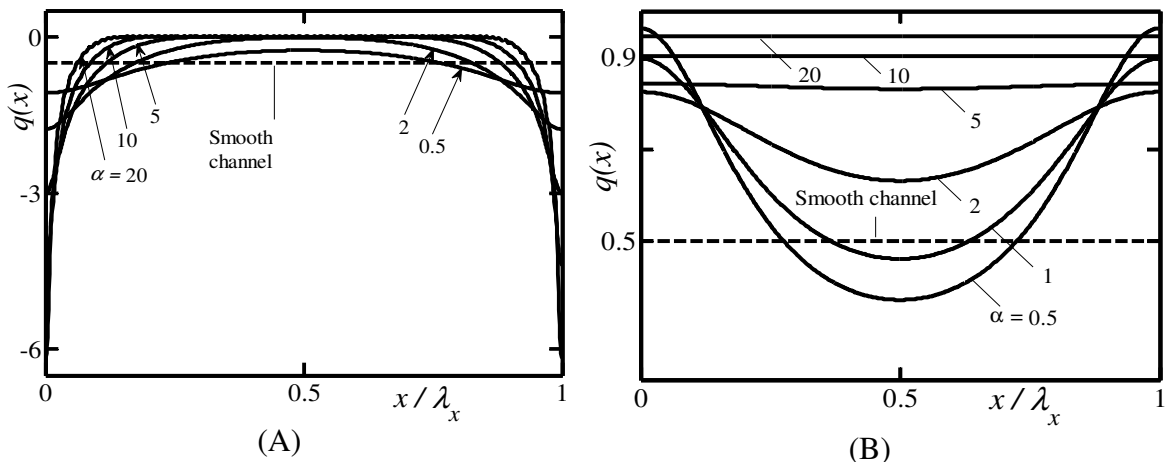
Figure 4-5: *Distributions of the local heat flux at the lower (Figure **4-5**A) and upper (Figure **4-5**B) walls for grooves described by Eq. (4.4.1) with the amplitude $S_L = 1$.*

Comparison of Figure **4-2**, Figure **4-5** and Figure **4-6** demonstrates that the heat flow increase occurs primarily due to a high concentration of the heat flux around the groove

tips and reduction of distance between the tips and the opposite wall; this heat flow becomes uniformly distributed when it reaches the smooth wall. Changes in the wetted surface area contribute marginally to the increase of the heat flow for small α and are irrelevant for large α.
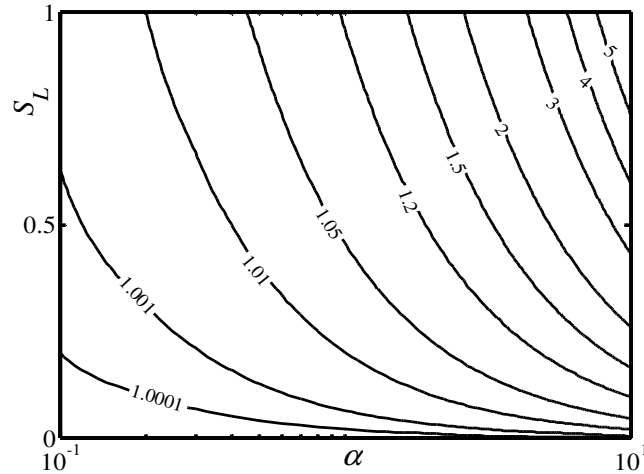
Figure 4-6: *Variations of the wetted surface area A/A_0 (see Eq. (4.3.13)) as a function of the groove amplitude S_L and the wave number α for the groove geometry described by Eq. (4.4.1).*

The presence of grooves affects the flow characteristics and this question has been studied for annular and planar flows in detail in Chapter 3 and Mohammadi & Floryan (2013a), respectively. It is useful to summarize the main observations before proceeding with the optimization question. The following discussion is carried out in the context of the same grooves as those used for discussion of conduction, i.e. the channel geometry is described by Eq. (4.4.1). Variation of f/f_0 as a function of α and S_L is illustrated in Fig. 7. For small α this variation is captured analytically (see Mohammadi & Floryan 2013b) in the form

$$\frac{f}{f_0} = \left(1 + \frac{3}{8}S_L^2\right)^{-2}\left[1 + \frac{S_L^2}{2}\left(\alpha^2 + \frac{3}{4}\right) + \frac{3\alpha^2}{32}S_L^4\right]. \tag{4.4.3}$$

The range of validity of this expression can be determined from the data presented in Figure **4-7**. The presence of grooves can result in either a reduction or an increase of the

drag. The reduction occurs for $\alpha < \alpha_c \approx 1$ where α_c is referred to as the critical wave number. The magnitude of α_c depends marginally on the groove amplitude while the magnitude of f/f_0 increases with an increase of the amplitude.
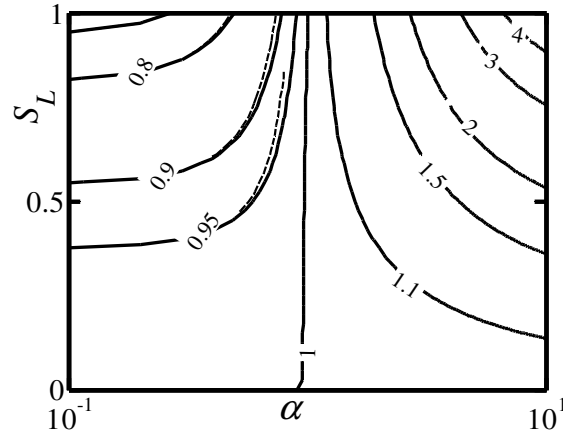
Figure 4-7: *Variation of f/f_0 as a function of the groove amplitude S_L and the wave number α for the geometry described by Eq. (4.4.1). Dashed lines identify asymptotic values for $\alpha \to 0$.*

The form of the velocity field shown in Figure **4-8** demonstrates that for small enough α the bulk of the flow takes place in the area corresponding to the widest channel opening, where formation of a flow tube with $w > 1$ is observed. This flow tube becomes elongated as α increases, its strength decreases and it completely disappears for $\alpha > 5$.
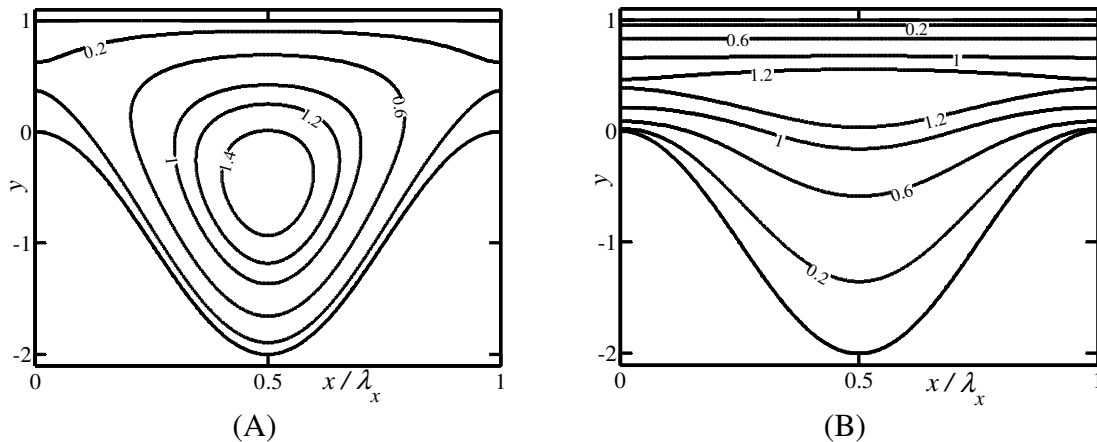
Figure 4-8: *Distribution of the w - velocity component for grooves described by Eq. (4.4.1) with amplitude $S_L = 2$ and the wave numbers $\alpha = 0.5$ (Figure **4-8**A) and $\alpha = 5$ (Figure **4-8**B).*

Figure **4-9** shows distributions of the shear stress along the walls. When $\alpha \leq \alpha_c$, the maximum of the stress at the grooved wall occurs at locations corresponding to the maximum channel opening and its magnitude decreases when $\alpha \to \alpha_c$ from below (see Figure **4-9**A). A further increase of α changes the qualitative character of the distribution, with the maxima occurring at the groove tips and their magnitude increasing with α. The distribution of the stress at the smooth wall is approximately sinusoidal, with the maximum always occurring above the trough. Increase of α results in a decrease of the stress' amplitude (see Figure **4-9**B); the stress becomes nearly constant for high enough α with its magnitude being larger than in the smooth channel.
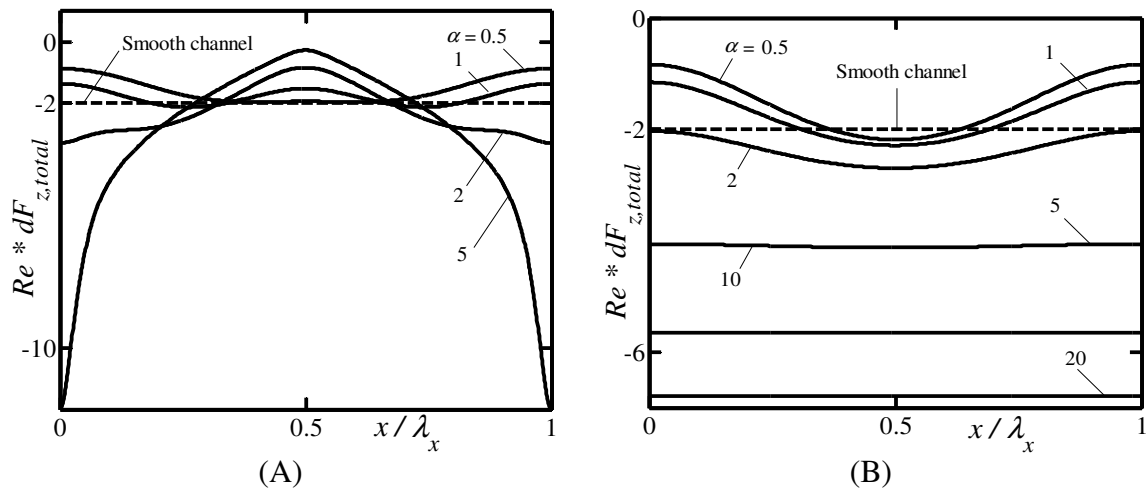
Figure 4-9: *Distribution of the z-component of shear acting at the lower ($Figure$ **4-9**A) and upper ($Figure$ **4-9**B) walls for grooves described by Eq. (4.4.1) with amplitude $S_L = 1$.*

The interplay between the heat flow and the flow resistance can be deduced from Figure **4-10** which displays variations of the heat flow and the friction factor as a function of α. While an increase of α leads to an increase of both Q/Q_0 and f/f_0, the variations of the friction factor are more pronounced, e.g. $f/f_0 \approx 7$ but $Q/Q_0 \approx 1.8$ when $\alpha = 30$. This observation is important for interpretation of the optimization results.

The above discussion is based on the analysis of grooves with shapes expressed by a single sinusoid. Grooves with more complex shapes may have different characteristics.

An arbitrary shape is expressed by Eq. (4.2.1a, b), which permits assessment of the role played by geometry details described by higher Fourier modes.
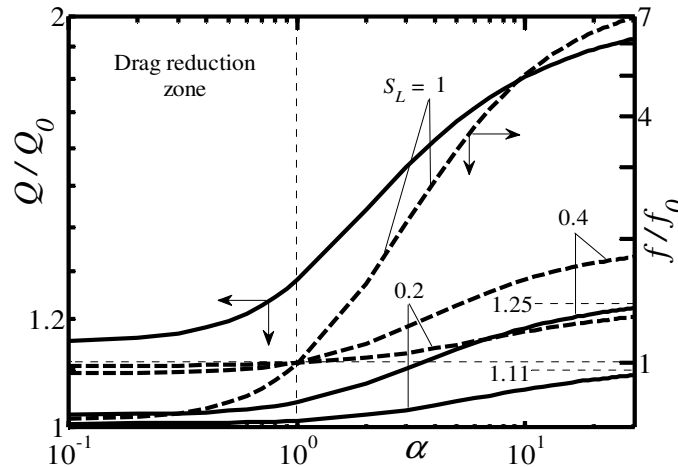
Figure 4-10: *Variations of the f/f_0 and Q/Q_0 for a channel with geometry described by Eq. (4.4.1) as a function of the groove wave number α.*

It has been shown in Chapter 3 that the reduced geometry model, where the actual shape is replaced by the leading Fourier mode from the corresponding Fourier expansion, captures flow losses with accuracy sufficient for most applications. The results described above apply, therefore, to prediction of flow losses for grooves with arbitrary shapes as long as such shapes can be expressed using Fourier expansions. The analysis of heat transfer, discussed above, demonstrates that the same concept does not apply to conduction. The heat transfer increases with an increase of α and, thus, inclusion of geometry details described by higher Fourier modes significantly alters the heat flow. As a result, the geometry cannot be simplified and the effect of the actual groove shape has to be analyzed on a case-by-case basis. The determination of the shape that provides the best overall system performance is discussed in the next section.

4.5 Optimization

It is assumed that the wavelength of the grooves has been selected but that their "best" shape remains to be determined. The "best" shape corresponds to the minimum of Ω

which may depend on the weighting factor β. Large β favors the minimization of flow losses, small β favors the maximization of heat transport. We shall discuss the suitable selection of β later in this Section.

It is instructive to explain geometry optimization using the real variables, i.e.

$$y_L(x) = -1 + \sum_{n=1}^{N_A} A_{n,L} \cos(n\alpha x + \varphi_{n,L}),$$
$$y_U(x) = 1 + \sum_{n=1}^{N_A} A_{n,U} \cos(n\alpha x + \varphi_{n,U}). \tag{4.5.1a, b}$$

The optimization yields the amplitudes $A_{n,L}$, $A_{n,U}$ and phase differences $\varphi_{n,L}$, $\varphi_{n,U}$. The symmetry arguments as well as the direct evaluations of Ω permit elimination of the effects of phase differences, i.e. the optimal shapes always correspond to the zero phase difference. The problem is, thus, reduced to finding the minimum of

$$\Omega = \Omega\big(A_{1,L}, \dots, A_{N_A,L}, A_{1,U}, \dots, A_{N_A,U}, \beta\big). \tag{4.5.2}$$

Since Eq. (4.5.1a, b) defines an uncountable number of geometries, the optimization is carried out by selecting classes of geometries that are of practical interest. This is done by imposing constraints in the form of the maximum permissible depths and the maximum permissible heights of the grooves, as measured from the reference smooth wall position. These constraints have the form

$$\max\left(\sum_{n=1}^{N_A} A_{n,L} \cos(n\alpha x)\right) \leq S_L, \quad \min\left(\sum_{n=1}^{N_A} A_{n,L} \cos(n\alpha x)\right) \geq -S_L, \tag{4.5.3a}$$

$$\max\left(\sum_{n=1}^{N_A} A_{n,U} \cos(n\alpha x)\right) \leq S_U, \quad \min\left(\sum_{n=1}^{N_A} A_{n,U} \cos(n\alpha x)\right) \geq -S_U. \tag{4.5.3b}$$

The solution of the optimization problem assumes that the optimal shape can be expressed in terms of Fourier expansions (4.5.1a, b) which need to have a sufficient rate of convergence in order to yield a practical solution. This fact brings in the importance of

the weighting factor β. The results discussed in the previous section demonstrate that the largest heat transport corresponds to the highest Fourier mode admitted in the solution. The use of small β gives preference to the heat transport and this leads to the divergence of the Fourier series. It may be concluded immediately that under such conditions the highest Fourier mode admitted in the solution defines the optimal shape. The use of large β gives preference to flow losses. Numerical experiments indicate that the optimal shape does not depend on β if $\beta > 0.15$, which corresponds to the elimination of the dominance of the heat transport process. All of the results reported in the remainder of this paper have been, therefore, obtained with $\beta = 1$ which provides a balance between the heat transport and the flow losses. $\Omega = 2$ corresponds to a smooth channel and improvements is system performance are signaled by $\Omega < 2$.
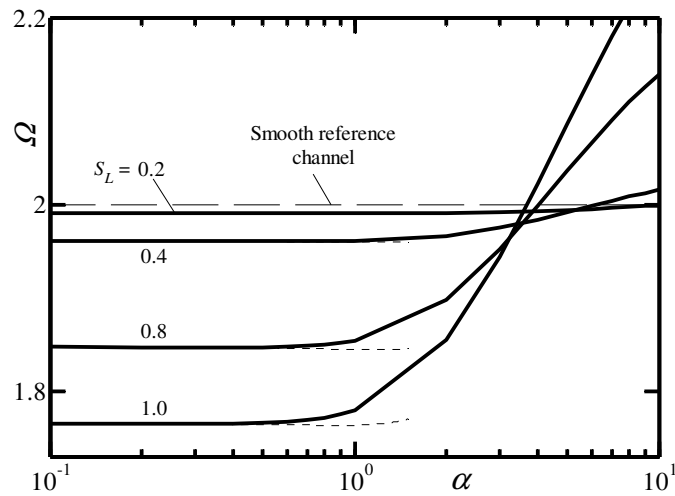
Figure 4-11: *Variations of the thermal enhancement factor Ω for a channel with geometry described by Eq. (4.4.1) as a function of the groove wave number α.*

Figure **4-11** displays variations of Ω for the simple geometry defined by Eq. (4.4.1). The asymptote for small α has the form

$$\Omega = \left[\frac{6 + 2\alpha^2 S_L^2 - 8\alpha^2}{3\sqrt{(2 - S_L)(2 + S_L)}} + \frac{4\alpha^2}{3}\right]^{-1}$$

$$+ \left(1 + \frac{3}{8}S_L^2\right)^{-2/3}\left[1 + \frac{S_L^2}{2}\left(\alpha^2 + \frac{3}{4}\right) + \frac{3\alpha^2}{32}S_L^4\right]^{1/3}.$$

(4.5.4)

The best system performance (smallest Ω) can be found for $\alpha < 1$, which corresponds to the drag reducing grooves. Such grooves represent the focus of the shape optimization. Ω quickly rises when the wave number increases above $\alpha = 1$ and it increases above the reference values of $\Omega = 2$ for $\alpha > 3$. The system performance significantly improves with an increase of the amplitude S_L but only when $\alpha < 3$ since the trend is reversed for larger α.

The convergence properties of the Fourier series defining the optimal shape are illustrated using a channel with the geometry of the lower wall represented by (4.5.1a, b) while keeping the upper wall smooth. The results for the friction factor presented in Figure **4-12**A demonstrate a rapid convergence of the expansion. A reduced order model based on 3-4 Fourier modes can capture the optimal shape with an accuracy sufficient for most applications. The results for the heat transfer show divergence of the Fourier expansions (not shown), as discussed above.

The results of tests for the thermal enhancement factor displayed in Figure **4-12**B demonstrate a rapid convergence of the Fourier series. The use of five Fourier modes allows approximation of the optimal shape with less than 5% error for the thermal enhancement factor. It may be concluded that the reduced geometry model based on the Fourier expansions can be used for determination of the optimal groove shape. The computational cost of optimization rapidly increases with an increase in the number of parameters. The optimizer minimizes a scalar multivariable cost function subject to a set of constraints starting at a given initial guess. The search method is gradient-based and, therefore, requires the cost and constraint functions to both be continuous and to have continuous first derivatives. The 'interior-point' optimization algorithm tries to satisfy bounds at every iterations (Byrd *et al.* 1999; 2000; Waltz *et al.* 2006) but it cannot guarantee identification of the global minimum. In order to minimize the probability of becoming trapped in a local minimum, one should start optimization with a small number of Fourier coefficients, say 3 or 4.
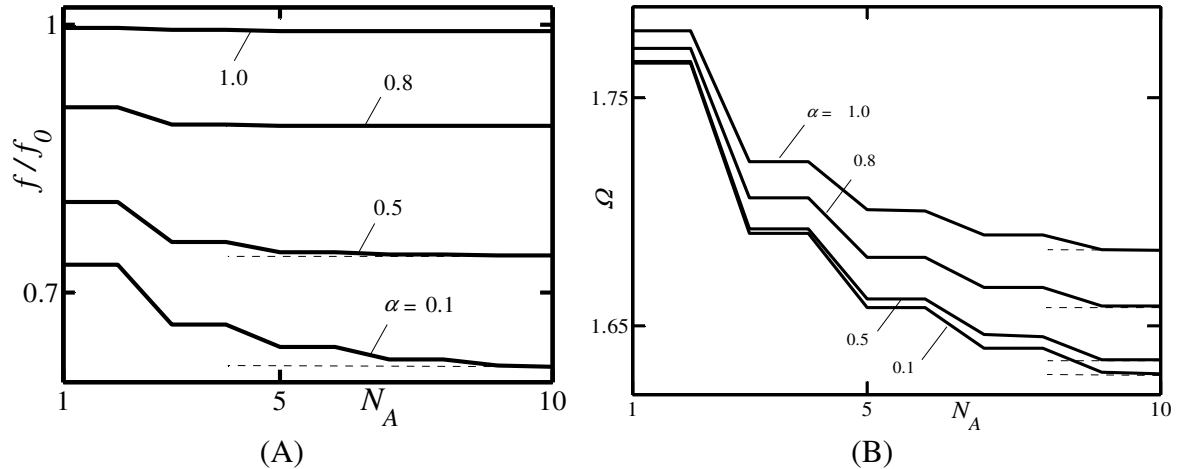
Figure 4-12: *Variations of the normalized friction factor f/f_0 and the thermal enhancement factor Ω for the equal-depth grooves with amplitude $S_L = 1$ as a function of the number of Fourier modes N_A used in the description of the groove geometry.*

When the solution converges, the number of Fourier coefficients is increased by one and the search is restarted using the most recent solution as the initial approximation and zero for the additional mode. This process is continued until a satisfactory approximation of the optimal shape is determined. This permits determination of the optimal shape even when the direct optimization fails. The question of identification of the global minimum has been confirmed by computing Ω directly for a number of test cases without the use of the optimization algorithm. Most of the results presented in this paper have been obtained with the convergence criteria set at 10^{-6} and using ten Fourier modes for geometry description as a precaution.

4.6 Results

Two classes of shapes have been considered, i.e. the equal-depth grooves and the unequal-depth grooves. In the former case, the grooves have the same maximum depth and height. In the latter case, the depth and height are different. We shall start discussion with the former case.

4.6.1 The equal-depth grooves

The equal-depth constraints are expressed by Eq. (4.5.3). The optimal configuration always corresponds to the largest admissible amplitude and, thus, the inequalities in (4.5.3) can be replaced by the equalities. We start the discussion with the grooves placed on the lower wall only (the upper wall is smooth). The evolution of the optimal shape as a function of the groove depth S_L is illustrated in Figure **4-13**. There are no significant differences between the shapes obtained for different α's and S_L's. All these shapes can be approximated by a universal trapezoid characterized by $a = b = \lambda/11$ and $c = d = 4.5\lambda/11$ (see Figure **4-13** for definitions of the symbols).
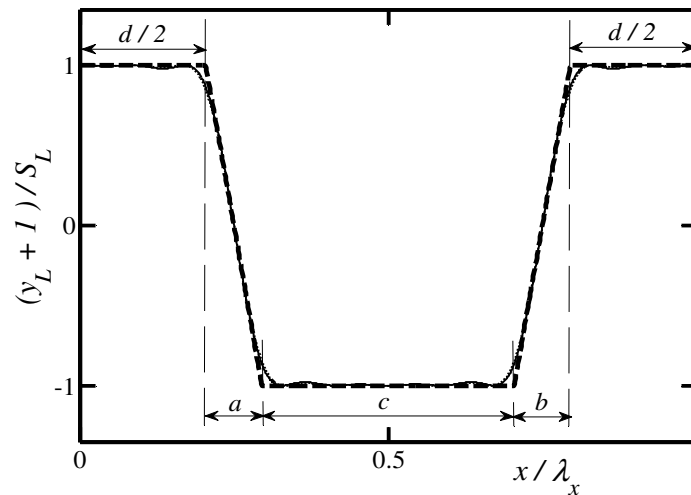
Figure 4-13: *The optimal shapes of the equal-depth grooves. Solid line identifies a groove with $S_L = 0.4$ and $\alpha = 0.1$, whilst dotted line is for $S_L = 1.6$ and $\alpha = 1$. The y-coordinate is scaled using the groove depth. Thick line illustrates the best-fitted trapezoid characterized by $a = b = \lambda/11$ and $c = d = 4.5\lambda/11$.*

Velocity isolines displayed in Figure **4-14**A for $\alpha = 0.1$ and $S_L = 0.4$ demonstrate that the stream tubes are more pronounced when one uses optimal grooves compared with the sinusoidal grooves. This leads to smaller velocity gradients at the walls and, thus, smaller shear stress. Variation of the shear stress shown in Figure 4-14B demonstrates reduction of its mean value for the optimal grooves compared with the sinusoidal grooves.

Variations of Q/Q_0, f/f_0 and Ω for the optimal grooves approximated by the universal trapezoid as a function of α and S_L are illustrated in Figure **4-15**, and the corresponding changes of the wetted surface area are illustrated in Figure **4-16**. The heat transfer is enhanced by increasing S_L and is nearly independent of α (Figure **4-15**A); this correlates with the increase of the wetted area associated with increase of S_L but does not correlate with the increase of the wetted area due to increase of α (see Figure **4-16**). The critical wave number α_c required to achieve drag reduction depends on the groove amplitude (Figure **4-15**B).

(A)   (B)
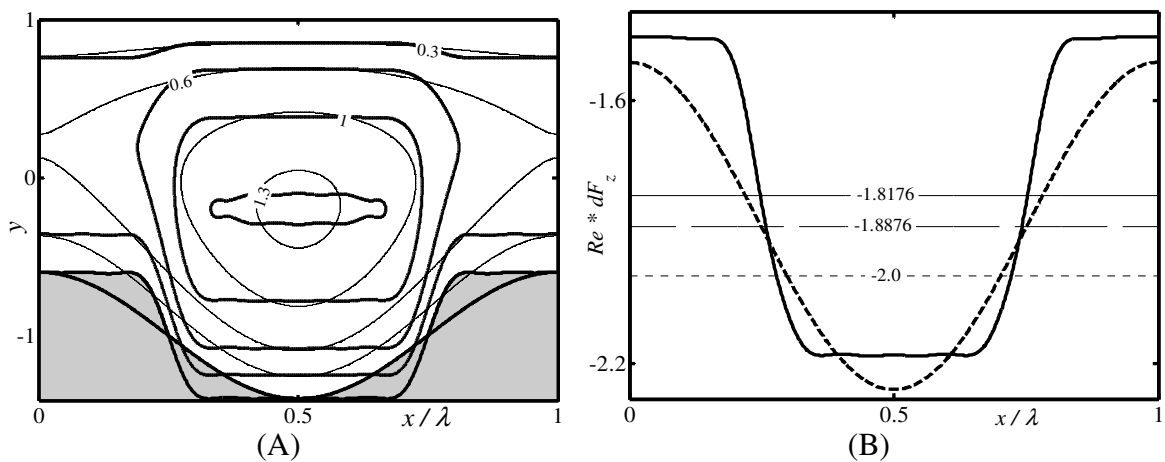
Figure 4-14: *Velocity isolines for the equal-depth optimal grooves (thick lines) and for the sinusoidal grooves (thin lines) with $S_L = 0.4$, $\alpha = 0.1$ are shown in Figure* **4-14***A. Distributions of the shear stress acting on the fluid at the lower wall for the same grooves are shown in Figure* **4-14***B. Solid, dashed and dotted lines in Figure* **4-14***B correspond to the optimal groove, the sinusoidal groove and the reference smooth wall. The corresponding total shear forces are -1.8173, -1.8878 and −2.*

The flow losses are reduced by decreasing α below α_c and by increasing S_L. Increase of the wetted area actually decreases pressure losses. The overall system performance becomes better for smaller α and larger S_L and a significant reduction of Ω below the smooth-channel value can be readily achieved. Increase of Ω correlates with increase of the wetted area due to increase of S_L but changes of the wetted area due to variations of α have almost no effect on Ω. The same figure displays performance improvements for the simple sinusoidal grooves. The optimized grooves offer about 30% advantage over sinusoidal grooves, with the gain increasing for higher groove depths.

Replacing the actual optimal shape by the universal trapezoid can produce an error. Figure **4-17** shows that this error is negligible for most of applications and, thus, the universal trapezoid can be assumed to represent the optimal shape. This conclusion underlines the generality of the results as there is no need to carry out any additional optimization studies.
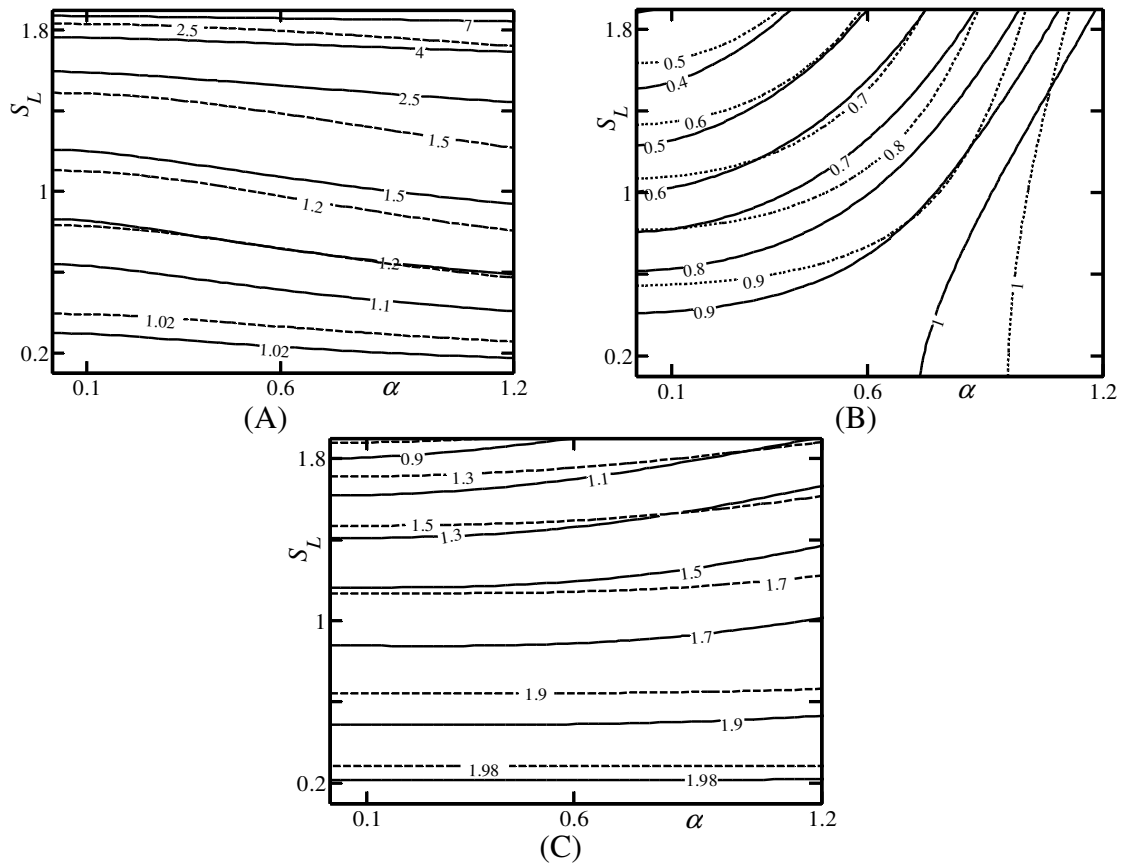
Figure 4-15: *Variations of the normalized heat transfer per unit length Q/Q_0 (Figure **4-15***A),*
*the normalized friction factor f/f_0 (Figure **4-15***B) and the thermal enhancement factor Ω*
*(Figure **4-15***C) as a function of the groove wave number α and the groove depth S_L for a*
channel with the lower wall fitted with the equal-depth grooves approximated by a trapezoid with
$a = b = \lambda/11$, $c = d = 4.5\lambda/11$ and a smooth upper wall. Dashed lines identify results for
the simple sinusoidal grooves.

Constraints corresponding to identical grooves placed on both walls are described by (4.5.3a) with $S_L = S_U$. The optimal shapes are displayed in Figure **4-18**. These shapes are

described by the universal trapezoid with $a = b = 1.25\lambda/11$, $c = d = 4.25\lambda/11$, i.e. they are nearly the same as in the case of grooves placed on one wall. Grooves on the opposite walls are shifted by a half wavelength with respect to each other.
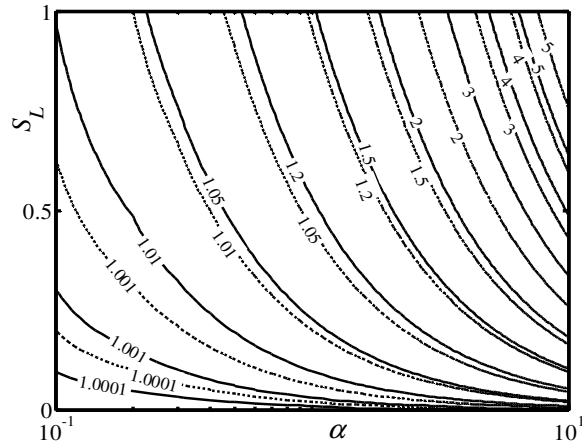
Figure 4-16: *Variations of the wetted surface area A/A_0 (see Eq.(4.3.13)) as a function of the groove wave number α for the same grooves as used in Figure **4-15**. Dashed lines identify results for the simple sinusoidal grooves.*
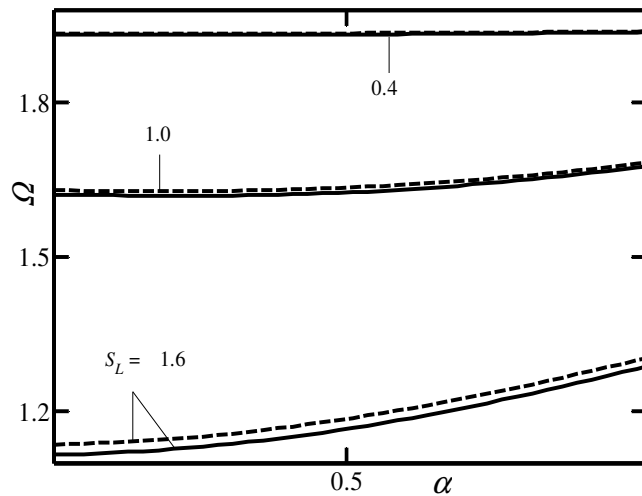
Figure 4-17: *Variations of the thermal enhancement factor as a function of the groove wave number α for the equal-depth grooves located on the lower wall. Solid and dashed lines correspond to grooves with the optimal and trapezoidal shapes, respectively.*
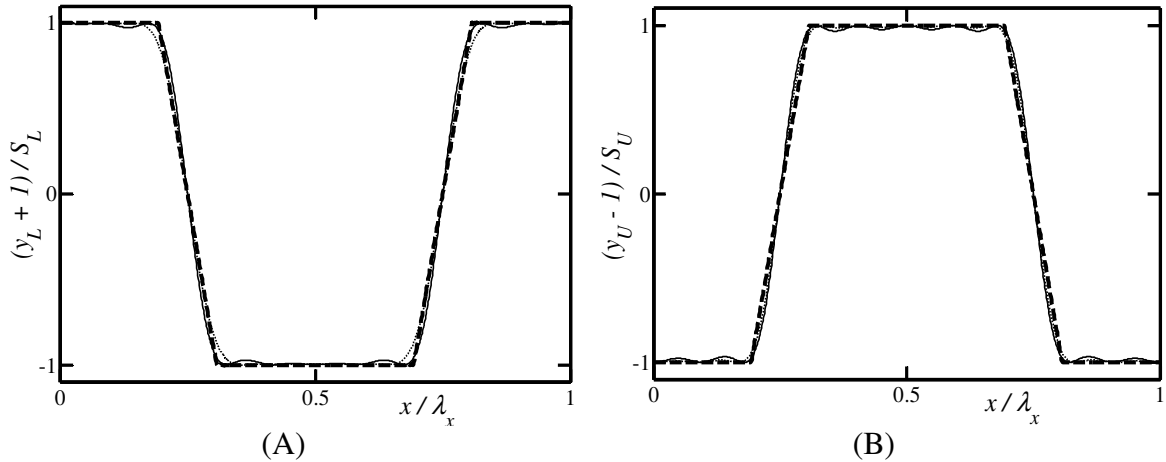
Figure 4-18: *The optimal shapes for the equal depth grooves placed on both walls. Solid line identifies $S_L = S_U = 0.2$ and $\alpha = 0.1$, whilst dotted line is for $S_L = S_U = 0.5$ and $\alpha = 1$. Thick lines illustrate the best-fitted trapezoids with $a = b = 1.25\lambda/11$ and $c = d = 4.25\lambda/11$.*
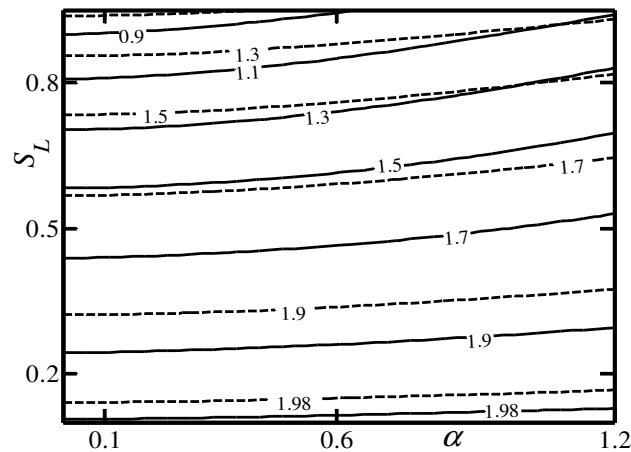
Figure 4-19: *Variations of the thermal enhancement factor Ω as a function of the groove wave number α and the groove depth S_L for a channel with the lower and upper walls fitted with the equal-depth grooves approximated by a trapezoid with $a = b = 1.25\lambda/11$ and $c = d = 4.25\lambda/11$. Both sets of grooves have identical geometries with the upper grooves moved by a half wavelength with respect to the lower grooves. Results for the simple sinusoidal grooves are illustrated using dashed lines.*

The variations of Ω as a function of S_L and α for grooves approximated by the trapezoid are shown in Figure **4-19**. It can be seen that the same Ω can be achieved either by working with the grooves placed on one wall or by working with the grooves with the amplitude reduced by 50% but placed on both walls. The results for simple sinusoidal

grooves displayed in the same figure illustrate the gains associated with the use of optimized grooves.

4.6.2 The unequal-depth grooves

Unequal-depth grooves may have different depth and height, and the relevant constraints have the form

$$\max\left(\sum_{n=1}^{N_A} A_{n,L}cos(n\alpha x)\right) \leq S_{L,max}, \qquad \min\left(\sum_{n=1}^{N_A} A_{n,L}cos(n\alpha x)\right) \geq -S_{L,min}, \qquad (4.6.1a, b)$$

$$\max\left(\sum_{n=1}^{N_A} A_{n,U}cos(n\alpha x)\right) \leq S_{U,max}, \qquad \min\left(\sum_{n=1}^{N_A} A_{n,U}cos(n\alpha x)\right) \geq -S_{U,min}. \qquad (4.6.2a, b)$$

The optimal shape always corresponds to the largest permitted groove height and depth and, thus, the inequalities in (4.6.1a, b) and (4.6.2a, b) can be replaced by equalities. We begin the discussion by considering grooves placed only on one wall, i.e. $S_{U,max} = S_{U,min} = 0$. Figure **4-20** shows variations of the thermal enhancement factor for grooves with the height $S_{L,max} = 1$ and different depths. It can be seen that Ω decreases monotonically for the range of $S_{L,min}$ considered when $\alpha \leq 0.2$. Ω changes in a non-monotonic manner for larger values of α and this documents the existence of a depth that gives the rise to the smallest Ω, i.e. the optimal depth D_{opt}. The optimal depth decreases when α increases.

Figure **4-21** illustrates the evolution of shape of the optimal grooves as a function of depth for a fixed height. It can be seen that for $S_{L,min} < S_{L,max}$ the optimal shape looks like a trapezoid but with a longer base than the universal trapezoid for the equal-depth grooves. The increase of $S_{L,min}$ above $S_{L,max}$ leads to the trapezoid morphing into a qualitatively different form. The same figure shows shapes corresponding to the optimal depth.
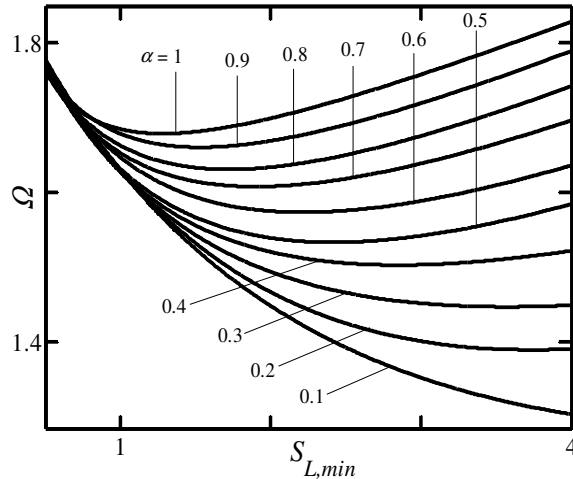
Figure 4-20: *Variations of the thermal enhancement factor Ω for a channel with the smooth upper wall and the optimal grooves with height $S_{L,max} = 1$ placed at the lower wall as a function of the depth of the grooves $S_{L,min}$.*

The combination of the optimal depth and the corresponding optimal shape is referred to as the optimal geometry. The evolution of the optimal geometry is illustrated in Figure **4-22**. The same shapes rescaled using the groove width at half height W_{half} are displayed in Figure **4-23**A. It can be seen that all the shapes nearly overlap and can be approximated by a Gaussian function in the form $y(x) = -exp(-3.5x^2)$ which defines the universal shape. The variations of D_{opt} and W_{half} required to relate the universal shape to the channel size are shown in Figure **4-23**B. The magnitude of the thermal enhancement factor that can be achieved using the optimal geometry is illustrated in Figure **4-24**.

(A)

(B)

(C)
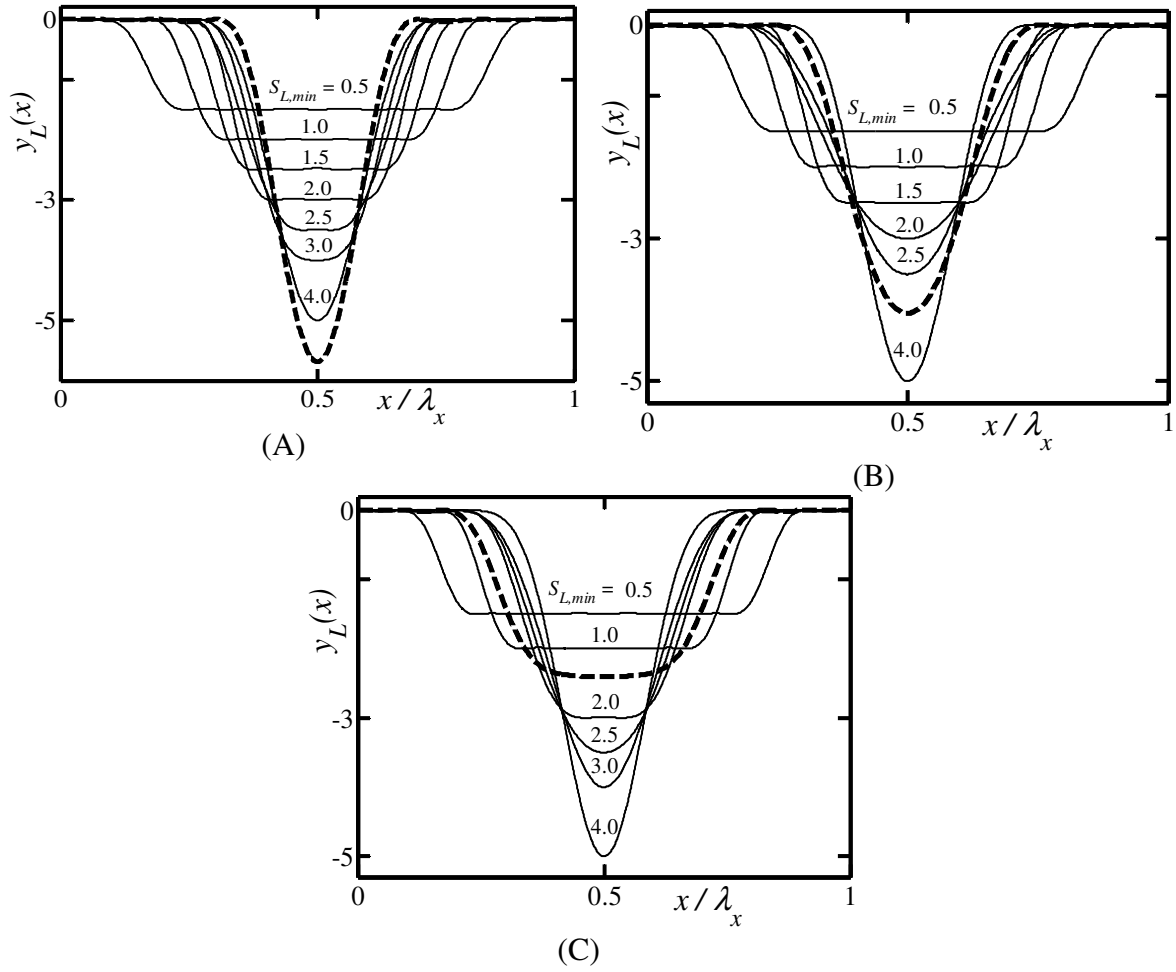
Figure 4-21: *Evolution of the shape of the optimal, unequal-depth grooves with height $S_{L,max} = 1$ placed on the lower wall as a function of the groove depth $S_{L,min}$. Results for $\alpha = 0.1, 0.5, 1$ are displayed in Figure **4-21**A, B and C, respectively. Dashed lines identify shapes corresponding to the optimal depth.*
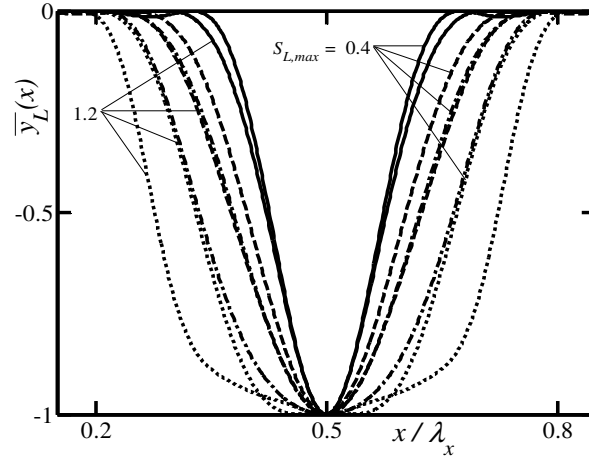
Figure 4-22: *Shapes of the unequal-depth grooves with height $S_{L,max}$ corresponding to the optimal depth placed at the lower wall. The y-coordinate is scaled using the groove peak-to-bottom distance $\bar{y}_L(x) = [y_L(x) - S_{L,min}]/(S_{L,max} - S_{L,min}) - 1$. Solid, dashed, dash-dotted, and dotted lines correspond to $\alpha = 0.1, 0.5, 0.8, 1.0$, respectively.*
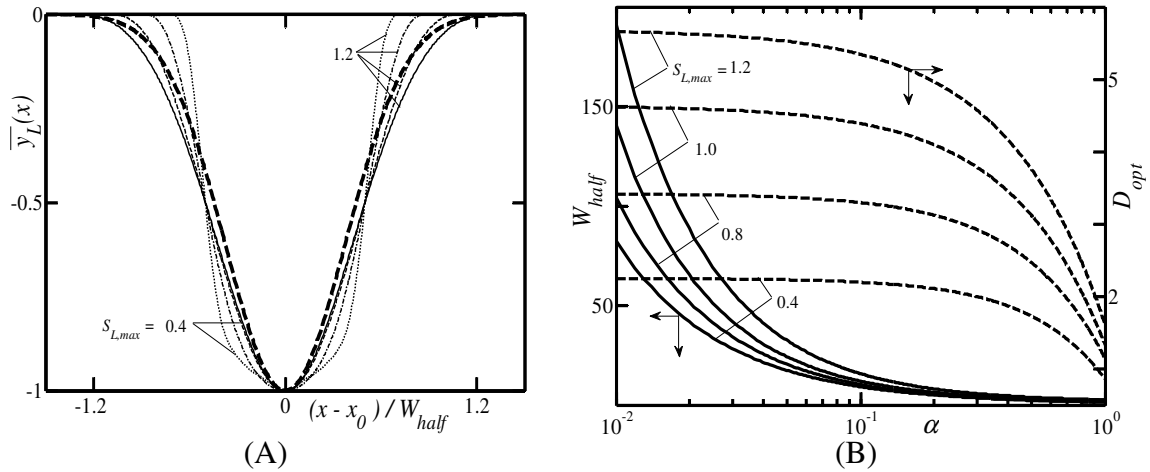
Figure 4-23: *Shapes of the grooves displayed in Figure **4-22** scaled in the x-direction with the groove width at half height W_{half} (Figure **4-23**A). Solid, dashed, dash-dotted, and dotted lines correspond to $\alpha = 0.1, 0.5, 0.8, 1.0$, respectively. Thick dashed line identifies the universal shape $\bar{y}(\bar{x}) = -exp(-3.5\bar{x}^2)$. Variations of the optimal depth D_{opt} and the corresponding width at half height W_{half} as a function of the groove wave number α are displayed in Figure* **4-23**B.
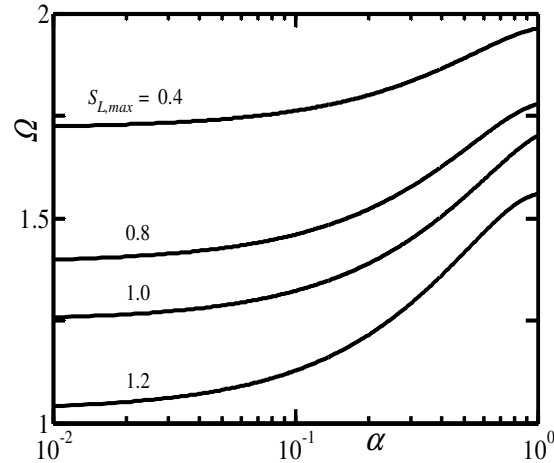
Figure 4-24: *Variations of the thermal enhancement factor Ω for the optimal geometry with grooves placed on only one wall.*

(A)   (B)
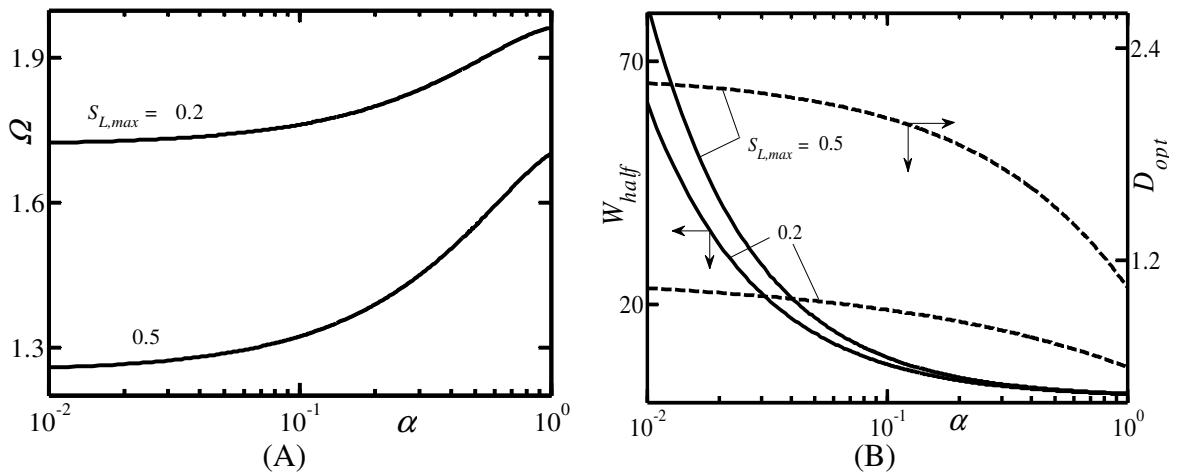
Figure 4-25: *Variations of the thermal enhancement factor Ω (Figure **4-25**A) and the corresponding optimal depth D_{opt} and the width at half height W_{half} (Figure **4-25**B) as a function of the groove wave number α for the optimal geometry with grooves placed on both walls and moved by half wavelength with respect to each other.*

The results displayed in Figure **4-25** correspond to grooves placed at both walls and moved by half wavelength with respect to each other. The constraints (4.6.1a, b) and (4.6.2a, b) have fixed $S_{U,min}=S_{L,max}$ while $S_{L,min}$ and $S_{U,max}$ are determined by the optimization process and, thus, correspond to the optimal depth. The optimal depth and

the corresponding groove shape for grooves at both walls are nearly the same as for grooves placed at only one wall. The placement of grooves at both walls produces nearly the same change in the thermal enhancement factor as placement of grooves at one wall only but with a double height (compare Figure **4-24** and Figure **4-25**A). The optimal depth D_{opt} and the width at half height W_{half} are nearly the same regardless of whether one or both walls are grooved (compare Figure **4-23**B and Figure **4-25**B).

4.7 Summary

When mixing augmentation is not available, heat can be transported across micro-channels by conduction only. A method to increase this heat flow has been proposed. The method relies on the use of grooves parallel to the flow direction. It has been shown that it is possible to find grooves that can increase the heat flow and, at the same, can decrease the flow pressure losses.

The optimal groove shape that maximizes the overall system performance has been determined under suitable imposed constraints. Two types of constraints have been used. The first enforces the same groove height and depth and leads to equal-depth grooves. The second keeps a fixed groove height but the groove depth is treated as an unknown that must be determined as a part of the optimization process leading to unequal-depth grooves. The optimization process was focused on the groove wave numbers that lead to reduced flow losses because such grooves produced superior gains for the overall system performance. It has been shown that the equal-depth optimal grooves can be closely approximated by a universal trapezoid. In the case of the unequal-depth groove, there exists a certain depth that leads to the best system performance. This depth, the optimal depth, and the corresponding groove shape define the optimal geometry. It has been shown that the groove shape in the optimal geometry can be approximated by a Gaussian function.

Chapter 5

5 Stability of Flow in a Channel with Longitudinal Grooves

5.1 Introduction

It has been shown in Chapter 4 that there exists a class of longitudinal grooves that can enhance heat transfer across the channel and at the same time reduce flow resistance, and the optimal forms of these grooves have been identified. These conclusions are valid as long as the flow remains laminar. Stability analysis is required in order to determine the range of Reynolds numbers where the laminar flows may exist.

This section is focused on the linear stability analysis of flows in a channel modified by longitudinal grooves. The main goal is to establish a relation between the critical stability conditions and the channel geometry. It is also of interest to identify the form of instability associated with the presence of the groove geometry. The analysis assumes a low disturbance environment and thus any processes associated with the transient growth are not considered. The reader is referred to the work of Szumbarski & Floryan (2006) for discussion of transient effects.

This chapter is organized as follows. Section 5.2 provides description of the flow in a channel modified by longitudinal grooves. In particular, Section 5.2.1 provides problem formulation, Sections 5.2.2 and 5.2.3 present the numerical solution and analytical approximation for the small wave number grooves, Description of the stationary state is given in Section 5.2.4. Linear stability analysis is discussed in Section 5.3; formulation and numerical solution are discussed in Sections 5.3.1 and 5.3.2, respectively. Section 5.4 discusses results for grooves of simple sinusoidal, arbitrary and optimal shapes. Short summary of the main conclusions is given in Section 5.5.

5.2 Flow in a channel with longitudinal grooves

5.2.1 Problem formulation

Consider flow along a straight channel extending to $\mp\infty$ in the x-direction. The flow is driven by a constant pressure gradient and has the form

$$\vec{V_0}(\vec{x}) = [u_0(\vec{x}), v_0(\vec{x})] = [u_0(y), 0] = [1 - y^2, 0], p_0(\vec{x}) = -2x/Re$$
$$\psi_0(\vec{x}) = -y^3/3 + y + 2/3, Q_0 = 4/3, \tag{5.2.1}$$

where the fluid movement is directed towards the positive x-axis, the Reynolds number Re is defined on the basis of the maximum x-velocity and the channel half height, $\vec{x} = (x\vec{i} + y\vec{j})$, the velocity vector is defined as $\vec{V_0} = (u_0\vec{i} + v_0\vec{j})$, ψ_0 stands for the stream function and Q_0 denotes the flow rate.

We modify this channel by placing longitudinal grooves of arbitrary shape on both walls (see Figure **5-1**). Geometry of the grooves is expressed in terms of Fourier series of the form

$$y_L(z) = -1 + \sum_{n=-N_A}^{N_A} H_L^{(n)} e^{in\beta z}, y_U(z) = 1 + \sum_{n=-N_A}^{N_A} H_U^{(n)} e^{in\beta z} \tag{5.2.2}$$

where $y_L(z)$ and $y_U(z)$ are locations of the lower and upper walls, respectively, N_A is the number of Fourier modes required to describe the geometry, β stands for the wave number, and $H_L^{(n)} = H_L^{*(-n)}$ and $H_U^{(n)} = H_U^{*(-n)}$ are the reality conditions where stars denote complex conjugates. The choice of $H_L^{(n)}$ and $H_U^{(n)}$ is restricted by the no-contact condition between the walls. Our interest is only in grooves that do not change the mean channel opening and, thus, $H_L^{(0)} = H_U^{(0)} = 0$.
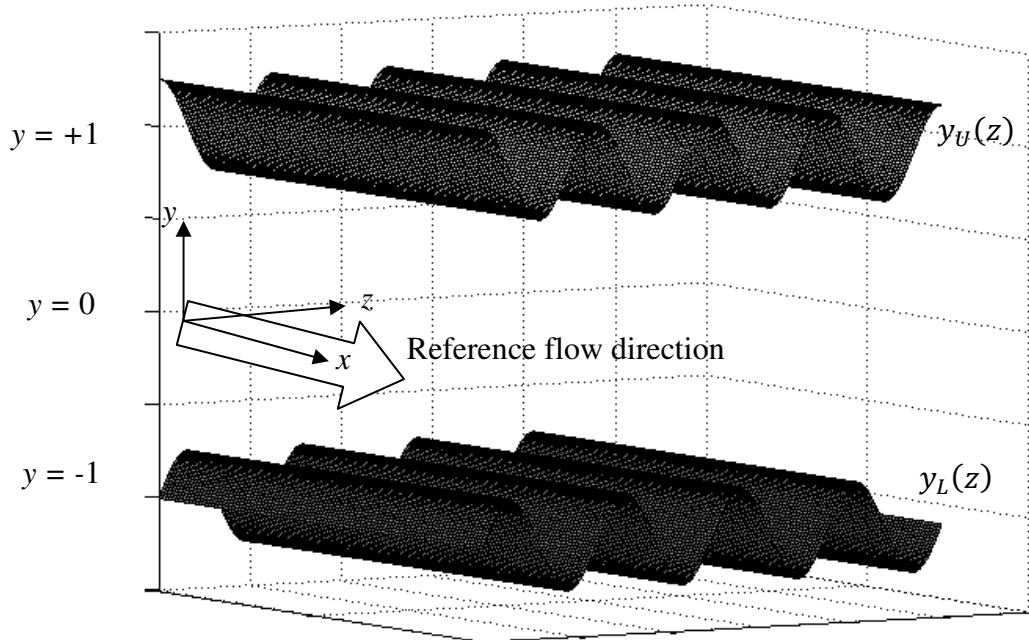
Figure 5-1: *Sketch of the flow system problem.*

The velocity field in the grooved channel is described by the axial momentum equation of the form

$$\frac{\partial^2 u_B}{\partial z^2} + \frac{\partial^2 u_B}{\partial y^2} = Re\frac{dp_B}{dx} \tag{5.2.3}$$

where the velocity vector has components $(u_B, 0, 0)$ in the (x, y, z) directions, and is supplemented by the boundary conditions of the form

$$u_B(y_L, z) = 0 , \ u_B(y_U, z) = 0 . \tag{5.2.4}$$

In the above, subscript B is used to denote flow quantities in the grooved channel. The fixed flow rate constraint of the form

$$Q = \frac{1}{2\pi/\beta}\int_{z=0}^{z=2\pi/\beta}\int_{y=y_L(z)}^{y=y_U(z)} u_B(y, z)dydz = \frac{4}{3} \tag{5.2.5}$$

is used as the closing condition. This constraint states that the flow rates in the smooth and grooved channels are identical. Addition of grooves changes the wall shear stress

distribution as well as the wetted surface area and, thus, necessitates use of a different pressure gradient in order to maintain the same flow rate. The magnitude of the pressure gradient modification provides a quantitative measure of drag changes induced by the grooves.

Flow in the grooved channel is represented as a superposition of the smooth-channel-flow and the grooved-induced modifications, i.e.

$$
\begin{aligned}
\overrightarrow{V_B}(\vec{x}) &= [u_B(y,z),0,0] = \overrightarrow{V_0}(\vec{x}) + \overrightarrow{V_1}(\vec{x}) \\
&= [u_0(y),0,0] + [u_1(y,z),0,0], p_B(\vec{x}) = p_0(\vec{x}) + p_1(\vec{x})
\end{aligned}
\tag{5.2.6}
$$

where subscript 1 identifies modifications. The resulting field equation, the boundary conditions and the constraint have the form

$$
\frac{\partial^2 u_1}{\partial z^2} + \frac{\partial^2 u_1}{\partial y^2} = Re\frac{dp_1}{dx},
\tag{5.2.7}
$$

$$
u_0(z,y_L) + u_1(z,y_L) = 0, \quad u_0(z,y_U) + u_1(z,y_U) = 0,
\tag{5.2.8}
$$

$$
Q = \frac{1}{2\pi/\beta}\int_{z=0}^{z=2\pi/\beta}\int_{y=y_L(z)}^{y=y_U(z)}[u_0(y) + u_1(y,z)]dydz = \frac{4}{3}.
\tag{5.2.9}
$$

5.2.2 Numerical solution

Spectrally accurate solution is desired. Two methods for dealing with the irregularities of the boundaries have been used, i.e., the immersed boundary condition method (IBC) (Mohammadi & Floryan 2012) and the domain transformation (DT) (see Chapter 4). The former method is more computationally efficient and, thus, has been used in the majority of the investigation, while the latter one has been used to investigate limiting cases and to provide accuracy check for the IBC method. The IBC method uses a regular solution domain with the flow domain placed in its interior and enforces the flow boundary conditions as internal constraints. The spatial discretization of the field equation uses Fourier expansion in the z-direction, i.e.

$$
u_1(y,z) = \sum_{n=-\infty}^{n=+\infty} u_1^{(n)}(y)e^{in\beta z},
\tag{5.2.10}
$$

where $u_1^{(n)} = u_1^{(-n)*}$ is the reality condition and star denotes the complex conjugate. The modal functions are discretized using Chebyshev expansions. The algebraic equations are constructed using the Galerkin projection method. The construction of the boundary constraints uses Fourier expansions for all boundary variables. Extraction of the lowest modes leads to the explicit form of the boundary constraints which are imposed using the tau concept. The flow rate constraint is discretized directly and is used as the condition required for the direct evaluation of the pressure correction simultaneously with the flow field. The number of Chebyshev polynomials and Fourier modes used in the solution were arrived at through numerical experimentation and had been selected to assure a minimum of six digits accuracy. Details of the algorithm can be found in Mohammadi & Floryan (2012). The DT method uses the same spatial discretization as the IBC method with the boundary conditions imposed in a classical manner using the tau concept. Details can be found in Chapter 4.

5.2.3 Small wave number approximation

The flow field can be evaluated analytically for the long wavelength grooves (Mohammadi & Floryan, 2013b). The solution domain is regularized using transformation of the form

$$\chi = \beta z, \varsigma = \frac{2[y - y_u(z)]}{y_u(z) - y_L(z)} + 1, \tag{5.2.11}$$

which maps the grooved channel into a straight strip in the (ς, χ) plane and the χ-coordinate plays the role of a slow scale. The field equation assumes the form

$$\frac{\partial^2 u_B}{\partial \varsigma^2} + g_1(\chi, \varsigma)\frac{\partial u_B}{\partial \varsigma} + g_2(\chi, \varsigma)\frac{\partial^2 u_B}{\partial \chi \partial \varsigma} + g_3(\chi, \varsigma)\frac{\partial^2 u_B}{\partial \chi^2} - g_4(\chi, \varsigma)Re\frac{dp_B}{dz} = 0, \tag{5.2.12}$$

where the known coefficients of the form

$$g_1(\chi, \varsigma) = \varsigma_{zz}/(\varsigma_z^2 + \varsigma_y^2), g_2(\chi, \varsigma) = 2\beta\varsigma_z/(\varsigma_z^2 + \varsigma_y^2), g_3(\chi, \varsigma)$$
$$= \beta^2/(\varsigma_z^2 + \varsigma_y^2) \ g_4(\chi, \varsigma) = 1/(\varsigma_z^2 + \varsigma_y^2) \tag{5.2.13}$$

contain information about the groove geometry. In the above

$$\varsigma_z = -\beta H^{-1}(G_\chi + \varsigma H_\chi), \varsigma_{zz} = -\beta^2 H^{-1}(2\beta^{-1}\varsigma_z G_\chi + G_{\chi\chi} + \varsigma H_{\chi\chi}),$$
$$\varsigma_y = H^{-1}, G = (y_U + y_L)/2, H = (y_U - y_L)/2.$$

(5.2.14)

The boundary conditions and flow rate constraint take the form

$$u_B(\chi, \mp 1) = 0, \quad Q = \frac{1}{2\pi} \int_{\chi=0}^{\chi=2\pi} \int_{\varsigma=-1}^{\varsigma=+1} H u_B(\chi, \varsigma) d\varsigma d\chi = \frac{4}{3}.$$

(5.2.15)- (5.2.16)

Assume solution in the form

$$u_B = U_0 + \beta U_1 + \beta^2 U_2 + \beta^3 U_3 + O(\beta^4),$$

(5.2.17)

$$p_B(x) = \left(\frac{dP_0}{dx} + \beta \frac{dP_1}{dx} + \beta^2 \frac{dP_2}{dx} + \beta^3 \frac{dP_3}{dx}\right) x + c + O(\beta^4)$$

(5.2.18)

where c is an arbitrary constant, substitute into the field equations, the boundary conditions and the constraint and retain the four leading-order terms. The resulting systems are given in Appendix F and their solutions have the form

$$U_0 = I_1^{-1}(1 - \varsigma^2)H^2, dP_0/dx = -2Re^{-1}I_1^{-1},$$

(5.2.19)

$$U_1 = 0, dP_1/dx = 0,$$

$$U_2 = -I_1^{-1}(1 - \varsigma^2)H^2(G_\chi^2 - H_\chi^2 - HH_{\chi\chi} - \varsigma HG_{\chi\chi}/3 - I_1^{-1}I_2), dP_2/dx$$
$$= -2Re^{-1}I_1^{-2}I_2,$$

$$U_3 = 0, dP_3/dx = 0,$$

where

$$I_1 = \frac{1}{2\pi} \int_{\chi=0}^{\chi=2\pi} H^3 d\chi, I_2 = \frac{1}{2\pi} \int_{\chi=0}^{\chi=2\pi} H^3(G_\chi^2 - H_\chi^2 - HH_{\chi\chi}) d\chi.$$

(5.2.20)

In the case of grooves of sinusoidal shape placed at the lower wall, i.e.

$$y_L(z) = -1 + S_L \cos(\beta z), y_U(z) = 1,$$

(5.2.21)

where S_L and β denote the groove amplitude and the wave number, respectively, the above expressions simplify to the following form

$$
\begin{aligned}
U_0(\chi,\varsigma) &= (1+3S_L^2/8)^{-1}(1-0.5S_L cos\chi)^2(1-\varsigma^2), \\
dP_0/dx &= -2Re^{-1}(1+3S_L^2/8)^{-1}, \\
U_1(\chi,\varsigma) &= 0, dP_1/dx = 0, \\
U_2(\chi,\varsigma) &= 0.5(1+3S_L^2/8)^{-1}(1-\varsigma^2)(1-0.5S_L cos\chi)^2 \\
&[S(cos\chi-0.5S_L cos^2\chi)(1-\varsigma/3)+(1+3S_L^2/8)^{-1}(S_L^2+3S_L^4/16)], \\
dP_2/dx &= -S_L^2 Re^{-1}(1+3S_L^2/8)^{-2}(1+3S_L^2/16), \\
U_3(\chi,\varsigma) &= 0, dP_3/dx = 0.
\end{aligned}
\tag{5.2.22}
$$

The range of validity of the above solution can be determined by comparing the pressure losses determined using the complete solution discussed in Section 5.2.2, i.e.

$$
\left(Re\frac{dp_B}{dx}\right)_{err} = \left|\left(Re\frac{dp_B}{dx}\right)_c - \left(Re\frac{dp_B}{dx}\right)_a\right|,
\tag{5.2.23}
$$

where subscripts a and c denote the asymptotic and the complete solutions, respectively. The results displayed in Figure **5-2** demonstrate that the asymptotic solution can be used up to $\beta = 0.5$ for the range of S of interest in this analysis.

5.2.4 Description of the flow

Introduction of grooves increases the wetted surface area and changes distribution of the wall shear stress, with both these effects contributing to changes in the drag experienced by the fluid. Results presented in Figure **5-3** for simple sinusoidal grooves given by Eq. (5.2.21) demonstrate that grooves with the wave number $\beta < \sim 0.965$ reduce the overall drag. This effect is associated with acceleration of the flow in the widest channel opening resulting in the formation of stream tubes of high velocity fluid; see (Mohammadi & Floryan 2013a) for detailed discussion. The pressure gradient reduction is well captured by the asymptotic solution (5.2.22) for $\beta < \sim 0.6$ (see Figure **5-2**). The magnitude of this reduction can be increased through the use of grooves with optimized shape (Chapter 3, Mohammadi & Floryan, 2013b).
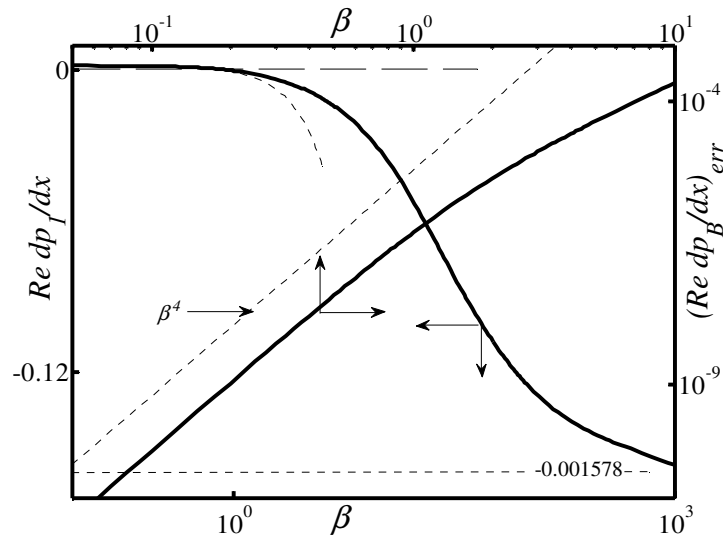
Figure 5-2: *Variations of the error $(dp/dx)_{err}$ of the small wave number approximation of the stationary state (see Eq. (5.2.23)) and variations of the pressure gradient correction $Re\ dp_1/dx$ for grooves with geometry described Eq. (5.2.21) with $S_L = 0.05$. Dotted lines show the pressure-gradient asymptote for $\beta \to 0$ and the lower bound for the pressure gradient for $\beta \to \infty$.*
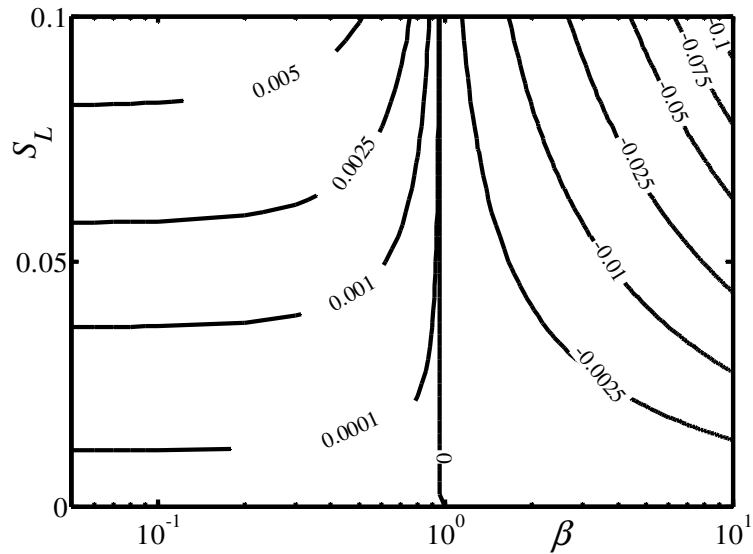
Figure 5-3: *Variations of the pressure gradient correction $Re\ dp_1/dx$ as a function of the groove wave number β and the groove height S_L for groove geometry described by Eq. (5.2.21).*

Flow topology becomes very simple when $\beta \to 0$ as the flow becomes nearly independent of the spanwise coordinate. Topology changes in a different manner for

$\beta \to \infty$ as the grooves become narrower and viscous friction prevents the fluid from moving inside the grooves (see Figure **5-4**) forcing the flow to lift up above the grooves. The mean geometric channel opening remains the same but the effective hydraulic channel opening decreases forcing the flow to accelerate above the grooves; nevertheless, the Reynolds number remains the same due to the fixed flow rate constraint. The flow topology can be described as consisting of nearly rectilinear flow above the grooves with a boundary layer of complex structure adjacent to the grooves. The lower bound on the pressure gradient correction can be determined by ignoring the boundary layer and approximating the flow with flow in a channel with height reduced by $S_L/2$, i.e.

$$Re\frac{dp_1}{dx} = 2\left[1 - \left(1 - \frac{S_L}{2}\right)^{-3}\right].$$

(5.2.24)

The above relation provides a good approximation for $\beta = O(10^2)$, as documented by the results displayed in Figure **5-2**.
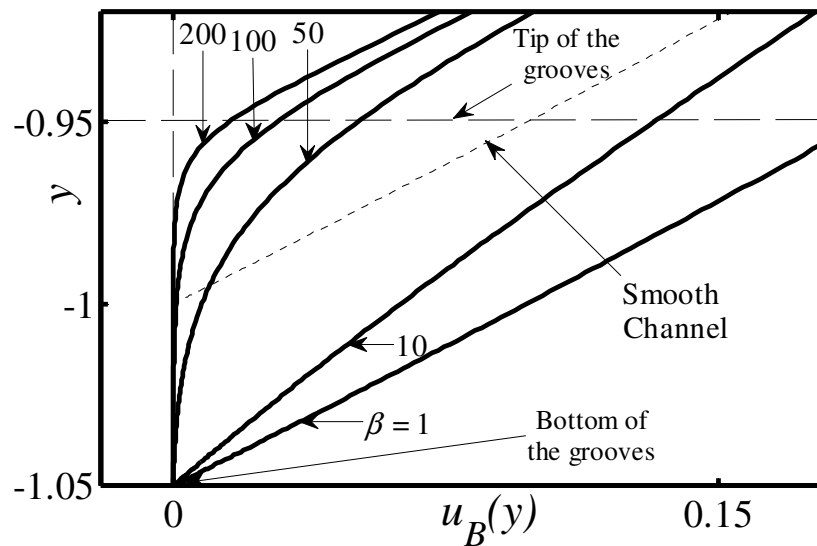
Figure 5-4: *Distributions of the streamwise velocity u_B in the middle of the groove with geometry described by Eq. (5.2.21) with $S_L = 0.05$.*

5.3 Linear stability analysis

The stability properties of the flow described above are of interest due to the drag reducing abilities of the long wavelength grooves; it is of interest to determine the maximum *Re* for which such flow remains laminar. The same grooves, especially grooves with short wavelengths, represent a special category of distributed surface roughness and, thus, it is of interest to determine how such roughness affects the onset of the laminar-turbulent transition. Both questions can be addressed with the help of the linear stability theory. It is assumed that the flow system has a low disturbance level and, thus, the stability question can be addressed using the asymptotic stability concept. In the case of noisy environment one would need to analyze transient disturbance growth (Szumbarski & Floryan, 2006).

5.3.1 Problem formulation

The stability analysis begins with the governing equations expressed in terms of the vorticity transport and continuity equations, i.e.

$$\partial \vec{\omega}/\partial t - (\vec{\omega}.\vec{\nabla})\vec{V} + (\vec{V}.\vec{\nabla})\vec{\omega} = Re^{-1}\nabla^2\vec{\omega}, \tag{5.3.1a}$$
$$\vec{\nabla}.\vec{V} = 0, \tag{5.3.1b}$$
$$\vec{\omega} = \vec{\nabla} \times \vec{V}, \tag{5.3.1c}$$

where $\vec{\omega}$ and $\vec{V}$ denote the vorticity and the velocity vectors, respectively. Three-dimensional disturbances are superposed on the base flow in the form

$$\vec{\omega} = \overrightarrow{\omega_B}(y,z) + \overrightarrow{\omega_D}(x,y,z,t), \vec{V} = \overrightarrow{V_B}(y,z) + \overrightarrow{V_D}(x,y,z,t) \tag{5-2}$$

where subscript D refers to the disturbance field. The flow quantities (3-2) are substituted into (3-1), the mean parts are subtracted and the equations are linearized. The resulting disturbance equations have the form

$$\frac{\partial \xi_D}{\partial t} - \eta_B \frac{\partial u_D}{\partial y} - \frac{\partial u_B}{\partial y}\eta_D - \varphi_B \frac{\partial u_D}{\partial z} - \frac{\partial u_B}{\partial z}\varphi_D + u_B \frac{\partial \xi_D}{\partial x}$$
$$= \frac{1}{Re}\left(\frac{\partial^2 \xi_D}{\partial x^2} + \frac{\partial^2 \xi_D}{\partial y^2} + \frac{\partial^2 \xi_D}{\partial z^2}\right), \tag{5.3.3a}$$

$$\frac{\partial \eta_D}{\partial t} - \eta_B \frac{\partial v_D}{\partial y} - \varphi_B \frac{\partial v_D}{\partial z} + u_B \frac{\partial \eta_D}{\partial x} + \frac{\partial \eta_B}{\partial y} v_D + \frac{\partial \eta_B}{\partial z} w_D$$

$$= \frac{1}{Re} \left(\frac{\partial^2 \eta_D}{\partial x^2} + \frac{\partial^2 \eta_D}{\partial y^2} + \frac{\partial^2 \eta_D}{\partial z^2} \right), \tag{5.3.3b}$$

$$\frac{\partial \varphi_D}{\partial t} - \eta_B \frac{\partial w_D}{\partial y} - \varphi_B \frac{\partial w_D}{\partial z} + u_B \frac{\partial \varphi_D}{\partial x} + \frac{\partial \varphi_B}{\partial y} v_D + \frac{\partial \varphi_B}{\partial z} w_D$$

$$= \frac{1}{Re} \left(\frac{\partial^2 \varphi_D}{\partial x^2} + \frac{\partial^2 \varphi_D}{\partial y^2} + \frac{\partial^2 \varphi_D}{\partial z^2} \right), \tag{5.3.3c}$$

$$\frac{\partial u_D}{\partial x} + \frac{\partial v_D}{\partial y} + \frac{\partial w_D}{\partial z} = 0, \tag{5.3.3d}$$

where $\overrightarrow{\omega_B} = (0, \eta_B, \varphi_B)$, $\overrightarrow{V_D} = (u_D, v_D, w_D)$, $\overrightarrow{\omega_D} = (\xi_D, \eta_D, \varphi_D)$. The homogeneous boundary conditions of the form

$$\vec{V}_D(x, y, z, t) = 0 \text{ at } y = y_L(z) \text{ and } y = y_U(z) \tag{5.3.4}$$

complete the formulation. Equations (5.3.3a-d) have coefficients that are functions of y and z and, thus, the solution can be written in the form

$$\overrightarrow{V_D}(x, y, z, t) = \overrightarrow{G_D}(y, z) e^{i(\delta x + \mu z - \sigma t)} + c.c. \tag{5.3.5a}$$
$$\overrightarrow{\omega_D}(x, y, z, t) = \overrightarrow{\Omega_D}(y, z) e^{i(\delta x + \mu z - \sigma t)} + c.c. \tag{5.3.5b}$$

where δ and μ are the real wave numbers, $\sigma = \sigma_r + i\sigma_i$, σ_i describes the rate of growth of disturbances, σ_r describes their frequency and c.c. stands for complex conjugate, i.e., the stability problem is posed as the temporal stability. $\vec{G}_D(y, z)$ and $\vec{\Omega}_D(y, z)$ are the z-periodic amplitude functions and, thus, they can be expressed in terms of the Fourier series of the form

$$\vec{G}_D(y, z) = \sum_{m=-\infty}^{m=+\infty} \left[g_u^{(m)}(y), g_v^{(m)}(y), g_w^{(m)}(y) \right] e^{im\beta z} + c.c. \tag{5.3.6a}$$

$$\vec{\Omega}_D(y, z) = \sum_{m=-\infty}^{m=+\infty} \left[g_\xi^{(m)}(y), i g_\eta^{(m)}(y), g_\varphi^{(m)}(y) \right] e^{im\beta z} + c.c. \tag{5.3.6b}$$

Substitution of Eq. (5.3.6) into Eq. (5.3.5) leads to the disturbance velocity and vorticity components of the form

$$\vec{V}_D(x,y,z,t) = \sum_{m=-\infty}^{m=+\infty} \left[g_u^{(m)}(y), g_v^{(m)}(y), g_w^{(m)}(y) \right] e^{i[\delta x + (\mu+m\beta)z - \sigma t]} + c.c. \qquad (5.3.7a)$$

$$\vec{\omega}_D(x,y,z,t) = \sum_{m=-\infty}^{m=+\infty} \left[g_\xi^{(m)}(y), i g_\eta^{(m)}(y), g_\varphi^{(m)}(y) \right] e^{i[\delta x + (\mu+m\beta)z - \sigma t]} + c.c. \qquad (5.3.7b)$$

Substitution of (5.3.7) and (5.2.10) into (5.3.3) and separation of Fourier modes leads to, after a rather lengthy algebra, a system of linear ordinary differential equations for $g_\eta^{(m)}(y)$ and $g_v^{(m)}(y)$ of the form

$$T^{(m)}(y)g_v^{(m)}(y) = \sum_{n=-\infty}^{n=+\infty} \left[H_v^{(m,n)}(y)g_v^{(m-n)}(y) + H_\eta^{(m,n)}(y)g_\eta^{(m-n)}(y) \right], \qquad (5.3.8a)$$

$$S^{(m)}(y)g_\eta^{(m)}(y) + C^{(m)}(y)g_v^{(m)}(y)$$
$$= \sum_{n=-\infty}^{n=+\infty} \left[E_v^{(m,n)}(y)g_v^{(m-n)}(y) + E_\eta^{(m,n)}(y)g_\eta^{(m-n)}(y) \right] \qquad (5.3.8b)$$

where $-\infty < m < +\infty$ and the explicit forms of the operators T, S, C, E_v, E_η, H_v, H_η are given in Appendix G. The above formulation is similar to the Bloch theory (Bloch, 1928) for systems with spatially periodic coefficients and to the Floquet theory (Coddington and Levinson, 1965) for systems with time periodic coefficients. Groove effects are contained in the right-hand-side (RHS) of (5.3.8) and in the boundary conditions (5.3.4). When the groove amplitude approaches zero, the RHS becomes zero and the modal equations decouple. In this limit, Eqs. (5.3.8) describe a system of oblique Tollmien-Schlichting (TS) waves propagating independently of each other. In analogy to the stability of parallel flows, we shall refer to the T, S and C operators as the Tollmien-Schlichting, Squire and coupling operators, respectively (Floryan, 1997).

Equations (5.3.8) together with the homogeneous boundary conditions (5.3.4) form an eigenvalue problem and have a nontrivial solution only for certain combinations of (δ, μ, σ) for the specified flow conditions (*Re*) and for the specified groove geometry (β, $H_L^{(n)}$, $H_U^{(n)}$). The required dispersion relation has to be determined numerically and the relevant methodology is described in the next section.

5.3.2 Numerical solution

The problem to be solved consists of an infinite system of ordinary differential equations (5.3.8) with the homogeneous boundary conditions (5.3.4). The Fourier expansions (5.3.7) are truncated after term N_N and the modal functions are discretized using the Chebyshev expansions of order N_T of the form

$$\left[g_v^{(m)}(y), g_\eta^{(m)}(y)\right] = \sum_{k=0}^{+\infty}\left[G_{k,v}^{(m)}, G_{k,\eta}^{(m)}\right]T_k(y) \approx \sum_{k=0}^{N_T}\left[G_{k,v}^{(m)}, G_{k,\eta}^{(m)}\right]T_k(y), \qquad (5.3.9)$$

where T_k denotes the Chebyshev polynomial of the kth order, and $G_{k,v}^{(n)}$ and $G_{k,\eta}^{(n)}$ stand for the unknown coefficients of the expansions. The Galerkin projection method is used to form a system of linear algebraic equations. Details of the discretization process are presented in Appendix H.

The homogeneous boundary conditions are enforced using the IBC method (Szumbarski & Floryan 1999). Appendix I provides details of the implementation process. Four equations for $G_{k,v}^{(n)}$ and two equations for $G_{k,\eta}^{(n)}$ corresponding to the highest Chebyshev polynomials are eliminated for each Fourier mode providing space for the imposition of the boundary relations (tau method).

The resulting homogeneous algebraic system can be posed in various ways. For the global solution the system is posed as a general eigenvalue problem of the form

$$AE = \sigma BE, \qquad (5.3.10)$$

where E denotes the eigenvectors and the σ-spectrum is determined numerically. These solutions are expensive numerically and suffer accuracy problems when large matrices are involved. Efficiencies can be found by using the Arnoldi method (Saad, 2003) which permits evaluation of only selected part of the spectrum. Local solutions are still more computationally efficient and more accurate but produce limited number of eigenvalues, mostly just one eigenvalue. These solutions are used for tracing selected eigenvalues

through the parameter space. The process starts with an initial guess either for the eigenvalue or for the eigenvector and iterations are used to converge to the true eigenvalue and/or eigenvector.

Three methods for eigenvalue tracing have been used. In the first method, one of the homogeneous boundary conditions is replaced by an inhomogeneous boundary condition imposed on a different quantity resulting in an inhomogeneous system which can be easily solved. The true eigenvalue is found if the solution of the inhomogeneous system happens to satisfy the eliminated boundary condition. Since this is not true in general, the eigenvalue is searched for by looking for the zero of the replaced boundary condition using the Newton-Raphson procedure. Boundary condition for the vertical velocity component at the lower wall has been replaced in this study with condition for the second derivative of the vertical velocity component. Good initial guess for σ significantly accelerates convergence. In the second method the eigenvalue is searched for by looking for zeros of determinant of $(A - \sigma B)$ where the system is posed as

$$(A - \sigma B)E = 0 \tag{5.3.11}$$

In the third method, the inverse iterations method, we compute an approximation for the eigenvector E_a corresponding to the unknown eigenvalue σ_a using an iterative process in the form

$$(A - \sigma_0 B)E^{(n+1)} = BE^n, \tag{5.3.12}$$

where σ_0 and E^0 are the eigenvalue and the eigenvector (an eigenpair) corresponding to the unaltered flow. If σ_a is the eigenvalue closest to σ_0, E^n converges to E_a. The eigenvalue σ_a is evaluated using formula

$$\sigma_a = E_a^T A E_a / E_a^T B E_a, \tag{5.3.13}$$

where T denotes the complex conjugate transpose. The inverse iterations method was found to be generally more efficient compared with the Newton-Raphson method. The tracing of eigenvalues has been extended over several Brillouin zones (Bloch, 1928) in

the μ-direction in order to demonstrate how the leading eigenvalue is affected by the groove wavelength. The tracing process needs to be carefully implemented for small β's as width of the Brillouin zones decreases rapidly and the eigenvalues become tightly spaced.

The accuracy and cost of the discretization depend on the rate of convergence of expansions (3-7) as well as Fourier expansions used in the construction of the boundary constraints (see Appendix I). Convergence can be assessed using energy of Fourier modes which is measured using the Chebyshev norm for the *x*-component of the disturbance velocity, i.e. $g_u^{(m)}(y)$, defined as

$$\left\|\Phi^{(n)}(y)\right\|_\omega = \left\{\int_{-1}^{1} g_u^{(m)}(y)g_u^{(m)*}(y)\omega(y)dy\right\}^{1/2}, \tag{5.3.14}$$

where $\omega(y) = 1/\sqrt{1-y^2}$ and star denotes complex conjugate. Results presented in Figure **5-5** demonstrate that the rate of convergence of these expansions strongly depends on β.
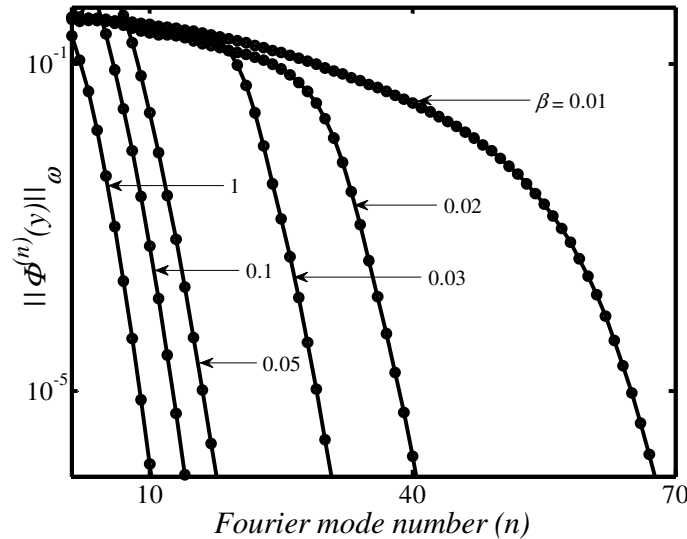
Figure 5-5: *Variations of the Chebyshev norm $\left\|\Phi^{(n)}(y)\right\|_\omega$ (see Eq. (5.3.14)) as a function of the Fourier mode number n for the groove geometry described by Eq. (5.2.21) with $S_L = 0.05$, for flow Reynolds number $Re = 6500$ and disturbance wave numbers $\delta = 1.02$, $\mu = 0$.*

The convergence is very good for $\beta \geq 0.1$ and use of ten Fourier modes guarantees a minimum of six digits accuracy. Decrease of β leads to a significant reduction of the convergence rate and achieving the same accuracy with $\beta = 0.01$ requires use of around 70 Fourier modes. Evaluation of the eigenvalues requires fewer modes as illustrated in Fig. 7, e.g. use of just five modes gives the six-digit accuracy when $\beta \geq 0.1$ but around 30 modes are required for $\beta = 0.01$.
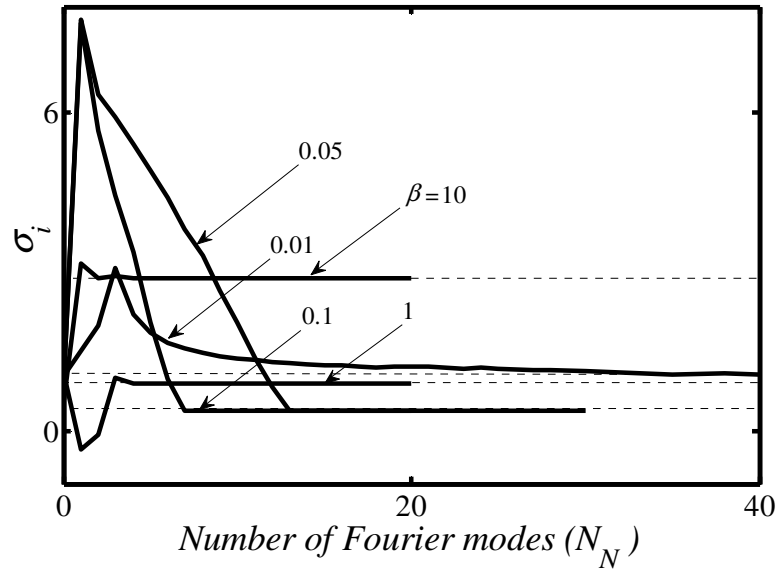
Figure 5-6: *Variations of the growth rate $\sigma_i \times 10^3$ of disturbances with the wave numbers $\delta = 1.02$ and $\mu = 0$ as a function of the number of Fourier modes used in the numerical solution of the stability problem for flow with the Reynolds number Re=6500 in the grooved channel with the groove geometry described by Eq. (5.2.21) with $S_L = 0.05$.*

5.4 Results

It is known that flow in a smooth channel becomes unstable at $Re = 5772$ with the two-dimensional (Tollmien-Schlichting, TS) waves with the wave number $\delta = 1.0205$ travelling in the downstream direction playing the critical role (Orszag, 1971). Once these waves reach sufficient amplitude, the disturbance growth becomes dominated by a three-dimensional secondary instability driven by a parametric resonance (Orszag and Patera, 1983). The instability has a subcritical character and an increase of the level of disturbances can reduce the critical Reynolds number down to $Re \approx 2700$ (Herbert,

1977). For a sufficiently high level of environmental disturbances the instability process can be dominated by the transient growth of disturbances with the optimal disturbances rather than the TS waves playing the critical role (Szumbarski & Floryan, 2006). Addition of grooves is expected to modify travelling waves but, at the same time, it might create new disturbance structures at the onset.

The role of the grooves in the instability process depends on their shape and amplitude. We begin discussion with the simple sinusoidal grooves placed at the lower wall only. The channel geometry is described by Eq. (5.2.21) with the amplitude S_L and the wave number β being the only geometrical parameters. This geometry corresponds to the leading Fourier mode in the Fourier expansion (5.2.2) representing an arbitrary shape. We shall limit our interests to small grooves, i.e. $S_L \leq 0.05$.

5.4.1 Sinusoidal grooves

Investigation of spectra under a variety of conditions lead to conclusion that there is only one class of unstable disturbances; these disturbances connect to the classical travelling waves in the limit of $S_L \to 0$. No sign of any instability that may lead to the formation of streamwise vortices has been found. This should not be surprising as longitudinal grooves do not generate centrifugal force field which is responsible for the formation of such vortices in the case of transverse grooves (Floryan, 2003).

The transition between the characteristics of disturbances in the grooved and smooth channels is illustrated in Figure **5-7** for a wide range of β's. It can be seen that disturbances in grooved channel evolve towards the same travelling wave as S_L is reduced. Figure **5-8** displays variations of the critical Reynolds number as a function of the orientation of the disturbance wave vector. The wave vector is defined as $\boldsymbol{q} = (\delta, \mu)$, it has magnitude $|\boldsymbol{q}| = (\delta^2 + \mu^2)^{1/2}$ and its orientation is expressed in term of the inclination angled defined as $\theta = \pm\tan^{-1}(\delta/\mu)$. During test computations the magnitude of the wave vector was kept constant while its orientation was varied. It can be seen that disturbances with the wave vector aligned with the flow direction have the smallest Re_c. Although the Squire theorem (Squire, 1933) does not apply to flows in grooved channels, these results lead to conclusion equivalent to the Squire theorem. The reader may note

that the critical disturbances are not two-dimensional in the grooved channel due to the modulating effect of geometry. We shall, nevertheless, refer to these disturbances as "two-dimensional" waves based on their properties in the limit $S_L \to 0$. The rest of this discussion will be focused on the "two-dimensional" waves unless otherwise explicitly noted.
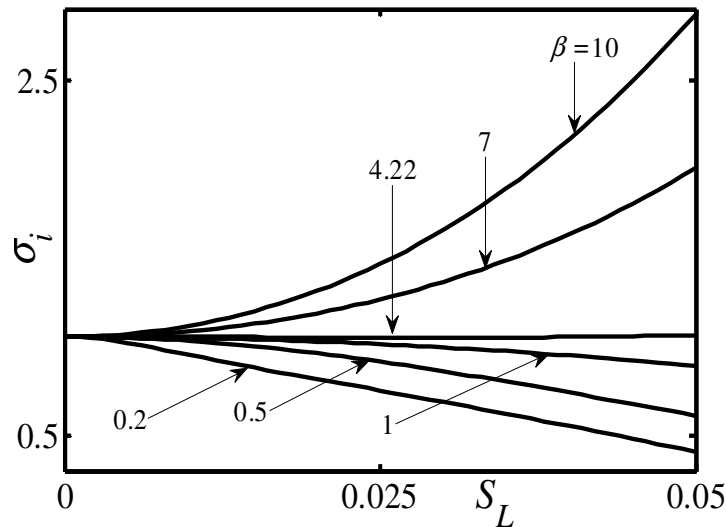
Figure 5-7: *Variation of the growth rate $\sigma_i \times 10^3$ of disturbances with the wave numbers $\delta = 1.02$ and $\mu = 0$ as a function of the groove amplitude S_L for the groove geometry described by Eq. (5.2.21) for flow with the Reynolds number $Re = 6500$.*

Results displayed in Figure **5-7** demonstrate that grooves may either stabilize or destabilize the flow depending on the groove wave number, with transition occurring at $\beta = \beta_{tran} \approx 4.22$ and being independent of the groove amplitude. Grooves with shorter wavelengths destabilize the flow with the growth rate increasing rapidly with an increase of S_L. Long wavelength grooves stabilize the flow but the decrease of the amplification rate is much weaker than the increase observed for the short wavelength grooves. The qualitatively different effects of β are well illustrated in Figure **5-9** which displays variations of the amplification rate as function of β for fixed S_L.
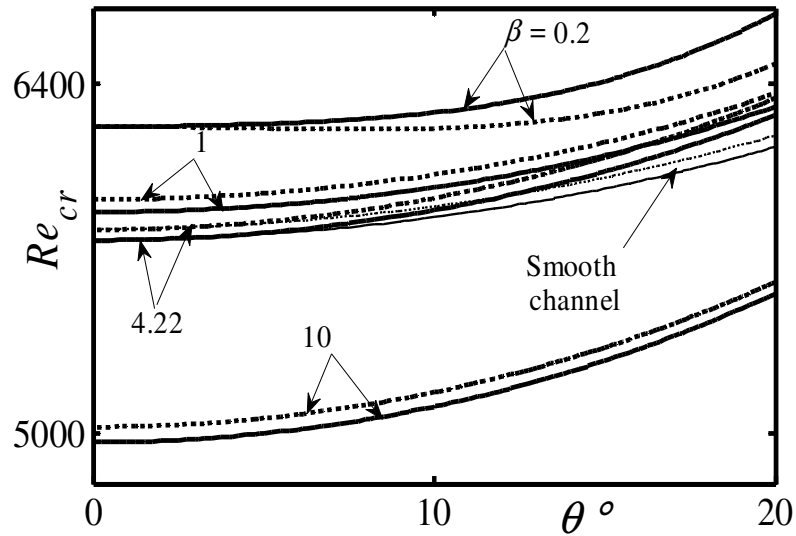
Figure 5-8: *Variations of the critical Reynolds number of disturbances with the wave vector* $\boldsymbol{q} = (\delta, \mu)$ *of constant magnitude as a function of its inclination angle* θ *for the groove geometry described by Eq. (5.2.21) with the amplitude* $S_L = 0.05$. *Solid lines correspond to* $|\boldsymbol{q}| = 1.02$ *and dotted lines to* $|\boldsymbol{q}| = 1.0$.
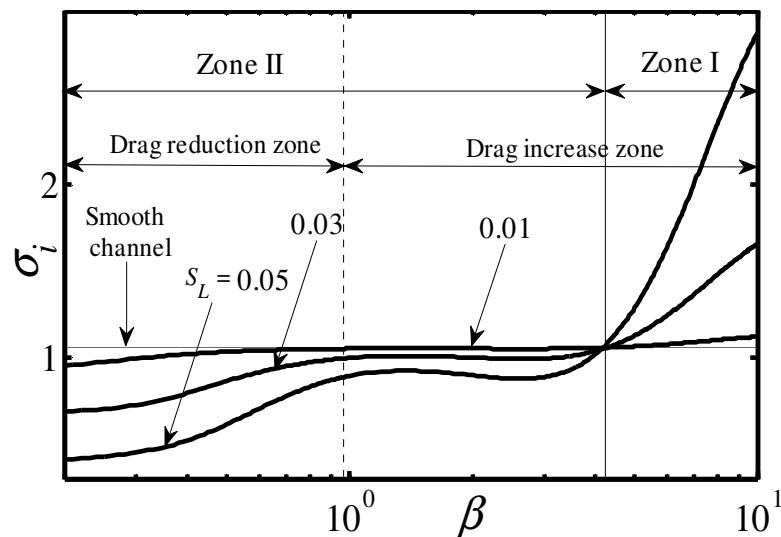
Figure 5-9: *Variations of the growth rate* $\sigma_i \times 10^3$ *of disturbances with the wave number* $\delta = 1.02$ *as a function of the groove wave number* β *for the groove geometry described by Eq. (5.2.21) for flow with the Reynolds number* $Re = 6500$. *Dotted-line indicates the wave number that separates the drag reducing and drag increasing zones.*

Rapid destabilization in zone I (large β) as well as gradual stabilization in zone II ($\beta =$ $0(1)$) are clearly visible. The groove wave number that corresponds to the transition between the drag reducing and the drag increasing grooves, i.e. β_{cr}, lies deep inside zone II and does not have any significance as far as stability properties of the flow are concerned.

Eigenfunctions $g_u^{(n)}(y)$ corresponding to the onset conditions displayed in Figure **5-10** for a wide range of β's permit description of the disturbance flow topology. The eigenfunctions are normalized with the maximum of $g_u^{(0)}(y)$ in the upper half of the channel, i.e. $max_{y \in [0,1]}\left|g_u^{(0)}(y)\right| = 1$. It can be seen that near the upper (smooth) wall and for large β the dominant eigenfunctions, i.e. eigenfunctions with index 0, are very similar to the eigenfunction in a smooth channel; higher eigenfunctions are negligible in this zone. Significant differences appear when β is reduced below $\beta_{tran} \approx 4.22$ with the magnitudes of the higher eigenfunctions reaching the level of about 80% of the dominant eigenfunction. The reader may note appearance of large differences between the phase of the dominant, "grooved" eigenfunction and the "smooth" eigenfunction.

Analysis of the lower part of the channel shows that higher eigenfunctions are always important close to the grooved wall; their magnitudes increase from about 20% of the dominant eigenfunction at large β to about 80% at small β. Noticeable differences in the phase distribution of the "smooth" and the dominant "grooved" eigenfunctions can be seen already at large β; these differences increase significantly as β decreases.

The topology of the disturbance velocity field at the onset is complex, highly three-dimensional and dependent on β, as illustrated in Figure **5-11** and Figure **5-12**. Pathlines in the *y-z* plane displayed in Figure **5-11** demonstrate simple structure of flow in the upper part of the channel for large enough β (see Figure **5-11**A, Figure **5-11**B) to be replaced by progressively more complex, three-dimensional topology as β decreases (see Figure **5-11**C , Figure **5-11**D). At small enough β the topology corresponds to appearance of a sink at the wall in the narrowest channel opening (Figure **5-11**C) and, for a still smaller β, it is supplemented by a source at a small distance away from the wall in the

widest channel opening (Figure **5-11**D) giving appearance of formation of a separation bubble.
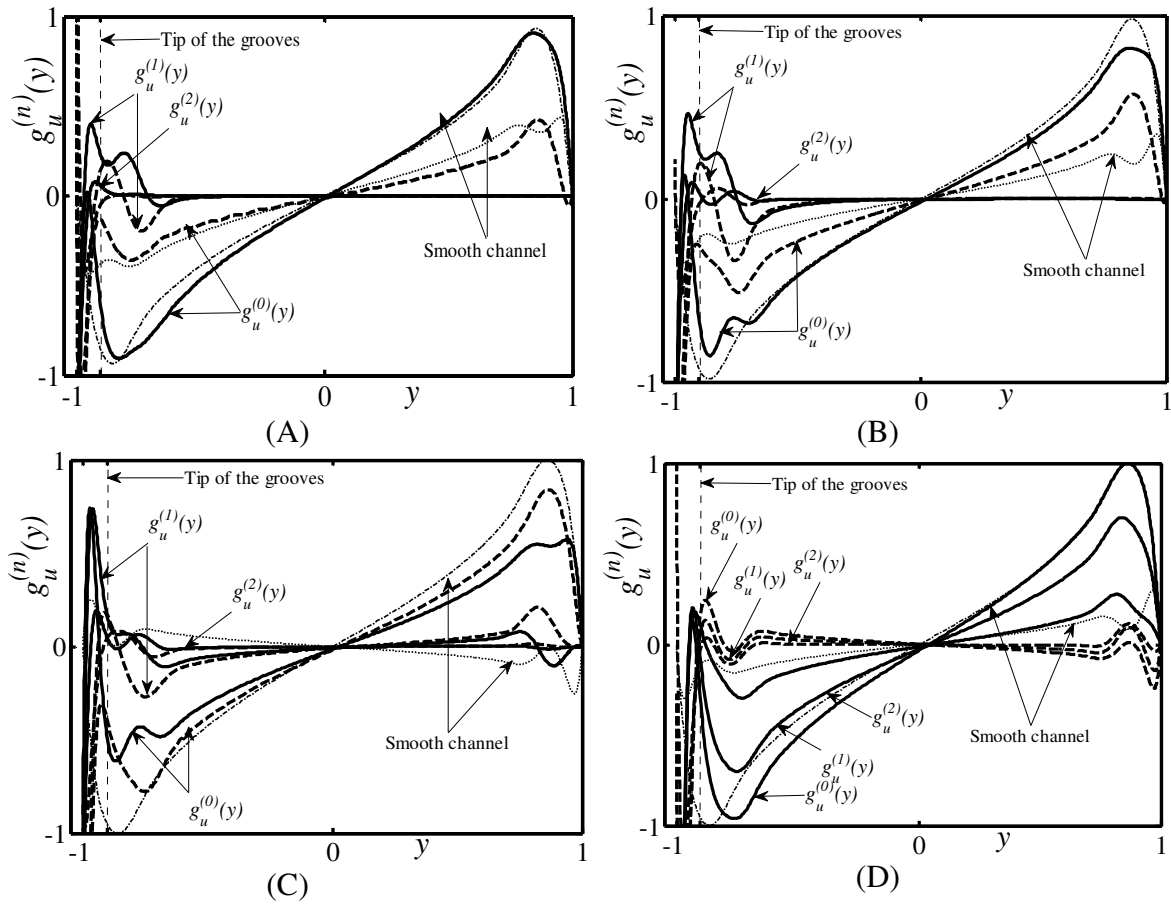
Figure 5-10: *Eigenfunctions $g_u^{(n)}(y)$, n = 0, 1, 2, describing two-dimensional travelling wave disturbances with the wave number δ =1.02 in a channel with grooves whose geometry is described by Eq. (5.2.21) with S_L = 0.05. Results displayed in Figs. 5-10A, B, C, and D correspond to the onset conditions for the groove wave numbers β =10, 4.22, 1.0, and 0.2, i.e. Re_{cr} = 5028.5, 5773.5, 5886, and 6227.5, respectively. The normalization condition $max_{y \in [0,1]} \left| g_u^{(0)}(y) \right|$ = 1 has been used for the presentation purposes. Solid and dash lines identify the real and imaginary parts. Thin dashed-dotted and dotted lines identify the real and imaginary parts of the eigenfunction for the smooth channel with the same Reynolds number.*

Flow topology close to the lower wall is more complex. At large β (Figure **5-11**A), source appears at the trough producing structure similar to a separation bubble. Decrease of β eliminates this bubble (Figure **5-11**B). Further decrease of β increases strength of

this source resulting in an unusual structure displayed in Figure **5-11**C. At $\beta = 0.2$ (Figure **5-11**D) the topology corresponds to that created by a line source parallel to the wall with the wall acting like a sink resulting in the formation of a distinct layer of trapped fluid adjacent to the wall. High level of three-dimensionality of the flow field is underscored by form of the pathlines in the (x,z)-plane at a fixed y. Figure **5-12** displays such pathlines at $y = 0$ for several values of β at the onset. Pathlines look like spirals for $\beta \approx \beta_{tran} \approx 4.22$ (see Figure **5-12**C and Figure **5-12**D), they look like closed loops for smaller β (see Figure **5-12**E and Figure **5-12**F) but appear to correspond to sets of point/line sinks for larger β (see Figure **5-12**A and Figure **5-12**B).

(A)   (B)
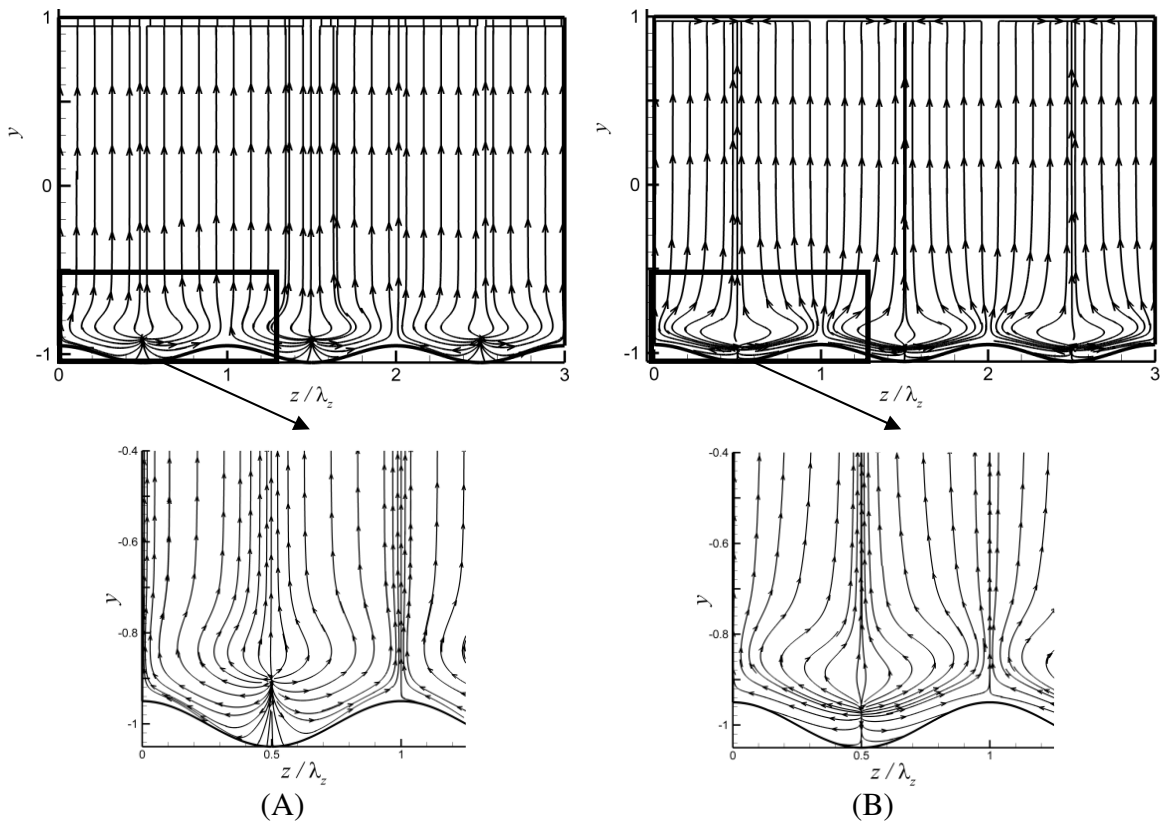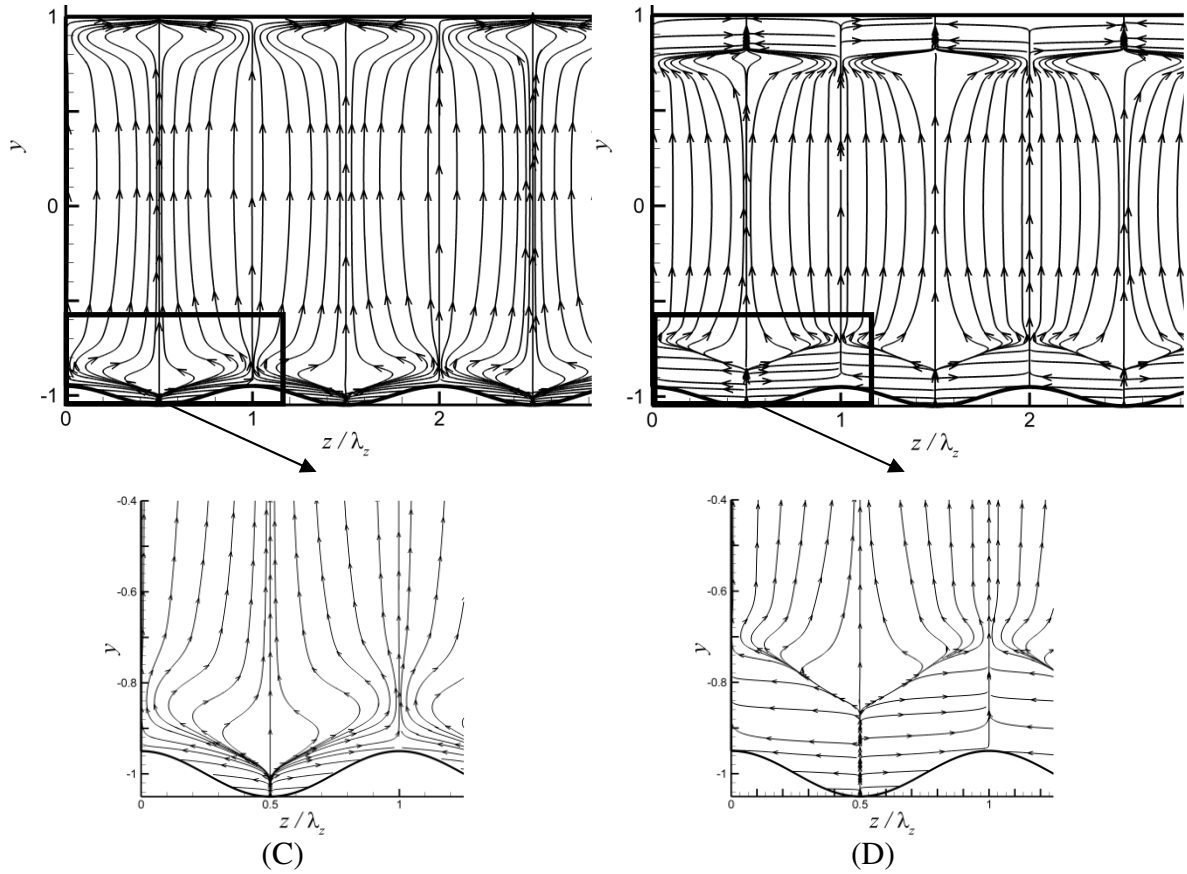
Figure 5-11: *Pathlines in the y-z plane for the disturbance flow field corresponding to "two-dimensional" disturbances with the wave number $\delta = 1.02$ at the onset for flow in a channel with grooves described by Eq. (5.2.21) with $S_L = 0.05$. Figures 5-11A, B, C and D display results for $(\beta, Re_c) = $ (10, 5028.5), (4.22, 5773.5), (1.0, 5886), (0.2, 6227.5), respectively.*
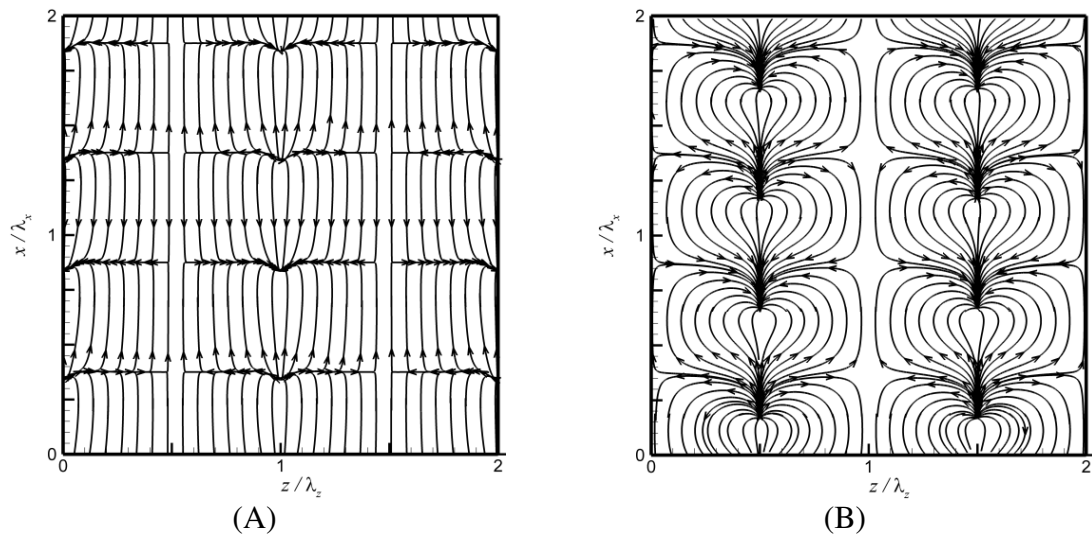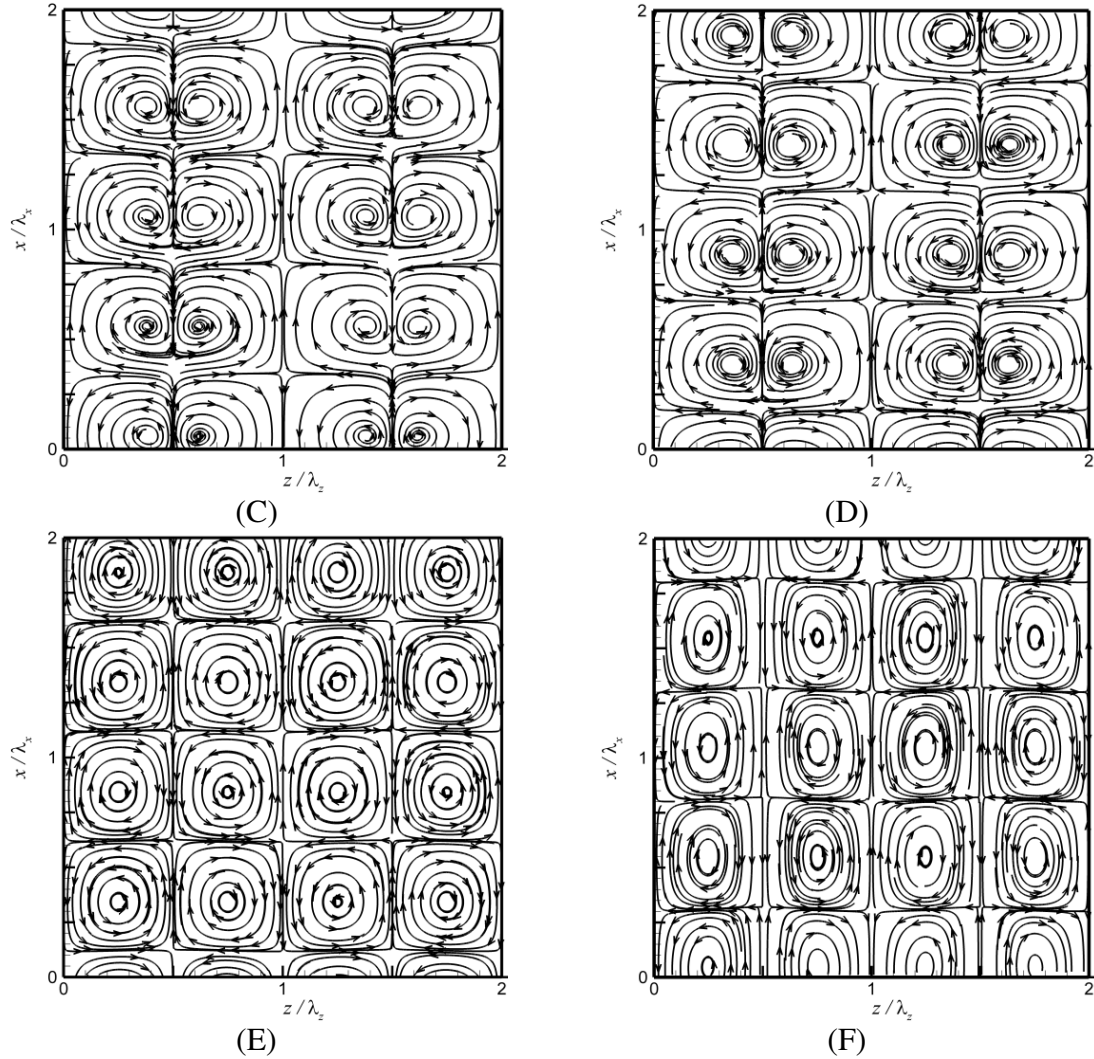
Figure 5-12: *Pathlines in the x-z plane at y = 0 for the disturbance flow field corresponding to "two-dimensional" disturbances with the wave number $\delta = 1.02$ at the onset for flow in a channel with grooves described by Eq. (5.2.21) with $S_L = 0.05$. Figures 5-12A, B, C, D, E and F display results for (β, Re_c) = (10, 5028.5), (5, 5652.4), (4.35, 5755), (4.22, 5773.5), (1.0, 5886), (0.5, 6073.1), respectively.*

The neutral curves for the "two-dimensional" waves in the (δ, Re)-plane are fairly similar to the analogous curves for the smooth channel, as illustrated in Figure **5-13**. At small β the critical Reynolds number decreases as the groove amplitude increases while the critical disturbance wave number δ_{cr} remains nearly unchanged (Figure **5-13**A). At $\beta = \beta_{tran}$ both Re_c and δ_{cr} are marginally affected by variations of S_L (Figure **5-13**B). At

large β the critical Reynolds numbers decrease as S_L increases while δ_{cr} marginally increases (Figure **5-13**C).

(A)

(B)

(C)
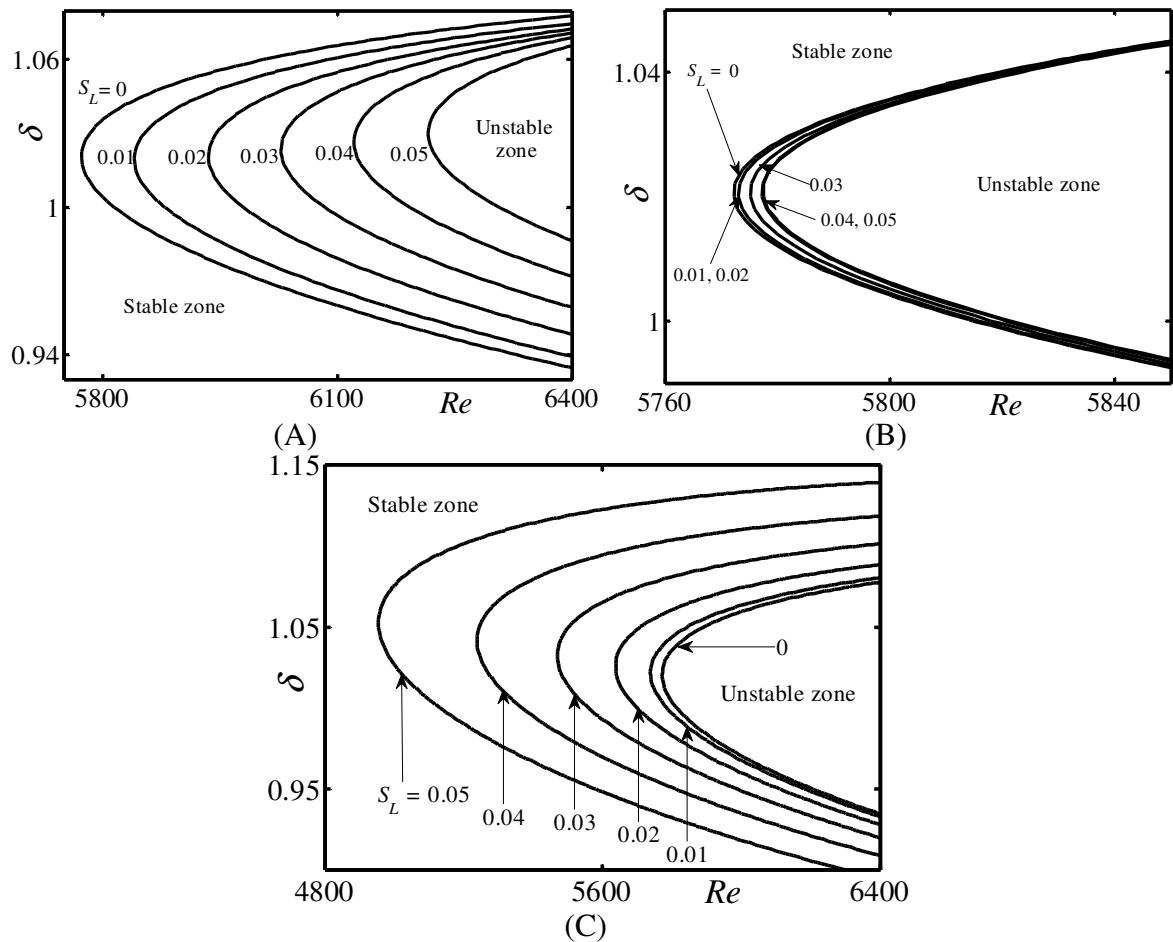
Figure 5-13: *Neutral curves in the* (Re, δ)-*plane for the "two-disturbances" with the wave numbers* $\delta = 1.02$ *in a channel with grooves whose geometry is described by Eq. (5.2.21). Figures 5-13A, B and C display results for the groove wave numbers* $\beta = 0.2, 4.22, 10,$ *respectively.*

The stabilizing/destabilizing effects of the grooves are well illustrated by the neutral curves in the (β, δ) plane. Figure **5-14**A displays results for the nominally subcritical Reynolds number $Re = 5500$. The flow is stable for small enough β's but becomes unstable once β reaches a certain minimum value; further increase of β results in a large expansion of the range of the unstable δ's. The minimum value of β required for the

onset of the instability decreases with an increase of S_L. A similar process can be observed for the nominally critical Reynolds number $Re = 5772.25$ (see Figure **5-14**B) where there is only one unstable δ for small enough β, but its range expands once β reaches a certain minimum, S_L-dependent value. Figure **5-14**C corresponds to the nominally supercritical Reynolds number $Re = 6000$. It can be seen that an increase of S_L decreases the range of unstable δ's for small β's, even leading to the complete flow stabilization. The process is opposite for $\beta > \beta_{tran} \approx 4.22$ where a large expansion of the unstable δ's is observed.
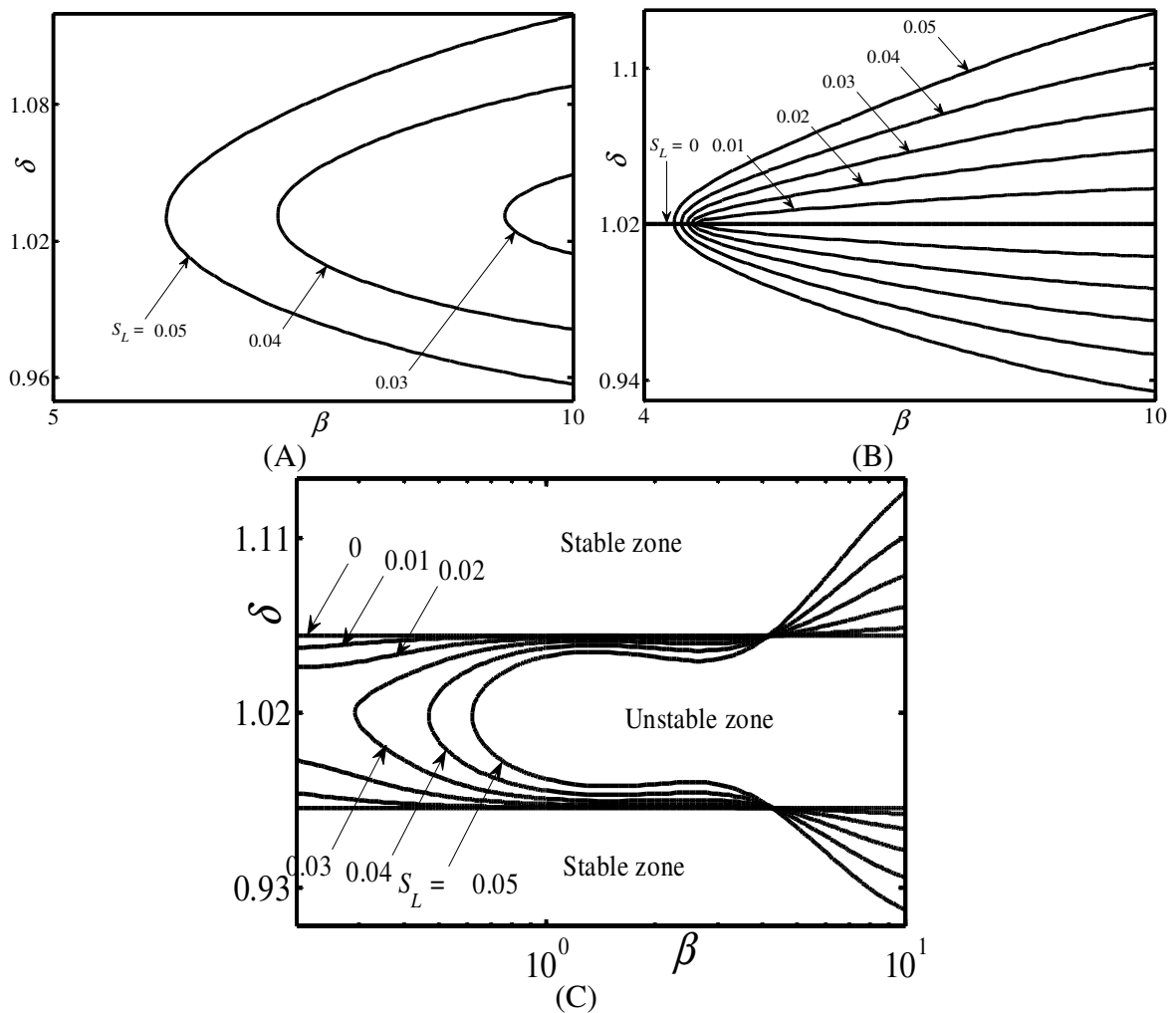
Figure 5-14: *Neutral curves in the (β, δ)-plane for the "two-dimensional" disturbances in a channel with grooves whose geometry is described by Eq. (5.2.21). Figures 5-14A, B and C display results for flow with $Re = 5500, 5772.25, 6000$, respectively.*

Figure **5-15** illustrates variations of the critical Reynolds number Re_c as a function of β and S_L and provides basis for a compact summary of the main results. The flow stability is not affected by the grooves with $\beta = \beta_{tran} \approx 4.22$ regardless of their amplitude. The flow is destabilized for larger β's with Re_c decreasing with as an increase of β and this destabilization is more effective for larger S_L's. The smallest critical Reynolds number of $Re_c = 4955$ is achieved for $\beta = 10$ and $S_L = 0.05$ which are the largest values of these parameters considered in the present study; further reduction of Re_c might be achieved with larger groove amplitudes and wave numbers. The flow is stabilized for $\beta < \beta_{tran} \approx 4.22$ as Re_c increases with and a decrease of β; the stabilization is more effective for larger S_L's. The largest critical Reynolds number of $Re_c = 6138$ is achieved for $\beta = 0.4$ and $S_L = 0.05$ which define the limits of the present investigation.
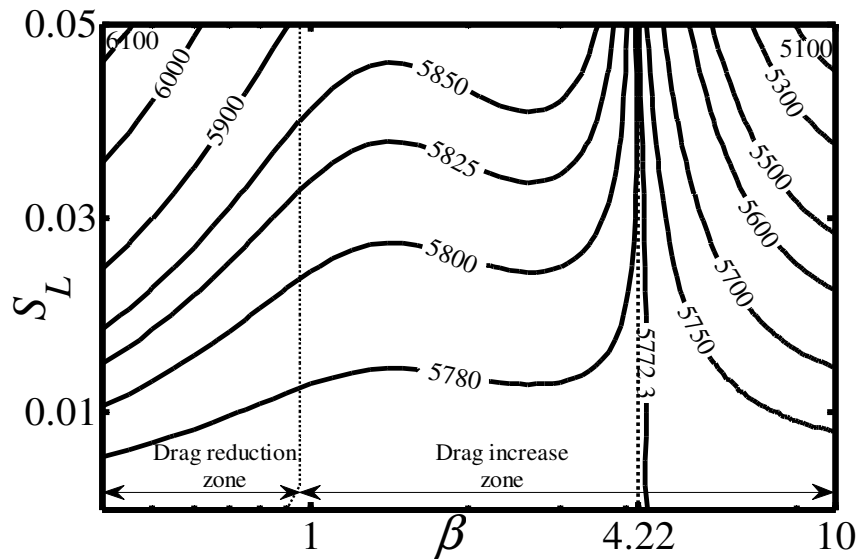
Figure 5-15: *Variations of the critical Reynolds number Re_c as a function of the groove wave number β and the groove amplitude S_L for channel with geometry described by Eq. (5.2.21). Dotted-line corresponds to $Re\, dp_1/dx = 0$.*

5.4.2 Grooves with arbitrary shapes

Section 5.4.1 provides a detailed discussion of the instability in a channel with sinusoidal grooves. We shall now turn our attention to grooves of arbitrary shapes. Grooves with triangular, trapezoidal and rectangular shapes shown in Figure **5-16** have been selected

for the analysis. Each shape has been represented using a Fourier expansion, e.g. Eq. (5.2.2), which has been truncated after a finite number of terms.
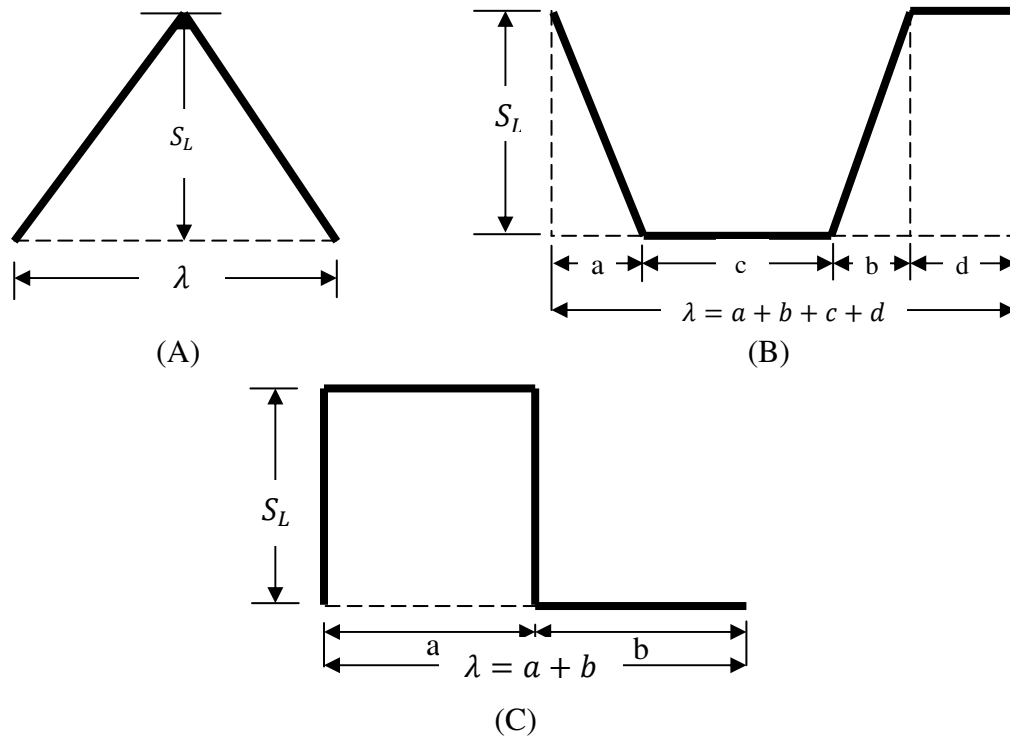
Figure 5-16: *Groove shapes used in this study: A- triangular groove, B- trapezoidal groove, C-rectangular groove. λ denotes the groove wavelength.*

Neutral stability curves of the type displayed in Figure **5-17** have been computed for each shape represented by different numbers of Fourier terms. It can be seen that the critical Reynolds numbers determined for the triangular grooves represented using either the leading term from the Fourier expansion, or the first two terms, or the first three terms are nearly identical. The same conclusion applies to the trapezoidal grooves; in this case the difference between shapes represented by either three or five Fourier modes is negligible. It can be concluded that the difference between Re_c determined either on the basis of shape represented by the leading Fourier mode from its Fourier representation or using the complete shape is at the most 0.05%. Rectangular grooves pose a challenge due to the existence of the Gibb's phenomenon (Wilbraham, 1848; Gibbs, 1898, 1899). In this case,

results displayed in Figure **5-17** demonstrate that one needs to use up to seven Fourier modes in the shape representation for the accurate determination of Re_c.
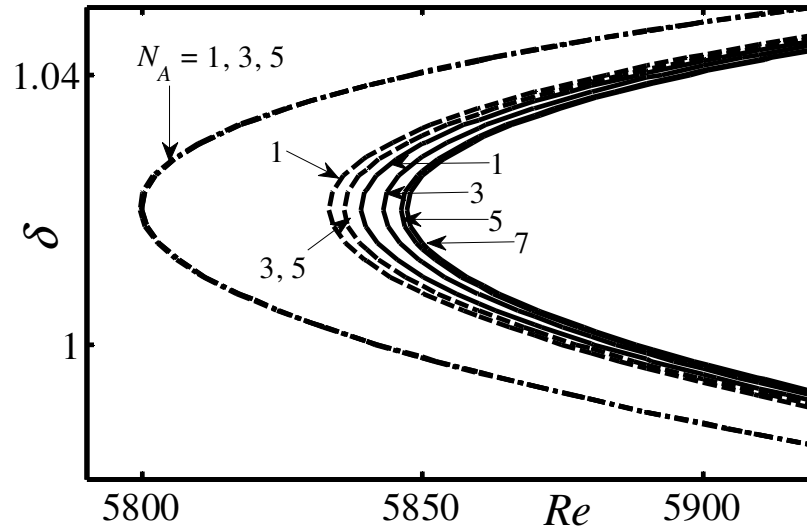
Figure 5-17: *The neutral curves in the (Re, δ)-plane for flow in channels with triangular grooves (solid lines), trapezoidal grooves (dashed lines; $a = b = \lambda/6$, $c = d = \lambda/3$, see Figure* **5-16***B for notation), and rectangular grooves (dashed-dotted lines: $a = b = \lambda/2$, see Figure* **5-16***C for notation). All grooves have the same amplitude $S_L = 0.05$ and the same wave number $\beta = 1$. Their shapes are described using 1, 3, 5, 7 leading Fourier modes from the complete Fourier expansion describing geometry.*

Use of only the leading Fourier mode results in the error of Re_c of the order of 0.5%. This demonstrates the generality of the results discussed in the previous section as the sinusoidal groove can be interpreted as representing an arbitrary groove replaced by the leading Fourier mode from its Fourier representation. Results illustrated in Figure **5-17** form basis of the reduced geometry model which significantly simplifies the analysis of effects of grooves on the flow stability. There is no need to study all possible shapes as results based on the leading Fourier mode provide accuracy sufficient for most applications. The stability characteristics can be determined only once and then made available in the tabulated/graphical form, i.e. see Section 5.4.1. The above discussion also demonstrates that the stability response of the flow is insensitive to details of the groove geometry.

5.4.3 Optimal grooves

It is known that longitudinal grooves are able to significantly reduce the laminar drag if the groove wave number is sufficiently small; this effect occurs only for grooves with $\beta < \beta_{cr} \approx 0.965$ (see Section 5.2.4). The best groove shape for the maximization of the drag reduction has been determined in Chapter 3 for the annular flow and by Mohammadi & Floryan (2013b) for the planar flow.
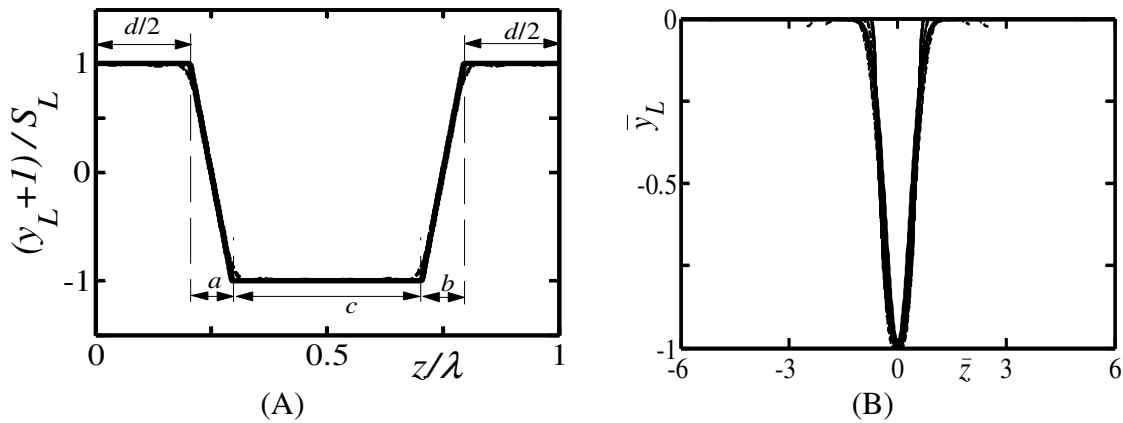
Figure 5-18: *The optimal shapes for $\beta = 0.2$, 0.5 for the equal-depth (Figure **5-18**A) and the unequal-depth grooves (Figure **5-18**B) with $S_L = 0.01$, 0.03, 0.05 in the former case and $S_{L,U} = 0.01$, 0.03, 0.05 in the latter case. The best-fitted trapezoid ($a = b = \lambda/8$, $c = d = 3\lambda/8$) overlaps within resolution of this figure with all grooves in Figure **5-18**A after shapes had been rescaled with the groove amplitude. The universal Gaussian function $\bar{y} = -e^{-4\bar{z}^2}$ overlaps within resolution of this figure with all grooves in Figure **5-18**B; shapes have been rescaled with the peak-to-bottom distance as the vertical length scale, i.e. $\bar{y}_L = (y_L + 1 - S_{L,u})/(D_{opt} + S_{L,u})$, and width at half height W_{half} as the horizontal length scale, i.e. $\bar{z} = (z - z_0)/W_{half}$.*

The shape of the optimal groove depends on the type of constraint. In the case of the equal-depth grooves both height and depth are subject to the same constraint. In the case of the unequal-depth grooves the height is set while the most efficient depth is determined through the optimization. In the former case, the optimal grooves are well approximated by a certain universal trapezoid (see Figure **5-18**A; $a = b = \lambda/8$ and $c = d = 3\lambda/8$). In the latter case, they are well approximated by a Gaussian function (see Figure **5-18**B; $\bar{y} = e^{-4\bar{z}^2}$). It is of interest to determine effects of such grooves on

the flow stability as this would provide a limit on their applicability. The optimization process requires access to more information about the groove geometry; the number of Fourier modes that has to be used increased to about 5-7 (Mohammadi & Floryan, 2013b) and forms basis for the reduced geometry model for optimization. In the stability analysis the optimal shapes were represented using at least ten Fourier modes in order to reduce the potential error margin.
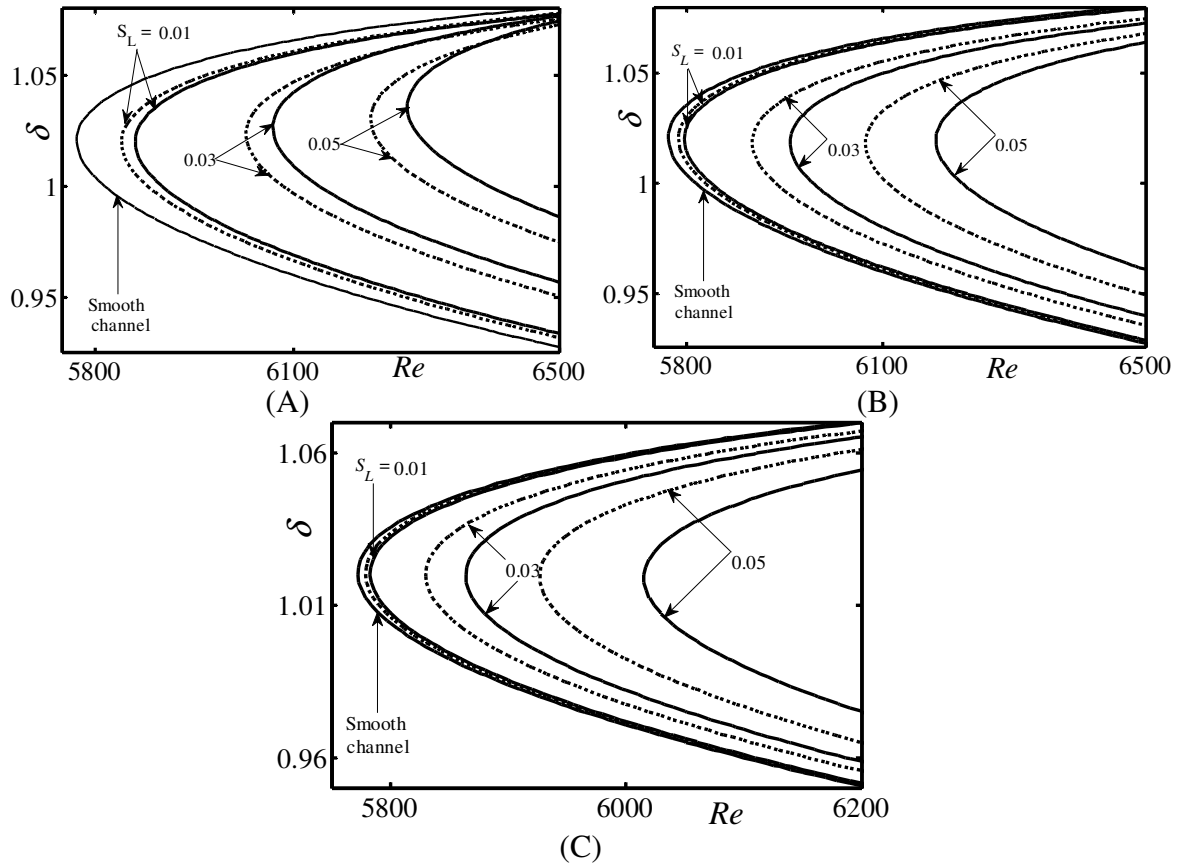
Figure 5-19: *Neutral curves in the (Re, δ)-plane for channel fitted with optimal, equal-depths grooves at the lower wall. Groove geometry is represented by the universal trapezoid with $a = b = \lambda/8$ and $c = d = 3\lambda/8$ (see Figure* **5-18***A for notation). Results for sinusoidal grooves are given for reference (dashed lines). Figure* **5-19***A, Figure* **5-19***B and Figure* **5-19***C provide results for the groove wave numbers $\beta = 0.2, 0.5,$ and 0.8, respectively.*

Neutral curves in the (Re, δ)-plane for the equal-depth grooves represented using the universal trapezoid are displayed in Figure **5-19**. It can be seen that such grooves stabilize

the flow beyond what is possible with the sinusoidal grooves, however, the corresponding increase of Re_c is fairly small. Figure **5-20** displays neutral curves for the unequal-depth grooves at the lower wall with heights fixed at $S_{L,U} = 0.01$, 0.03, 0.05 and depths determined by the optimization process. There are no reference curves as a single Fourier mode cannot capture such geometries. Since the optimal depth increases significantly with reduction of β and increase of $S_{L,U}$, results are presented only for those cases where the depth did not breach the limit of 0.05 used throughout this analysis. It can be seen that the range of stabilization achieved with these grooves is similar to that found in the case of the equal-depth grooves (compare Figure **5-19** and Figure **5-20**).
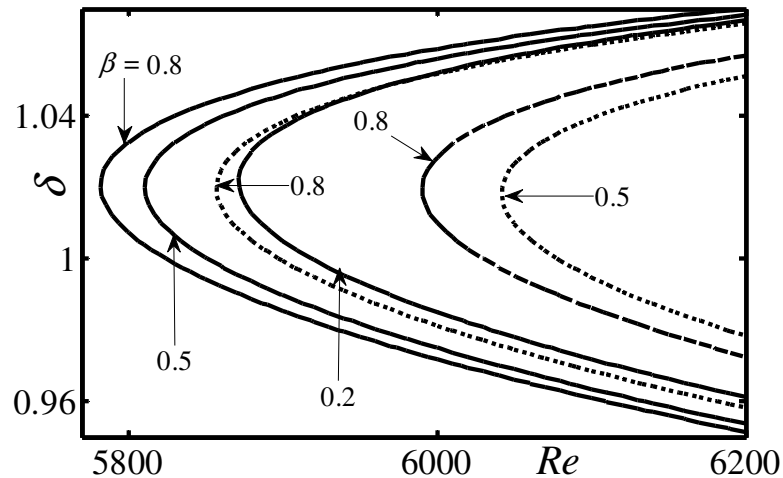
Figure 5-20: *Neutral curves in the (Re, δ)-plane for channel fitted with the optimal unequal-depth grooves at the lower wall. Groove geometry is represented using the universal Gaussian function. Solid, dashed and dashed-dotted lines correspond to grooves with the amplitudes $S_{L,U} = 0.01$, 0.03 and 0.05, respectively. Results are presented only for these cases where the optimal depth has not breached the limit of 0.05 used throughout this analysis. Three curves are given for $\beta = 0.8$ ($S_{L,U} = 0.01$, 0.03, 0.05), two curves are given for $\beta = 0.5$ ($S_{L,U} = 0.01$, 0.03) and one curve is given for $\beta = 0.2$ ($S_{L,U} = 0.01$).*

5.5 Summary

Analysis of stability of flow in a channel fitted with longitudinal grooves has been carried out. Only grooves with amplitude less than 0.05 were considered. Grooves may have an arbitrary but Fourier transformable form. As there is an uncountable number of possible

groove shapes, the applicability of the reduced geometry concept has been investigated; it has been shown that such model applies to the analysis of flow stability in the presence of longitudinal grooves.

Detailed analysis has been carried out for sinusoidal grooves, i.e., grooves represented by a single Fourier mode. Only disturbances corresponding to travelling waves in the limit of zero groove amplitude have been found. It has been shown that disturbances corresponding to the two-dimensional waves in the limit of zero groove amplitude play the critical role in the grooved channel.

Presence of grooves leads to flow stabilization for groove wave numbers $\beta < \beta_{tran} \approx$ 4.22 and flow destabilization for larger β's. The destabilization is quite strong as the critical Reynolds number increases fairly rapidly with an increase of β, but stabilization associated with the reduction of β is mild.

The topology of the disturbance velocity field at the onset is highly three-dimensional. Its structure is rather simple for large β's with groove effects limited to the neighborhood of the grooved wall. Reduction of β below β_{tran} leads to large changes and increased complexity of the flow structure with groove effects visible in the whole domain.

Special attention has been paid to the effects of long wavelength, drag reducing grooves. It has been shown that such grooves lead to a small increase of the critical Reynolds number compared with the smooth channel. The stabilizing effect has been found in the case of the optimal equal-depth grooves as well as in the case of the optimal unequal-depth grooves.

6 Conclusions and Recommendations

6.1 Conclusions

Responses of the annular and planar flows to the presence of grooves have been studied. The analysis started with the development of the required methodology, i.e., spectrally accurate algorithms capable of capturing effects of grooves. New algorithms suitable for analysis of flows in annuli bounded by walls with either axisymmetric or longitudinal grooves have been developed. The algorithms use Fourier expansions in the azimuthal and axial directions and Chebyshev expansions in the radial direction. The computational domain has a regular form with the boundaries of the flow domain immersed inside the computational domain. The flow boundary conditions are enforced using the immersed boundary conditions concept (IBC). The field equations are converted into algebraic equations using Galerkin projection method. The complete discretization process for the field equations is independent of geometry of the flow domain and can be done once regardless of the groove shape being of interest. Information about the groove geometry enters discretization process in the form of boundary relations. These relations need to be changed as a function of geometry being of interest but the associated cost represents a minimal fraction of the overall cost of the computations. The proposed algorithms are therefore well suited for analyses that involve geometry optimization. The complete matrix of coefficient includes contributions from the field equations, which remains the same regardless of geometry being of interest, and contributions from the boundary relations. A special linear solver that takes advantage of the structure of this matrix has been developed. This solver increases computational speed by a factor $O(100)$ and reduces storage requirement by a factor of $O(100)$ as compared to methods that do not take advantage of the matrix structure. Various tests have been carried out in order to demonstrate the spectral accuracy of the discretization process and the spectral accuracy of the enforcement of the boundary conditions using the IBC concept.

A systematic analysis of variations of the pressure gradient required to maintain laminar flows through an annuli fitted with longitudinal grooves has been carried out. The main objective of the analysis was the identification of the forms of the grooves that result in the reduction of the pressure gradient below the level needed to maintain the same flow

in the smooth annuli. It has been demonstrated that the groove-induced changes in the pressure drop can be represented as a superposition of a pressure drop due to a change in the average position of the bounding cylinders and a pressure drop due to the flow modulations induced by the shape of the grooves. The former effect can be evaluated analytically while the latter requires explicit computations.

Detailed analysis of the modulation effects has been carried out. It has been demonstrated that a reduced order model is an effective tool for the extraction of features of groove geometry that are relevant to the drag generation. In the case of the equal-depth grooves, one Fourier mode from the Fourier expansion representing the annulus geometry is sufficient to predict pressure losses with accuracy sufficient for most applications. The maximum depth and the maximum height are the same for such grooves. It is shown that the presence of the grooves may lead to a reduction of the pressure loss in spite of an increase of the surface wetted area. The drag decreasing grooves are characterized by the groove wave number M/R_1 smaller than a certain critical value, where M denotes the number of grooves being used and R_1 stands for the radius of the annulus; this number marginally depends on the groove amplitude and does not depend on the flow Reynolds number. It has been shown that the drag reduction mechanism relies on the re-arrangement of the bulk flow that leads to the largest mass flow taking place in the area of the largest annulus opening.

A search for the form of the grooves that results in the largest drag decrease, i.e. the optimal shape, has been carried out. It has been shown that the reduced order model involving 3-4 Fourier modes is able to capture drag reducing characteristics of such grooves with accuracy sufficient for most applications. It has been shown that the shape of the optimal grooves depends on the constraints. Detailed analysis has been carried out for two classes of constraints, i.e. the equal-depth grooves and the un-equal-depth grooves.

It has been found that in the case of the equal-depth grooves the optimal shape changes vary little as a function of the flow and geometry parameters and can be approximated using a special form of trapezoid. The error of such an approximation is generally

negligible unless the geometry parameters place the groove closed to the border that separates the drag-reducing grooves from the drag increasing grooves. The optimal grooves have nearly the same form regardless of whether they are placed at the inner or at the outer cylinders. The most effective placement of the grooves at both cylinders corresponds to the half wavelength shift in the circumferential direction between both sets of grooves with their shapes being nearly identical to those found in the case of annuli with only one grooved cylinder. Approximately the same drag reduction is produced by fitting one cylinder with grooves as fitting both cylinders but with the grooves with half amplitude.

Drag reduction is a non-monotonic function of the groove depth in the case of the unequal-depth grooves. In this case, the maximum height and the maximum depth are not the same. The depth that gives the largest drag reduction for a given height, the optimal depth, as well as the corresponding groove shape define the optimal geometry. The properties of the optimal geometry can be determined directly through the optimization process. It has been shown that the optimal shape forming the optimal geometry can be approximated using a Gaussian function. The maximum possible drag reduction, corresponding to the optimal geometry, has been determined for a range of parameters of practical interest. It has been shown that this reduction is significantly larger than the reduction associated with the equal-depth grooves. The optimal geometry is nearly the same for the outer and inner cylinders. Placement of grooves on both cylinders produces the largest drag reduction when they are shifted with respect to each other by a half wavelength in the circumferential direction.

Analysis of the heat transport in a channel with differentially heated walls has been carried out. The analysis has been carried out under the subcritical conditions when no secondary flow structures may appear in a natural manner. A method has been sought for maximization of the heat flow across the channel through the improvement of the conductive heat transport rather than through the creation of additional flow mixing. The increase of the heat transport needs to occur in a manner that does not increase but, preferably, decreases the flow losses. The channel was modified by fitting either one or both walls with grooves parallel to the flow direction. The shape of the grooves that

would produce the best improvement in the overall system performance has been sought. The system performance was measured using the thermal enhancement factor whose reduction measures the performance gains.

Grooves with arbitrary shapes have been considered. It has been demonstrated that a reduced geometry model, where the actual shape of the groove is replaced by the dominant Fourier mode from the Fourier expansion representing this geometry, can be used to approximate the flow losses with an acceptable accuracy. This means that fine geometry details are irrelevant as far as the flow losses are concerned. The overall parameterization of the flow losses in terms of the groove wave number and the amplitude has been given. The available results show that the presence of grooves reduces the flow losses when grooves with a sufficiently long wavelength are used. The reduced geometry model cannot be used to approximate the heat flow as fine details of groove geometry contribute significantly to the overall heat flow. The overall parameterization of the heat flow in terms of the groove wave number and the amplitude shows an increase of the heat flow, regardless of the groove wave number, compared to the smooth channel, with the magnitude of the heat flow gain significantly increasing with an increase of the groove wave number.

It is possible to use the reduced geometry model when a balanced approach is considered, i.e. an increase of the heat flow is as important as a decrease of the flow losses. The groove shape optimization has been carried out under such conditions. It has been shown that the use of 4-5 Fourier modes was sufficient to capture the optimal shapes. Two types of constraints have been used. The first enforces the same groove height and depth and leads to the equal-depth grooves. The second keeps a fixed groove height but the groove depth is treated as an unknown that must be determined as a part of the optimization process leading to the unequal-depth grooves. The optimization process has been focused on the groove wave numbers that lead to reduced flow losses because such grooves produce superior gains for the overall system performance. It has been shown that the equal-depth optimal grooves can be closely approximated by a universal trapezoid. In the case of the unequal-depth groove, there exists a certain depth that leads to the best system performance. This depth, the optimal depth, and the corresponding groove shape define

the optimal geometry. It has been shown that the groove shape in the optimal geometry can be approximated by a Gaussian function.

Use of the optimized grooves improves system performance by about 20-30% compared to simple sinusoidal grooves. When both walls are grooved, the best performance corresponds to grooves shifted with respect to each other by half wavelength. Similar performance is achieved either by placing grooves on one wall or by placing them on both walls but with amplitude reduced by 50%.

The above predictions apply to laminar flows only. The range of the Reynolds numbers where laminar flows may exist can be determined using stability analysis.

Analysis of stability of flow in a channel fitted with longitudinal grooves has been carried out. Only grooves with amplitude less than 0.05 were considered. It is known that, in general, effects of grooves can be divided into effects associated with the change in the mean position of the wall and the effects associated with the shape-induced modulations. This analysis has been focused on the modulation effects. Grooves may have an arbitrary but Fourier transformable form. As there is an uncountable number of possible groove shapes, the applicability of the reduced geometry concept has been investigated; it has been shown that such model applies to the analysis of flow stability in the presence of longitudinal grooves. This model permits replacement of an arbitrary groove with the leading term from the Fourier expansion describing its geometry. The difference between the critical Reynolds numbers determined using either the complete groove geometry or just the leading Fourier term from its Fourier representation is below 1% for the system parameters used in this study.

Detailed analysis has been carried out for sinusoidal grooves, i.e., grooves represented by a single Fourier mode. Only disturbances corresponding to the travelling waves in the limit of zero groove amplitude have been found. It is known that the two-dimensional waves play a critical role in a smooth channel. It has been shown that disturbances corresponding to the two-dimensional waves in the limit of zero groove amplitude play the critical role in the grooved channel.

Presence of grooves leads to the flow stabilization for the groove wave numbers $\beta <$ $\beta_{tran} \approx 4.22$ and the flow destabilization for larger β. The destabilization is quite strong as the critical Reynolds number increases fairly rapidly with an increase of β, but stabilization associated with the reduction of β is mild. The stabilizing/destabilizing effects increase with an increase of the groove amplitude. Variations of the critical Reynolds number over the whole range of the groove wave numbers and the groove amplitudes of interest have been given. There results permit assessment of the stability properties of grooves of an arbitrary shape through invocation of the reduced geometry model.

The topology of the disturbance velocity field at the onset is highly three-dimensional. Its structure is rather simple for large β's with groove effects limited to the neighborhood of the grooved wall. Reduction of β below β_{tran} leads to large changes and increased complexity of the flow structure with groove effects visible in the whole flow domain.

Special attention has been paid to the effects of long wavelength, drag reducing grooves. It has been shown that such grooves lead to a small increase of the critical Reynolds number compared with the smooth channel. The stabilizing effect has been found in the case of the optimal equal-depth grooves as well as in the case of the optimal unequal-depth grooves. It can be concluded that the use of the drag reducing grooves does not lead to an early breakdown into turbulence and, thus, the flow should remain laminar over the same range of Reynolds numbers as found in the case of smooth channel.

6.2 Recommendations for future work

Effects of a certain class of surface topographies on the heat and fluid flow characteristics have been presented in this dissertation. In order to further advance knowledge in this area, the following directions may be considered for the future work:

i) In this dissertation, the effects of longitudinal grooves on annular flows have been investigated. A similar analysis can be extended to transverse grooves. The required algorithm, which can deal with flows in annuli bounded by transverse grooves, has already been developed as a part of this dissertation. The analysis

can also be extended to three-dimensional grooves. There should be no conceptual difficulties associated with the development of the necessary tools as the methodology used in this dissertation is in principle capable of dealing with arbitrary three-dimensional grooves. It may necessary to develop efficient solvers that would permit to solve the flow problem with a reasonable computational cost. Development of such tools provides flexibility required to study all possible groove shapes that are of practical interest in various engineering fields.

ii) Time-dependent surface topographies are encountered in many practical applications. The algorithms proposed in this research can be extended to solve problems involving time-dependent geometries.

iii) Presence of grooves changes the stability characteristics of annular flows. Studying the stability behavior of annular flow in the presence of different classes of surface grooves is of great interest and can represent an avenue for further research. For that purpose, the linear stability equations should be developed in such a way that they can account for three-dimensional disturbances. These equations can be solved to determine the stability properties of different forms of grooves.

iv) Although a vast amount of work has been devoted to studying the effects of surface irregularities in the fully turbulent flow regime, the conclusions regarding their effects are not complete and thus there still exists many opportunities for research to be conducted in this field. A systematic analysis of the effects of different features of surface geometries on turbulent flow response is of special interest.

v) Natural convection is driven by buoyancy force, which was not included in the analysis carried out as a part of this research. Contribution of buoyancy can be considered in the further analysis of heat transfer.

vi) With the knowledge of the findings presented in this dissertation, new research in the area of the experimental fluid dynamics can be proposed. It is worthwhile to

set up experiments to verify the current predictions and to use this knowledge for the development of new, energy efficient devices.

References

Adachi, T. & Imai, S. 2007 Three-dimensional linear stability of natural convection in horizontal concentric annuli, *Inter. J. Heat and Mass Transfer*, **50**, 1388-1396.

Allen, P. H. G. & Karayiannis, T. G. 1995 Electrohydrodynamic enhancement of heat transfer and fluid flow, Review paper, *Heat Recovery Systems & CHP,* **15**, 389-423.

Angelis, V. D., Lombardi, P. & Banerjee, S. 1997 Direct numerical simulation of turbulent flow over a wavy wall, *Phys. Fluids*, **9**, 2429-2442.

Asai, M. & Floryan, J. M. 2006 Experiments on the linear instability of flow in a wavy channel, *Eur. J. Mech. B/Fluids,* **25**, 971–986.

Bakhsheshi, M. F., Floryan, J. M. & Kaloni, P. N. 2011 Spectral Method for Analyzing Motions of Ellis Fluid over Corrugated Boundaries. *J. Fluid Engineering*, **133**, 021401.

Bayly B. J., Orszag, S. A. & Herbert, T. 1988 Instability Mechanisms in Shear-Flow Transition, *Ann. Rev. Fluid Mech.* **20**, 359-391.

Bechert, D. W. & Bartenwerfer, M. 1989 The viscous flow on surfaces with longitudinal ribs, *J. Fluid Mech.,* **206**, 105–129.

Bechert, D. W., Bruse, M. , Hage, W. , Van Der Hoeven, J. G. T. & Hoppe, G. 1997, Experiments on drag-reducing surfaces and their optimization with an adjustable geometry, *J. Fluid Mech.,* **338**, 59–87.

Bénard, H. 1900 Les tourbillons cellulaires dans une nappe liquide, *Revue Gen. Sci. Pure Appl.*, **11**, 1261-1271.

Bergles, A. E. 1998 *Handbook of Heat Transfer*, McGraw-Hill, New York, NY, USA, 3rd edition.

Bergles, A. E. 2001 The implications and challenges of enhanced heat transfer for the chemical process industries, *Chemical Engineering Research and Design,* **79,** 437–444.

Bloch, F. 1928 Über die Quantenmechanik der Elektronen in Kristallgittern, *Z. Physik,* **52**, 555–600.

Bodenschatz, E., Pesh, W. & Ahlers, G., 2000, Recent developments in Rayleigh-Bénard convection, *Ann. Rev. Fluid Mech.,* 32, 709-778.

Byrd, R. H., Hribar, M. E. & Nocedal, J. 1999 An interior point algorithm for large-scale nonlinear programming, *SIAM Journal on Optimization,* **9**, 877-900.

Byrd, R. H., Gilbert, J. C. & Nocedal, J. 2000 A trust region method based on interior point techniques for nonlinear programming, *Mathematical Programming,* **89**, 149-185.

Chang, S. W., Liou, T. M., Chiang, K. F. & Hong, G. F. 2008 Heat transfer and pressure drop in rectangular channel with compound roughness of V-shaped ribs and deepened scales, *Int. J. Heat Mass Transfer,* **51,** 457–468.

Cheng, C. H., Chan, C. K. & Lai, G. J. 2008 Shape design of millimeter-scale air channels for enhancing heat transfer and reducing pressure drop, *Int. J. Heat Mass Transfer,* **51**, 2335–2345.

Cheng, Y. P., Teo, C. J. & Khoo, B. C. 2009 Microchannels flows with superhydrophobic surfaces: effects of Reynolds number and pattern width to channel height ratio, *Phys. Fluids,* **21**, 1–12.

Cho, H. H., Wu, S. J. & Kwon, H. J. 2000 Local Heat/Mass Transfer Measurement in a Rectangular Duct with Discrete Ribs, *ASME J. Turbomachinery,* **122**, 579-586.

Choi, K. S. & Orchard, D. 1997 Turbulence management using riblets for heat and momentum transfer. *Exp. Thermal Fluid Sci*., **15**, 109–124.

Chyu, M. K. & Natarjan, V. 1996 Heat transfer on the base surface of three-dimensional protruding elements, *Int. J. Heat Mass Transfer,* **39**, 2925-2935.

Coddington, E. A., Levinson, N. 1965 *Theory of Ordinary Differential Equations*, McGraw-Hill.

Coleman, T. F., Li, Y. 1996 An interior, trust region approach to nonlinear minimization subject to bounds, *SIAM J. on Optimization,* **6**, 418-445.

Coleman, T. F., Li, Y. 1994 On the convergence of reflective Newton method for large-scale nonlinear minimization subject to bounds, *Mathematical Programming,* **67**, 189-224.

Cotrell, D.L., Pearlstein, A.L., 2006, Linear stability of spiral and annular Poiseuille flow for small radius ratio, *J. Fluid Mech.*, **547**, 1-20.

Croce, G. & D'Agaro, P. 2005 Numerical simulation of roughness effect on microchannel heat transfer and pressure drop in laminar flow, *J. Phys. D: Appl. Phys.*, **38**, 1518-1530.

Darcy, H. 1857 *Recherches expérimentales relatives au mouvement de l'eau dans les tuyaux.*, Paris, Mallet-Bachelier.

Davis, A. M. J. & Lauga, E. 2009 The friction of a mesh-like super-hydrophobic surface, *Phys. Fluids,* **21**, 1–8.

Del Rey Fernandez, D. C., Husain, S. Z. & Floryan, J. M. 2010 Immersed Boundary Conditions Method for Heat Conduction Problems in Slots with Time-Dependent Geometry, *Int. J. Numer. Meth. Fluids*, **67**, 478-500.

Dewan, A. Mahanta, P., Raju, K. S. & Kumar, P. S. 2004 Review of passive heat transfer augmentation techniques, *Proceedings of the Institution of Mechanical Engineers, Part A: J. Power and Energy,* **218**, 509-527.

Dou, H.S., Khoo, B.C. & Tsai, H.M. 2010 Determining the critical conditions of turbulent transition in s fully developed annulus flow, *J. Petroleum Science and Engineering,* **73**, 41-47.

Dou, H. S. 2011 Physics of flow instability and turbulent transition in shear flows, *Int. J. of Physical Science*, **6**, 1411-1425.

Dyko, M. P., Vafai, K. & Mojtabi, A. K. 1999 A numerical and experimental investigation of stability of natural convective flows within a horizontal annulus, *J. Fluid Mech.*, **381**, 27-61.

Eckhardt, B., Schneider, T. M., Hof, B. & Westerweel, J. 2007 Turbulent transition in pipe flow, *Annu. Rev. Fluid Mech.*, **39**, 447–468.

Fabbri, G. 1997 A genetic algorithm for fin profile optimization, *Int. J. Heat Mass Transfer,* **40**, 2165–2172.

Fabbri, G. 1998 Heat transfer optimization in finned annular ducts under laminar flow conditions, *Heat Transfer Eng.,* **19**, 42–54.

Fabbri, G. 1998 Heat transfer optimization in internally finned tubes under laminar flow conditions, *Int. J. Heat Mass Transfer,* **41**, 1243–1253.

Fabbri, G. 1998 Optimization of heat transfer through finned dissipators cooled by laminar flow, *Int. J. Heat Fluid Flow,* **19,** 644–654.

Fiebig, M. 1995 Embedded vortices in internal flow: heat transfer and pressure loss enhancement, *Int. J. Heat and Fluid Flow,* **16**, 376-388.

Floryan, J. M. 1997 Stability of wall-bounded shear layers in the presence of simulated distributed surface roughness. *J. Fluid Mech.,* **335**, 29–55.

Floryan, J. M. 2002 Centrifugal instability of Couette flow over a wavy wall, *Phys. Fluids,* **14**, 312–322.

Floryan, J. M. 2003 Vortex instability in a converging-diverging channel, *J. Fluid Mech*., **482**, 17–50.

Floryan, J. M. 2005 Two-dimensional instability of flow in a rough channel. *Phys. Fluids*., **17**,044101.

Floryan, J. M. 2007 Three-dimensional instabilities of laminar flow in a rough channel and the concept of hydraulically smooth wall, *Eur. J. Mech. B/Fluids,* **26**, 305–329.

Floryan, J. M. & Floryan, C. 2010 Travelling wave instability in a diverging-converging channel, *Fluid Dyn. Res.,* **42**, 025509.

Floryan, J. M. & Asai, M. 2011 On the transition between distributed and isolated surface roughness and its effect on the stability of channel flow. *Phys. Fluids,* **23**, 104101.

Freai, C., Lűscher, P. & Wintermantel, E. 2000 Thread-annular flow in vertical pipes, *J. Fluid Mech.,* **410**, 185-210.

Frohnapfel, B., Jovanović, J. & Delgado, A. 2007 Experimental investigations of turbulent drag reduction by surface-embedded grooves, *J. Fluid Mech.,* **590**, 107–116.

Gad-el-Hak, M., Pollard A. & Bonnet J. P. *Flow Control*, Springer, 1997

Gage, K. S. & Reid W. H. 1968 The stability of thermally stratified plane Poiseuille flow, *J. Fluid Mech.*, **33**, 21-32.

Gamrat, G., Favre-Marinet, M., Le Person, S., Bavière, R. & Ayela, F. 2008 An experimental study and modeling of roughness effects on laminar flow in microchannels. *J. Fluid Mech.,* **594**, 399–423.

Garcia-Mayoral, R., & Jimenez, J., 2011 Hydrodynamic stability and breakdown of the viscous regime over riblets, *J.Fluid Mech.,* **678**, 317-347.

Garg, V. K. 1980 Spatial stability of concentric annular flow. *J. Phys. Soc. Japan,* **49**, 1577–1583.

Gee, D. L. & Webb, R. L. 1980 Forced convection heat transfer in helically rib-roughened tubes, *Int. J. Heat Mass Transfer,* **23**, 1127-1136.

Gibbs, J. W. 1898 Fourier's Series, *Nature,* **59**, (1522), 200.

Gibbs, J. W. 1899 Fourier's Series, *Nature,* **59**, (1539), 606.

Girault, V., Glowinski, R. & Pan, T. W. 2000 A Fictitious-domain method with distributed multiplier for the Stokes problem, *Appl. Nonlinear Anal.,* Springer, 159–174.

Hagen, G. 1854 Uber den Einfluss der Temperatur auf die Bewegung des Wasser in Röhren. *Math. Abh. Akad. Wiss.,* **17**, Berlin.

Heaton, J. 2008 Linear instability of annular Poiseuille flow, *J. Fluid Mech.,* **610**, 391-406.

Herbert, T., 1977, Finite amplitude stability of plane parallel flows, *AGARD Conf. Proc.*, **224**, 3.1-3.10.

Herwig, H., Gloss, D. & Wenterodt, T. 2008 A new approach to understanding and modeling the influence of wall roughness on friction factors for pipe and channel flows. *J. Fluid Mech.,* **613**, 35–53.

Husain, S. Z. & Floryan, J. M. 2007 Immersed boundary conditions method for unsteady flow problems described by the Laplace operator, *Int. J. Numer. Meth. Fluids,* **56**, 1765–1786.

Husain, S. Z. & Floryan, J. M. 2008a Implicit spectrally-accurate method for moving boundary problems using immersed boundary conditions concept, *J. Comput. Phys.*, **227**, 4459–4477.

Husain, S. Z. & Floryan, J. M. 2008b Gridless spectral algorithm for Stokes flow with moving boundaries, *Comput. Methods Appl. Mech. Engrg.,* **198**, 245–259.

Husain, S. Z. & Floryan, J. M. 2010 Spectrally-accurate algorithm for moving boundary problems for the Navier-Stokes equations, *J. Comput. Phys.,* **229**, 2287–2313.

Husain, S. Z. & Floryan, J. M. 2013 Efficient solvers for the IBC method, *Computers & Fluids*, **84**, 127-140

Husain, S. Z., Szumbarski, J. & Floryan, J. M. 2009 Over-determined formulation of the immersed boundary condition method, *Comput. Methods Appl. Mech. Engrg*., **199**, 94–112.

Jacobi, A. M. & Shah, R. K. 1998 Air-side flow and heat transfer in compact heat exchangers: A discussion of enhancement mechanisms, *Heat Transfer Eng,* **19**, 29-41.

Jackson, D. & Launder, B. 2007 Osborne Reynolds and the Publication of His Papers on Turbulent Flow, *Annu. Rev. Fluid Mech*. **39**, 19–35.

Jiang, Y. & Floryan, J. M. 2005 Finite-difference 4th-order compact scheme for the direct numerical simulation of instabilities of shear layers, *Int. J. Numer. Meth. Fluids*, **48**, 1259-1281.

Jimenez, J. 2004 Turbulent flows over rough walls, *Ann. Rev. Fluid Mech*., **36**, 173–196.

Judy, J., Maynes, D. & Webb, B. W. 2002 Characterization of frictional pressure drop for liquid flows through microchannels, *Int. J. Heat Mass Transfer,* **45**, 3477-3489.

Jung, Y. C. & Bhushan, B. 2010 Biomimetic structures for fluid drag reduction in laminar and turbulent flows, *J. Phys.: Condens. Matter,* **22,** 1–9.

Kandlikar, S. G., Schmitt, D., Carrano, A. L. & Taylor J. B. 2005 Characterization of surface roughness effects on pressure drop in single-phase flow in mini-channels, *Phys. Fluids,* **17,** 1–11.

Kang, S., Patil, B. & Zarate, J. A. 2001 Isothermal and heated turbulent upflow in a vertical annular channel-part I experimental measurements. *Inter. J. Heat Mass Transfer*, **44**, 1171–1184.

Kim, K. Y. & Kim, S. S. 2002 Shape optimization of rib-roughened surface to enhance turbulent heat transfer, *Int. J. Heat Mass Transfer,* **45**, 2719–2727.

Kleinstreuer, C. & Koo, J. 2004 Computational analysis of wall roughness effects for liquid flow in micro-conduits, *J. Fluid Eng.,* **126,** 1–9.

Labonia, G. & Guj, G. 1998 Natural convection in a horizontal concentric cylindrical annulus: oscillatory flow and transition to chaos, *J. Fluid Mech.*, **375**, 179-202.

Lee, J. S., Xu, X. & Pletcher, R. H. 2004 Large eddy simulation of heated vertical annular pipe flow in fully developed turbulent mixed convection, *Inter. J. of Heat and Mass Transfer*, **47**, 437-446.

Ligrani, P. M., Oliviera, M. M. & Blaskovich, T. 2003 Comparison of heat transfer augmentation techniques, *AIAA J.*, **41,** 337-362.

Lindemann, A. 1985 Turbulent Reynolds analogy factors for nonplanar surface microgeometries. *J. Spacecraft*, **22**, 581–582.

Liu, D. & Garimella, S. V. 2004 Investigation of liquid flow in microchannels, *AIAA J. Thermophys. Heat Transfer,* **18**, 65–72.

Lu, G. & Wang, J. 2008 Experimental investigation on flow characteristics in a narrow annulus, *Heat and Mass Transfer*, **44** (4), 495-499.

Lucini, P., Manzo, F. & Pozzi, A., 1991, Resistance of grooved surface to parallel flow and cross-flow, *J. Fluid Mech.*, **228**, 87-109.

Mahadevan, R. & Lilley, G. M. 1977 The stability of axial flow between concentric cylinders to asymmetric disturbances. AGARD CP 224, pp. 9-1–9-10.

Manson, J. C. & Handscomb, D. C. 2003 *Chebyshev polynomials*, CRC Press, Boca Raton Florida.

Marcello, A., Medeiros, F. & Silva-Freire, A. P. 1992 The transfer of heat in turbulent boundary layers with injection or suction: universal laws and Stanton number equation, *Int. J. Heat Mass Transfer,* **35**, 991-995.

Maynes, D., Jeffs, K., Woolford, B. & Webb, B. W. 2007 Laminar flow in a microchannel with hydrophobic surface patterned microribs oriented parallel to the flow direction, *Phys. Fluids,* **19**, 1–12.

McLean, J. W. 1983 Computations of turbulent flow over a moving wavy boundary, *Phys. Fluids*, **26**, 2065-2073.

Mittal, R. & Iaccarino, G. 2005 Immersed boundary methods, *Annu. Rev. Fluid Mech.,* **37**, 239–261.

Mohammadi, A., Floryan, J. M. & Kaloni, P. N. 2010 Spectrally accurate method for analysis of stationary flows of second-order fluids in rough micro-channels, *Int. J. Numer. Meth. Fluids,* **66**, 509-536.

Mohammadi, A. & Floryan, J. M. 2012a Spectral algorithm for the analysis of flows in grooved channels. *Intl J. Numer. Meth. Fluids* **69**, 606–638.

Mohammadi, A. & Floryan, J. M. 2012b Mechanism of drag generation by surface corrugation, *Phys. Fluids,* **24**, 013602.

Mohammadi, A. & Floryan, J. M. 2013a Pressure losses in grooved channels, *J. Fluid Mech.*, **725**, 23-54.

Mohammadi, A. & Floryan, J. M. 2013b Groove Optimization for Drag Reduction, *Phys. Fluids,* **25***,* 113601.

Moody, L. F. & Princeton N. J. 1944 Friction factors for pipe flow. *Trans. ASME,* **66**, 671–684.

Morini, G. L. 2004 Single-phase convective heat transfer in microchannels: a review of experimental results *Int. J. Thermal Sci*., **43**, 631–651.

Morkovin, M. V. 1990 On roughness-induced transition: facts, views and speculations. In *Instability and Transition* (ed. M.Y.Hussaini and R.G.Voigt), 1, 281–295. ICASE/NASA LARC Series, Springer, New York.

Mott, J. E. & Joseph, D. D. 1968 Stability of parallel flow between concentric cylinders, *Phys. Fluids*, **11**(10), 2065-2073.

Nesis, E. I., Shatalov, A. F. & Karmatskii, N. P. 1994 Dependence of the heat transfer coefficient on the vibration amplitude and frequency of a vertical thin heater, *J. Engineering Physics and Thermophysics,* **67**, No. 1-2.

Nikuradse, J. 1933 Strömungsgesetze in Rauhen Rohren, *VDI-Forschungscheft* #361; also *NACA TM* 1292 (1950).

Nicolas, X. 2002 Bibliographical review on the Poiseuille-Rayleigh-Bénard flows: the mixed convection flows in horizontal rectangular ducts heated from below, *International Journal of Thermal Sciences*, **41**, 961-1016.

Nobile, E., Pinto, F. & Rizzetto, G. 2006 Geometric parameterization and multiobjective shape optimization of convective periodic channels, *Numerical Heat Transfer, Part B,* **50,** 425-453

Ng, C. O. & Wang, C. Y. 2009 Stokes shear flow over a grating: implication for superhydrophobic slip, *Phys. Fluids,* **21**, 1–12.

Nye, J. F. 1969 A calculation on the sliding of ice over a wavy surface using a Newtonian viscous approximation. *Proc. Roy. Soc. A,* **311**, 445–467.

Orszag, S. A. 1971 Accurate solutions of the Orr-Sommerfeld stability equation, *J. Fluid Mech*. **50**, 689-704.

Orszag, S.A, and Patera, A.T. 1983, Secondary instability of wall-bounded shear flows, *J. Fluid Mech*. **128**, 347-385.

Padilla, E. L. M. & Silveira-Neto, A. 2008 Large-eddy simulation of transition to turbulence in natural convection in a horizontal annular cavity, *Inter. J. Heat and Mass Transfer*, **51**, 3656-3668.

Papanastasiou, T. C., Georgiou, G. C. & Alexandrou, A. N. 1999 *Viscous Fluid Flow*, CRC Press.

Papautsky, I., Brazzle, J., Ameel, T. & Frazier, A. B. 1999 Laminar fluid behavior in microchannels using micropolar fluid theory. *Sensors Actuators A,* **73**, 101–108.

Parussini, L. 2008 Fictitious domain approach via Lagrange multipliers with least squares spectral Element Method, *J. Sci. Comput*., **37**, 316–335.

Petrone, G. A., Chenier, E. & Lauriat, G. 2006 Stability analysis of natural convective flows in horizontal annuli: Effects of the axial and radial aspect ratios, *Phys. Fluids*, **18**, 104107.

Peskin, C. S. 1981 The fluid dynamics of heart valves: experimental, theoretical and computational methods. *Annu. Rev. Fluid Mech*., **14**, 235–259.

Peskin, C. S. 2002 The immersed boundary method, *Acta Numerica,* **11**, 479–517.

Rayleigh, J. W. S. 1880 On the stability, or instability, of certain fluid motions. *In Scientific Papers of Lord Rayleigh*, **1,** 474-487.

Rayleigh, J. W. S. 1916 On convection currents in a horizontal layer of fluid, when the higher temperature is on the under side, *Phil. Mag.*, **32**, 529-546.

Reynolds, O. 1883 An experimental investigation of the circumstances which determine whether the motion of water shall be direct or sinuous, and of the law of resistance in parallel channels. *Philos. Trans. R. Soc. London,* **174**, 935–982.

Saad, Y. 2003 *Iterative methods for sparse linear systems*, SIAM.

Saric, W. S., Carrillo, R. B. & Reibert, M. S. 1998 Nonlinear Stability and Transition in 3-D Boundary Layers. *Meccanica,* **33**,469–487.

Schlichting, H. 1979 *Boundary Layer Theory*. 7th ed., McGraw-Hill.

Seong-Ryong, P. & Wallace, J. M. 1994 Flow alteration and drag reduction by riblets in a turbulent boundary layer, *AIAA J.*, **32.1**, 31-38.

Sharp, K. V. & Adrian, R. J. 2004 Transition from laminar to turbulent flow in liquid filled microtubes. *Exps Fluids,* **36**, 741–747.

Siddique, M., Khaled, A. R. A., Abdulhafiz, N. I. & Boukhary, A. Y. 2010 Recent Advances in Heat Transfer Enhancements: A Review Report, *Int. J. Chemical Engineering,* **2010,** 1-28.

Sobhan, C. B. & Garimella, S. V. 2001 A comparative analysis of studies on heat transfer and fluid flow in microchannels. *Microscale Thermophys. Engng,* **5**, 293–311.

Squire, H. B. 1933 On the stability of three-dimensional distribution of viscous fluid between parallel walls, *Proc. Roy. Soc. London* **A142**, 621-628.

Stalio, E. & Nobile, E. 2003 Direct numerical simulation of heat transfer over riblets, *Int. J. Heat Fluid Flow,* **24**, 356–371.

Szumbarski, J. & Floryan, J. M. 1999 A direct spectral method for determination of flows over corrugated boundaries, *J. Comput. Phys.,* **153**, 378-402.

Szumbarski, J. & Floryan, J. M. 2006 Transient disturbance growth in a corrugated channel, *J. Fluid Mech.,* **568**, 243–272.

Thomas, S. C., Lykins, R. C. & Yerkes, K. L. 2001 Fully-developed laminar flow in sinusoidal grooves, *J. Fluid Eng.,* **123**, 656–661.

Tuckermann D. B. & Pease, R. F. 1981 High-performance heat sinking for VSLI, *IEEE Electron Dev.,* **2**, 126-129

Tullis, S. & Pollard, A. 1993 Modeling the time dependent flow over riblets in the viscous wall region, *Applied Scientific Research*, **50**, 299-314.

Valdes, J. R., Miana, M. J., Pelegay, J. L., Nunez, J. L. & Pűtz, T. 2007 Numerical investigation of the influence of roughness on the laminar incompressible fluid flow through annular microchannels, *Int. J. Heat Mass Transfer,* **50**, 1865-1878.

Walton, A. G., Labadin, J. & Yiong, S. P. 2010 Axial flow between sliding, non-concentric cylinders with applications to thread injection, *Quarterly Journal of Mechanics and Appl Math,* **63** 315-334.

Waltz, R. A., Morales, J. L., Nocedal, J. & Orban, D. 2006 An interior algorithm for nonlinear optimization that combines line search and trust region steps, *Mathematical Programming,* **107**, 391-408.

Walsh, M. J. & Weinstein L. 1979 Drag and heat transfer characteristics of small longitudinal ribbed surfaces. *AIAA J.*, **17**, 770–771.

Walsh, M. J. 1980 Drag characteristics of V-groove and transverse curvature riblets. In *Viscous Drag Reduction* (ed. *G.* R. Hough), *AIAA* **72**, 168–184.

Walsh, M. J. 1983 Riblets as a viscous drag reduction technique, *AIAA J.,* **21**, 485–486.

Wang, C. Y. 2003 Flow over a surface with parallel grooves, *Phys. Fluids*, **15**, 1114–1121.

Wibel, W. & Ehrhard, P. 2006 Experiments on liquid pressure-drop in rectangular micro-channels, subject to non-unity aspect ratio and finite roughness. *Proceedings of International Conference on Nano-channels*, *Micro-channels and Mini-channels*, June 19–21, Ireland, ICNMM2006-96116, 1–8.

Wibel, W. & Ehrhard, P. 2007 Experiments on the laminar/turbulent transition of liquid flows in rectangular micro channels. *Proceedings of the Fifth International Conference on Nanochannels*, *Microchannels and Minichannels*, June 18–20, Mexico, ICNMM2007, 1–8.

Xia, G., Chai, L., Zhou, M. & Wang, H. 2011 Effects of structural parameters on fluid flow and heat transfer in a microchannel with aligned fan-shaped reentrant cavities, *Int. J. Thermal Sciences,* **50**, 411-419.

Yoo, J. S. 1998 Natural convection in a narrow horizontal cylindrical annulus: $Pr \leq 0.3$, *Inter. J. of Heat and Mass Transfer*, **41**, 3055-3073.

Zarate, J. A., Roy, R. P. & Laporta, A. 2001. Isothermal and heated turbulent upflow in a vertical annular channel-part II numerical simulations. Inter. J. Heat Mass Transfer, 44, 1185–1199.

Appendices

Appendix A

Appendix A: Final discretized form of the field equation for the flow in annulus with transverse grooves

$$
\begin{aligned}
Re^{-1}\Big\{ & n^4\big[E_1\langle T_j, \xi^3 T_k\rangle + E_2\langle T_j, \xi^2 T_k\rangle + E_3\langle T_j, \xi T_k\rangle + E_4\langle T_j, T_k\rangle\big] \\
& + n^2\big[E_5\langle T_j, \xi^2 DT_k\rangle + E_6\langle T_j, \xi DT_k\rangle + 2E_7\langle T_j, DT_k\rangle\big] - 3E_8\langle T_j, DT_k\rangle \\
& -n^2\big[E_5\langle T_j, \xi^3 D^2 T_k\rangle + 6E_6\langle T_j, \xi^2 D^2 T_k\rangle + 6E_7\langle T_j, \xi D^2 T_k\rangle + E_9\langle T_j, D^2 T_k\rangle\big] \\
& + 3E_8\langle T_j, \xi D^2 T_k\rangle + E_{10}\langle T_j, D^2 T_k\rangle \\
& - 2\big[E_8\langle T_j, \xi^2 D^3 T_k\rangle + 2E_{10}\langle T_j, \xi D^3 T_k\rangle + 2E_{11}\langle T_j, D^3 T_k\rangle\big] \\
& + E_8\langle T_j, \xi^3 D^4 T_k\rangle + 3E_{10}\langle T_j, \xi^2 D^4 T_k\rangle + E_{11}\langle T_j, \xi D^4 T_k\rangle + E_{12}\langle T_j, D^4 T_k\rangle\Big\} G_k^{(n)} \\
= & -n^2\big[E_{13}\langle T_j, \xi^4 T_k\rangle + 4E_{14}\langle T_j, \xi^3 T_k\rangle\big] G_{zr,k}^{(n)} + nE_{15}\langle T_j, \xi^3 T_k\rangle G_{rr,k}^{(n)} \\
& + (E_{18} - 6n^2 E_{16})\langle T_j, \xi^2 T_k\rangle G_{zr,k}^{(n)} + 3nE_{17}\langle T_j, \xi^2 T_k\rangle G_{rr,k}^{(n)} \\
& 2(E_{21} - 2n^2 E_{19})\langle T_j, \xi T_k\rangle G_{zr,k}^{(n)} + 3nE_{20}\langle T_j, \xi T_k\rangle G_{rr,k}^{(n)} \\
& + \big[(E_{24} - n^2 E_{22})\langle T_j, T_k\rangle G_{zr,k}^{(n)} + nE_{23}\langle T_j, T_k\rangle G_{rr,k}^{(n)}\big] \\
& + E_{15}\langle T_j, \xi^4 DT_k\rangle\big[G_{rr,k}^{(n)} - G_{zz,k}^{(n)}\big] \\
& + \Big\{4E_{17}\big[G_{rr,k}^{(n)} - G_{zz,k}^{(n)}\big] - E_{18}G_{zr,k}^{(n)}\Big\}\langle T_j, \xi^3 DT_k\rangle \\
& + \Big\{6E_{20}\big[G_{rr,k}^{(n)} - G_{zz,k}^{(n)}\big] - 3E_{21}G_{zr,k}^{(n)}\Big\}\langle T_j, \xi^2 DT_k\rangle \\
& + \Big\{4E_{23}\big[G_{rr,k}^{(n)} - G_{zz,k}^{(n)}\big] - 3E_{24}G_{zr,k}^{(n)}\Big\}\langle T_j, \xi DT_k\rangle \\
& + \Big\{E_{25}\big[G_{rr,k}^{(n)} - G_{zz,k}^{(n)}\big] - E_{26}G_{zr,k}^{(n)}\Big\}\langle T_j, \xi DT_k\rangle \\
& - \big[E_{18}\langle T_j, \xi^4 D^2 T_k\rangle + 4E_{21}\langle T_j, \xi^3 D^2 T_k\rangle + 6E_{24}\langle T_j, \xi^2 D^2 T_k\rangle \\
& + 4E_{26}\langle T_j, \xi D^2 T_k\rangle + E_{27}\langle T_j, D^2 T_k\rangle\big] G_{zr,k}^{(n)},
\end{aligned}
\tag{A-1}
$$

where $j \in [0, N_T]$, $n \in [-N_M, N_M]$ and the coefficients E_i's are defined in Section 2.2.3.1. Equation (A-1) contains inner products of the type $\langle T_j, \xi^l D^m T_k\rangle$ where $0 \le l \le 4$ and $0 \le m \le 4$. Description of the method used for efficient evaluation of these products begins with the simplest products first.

Inner product of two Chebyshev polynomials is evaluated using their orthogonality properties, i.e.,

$$\langle T_j, T_k \rangle = \frac{\pi}{2} C_k \delta_{j,k},$$ (A-2)

where $\delta_{j,k}$ denotes the Kronecker delta function and

$$C_k = \begin{cases} 2, k = 0 \\ 1, k \geq 1 \end{cases}.$$ (A-3)

Evaluation of products involving the first derivative of a Chebyshev polynomial begins with expressing this derivative in terms of Chebyshev polynomials, i.e.,

$$DT_k = 2 \sum_{x=0}^{k-1} \frac{k T_x}{C_x}, k - x = \text{odd}, k \geq x + 1.$$ (A-4)

The inner product of this derivative and T_j can be evaluated as

$$\langle T_j, DT_k \rangle = 2 \sum_{x=0}^{k-1} \frac{\langle T_j, T_x \rangle}{C_x}, k - x = \text{odd}, k \geq x + 1.$$ (A-5)

Substitution of (A-2) into (A-5) brings the inner product to a simple form suitable for efficient evaluation, i.e.,

$$\langle T_j, DT_k \rangle = k\pi, k - j = \text{odd}, k \geq j + 1.$$ (A-6)

Evaluation of products involving the second derivative of a Chebyshev polynomial begins with expressing this derivative in terms of Chebyshev polynomials, i.e.,

$$D^2 T_k = \sum_{x=0}^{k-1} \frac{k(k^2 - x^2) T_x}{C_x}, k - x = \text{even}, k \geq x + 2.$$ (A-7)

The same procedure as used before brings the product to the form suitable for efficient evaluation, i.e.,

$$\langle T_j, D^2 T_k \rangle = k(k^2 - j^2)\pi/2 \,, k - j = \text{even}, k \geq j + 2. \tag{A-8}$$

Differentiation of (A-7) with respect to ξ leads to an expression for the third derivative of a Chebyshev polynomial

$$D^3 T_k = \sum_{x=0}^{k-1} \frac{k(k^2 - x^2)DT_x}{C_x}, k - x = \text{even}, k \geq x + 2. \tag{A-9}$$

Substitution of (A-4) into (A-9) and use of (A-2) result in

$$\langle T_j, D^3 T_k \rangle = \sum_{x=0}^{k-2} \frac{k(k^2 - x^2)\pi x}{C_x}, k - x = \text{even}, k \geq x + 2, x - j = \text{odd}, \tag{A-10}$$
$$x \geq j + 1.$$

Product involving the forth derivative can be evaluated using the same procedure as used in the case of $\langle T_j, D^3 T_k \rangle$. The final expression suitable for efficient evaluation has the form

$$\langle T_j, D^4 T_k \rangle = \sum_{x=0}^{k-2} \frac{k(k^2 - x^2)}{C_x} \left[\frac{x(x^2 - j^2)\pi}{2} \right], k - x = \text{even}, k \geq x + 2 \geq j + 4, \tag{A-11}$$
$$x - j = \text{even}.$$

Evaluation of products of type $\langle T_j, \xi^l D^m T_k \rangle$ begins with expressing ξ^l in terms of Chebyshev polynomials, i.e.,

$$\xi = \sum_{m=0}^{1} A_m T_m(\xi) \,, \xi^2 = \sum_{m=0}^{2} B_m T_m(\xi) \,, \xi^3 = \sum_{m=0}^{3} C_m T_m(\xi),$$
$$\xi^4 = \sum_{m=0}^{4} D_m T_m(\xi), \tag{A-12}$$

where $A_m = [0\ 1]$, $B_m = [1/2\ 0\ 1/2]$, $C_m = [0\ 3/4\ 0\ 1/4]$ and $D_m = [3/8\ 0\ 1/2\ 0\ 1/8]$. This leads to the appearance of products of Chebyshev polynomials, which need to be expressed in terms of Chebyshev polynomials. This is accomplished using the following relation

$$T_m(\xi)T_n(\xi) = \frac{1}{2}\left[T_{m+n}(\xi) + T_{|m-n|}(\xi)\right] \tag{A-13}$$

Substitution of (A-12) and (A-13) into definition of the scalar product brings this product into a form that can be arranged for the final computation using formulae presented above. Product $\langle T_j, \xi^l D^m T_k \rangle$ for $l = 2$ is written explicitly in order to assist the reader interested in the implementation of this method. This product has the form

$$\langle T_j, \xi^2 D^m T_k \rangle = \int_{\xi=-1}^{\xi=1} \frac{T_j(\xi)\xi^2 D^m T_k(\xi)}{\sqrt{1-\xi^2}}\,d\xi$$
$$= \frac{1}{2}\int_{\xi=-1}^{\xi=1} \frac{T_j(\xi)D^m T_k(\xi)}{\sqrt{1-\xi^2}}\,d\xi + \frac{1}{4}\int_{\xi=-1}^{\xi=1} \frac{T_{j+2}(\xi)D^m T_k(\xi)}{\sqrt{1-\xi^2}}\,d\xi$$
$$+ \frac{1}{4}\int_{\xi=-1}^{\xi=1} \frac{T_{|j-2|}(\xi)D^m T_k(\xi)}{\sqrt{1-\xi^2}}\,d\xi \tag{A-14}$$
$$= \frac{\langle T_j, D^m T_k \rangle}{2} + \frac{\langle T_{j+2}, D^m T_k \rangle}{4} + \frac{\langle T_{|j-2|}, D^m T_k \rangle}{4}.$$

where method for evaluation of each individual product on the right hand side has been explained before.

Appendix B

Appendix B: Evaluation of Fourier coefficients of the Chebyshev polynomials evaluated at the inner and outer cylinder

Evaluation of Fourier Coefficients in Expansions (2.2.27) begins with the expansions for lowest order Chebyshev polynomial, i.e., $w_{in,k}^{(m)}$ with $k = 0$ and $k = 1$.

$$T_0 = 1 \Longrightarrow \sum_{m=-\infty}^{+\infty} w_{in,0}^{(m)} e^{in\alpha z} = 1 \Longrightarrow \begin{cases} w_{in,0}^{(0)} = 1 \\ w_{in,0}^{(m)} = 0, m \neq 0 \end{cases}, \tag{B-1}$$

$$T_1[\xi_{in}(z)] = \xi_{in}(z) \Longrightarrow \sum_{m=-\infty}^{+\infty} w_{in,1}^{(m)} e^{in\alpha z} = \sum_{m=-\infty}^{+\infty} A_{in}^{(m)} e^{in\alpha z} \Longrightarrow w_{in,1}^{(m)} = A_{in}^{(m)}. \tag{B-2}$$

The remaining coefficients $w_{in,k}^{(m)}$ ($k \geq 2$) can be computed using the following recursion relation

$$T_{k+1}[\xi_{in}(z)] = 2\xi_{in}(z) T_k[\xi_{in}(z)] - T_{k-1}[\xi_{in}(z)] \Longrightarrow$$
$$w_{in,k+1}^{(m)} = 2 \sum_{n=-N_A}^{N_A} A_{in}^{(n)} w_{in,k}^{(m-n)} - w_{in,k-1}^{(m)}, k \geq 2. \tag{B-3}$$

Evaluation of coefficients of the expansions of derivatives of the Chebyshev polynomials also begins with the polynomials of the lowest order, i.e.,

$$DT_0 = 0 \Longrightarrow \sum_{m=-\infty}^{+\infty} d_{in,0}^{(m)} e^{in\alpha z} = 0 \Longrightarrow d_{in,0}^{(0)} = 0, \tag{B-4}$$

$$DT_1 = 1 \Longrightarrow \sum_{m=-\infty}^{+\infty} d_{in,0}^{(m)} e^{in\alpha z} = 1 \Longrightarrow \begin{cases} d_{in,0}^{(0)} = 1 \\ d_{in,0}^{(m)} = 0, m \neq 0 \end{cases}, \tag{B-5}$$

$$DT_2[\xi_{in}(z)] = 4\xi_{in}(z) \Longrightarrow \sum_{m=-\infty}^{+\infty} d_{in,2}^{(m)} e^{in\alpha z} = \sum_{m=-\infty}^{+\infty} 4A_{in}^{(m)} e^{in\alpha z}$$
$$\Longrightarrow d_{in,2}^{(m)} = 4A_{in}^{(m)}. \tag{B-6}$$

The remaining coefficients $d_{in,k}^{(m)}, k \geq 3$ can be computed using the following recursive formula

$$DT_{k+1}[\xi_{in}(z)] = 2T_k[\xi_{in}(z)] + 2\xi_{in}(z)DT_k[\xi_{in}(z)] - DT_{k-1}[\xi_{in}(z)] \Longrightarrow$$

$$d_{in,k+1}^{(m)} = 2 \sum_{n=-N_A}^{N_A} A_{in}^{(n)} d_{in,k}^{(m-n)} - d_{in,k-1}^{(m)} - w_{in,k}^{(m)}, k \geq 3. \qquad \text{(B-7)}$$

Appendix C

Appendix C: Explicit form of geometrical coefficients of asymptotic solution ($R_1 \rightarrow \infty$).

$$F_{A,1} = \frac{R_1^{-1} H_1(\eta, \xi)}{1 + F(\eta, \xi)/R_1} + \frac{H_3(\eta, \xi)}{[1 + F(\eta, \xi)/R_1]^2},$$

$$F_{A,2} = H_1^2(\eta, \xi) + \frac{H_2^2(\eta, \xi)}{[1 + F(\eta, \xi)/R_1]^2}, F_{A,3} = \frac{2\alpha H_2(\eta, \xi)}{[1 + F(\eta, \xi)/R_1]^2}, \quad \text{(C-1)}$$

$$F_{A,4} = \frac{\alpha^2}{[1 + F(\eta, \xi)/R_1]^2},$$

$$H_1(\eta, \xi) = 2f^{-1}(\xi) \quad \text{(C-2)}$$

$$H_2(\eta, \xi) = -\alpha\{[y_{out}(\xi) + y_{in}(\xi)]_\xi + \eta f_\xi(\xi)\}f^{-1}(\xi) \quad \text{(C-3)}$$

$$H_3(\eta, \xi) = -\alpha^2\{[y_{out}(\xi) + y_{in}(\xi)]_{\xi\xi} + \eta f_{\xi\xi}(\xi) + 2\alpha^{-1}H_2(\eta, \xi)f_\xi(\xi)\}f^{-1}(\xi) \quad \text{(C-4)}$$

$$F(\eta, \xi) = [\eta f(\xi) + y_{out}(\xi) + y_{in}(\xi)]/2, f(\xi) = y_{out}(\xi) - y_{in}(\xi). \quad \text{(C-5)}$$

Coefficients (C-2)-(C-5) simplify in the case of geometry described by Eq. (3.3.6) (sinusoidal grooves placed at the inner cylinder) to the form

$$F(\eta, \xi) = 1 + 0.5(\eta - 1)f(\xi), \quad f(\xi) = 1 - 0.5 S_{in}cos\xi, \quad \text{(C-6)}$$

$$H_1(\eta, \xi) = 2f^{-1}(\xi), \quad H_2(\eta, \xi) = -0.5\alpha S_{in}sin\xi(\eta - 1)f^{-1}(\xi), \quad \text{(C-7)}$$

$$H_3(\eta, \xi) = 0.25\alpha^2(\eta - 1)f^{-2}(\xi)[S_{in}^2(1 + sin^2\xi) - 2S_{in}cos\xi] . \quad \text{(C-8)}$$

Appendix D

Appendix D: Asymptotic solution $(R_1 \to \infty)$ for annulus with sinusoidal grooves placed at the outer cylinder

Shape of the annulus is given as

$$r_{in}(\theta) = R_1, \ r_{out}(\theta) = 1 + R_1 + 0.5 S_{out} \cos(M\theta), \tag{D-1}$$

and solution has the form

$$\hat{v}_0(\eta) = (1 + 3S_{out}^2/8)^{-1} g^2(\xi)(1 - \eta^2), \tag{D-2}$$

$$\frac{\partial \hat{p}_0}{\partial z} = -\frac{8}{Re}(1 + 3S_{out}^2/8)^{-1}, \tag{D-3}$$

$$\hat{v}_1(\eta) = g^2(\xi)(1 + 3S_{out}^2/8)^{-1}(1 - \eta^2)[\eta g(\xi)/6 \\ + 3S_{out}^2(1 + 3S_{out}^2/8)^{-1}(1 + S_{out}^2/16)/16], \tag{D-4}$$

$$\frac{\partial \hat{p}_1}{\partial z} = \frac{3S_{out}^2}{2Re}(1 + 3S_{out}^2/8)^{-2}(1 + S_{out}^2/16) \tag{D-5}$$

where

$$g(\xi) = 1 + 0.5 S_{out} \cos(\xi). \tag{D-6}$$

Appendix E

Appendix E: Evaluation of the axial force and stress tensor components at the inner and outer cylinders of the annulus fitted with longitudinal grooves

$$\tau_{rz} = -Re^{-1}B(\xi)^{-1} \sum_{n=-N_M}^{N_M} \sum_{k=0}^{N_T} G_k^{(n)} DT_k(-1)e^{inM\xi}, \tag{E-1}$$

$$\tau_{\theta z} = -Re^{-1}r_{in}(\xi)^{-1} \left[G_2(\xi, -1) \sum_{n=-N_M}^{N_M} \sum_{k=0}^{N_T} G_k^{(n)} DT_k(-1)e^{inM\xi} \right. $$
$$\left. + \sum_{n=-N_M}^{N_M} \sum_{k=0}^{N_T} inM G_k^{(n)}(-1)^k e^{inM\xi} \right]. \tag{E-2}$$

Expression for the shear stress along the surface of the cylinder takes the form

$$dF_{total,z} = \left\{ 1 + \left[\left(\sum_{n=-N_A}^{N_A} inM H_{in}^{(n)} e^{inM\xi} \right) r_{in}(\xi)^{-1} \right]^2 \right\}^{-1/2}$$
$$\left\{ -Re^{-1}r_{in}(\xi)^{-2} \left[G_2(\xi, -1) \sum_{n=-N_M}^{N_M} \sum_{k=0}^{N_T} G_k^{(n)} DT_k(-1)e^{inM\xi} \right. \right.$$
$$\left. + \sum_{n=-N_M}^{N_M} \sum_{k=0}^{N_T} inM G_k^{(n)}(-1)^k e^{inM\xi} \right] \sum_{n=-N_A}^{N_A} inM H_{in}^{(n)} e^{inM\xi}$$
$$\left. + Re^{-1}B(\xi)^{-1} \sum_{n=-N_M}^{N_M} \sum_{k=0}^{N_T} G_k^{(n)} DT_k(-1)e^{inM\xi} \right\}. \tag{E-3}$$

Appendix F

Appendix F: The small wave number limit solution for the basic state of the flow in a channel with longitudinal grooves

The governing equations, the boundary conditions and the constraints forming the four leading order systems resulting from the small wave number approximation (see Section 2.3):

$$O(\beta^0): \frac{\partial^2 U_0}{\partial \varsigma^2} - ReH^2 \frac{dP_0}{dx} = 0, U_0(\chi, \pm 1) = 0, \frac{1}{2\pi} \int_{\chi=0}^{\chi=2\pi} \int_{\varsigma=-1}^{\varsigma=1} HU_0 d\varsigma d\chi = \frac{4}{3}, \qquad \text{(F-1)}$$

$$O(\beta^1): \frac{\partial^2 U_1}{\partial \varsigma^2} - ReH^2 \frac{dP_1}{dx} = 0, U_1(\chi, \pm 1) = 0, \int_{\chi=0}^{\chi=2\pi} \int_{\varsigma=-1}^{\varsigma=1} HU_1 d\varsigma d\chi = 0, \qquad \text{(F-2)}$$

$$O(\beta^2): \frac{\partial^2 U_2}{\partial \varsigma^2} - ReH^2 \frac{dP_2}{dx} + \left[2H_\chi G_\chi + 2\varsigma H_\chi^2 - H(G_{\chi\chi} + \varsigma H_{\chi\chi})\right] \frac{\partial U_0}{\partial \varsigma}$$

$$- 2H(G_\chi + \varsigma H_\chi) \frac{\partial^2 U_0}{\partial \varsigma \partial \chi} + H^2 \frac{\partial^2 U_0}{\partial \chi^2} + ReH^2(G_\chi + \varsigma H_\chi) \frac{dP_0}{dx} \qquad \text{(F-3)}$$

$$= 0, U_2(\chi, \pm 1) = 0, \int_{\chi=0}^{\chi=2\pi} \int_{\varsigma=-1}^{\varsigma=1} HU_2 d\varsigma d\chi = 0,$$

$$O(\beta^3): \frac{\partial^2 U_3}{\partial \varsigma^2} - ReH^2 \frac{dP_3}{dx} = 0, U_3(\chi, \pm 1) = 0, \int_{\chi=0}^{\chi=2\pi} \int_{\varsigma=-1}^{\varsigma=1} HU_3 d\varsigma d\chi = 0, \qquad \text{(F-4)}$$

Appendix G

Appendix G: Definitions of operators T, S, C, E_v, E_η, H_v, H_η appearing in the linear disturbance equations of flow in a channel with longitudinal grooves

$$T^{(m)}(y) = Re^{-1}(D^2 - k_m^2)^2 + i(D^2 - k_m^2)[\sigma - \delta u_0(y)] + i\delta D^2 u_0(y) \tag{G-1}$$

$$S^{(m)}(y) = Re^{-1}[D^2 - k_m^2 - i\delta Re u_0(y) + i\sigma], \tag{G-2}$$

$$C^{(m)}(y) = t_m D u_0(y) \tag{G-3}$$

$$H_v^{(m,n)}(y) = -i\delta(D^2 + k_m^2)u_1^{(n)}(y) + \frac{2in\beta t_{m-n}}{k_{m-n}^2} D u_1^{(n)}(y)D$$

$$+ \frac{i\delta}{k_{m-n}^2}[k_m^2 - (n\beta)^2]u_1^{(n)}(y)D^2, \tag{G-4}$$

$$H_\eta^{(m,n)}(y) = \frac{2n\beta\delta^2}{k_{m-n}^2}\left[D u_1^{(n)}(y) + u_1^{(n)}(y)D\right], \tag{G-5}$$

$$E_v^{(m,n)}(y) = \left[-t_m D u_1^{(n)}(y) + n\beta\left(1 + \frac{n\beta t_{m-n}}{k_{m-n}^2}\right)u_1^{(n)}(y)D\right], \tag{G-6}$$

$$E_\eta^{(m,n)}(y) = i\delta\left(1 - \frac{n^2\beta^2}{k_{m-n}^2}\right)u_1^{(n)}(y), \tag{G-7}$$

$$t_m = \mu + m\beta, \quad k_m^2 = \delta^2 + t_m^2, \tag{G-8}$$

where $D^n = d^n/dy^n$.

Appendix H

Appendix H: Discretization of the disturbance equations of flow in a channel with longitudinal grooves

The flow domain is contained between $(-1 - y_b)$ and $(1 + y_t)$, where y_b and y_t denote locations of the groove extremities. In order to use the standard definition of the Chebyshev polynomials, this domain is mapped into (-1,1) using transformation of the form

$$\hat{y} = [y - (1 + y_t)]\Gamma + 1, \Gamma = 2(2 + y_t + y_b)^{-1}. \tag{H-1}$$

The T, S, C, E_v, E_η, H_v, H_η operators in the new coordinates system take the form

$$T^{(m)}(\hat{y}) = Re^{-1}(\Gamma^2 D^2 - k_m^2)^2 + i(\Gamma^2 D^2 - k_m^2)[\sigma - \delta u_0(\hat{y})] \\ + i\delta\Gamma^2 D^2 u_0(\hat{y}) \tag{H-2}$$

$$S^{(m)}(\hat{y}) = Re^{-1}[\Gamma^2 D^2 - k_m^2 - i\delta Re u_0(\hat{y}) + i\sigma], \tag{H-3}$$

$$C^{(m)}(\hat{y}) = t_m \Gamma D u_0(\hat{y}) \tag{H-4}$$

$$H_v^{(m,n)}(\hat{y}) = -i\delta(\Gamma^2 D^2 + k_m^2)u_1^{(n)}(\hat{y}) + \frac{2in\beta t_{m-n}\Gamma^2}{k_{m-n}^2} D u_1^{(n)}(\hat{y})D \\ + \frac{i\delta\Gamma^2}{k_{m-n}^2}[k_m^2 - (n\beta)^2]u_1^{(n)}(\hat{y})D^2, \tag{H-5}$$

$$H_\eta^{(m,n)}(\hat{y}) = \frac{2n\beta\delta^2\Gamma}{k_{m-n}^2}\left[D u_1^{(n)}(\hat{y}) + u_1^{(n)}(\hat{y})D\right], \tag{H-6}$$

$$E_v^{(m,n)}(\hat{y}) = \Gamma\left[-t_m D u_1^{(n)}(\hat{y}) + n\beta\left(1 + \frac{n\beta t_{m-n}}{k_{m-n}^2}\right)u_1^{(n)}(\hat{y})D\right] \tag{H-7}$$

$$E_\eta^{(m,n)}(\hat{y}) = i\delta\left(1 - \frac{n^2\beta^2}{k_{m-n}^2}\right)u_1^{(n)}(\hat{y}). \tag{H-8}$$

The unknown modal functions are expressed as Chebyshev expansions (5.3.9) and the mean flow and the reference flow quantities are expressed in term of the relevant Chebyshev expansions of the form

$$u_1^{(n)}(\hat{y}) = \sum_{k=0}^{N_T} G_{l,B}^{(n)} T_k(\hat{y}), \tag{H-9}$$

$$u_0(\hat{y}) = -T_2(\hat{y})/(2\Gamma^2) - 2(1 + y_t - 1/\Gamma)T_1(\hat{y})/\Gamma$$
$$+ [1 - (1 + y_t - 1/\Gamma)^2 - 1/(2\Gamma^2)]T_0(\hat{y}),$$
$$Du_0(\hat{y}) = -2\,T_1(\hat{y})/(\Gamma^2) - 2(1 + y_t - 1/\Gamma)T_0(\hat{y})/\Gamma\,, D^2u_0(\hat{y})$$
$$= -2T_0(\hat{y})/\Gamma^2 \tag{H-10}$$

Substitution of (C-9)-(C-10) into (C-2)-(C8) results in an algebraic system of the form

$$\sum_{k=0}^{N_T}\{Re^{-1}\Gamma^4 D^4 T_k - \Gamma^2(2Re^{-1}k_m^2 + i\delta u_0)D^2 T_k$$
$$+ [Re^{-1}k_m^4 + i\delta(\Gamma^2 D^2 u_0 + k_m^2 u_0)]T_k\}\,G_{k,v}^{(m)}$$
$$- \sum_{n=-N_N}^{+N_N}\sum_{k=0}^{+N_T}\left[H_v^{(m,n)}T_k G_{k,v}^{(m-n)} + H_\eta^{(m,n)}T_k G_{k,\eta}^{(m-n)}\right] \tag{H-11a}$$
$$= -i\sigma \sum_{k=0}^{+N_T}(\Gamma^2 D^2 T_k - k_m^2 T_k)G_{k,v}^{(m)},$$

$$\sum_{k=0}^{N_T}[Re^{-1}\Gamma^2 D^2 T_k - (Re^{-1}k_m^2 + i\delta u_0)T_k]G_{k,\eta}^{(m)} + t_m\Gamma Du_0 T_k G_{k,v}^{(m)}$$
$$- \sum_{n=-N_N}^{+N_N}\sum_{k=0}^{+N_T}\left[E_v^{(m,n)}T_k G_{k,v}^{(m-n)} + E_\eta^{(m,n)}T_k G_{k,\eta}^{(m-n)}\right] = -i\sigma \sum_{k=0}^{+N_T}T_k G_{k,\eta}^{(m)}. \tag{H-10b}$$

Application of the Galerkin projection method leads to a linear system for the expansion coefficients of the form

$$\sum_{k=0}^{N_T}[Re^{-1}\Gamma^4\langle T_j, D^4 T_k\rangle - 2Re^{-1}k_m^2\Gamma^2\langle T_j, D^2 T_k\rangle + Re^{-1}k_m^4\langle T_j, T_k\rangle$$
$$- i\delta\Gamma^2\langle T_j, u_0 D^2 T_k\rangle + i\delta k_m^2\langle T_j, u_0 T_k\rangle$$
$$+ i\delta\Gamma^2\langle T_j, D^2 u_0 T_k\rangle]G_{k,v}^{(m)} + \sum_{n=-N_N}^{N_N}\sum_{l=0}^{N_T}\left[i\delta k_m^2\langle T_j, T_l T_k\rangle + i\delta\,\Gamma^2\langle T_j, D^2 T_l T_k\rangle\right.$$
$$- \frac{2in\beta\delta t_{m-n}\Gamma^2}{k_{m-n}^2}\langle T_j, DT_l DT_k\rangle \tag{H-12a}$$
$$\left. - \frac{i\delta\Gamma^2(k_m^2 - n^2\beta^2)}{k_{m-n}^2}\langle T_j, T_l D^2 T_k\rangle\right]G_{l,B}^{(n)}G_{k,v}^{(m-n)}$$
$$- \sum_{n=-N_N}^{N_N}\sum_{l=0}^{N_T}\frac{2n\beta\delta^2\Gamma}{k_{m-n}^2}\left(\langle T_j, DT_l T_k\rangle + \langle T_j, T_l DT_k\rangle\right)G_{l,B}^{(n)}G_{k,\eta}^{(m-n)}$$

$$= -i\sigma\big(\Gamma^2\langle T_j, D^2 T_k\rangle - k_m^2\langle T_j, T_k\rangle\big)G_{k,v}^{(m)},$$

$$\sum_{k=0}^{N_T}\Big[Re^{-1}\Gamma^2\langle T_j, D^2 T_k\rangle - Re^{-1}k_m^2\langle T_j, T_k\rangle - i\delta\langle T_j, u_0 T_k\rangle\Big]G_{k,\eta}^{(m)}$$

$$+ t_m\Gamma\langle T_j, Du_0 T_k\rangle G_{k,v}^{(m)}$$

$$+ \sum_{n=-N_N}^{N_N}\sum_{l=0}^{N_T}\Big[t_m\Gamma\langle T_j, DT_l T_k\rangle - n\beta\Gamma\left(1 + \frac{n\beta t_{m-n}}{k_{m-n}^2}\right)\langle T_j, T_l DT_k\rangle\Big]G_{l,B}^{(n)}G_{k,v}^{(m-n)} \qquad \text{(H-11b)}$$

$$+ \sum_{n=-N_N}^{N_N}\sum_{l=0}^{N_T} i\delta\left(\frac{n^2\beta^2}{k_{m-n}^2} - 1\right)\langle T_j, T_l T_k\rangle\, G_{l,B}^{(n)}G_{k,\eta}^{(m-n)} = -i\sigma\langle T_j, T_k\rangle G_{k,\eta}^{(m)}.$$

The inner product $\langle T_j, D^n T_l D^m T_k\rangle$ is defined as

$$\langle T_j, D^n T_l D^m T_k\rangle = \int_{-1}^{1} T_j(\hat{y})\, D^n T_l(\hat{y}) D^m T_k(\hat{y})\omega(\hat{y})d\hat{y}, \qquad \text{(H-13)}$$

where $\omega(y) = 1/\sqrt{1 - y^2}$. Evaluation of these products can be simplified by taking advantage of the orthogonality properties of the Chebyshev polynomials (Moradi and Floryan, 2011).

Appendix I

Appendix I: Description of boundary relations required to complete formulation of the linear stability problem.

The homogeneous boundary conditions (5.3.4) need to be expressed in terms of $\eta^{(m)}(\hat{y})$ and $g_v^{(m)}(\hat{y})$. They can be written for the lower wall in the form

$$u_D(x, \hat{y}_L, z, t) = \sum_{n=-N_N}^{+N_N} \left[\frac{i\delta\Gamma}{k_n^2} Dg_v^{(n)}(\hat{y}_L) - \frac{t_n}{k_n^2}\eta^{(n)}(\hat{y}_L) \right] e^{i[\delta x + (\mu + n\beta)z - \sigma t]} = 0 \ , \tag{I-1}$$

$$v_D(x, \hat{y}_L, z, t) = \sum_{n=-N_N}^{+N_N} g_v^{(n)}(\hat{y}_L) e^{i[\delta x + (\mu + n\beta)z - \sigma t]} = 0 \ , \tag{I-2}$$

$$w_D(x, \hat{y}_L, z, t) = \sum_{n=-N_N}^{+N_N} \left[\frac{it_n\Gamma}{k_n^2} Dg_v^{(n)}(\hat{y}_L) + \frac{\delta}{k_n^2}\eta^{(n)}(\hat{y}_L) \right] e^{i[\delta x + (\mu + n\beta)z - \sigma t]} = 0. \tag{I-3}$$

Location of this wall is given as

$$\hat{y}_L(z) = \sum_{n=-N_A}^{N_A} A_L^{(n)} e^{in\beta z} \tag{I-4}$$

where $A_L^{(n)} = -\Gamma\left(2 + y_t - H_L^{(n)}\right) + 1$ for $n = 0$ and $A_L^{(n)} = \Gamma H_L^{(n)}$ for $n \neq 0$. As the first step, consider boundary condition (D-1). Substitution of (5.3.9) into (I-1) leads to

$$\sum_{n=-N_N}^{+N_N} \sum_{k=0}^{+N_T} \frac{i\delta\Gamma}{k_n^2} DT_k(\hat{y}_L(z)) G_{k,v}^{(n)} e^{i[\delta x + (\mu + n\beta)z - \sigma t]}$$
$$- \sum_{n=-N_N}^{+N_N} \sum_{k=0}^{+N_T} \frac{t_n}{k_n^2} T_k(\hat{y}_L(z)) G_{k,\eta}^{(n)} e^{i[\delta x + (\mu + n\beta)z - \sigma t]} = 0. \tag{I-5}$$

Values of Chebyshev polynomials and their first derivative along the wall appearing in the above relation, i.e. $T_k(\hat{y}_L(z))$ and $DT_k(\hat{y}_L(z))$, represent periodic functions of z and, thus, can be expressed using Fourier expansions of the form

$$T_k\big(\hat{y}_L(z)\big) = \sum_{m=-\infty}^{+\infty} (w_L)_k^{(m)} e^{im\beta z} \,, DT_k\big(\hat{y}_L(z)\big) = \sum_{m=-\infty}^{+\infty} (d_L)_k^{(m)} e^{im\beta z}. \tag{I-6}$$

The reader may note that substitution of (D-6) into (D-5) leads to a certain Fourier expansion whose convergence rate affects the number of Fourier modes that have to be used in the solution. The expansion has, in general, a different convergence rate from expansion (3-7).

Evaluation of coefficients $(w_L)_k^{(m)}$ begins with the lowest order Chebyshev polynomial, i.e.

$$T_0 = 1 \Rightarrow \sum_{m=-\infty}^{+\infty} w_{L,0}^{(m)} e^{im\beta z} = 1 \Rightarrow \begin{cases} w_{L,0}^{(0)} = 1 \\ w_{L,0}^{(m)} = 0, m \neq 0 \end{cases}, \tag{I-7}$$

$$T_1[\hat{y}_L(z)] = \hat{y}_L(z) \Rightarrow \sum_{m=-\infty}^{+\infty} w_{L,1}^{(m)} e^{im\beta z} = \sum_{m=-\infty}^{+\infty} A_L^{(m)} e^{im\beta z} \Rightarrow w_{L,1}^{(m)}$$
$$= A_L^{(m)}. \tag{I-8}$$

The remaining coefficients $w_{L,k}^{(m)}$ ($k \geq 2$) can be computed using the Chebyshev recursion relation which results in

$$w_{L,k+1}^{(m)} = 2 \sum_{n=-N_A}^{N_A} A_L^{(n)} w_{L,k}^{(m-n)} - w_{L,k-1}^{(m)}, k \geq 2. \tag{I-9}$$

Evaluation of the coefficients $(d_L)_k^{(m)}$ also begins with the lowest order polynomial, i.e.

$$DT_0 = 0 \Rightarrow \sum_{m=-\infty}^{+\infty} d_{L,0}^{(m)} e^{im\beta z} = 0 \Rightarrow d_{L,0}^{(0)} = 0, \tag{I-10}$$

$$DT_1 = 1 \Rightarrow \sum_{m=-\infty}^{+\infty} d_{L,0}^{(m)} e^{im\beta z} = 1 \Rightarrow \begin{cases} d_{L,0}^{(0)} = 1 \\ d_{L,0}^{(m)} = 0, m \neq 0 \end{cases}, \tag{I-11}$$

$$DT_2[\hat{y}_L(z)] = 4\hat{y}_L(z) \Longrightarrow \sum_{m=-\infty}^{+\infty} d_{L,2}^{(m)} e^{im\beta z} = \sum_{m=-\infty}^{+\infty} 4A_L^{(m)} e^{im\beta z} \Longrightarrow d_{in,2}^{(m)}$$

$$= 4A_{in}^{(m)}. \tag{I-12}$$

The remaining coefficients $d_{L,k}^{(m)}, k \geq 3$ can be computed using the Chebyshev recursive formula and have the following form

$$d_{L,k+1}^{(m)} = 2 \sum_{n=-N_A}^{N_A} A_L^{(n)} d_{L,k}^{(m-n)} - d_{L,k-1}^{(m)} - w_{L,k}^{(m)}, k \geq 3. \tag{I-13}$$

Substitution of (I-6) into (I-5) and separation of Fourier modes lead to boundary relation of the form

$$\sum_{n=-N_N}^{+N_N} \sum_{k=0}^{+N_T} \frac{i\delta\Gamma}{k_m^2} (d_L)_k^{(n-m)} G_{k,v}^{(n)} - \sum_{n=-N_N}^{+N_N} \sum_{k=0}^{+N_T} \frac{t_m}{k_m^2} (w_L)_k^{(n-m)} G_{k,\eta}^{(n)} = 0 \tag{I-14}$$

which expresses condition (D-1). Following the same procedure, the boundary conditions for v_D and w_D can be written in the form

$$\sum_{n=-N_N}^{+N_N} \sum_{k=0}^{+N_T} (w_L)_k^{(n-m)} G_{k,v}^{(n)} = 0. \tag{I-15}$$

$$\sum_{n=-N_N}^{+N_N} \sum_{k=0}^{+N_T} \frac{it_m\Gamma}{k_m^2} (d_L)_k^{(n-m)} G_{k,v}^{(n)} + \sum_{n=-N_N}^{+N_N} \sum_{k=0}^{+N_T} \frac{\delta}{k_m^2} (w_L)_k^{(n-m)} G_{k,\eta}^{(n)} = 0. \tag{I-16}$$

Boundary relations for the upper wall can be obtained by simply changing subscript 'L' into 'U' in the above equations. These relations provide the groove-induced coupling between different Fourier modes. The other coupling is provided by the field equations (3-8).

In general, the total number of the available boundary relations is $N_N + N_T N_A$, where N_N is the number of Fourier modes used in the discretization of the field equations, N_T is the number of the Chebyshev polynomials used in the discretization of the modal functions and N_A denotes the number of Fourier modes used to describe the groove geometry. Since only N_N modes are used in the numerical solution, one can enforce only N_N of these conditions. The remaining conditions can either be used *a posteriori* as a convenient test for the consistency of the algorithm or can be utilized directly leading to the over-determined formulation (Husain, Floryan & Szumbarski 2009).

Appendix J

Appendix J: Copyright releases

I.1 John Wiley and Sons

This is a License Agreement between Hadi Vafadar Moradi ("You") and John Wiley and Sons ("John Wiley and Sons"). The license consists of your order details, the terms and conditions provided by John Wiley and Sons, and the payment terms and conditions.

License Number	3259450764022
License date	Oct 31, 2013
Licensed content publisher	John Wiley and Sons
Licensed content publication	International Journal for Numerical Methods in Fluids
Licensed content title	Algorithm for analysis of flows in ribbed annuli
Licensed copyright line	Copyright © 2011 John Wiley & Sons, Ltd.
Licensed content author	H. V. Moradi,J. M. Floryan
Licensed content date	May 2, 2011
Start page	805
End page	838
Type of use	Dissertation/Thesis
Requestor type	Author of this Wiley article
Format	Print and electronic
Portion	Full article
Will you be translating?	No
Total	0.00 USD

I.2 Cambridge University Press

This is a License Agreement between Hadi Vafadar Moradi ("You") and Cambridge University Press ("Cambridge University Press"). The license consists of your order details, the terms and conditions provided by Cambridge University Press, and the payment terms and conditions.

License Number	3259451077646
License date	Oct 31, 2013
Licensed content publisher	Cambridge University Press
Licensed content publication	The Journal of Fluid Mechanics
Licensed content title	Flows in annuli with longitudinal grooves
Licensed content author	H. V. Moradi and J. M. Floryan
Licensed content date	Feb 10, 2013

Volume number	716
Issue number	-1
Start page	280
End page	315
Type of Use	Dissertation/Thesis
Requestor type	Author
Portion	Full article
Author of this Cambridge University Press article	Yes
Author / editor of the new work	Yes
Order reference number	
Territory for reuse	World
Title of your thesis / dissertation	Effects of Surface Topographies on Heat and Fluid Flows
Expected completion date	Jan 2014
Estimated size(pages)	300
Total	0.00 USD

I.3 Elsevier

This is a License Agreement between Hadi Vafadar Moradi ("You") and Elsevier ("Elsevier"). The license consists of your order details, the terms and conditions provided by Elsevier, and the payment terms and conditions.

License Number	3259441364885
License date	Oct 31, 2013
Licensed content publisher	Elsevier
Licensed content publication	International Journal of Heat and Mass Transfer
Licensed content title	Maximization of heat transfer across micro-channels
Licensed content author	Hadi Vafadar Moradi,Jerzy Maciej Floryan
Licensed content date	November 2013
Licensed content volume number	66
Number of pages	14
Type of Use	reuse in a thesis/dissertation
Portion	full article
Format	both print and electronic
Are you the author of this Elsevier article?	Yes
Will you be translating?	No
Order reference number	

Title of your thesis/dissertation	Effects of Surface Topographies on Heat and Fluid Flows
Expected completion date	Jan 2014
Estimated size (number of pages)	300
Elsevier VAT number	GB 494 6272 12
Permissions price	0.00 USD
VAT/Local Sales Tax	0.00 USD / 0.00 GBP
Total	0.00 USD

Curriculum Vitae

Name:	Hadi Vafadar Moradi
Post-secondary Education and Degrees:	Amir Kabir University of Technology (Tehran Polytechnic) Tehran, Iran 1998-2003 BSc.
	Iran University of Science and Technology Tehran, Iran 2003-2006 MSc.
	The University of Western Ontario London, Ontario, Canada 2009-2014 Ph.D.
Related Work Experience	Teaching Assistant The University of Western Ontario 2008-2013

Publications (Journals):

Moradi, H. V. & Floryan, J. M. 2012 Algorithm for Analysis of Flows in Ribbed Annuli, *Int. J. Numerical Methods in Fluid*, **68**, 805-838.

Moradi, H. V. & Floryan, J. M. 2013 Flows in Annuli with Longitudinal Grooves, *J. Fluid Mech.*, **716**, 280-315.

Moradi, H. V. & Floryan, J. M. 2013 Maximization of heat transfer across micro-channels, *Int. J. Heat & Mass Transfer*, **66**, 517-530.

Publications (Conferences):

Hosseinalipour, S. M. & Moradi, H. V. 2006 Comparison of Perfect and Real Gas Flow over Blunt Body Using AUSMDV and AUSM+, *2nd International Conference from Scientific Computing to Computational Engineering*, 5-8 July, Athens, Greece.

Moradi, H. V. & Hosseinalipour, S. M. 2006 On the Performance of AUSM based Schemes in Hypersonic Flow with Equilibrium Gas Effects, *14th AIAA/AHI Space Planes and Hypersonic Systems and Technologies Conference*, 5-7 November, Canberra, Australia.

Moradi, H. V. & Hosseinalipour, S. M. 2008 Hypersonic Two-Dimensional Navier-Stokes Computation with Equilibrium Gas Effects on a Hybrid Mesh, *15th AIAA*

Space Planes and Hypersonic Systems and Technologies Conference, Dayton, Ohio, United States.

Moradi, H. V. & Floryan, J. M. 2010 Spectrally Accurate Method for Analysis of Flows in Annuli bounded by Corrugated Walls, *18th Annual Conference of the CFD Society of Canada*, May 17–19, London, Ontario, Canada.

Moradi, H. V. & Floryan, J. M. 2011 Efficient Methods for Analysis of Flows in Grooved Annuli*, International conference on Applied Mathematics, Modeling and Computational Science*, , July 25-29, Waterloo, Canada.

Floryan, J. M. & Moradi, H. V. 2012 Grooved Surfaces for Laminar Drag Reduction, *American Mathematical Society (AMS), ICNAAM2012: 3rd Symposium on Semigroups of Linear Operators and Applications*, 19-25 September, Kos, Greece.

Moradi, H. V. & Floryan, J. M. 2012 Groove-Induced Drag Reduction in Annular Flows, *18th Australasian Fluid Mechanics Conference,* 3-7 December, Launceston, Australia.

Moradi, H. V. & Floryan, J. M. 2013 Channel Flow Modulated by Suction - Numerical Solution of the Linear Stability Equations, *21st Annual Conference of the CFD Society of Canada*, May 6-9, Sherbrooke, Quebec, Canada.

Moradi, H. V. & Floryan, J. M. 2013 Heat Transfer Intensification in Micro-Conduits, *24th CANCAM conference*, June 2-6, Saskatoon, Saskatchewan, Canada.